Developing Novel Processes in Chemistry for Several Types of Nanoparticles

A thesis submitted to The University of Manchester for the Doctor of Philosophy degree in the Faculty of Engineering and Physical Sciences

2011

Ahmed Mohammed Said Lutfi Abdelhady

School of Chemistry, The University of Manchester, Oxford Road, Manchester,

M13 9PL

Table of Contents

List of Figures

Chapter I

Chapter II

Chapter III

List of Tables

Abbreviations

VB	Valance band
CB	Conduction band
Eg	Band gap
0D	Zero-dimensional
1D	One-dimensional
2D	Two-dimensional
OLA	Oleylamine
HDA	Hexadecylamine
DDT	Dodecanethiol
ODE	Octadecene
TOPO	Trioctylphosphine oxide
TOPSe	Trioctylphosphine selenide
PTFE	Polytetrafluoroethylene
UV-Vis	Ultra violet - visible
FWHM	Full width half maxima
PL	Photoluminescence
QY	Quantum yield
MEG	Multiple Exciton Generation
ML	Monolayer
p-XRD	Powder X-ray diffraction
TEM	Transmission electron microscopy
HRTEM	High-resolution transmission electron microscopy
SAED	Selected area electron diffraction
EDAX	Energy dispersive X-ray analysis
ET	Electron tomography
FFT	Fast Fourier transform
LED	Light emitting diodes
SSP	Single Source precursor
Me	Methyl
Et	Ethyl
^{i}Pr	Isopropyl
Hex	Hexyl
et al.	Et alia
etc.	Et cetra
ca.	Circa
e.g.	Exempli gratia
i.e	Id est

Abstract

The work presented in this thesis reports the use of a series of novel thiobiuret metal complexes [$M(SON(CN^{i}Pr_2)_2)_n$] (M = Cu, Ni, Fe, Zn, Cd or In; n = 2 or 3) for the first time as single source precursors for the colloidal synthesis of metal sulfide nanoparticles. Other single source precursor(s) were also used for the synthesis of CdSe, CdS, CdSe/CdS core/shell, CdSeS alloys and $Cu_{2-x}S$ nanoparticles in microfluidic reactors.

Thermolysis experiments of [$Cu(SON(CN^{i}Pr_2)_2)_2$] using only oleylamine produced Cu_7S_4 nanoparticles as a mixture of monoclinic and orthorhombic phases. Pure orthorhombic Cu_7S_4 nanoparticles were obtained when a solution of precursor in octadecene was injected into hot oleylamine whereas, $Cu_{1.94}S$ nanoparticles were obtained when a solution of the precursor in oleylamine was injected into hot dodecanethiol. The thermolysis of [$Ni(SON(CN^{i}Pr_2)_2)_2$] gave Ni_3S_4 in all cases except when precursor solution in oleylamine was injected into hot octadecene which produced NiS nanoparticles. The thermolysis of [$Fe(SON(CN^{i}Pr_2)_2)_3$]in oleylamine/oleylamine produced Fe_7S_8 nanoparticles but other combinations, in most cases, gave amorphous material. Thermolysis of [$Zn(SON(CN^{i}Pr_2)_2)_2$] in oleylamine produced spherical ZnS nanoparticles. Particles with size smaller than 4.3 nm had a cubic phase, whereas the particles with size larger than 4.3 nm had a hexagonal crystal structure as suggested by the selected area electron diffraction. Powder X-Ray diffraction showed that the CdS nanoparticles obtained from the thermolysis of [$Cd(SON(CN^{i}Pr_2)_2)_2$] in oleylamine were cubic under all reaction conditions except when dodecanethiol was used as an injection solvent which produced hexagonal CdS. β-In_2S_3 were synthesized from the thermolysis of [$In(SON(CN^{i}Pr_2)_2)_3$]. Transmission electron microscopy showed that the copper, nickel and iron sulfide nanoparticles had various morphologies such as spherical, hexagonal disks, trigonal disks, rods or wires; depending on the reaction temperature, concentration of the precursor, the growth time and the solvent/capping agent combination. The zinc and cadmium sulfide nanoparticles were mostly spherical whereas the indium sulfide nanoparticles were produced in the form of ultra-thin (< 1.0 nm) nanorods or nanowires.

$Zn_xCd_{1-x}S$ and $CuInS_2$ nanoparticles were synthesised from the 1,1,5,5-tetra-*iso*-propyl-4-thiobiureto complexes of Zn, Cd and Cu, In, respectively. Powder X-ray diffraction showed that the obtained $Zn_xCd_{1-x}S$ nanoparticles are cubic under all reaction conditions. The $Zn_xCd_{1-x}S$ nanoparticles had an average diameter between 3.5 to 6.4 nm as shown by transmission electron microscopy. The optical properties of the $Zn_xCd_{1-x}S$ nanoparticles were highly dependent on the ZnS to CdS precursor ratio and the solvents/capping agents. Chalcopyrite (tetragonal), wurtzite (hexagonal) or a mixture of both $CuInS_2$ nanoparticles were obtained depending on the reaction conditions. TEM showed that the $CuInS_2$ nanoparticles could be synthesised with different morphologies (spherical, hexagonal, trigonal or cone). Luminescent $CuInS_2$ nanoparticles were obtained only in the absence of oleylamine.

[$Cd(S_2CNMe^{n}Hex)_2$], [$Cd(Se_2P(^{i}Pr)_2)_2$] and [$Cu(SON(CN^{i}Pr_2)_2)_2$] were used as single source precursor(s) for the synthesis of CdS, CdSe, CdSe/CdS core/shell, CdSeS alloys and $Cu_{2-x}S$ in microfludic reactor. The CdS nanoparticles were in size range of 5.0 to 8.0 nm whereas the CdSe nanoparticles were ultra small (*ca*. 2 nm) with blue luminescence. The CdSe/CdS core/shell and the CdSeS alloys were bluish green or green luminescent depending on their size. The copper sulfide nanoparticles were found to be monoclinic Cu_7S_4 or monoclinic Cu_7S_4 with minor impurities of rhombohedral Cu_9S_5 depending on the reaction conditions.

Declaration

I hereby declare that no part of this thesis has been submitted in support of an application for any degree or qualification of The University of Manchester or any other university or institution of learning. All work included was completed at The University of Manchester.

……

Ahmed Lutfi Abdelhady

Copyright and ownership of intellectual property rights

(i) The author of this thesis owns any copyright in it (the "copyright") and he has given The University of Manchester the right to use such copyright for any administrative, promotional, educational and/or teaching purposes.

(ii) Copies of this thesis, either in full or in extracts, may be made only in accordance with the regulations of the John Rylands University Library of Manchester. Details of these regulations may be obtained from the librarian. This page must be part of any such copies.

(iii) The ownership of any patents, design, trademarks and any all other intellectual property rights except for the copyright and any reproductions of copyright works, for example graphs and tables which may be described in this thesis, may not be owned by the author and may be owned by third parties. Such intellectual property rights and reproductions cannot and must not be made available for use without prior permission of the owner(s) of the relevant intellectual property rights and/or reproduction.

(iv) Further information on the conditions under which disclosures and exploitation may take place is available from the Head of School of Chemistry.

This thesis is dedicated to my dear parents, my wife and to all martyrs of the 2011 Egyptian revolution

Acknowledgment

All praise and thanks are due to Allah.

I would like to say a huge thank you to my supervisor Prof. Paul O'Brien for his precious help, guidance and encouragement throughout my degree. I would also like to thank Dr. M. Azad Malik and Dr. M. Afzaal for their help and advices. I gratefully acknowledge the financial support from the Egyptian Cultural Affairs and Missions Sector.

I appreciatively acknowledge Dr. Sarah Haigh for helping me with the TEM and for doing the electron tomography sample. I also wish to thank all POB group members past and present especially; Dr. Chinh Nguyen, Dr. Karthik Ramasamy, Dr. Weerakanya Maneeprakorn and Dr. Katayune Presland.

I want to state my deepest gratitude towards my parents for their full support, encouragement and for having faith in me. Last but by no means least my dear, beautiful and loving wife for making everything easier.

Chapter One

Introduction

Generally, nanoparticles are defined as particles of semiconductors, metals, alloys or any other material with a size range of 1 – 100 nm, having different properties compared to the bulk material with the same chemical composition.[1] The preparation of nanoparticles dates back to the 19th century, when Faraday[2] reported the preparation of colloidal gold nanoparticles. Current interest in these materials is due to the unique chemical and physical properties which arise with the huge reduction in size. The change in the properties at the nanometer-scale is a result of different causes in different materials.[3] In semiconductor nanoparticles (quantum dots), it is due to the confinement of the electronic motion to a length scale which is smaller than the bulk exciton (electron-hole pair) Bohr radius a characteristic property for the electronic motion in bulk semiconductors. Surface Plasmon absorption, is a new strong absorption observed when noble metals, *e.g.* Au, are prepared in the nanometer-scale. This new absorption is due to the collective oscillation of the electrons in the conduction band from one surface of the particle to the other. In transition metals nanoparticles, the high surface to volume ratio plus the ability of getting different nanoparticle sizes and shapes makes them useful in catalysis.

These changes in the properties of the materials make them useful for a wide variety of applications such as biological labelling,[4,5] *i.e.* semiconductor nanoparticles can be fluorescent, providing very sensitive luminescent character. Such nanocrystals can be modified to be water soluble in order to take advantage of the many biological and biochemical applications. Semiconductor nanoparticles are also used in photovoltaic devices because of its high intrinsic carrier mobilities. Quantum dot based photovoltaic cells were found to show high effectiveness of converting incident light energy to electrical energy with reduced current losses, and were also found to be incredibly encouraging for more commercially, practical and inexpensive renewable energy sources.[6,7] Light emitting diodes are becoming more based on semiconductor nanoparticles due to the narrow emission band and the fact that these materials can convert electrical power into light with an efficiency of 30%.[8,9]

1.1 Semiconductors

A semiconductor is a material with electrical conductivity between that of a conductor and that of an insulator. In the absence of applied electric fields, the resistance of semiconductors and insulators is almost the same. Some factors such as temperature can control the electrical properties of the semiconductors because of their smaller band gaps. Semiconductors are highly important in industry and new electronic devices such as digital audio players, televisions, cellular phones and computers. In bulk semiconductors, at low temperature, the lower energy levels (valence band-VB) are filled with electrons, while the higher energy levels (conduction band-CB) are unoccupied. The energy difference between the two bands is known as the band gap (E_g). Materials with a band gap between 0.3 and 3.8 eV are considered as semiconductors.[10] At higher temperatures, electrons in the VB gain enough energy to be excited to the CB, leaving a hole in the VB. The number (n) of the formed electron–hole pairs and their mobility (μ) controls the conductivity (σ) of the semiconductor according to equation (1.1), where q is the charge of the carrier.[10]

$$\sigma = qn_e\mu_e + qn_h\mu_h \qquad (1.1)$$

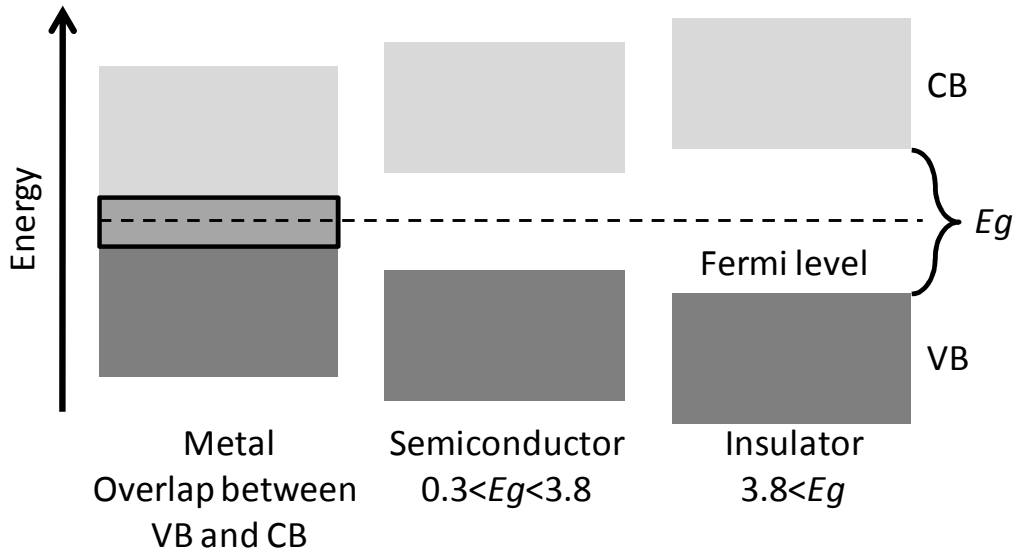

Fig. 1.1 Comparison of the electronic band structures of metals, semiconductors and insulators.

1.1.1 Classification of semiconductors

1.1.1.1 Semiconductors according to their purity

1.1.1.1.1 Intrinsic semiconductors

Pure semiconductors are known as intrinsic semiconductors and they are characterised by an equal number of charge carriers, *i.e.* number of excited electrons and number of holes are equal. Silicon, germanium, cadmium sulfide and copper indium disulfide are some examples of intrinsic semiconductors.

1.1.1.1.2 Extrinsic semiconductors

The electrical properties of these extremely pure semiconductors (intrinsic semiconductors) can be modified by a process known as doping, where impurities are introduced to the pure semiconductor forming extrinsic semiconductors. Each impurity atom adds an electron or a hole which flow freely. Extrinsic semiconductors are divided into two types depending on the kind of impurity.

- **n-type semiconductor**

n-type semiconductors are semiconductors with extra conduction electrons and hence the fermi level lies closer to the CB edge. Such semiconductor can be obtained by doping a group IV atom (silicon, germanium or tin) which has 4 valance electrons with a group V atom (phosphorus, arsenic or antimony) which has 5 valance electrons.

- **p-type semiconductor**

p-type semiconductors are semiconductors with extra positive charge carriers (hole), where the doping material accepts an electron from the semiconductor and moves the fermi level closer to the VB edge. A good example of a p-type semiconductor is doping silicon (tetravalent) with a trivalent group III atom (boron, gallium or aluminium).

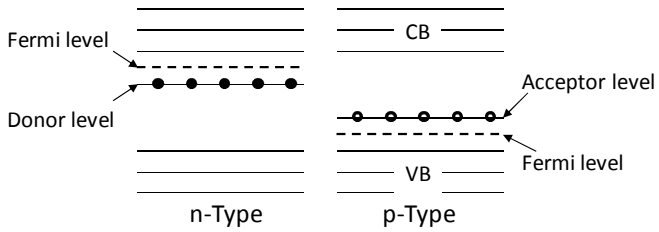

Fig. 1.2 Band gap diagrams of n-type and p-type semiconductors.

1.1.1.2 Semiconductors according to their optical properties

1.1.1.2.1 Direct band gap semiconductor

In direct band gap semiconductors, the transition of an excited electron from CB to VB involves no change in crystal momentum (K) (vibrational energy) as the minimum energy of the CB lies directly above the maximum energy of the VB in momentum space (Fig. 1.3(a)). Hence, the energy released from the electron-hole recombination is in the form of light photon, *i.e.* radiative recombination. Direct band gap semiconductors are characterised with a high absorption coefficient (α) which is related to the photon energy (hν) according to equation 1.2.[10] Examples of direct band gap semiconductors include: GaAs, CdS, CdSe and ZnS.

$$\alpha h\nu \propto (E_g - h\nu)^{1/2} \qquad (1.2)$$

1.1.1.2.2 Indirect band gap semiconductors

Indirect band gap means that as the excited electron returns from the CB to the VB, it underges a significant change in momentum as the minimum energy in the CB is shifted by a k-vector relative to the VB (Fig. 1.3(b)). In order to conserve momentum, the recombination of the electron-hole involves absorption or emission of a phonon which does not occur very frequently and therefore, indirect band gap semiconductors are inefficient light emitters. Such semiconductors have a low absorption coefficient (α) which is related to the photon energy (hν) according to equation 1.3. Examples of indirect band gap semiconductors include: Si and Ge.

$$\alpha h\nu \propto (E_g - h\nu)^{2} \qquad (1.3)$$

It is worth mentioning that Tauc *et al.*[11] reported that there is no conservation of momentum even for the direct band gap amorphous material.

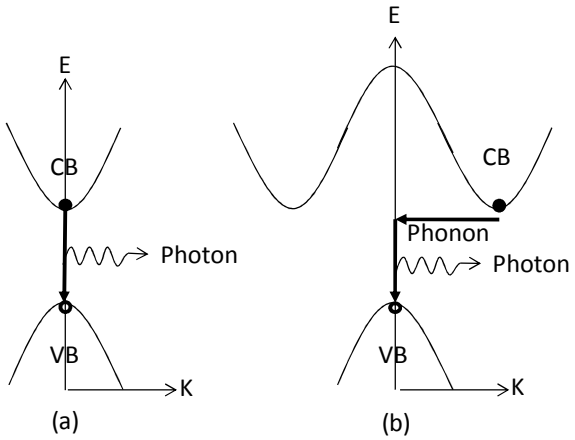

Fig. 1.3 Electron-hole recombination in (a) direct band gap semiconductor and (b) indirect band gap semiconductor.

1.2 Nanocrystalline semiconductors

1.2.1 Formation mechanism

The synthesis of monodispersed nanoparticles with size distribution $\sigma_r \leq 5\%$ is essential for most of the earlier mentioned nanoparticle-based applications.[12] Good understanding of the theory behind the formation of the nanoparticles will help to improve the synthetic routes applied for the synthesis of particular size and shape nanoparticles. Generally, the formation mechanism of monodispersed nanoparticles involves two separate steps: a rapid nucleation followed by a slow growth (Fig. 1.4).[12-21]

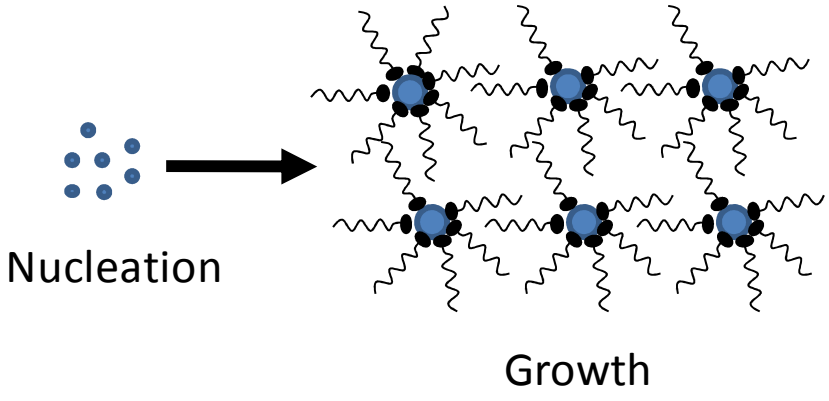

Fig. 1.4 Illustration of the nucleation and growth steps.

1.2.1.1 Nucleation

Nucleation could be either homogenous or heterogeneous. Homogenous nucleation takes place in the absence of any foreign material such as dust particles, bubbles or solid surfaces.[3,12,13] For nucleation to occur, the solution must be supersaturated. The degree of supersaturation (S) is given by $S = C/C_{eq}$, where C and C_{eq} are the concentrations of the solute at saturation and at equilibrium. The difference between the two concentrations is known as the driving force for precipitation. As nucleation starts in the supersaturated solution, nuclei with critical radius r_c exist in an equilibrium state. The critical radius corresponds to the minimum radius for a stable nucleus. Nuclei with radius smaller than r_c will dissolve whereas, the ones with radius bigger than r_c will grow forming stable nuclei which will grow forming particles. r_c can be obtained for a spherical particle by setting $d\Delta G/dr = 0$, where ΔG is the free energy of formation which is the sum of the excess surface free energy and the volume excess free energy. Thus:

$$\Delta G = 4\pi r^2\gamma + \frac{4}{3}\pi r^3 \Delta G_V \tag{1.4}$$

$$d\Delta G/dr = 8\pi r\gamma + 4\pi r^2 \Delta G_V \tag{1.5}$$

Where, γ is the interfacial tension and ΔG_V is the free energy change per unit volume. γ is always positive whereas, ΔG_V is negative as long as the solution is supersaturated.

At $d\Delta G/dr = 0$,

$$r_c = -2\gamma/\Delta G_V \tag{1.6}$$

From equations 1.4 and 1.6 we get:

$$\Delta G_c = \frac{16\pi\gamma^3}{3(\Delta G_V)^2} \tag{1.7}$$

Where, ΔG_c is the critical free energy which is the maximum value of ΔG and observed when $r = r_c$ as illustrated in Fig. 1.5. In other words, ΔG_c is the amount of energy required for the formation of stable nuclei.

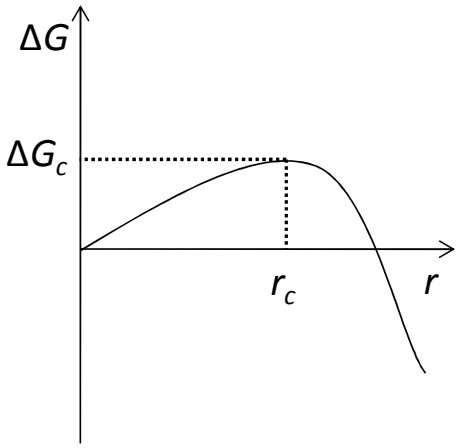

Fig. 1.5 Illustration of the free energy as a function of the growth particle size.

Since the basic Gibbis-Thomson relationship for non-electrolyte is given by:

$$\ln S = \ 2\gamma v/kTr \tag{1.8}$$

Where, *v* is the molar volume, *k* is Boltzmann constant and *T* is the temperature.

Hence equation 1.7 becomes:

$$\Delta G_c = \frac{16\pi\gamma^3 v^2}{3(kT\ \ln S)^2} \tag{1.9}$$

The rate of nucleation, as most thermally activated reactions, can be written in an Arrhenius reaction rate constant form:

$$\frac{dN}{dt} = A\ exp\left[-\frac{\Delta G_c}{kT}\right] = \ A\ exp\left[\frac{16\pi\gamma^3 v^2}{3k^3T^3(\ln S)^2}\right] \tag{1.10}$$

Equation 1.10 shows that the temperature, interfacial tension and degree of supersaturation are the key factors controlling the nucleation rate. In case of non-spherical nucleus, the term 16π/3 should be replaced with an appropriate value.[13]

This thermodynamic model has got some limitations[12] as γ and Δ*G* are not constants but highly size-dependent in case of nanoparticles.[22] Small nanoparticles have high tendency to decrease the surface free energy by changing the crystal structure or by reconstructing the surface structure. [16,18,23]

1.2.1.2 Growth

One of the main factors for the synthesis of monodispersed nanoparticles is inducing only one single nucleation and avoiding any secondary nucleation taking place during the growth step. According to equation 1.10, the nucleation step is terminated once the concentration drops below the critical level or by the rapid injection of the precursor(s) into a hot coordinating solvent (hot-injection method) and consequently a rapid drop in temperature.[3,18,19] The termination of the nucleation step with large amounts of the precursor(s) left in solution allows for the growth step through molecular addition to take place. During the growth process there are two competing effects: focusing and defocusing.[3,12-14,21,24,25] The focusing mode leads to a narrow size distribution, whereas the defocusing mode results in a broad size distribution. Focusing effect takes place when the growth is diffusion controlled where only mass-transport processes are considered.[12,24,25] On the other hand, reaction controlled growth process is observed when the growth rate depends more on the reaction kinetics. Under reaction controlled growth the defocusing effect prevails. Riess[26] provided a simple model for the growth rate and narrowing of the size distribution based on growth by diffusion. The model showed that the growth rate of a particle is inversely proportional to its radius (equation 1.11). Thus, smaller particles grow faster than the larger ones and size distribution gets narrower as long as all particles are growing and secondary nucleation is avoided.

$$\frac{dr}{dt} = \frac{vD}{r}(C_b - C_s) \qquad (1.11)$$

Where, dr/dt is the growth rate, D is the diffusion coefficient, C_b and C_s are the concentration in the bulk of the solution and at the particle surface, respectively.

The defocusing effect which is also known as the Ostwald ripening is based on the solubility of the particles as a function of their size.[3,12-14,21,24,25,27] Smaller particles are less stable and hence, tend to dissolve whereas larger particles continue to grow. This phenomenon can be explained by the change in the chemical potential ($\Delta\mu$) due to the change in the surface free energy of area (A).[12,27] According to equation 1.12, smaller particles have higher chemical potential which makes their growth difficult and therefore, dissolves easier.

$$\Delta\mu = \mu(r) - \mu^{\circ} = \gamma \frac{dA}{dn} \tag{1.10}$$

Where, μ(r) and μ° are the chemical potentials of a spherical particle with radius r and bulk crystal, respectively and n represent the number of particles.

Since dA = 8πrdr and dn = 4π^2dr/v, equation 1.12 can be written as:

$$\Delta\mu = \frac{2\gamma v}{r} \tag{1.13}$$

Talapin *et al.*[24] combined both effects to study the evolution of a single nanoparticle or an ensemble of nanoparticles in a colloidal solution. The following equations represent the size-dependent growth rate:

$$\frac{dr^*}{d\tau} = \frac{S - exp(1/r^*)}{r^* + K \exp(\alpha/r^*)} \tag{1.14}$$

$$r^* = \frac{RT}{2\gamma v} r \tag{1.15}$$

$$\tau = \frac{R^2 T^2 D C_{eq}}{4\gamma^2 v} \tag{1.16}$$

$$K = \frac{RT}{2\gamma v} \frac{D}{k_p^{\circ}} \tag{1.17}$$

Where, r*, τ and K are dimensionless parameters, α is the transfer coefficient, k_p° is the growth or precipitation rate constant for the bulk crystal.

In equation 1.14, K represents the ratio between the diffusion rate and the reaction rate. At very small K values (K <<< 1), the growth is diffusion-controlled whereas, at high K values (K >>> 1), the growth is reaction-controlled. Similar to the nucleation step, there is a critical radius r_c for the formation of a stable particle which is highly dependent on S (equation 1.18). Particles with $r > r_c$ are stable and diffusion-controlled growth takes place, like Riess model where focusing effect is observed. In contrast, when $r < r_c$ the crystal chemical potential becomes more effective where smaller unstable particles tends to dissolve and Ostwald ripening is observed. As a conclusion, the focusing effect requires small K values and high S values.

$$r_c = \frac{2\gamma v}{RT \ln S} \quad (1.18)$$

The above observations were confirmed experimentally by Alivisatos *et al.*[21] on the synthesis of CdSe nanoparticles. They reported a rapid nucleation that terminates when the temperature or degree of supersaturation drops below a critical level. They also reported that focusing occurs when the precursor concentration in solution is higher than the solubilities of all the particles present. As the precursor concentration drops below a critical level due to the growth of the nanoparticles, small nanoparticles dissolve and larger ones grow resulting in a broader size distribution, or defocusing. Therefore, the synthesis of monodispersed nanoparticles can be achieved by stopping the reaction while it is still in the focusing mode. If the reaction enters the defocusing mode, monodispersed nanoparticles could still be obtained *via* different routes. The first route is by allowing the reaction to proceed for long enough times to completely dissolve the smaller particles.[3] Another route involves the use of the multiple injection method in which a second injection of the molecular precursors will cause refocusing.[21] However, a second injection may cause a secondary nucleation and therefore requires high precision. Alternatively, focusing of the size distribution can be achieved by the addition of small sized sacrificial nanoparticles in a process known as quantised Ostwald ripening.[25] These sacrificial nanoparticles should be of a size smaller than the critical radius.

1.2.1.3 Nanocrystals stabilisation

Because of the high surface-to-volume ratio, surface passivating materials known as surfactants or capping agents must be used in the nanocrystals synthesis process.[3,17] Surfactants are composed of a long hydrocarbon tail and a polar head (Fig. 1.6), in which the hydrocarbon tail controls the solubility and stability of the nanocrystals whilst, the polar head bond to the surface of the nanocrystals through a donor atom such as N, O or S.[17] Common capping agents include alkylamines such as oleylamine (OLA) ($CH_3(CH_2)_7CH{=}CH(CH_2)_7CH_2NH_2$) and hexadecylamine (HDA) ($CH_3(CH_2)_{15}NH_2$), alkanthiols such as dodecanethiol (DDT) ($CH_3(CH_2)_{11}SH$), carboxylic acids such as oleic acid ($CH_3(CH_2)_7CH{=}CH(CH_2)_7COOH$) and alkylphosphine oxides such as

trioctylphosphine oxide (TOPO) $[CH_3(CH_2)_7]_3PO$. Using a mixture of these capping agents could be beneficial for the synthesis of monodispersed nanoparticles. The capping agents can influence the nucleation and growth steps of the nanocrystals, and the interparticle spacing between adjacent nanocrystals.[28] The phase,[29] morphology[30] and optical properties[31] of the nanocrystals are all dependent on the capping agent.

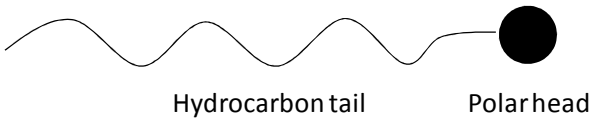

Fig. 1.6 Illustration of the capping agent.

1.2.2 Shape evolution mechanism

The properties of the nanoparticles are not only size-dependent, but also shape-dependent.[3,20,32-35] Zero-dimensional (0D) (dots),[18,36-40] one-dimensional (1D)[20,30,34,41-45] (rods, wires and tubes) and two-dimensional (2D)[44-46] (disks and plates) of different semiconductor nanoparticles have been synthesised by different methods such as thermal decomposition method, hydrothermal method and solvothermal method.

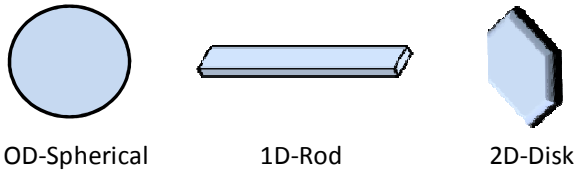

Fig. 1.7 Illustration of different possible shapes.

1.2.2.1 Classical thermodynamic model

This classical model is based on Gibbs-Curie-Wulff theorem, which proposes that the growth of a particular shape is governed by the relative specific surface energy of individual crystallographic faces of that shape.[47] Generally, crystals grow into the shape minimizing the overall free energy. This pure thermodynamic model does not account for some shapes which evolve far away from the thermodynamic equilibrium.[35] Thermodynamically, even the spherical shaped nanoparticles are not stable unless capped by different stabilising groups.[3]

1.2.2.2 Effective monomer model

The formation of the different nanoparticles shapes was found to be kinetic controlled.[3,13,35,41] The concentration of the monomer in solution determines the shape of the formed nanoparticles as observed by Peng *et al.*[35,41] Low monomer concentration, produce dot shaped nanoparticles while a median monomer concentration supports the growth of elongated rice shaped nanoparticles. At a high monomer concentration, magic-sized nanoclusters are formed during the nucleation step which promotes the formation of nanorods. Multi-armed structures (tetrapod-shaped) are formed at an extremely high monomer concentration. The critical nuclei necessary for the formation of elongated structures can be much smaller than that required for dots.[41] Synthesis of elongated nanoparticles requires small amount of nuclei and high chemical potential.[41] The production of small amount of nuclei results in high concentration of the monomer remaining in solution providing high chemical potential. Moreover, the production of elongated nanoparticles is enhanced using more stable precursors.[41] The effect of the type of the precursor on the shape of the nanoparticles was also explored by O'Brien *et al.*[48] and showed that when $CdCl_2$ or $CdSO_4$ were used as a cadmium precursor, spherical CdSe nanoparticles were formed whereas, $Cd(CO_3)_2$ led to rod shaped CdSe particles.

1.2.2.3 Selective adsorption model

Some surfactants can bind to different facets of the nanoparticle with different strength hence, altering the growth rate of these different facets (Fig. 1.8).[17,30] Weak binding of the surfactant to a particular facet, permits its faster growth whereas, strong binding surfactants restrain the growth of the facets. A mixture of surfactants is normally useful in controlling different growth rates in different crystallographic directions. This model is usually applied for materials with distinctive axis of symmetry (*e.g.* hexagonal CdSe) which will be either the faster or the restrained growth direction. It is noteworthy that at high monomer concentration the reaction is kinetically controlled and the facets which are less strongly binded to the surfactant will grow faster.[15] Conversely, at a low monomer concentration the reaction is thermodynamically driven and the monomer will be released from the less passivated facets and deposit on the other facets. As an example for the effect of the surfactants, Alivisatos *et al.*[30] reported the synthesis of CdSe nanorods, arrows and

tetrapods in a mixture of hexylphosphonic acid and trioctylphosphine oxide by controlling the ratio between the surfactants.

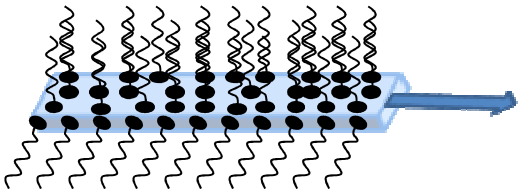

Fig. 1.8 Illustration of the selective adsorption model.

1.2.2.4 Oriented attachment model

Oriented attachment is a special case of growth by aggregation. It was first reported for TiO_2 by Penn and Banfield,[49-51] were particles coalescence at specific dimensionally similar crystallographic surfaces removing high energy facets and reducing the overall surface energy (Fig. 1.9). According to this model, nanorods[52] or nanowires[53,54] can be synthesised from nanodots even for materials crystallizing in a highly symmetric structures such as cubic ZnS.[52] The nanorods or nanowires are characterised with the same diameter of the nanodots but their lengths are much longer.[17] Rings[54] and branched nanocrystals[55] can also be synthesised using this mechanism. This secondary growth is because of the dipole-dipole interaction between the nanodots which occurs if the dipole attraction is higher than the thermal energy.[52] The surfactant can play an important role in this mechanism where partial removal of the surfactant or using a weaker binding molecule could assist the particles coalescence.[52,53] Stacking faults, twin planes or intergrowth which may count as nucleation sites for new phases are considered as a result of the oriented attachment growth.[49] High resolution transmission electron microscopy is the only technique that can investigate the oriented attachment mechanism. Dimpled boundaries and defects such as edge dislocations are evidences of this mechanism.[56]

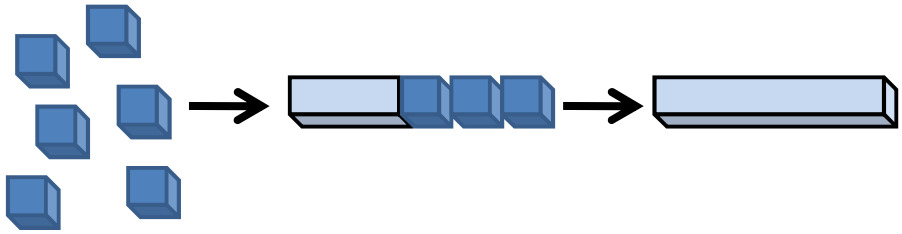

Fig. 1.9 Illustration of oriented attachment model.

1.3 Nanoparticles synthesis

There are two different routes for the synthesis of nanoparticles. The first route is called "top – down" in which the dimensionality of the solid material has been gradually reduced using different physical lithographic methods.[3] These physical methods are beneficial for the production of large quantities of the nanoparticles, but controlling the size is very difficult to be achieved.[12] The second route is known as "bottom – up" which is considered as a chemical method for obtaining the particles in solution through the gradual addition of atoms to each other.[3] The chemical methods are more reliable for the synthesis of size controlled nanoparticles, despite their subgram yields.[12] An ideal, synthetic route should produce highly crystalline nanoparticles of high purity, narrow size distribution, and surface passivated. The different wet chemistry methods include:

1.3.1 Synthesis in confined matrices

Different templates have been used for the preparation of semiconductor nanoparticles, such as zeolites,[57] reverse micelles,[58] and polymers.[59] These templates can be considered as reaction compartments which limit the growth of the nanoparticles size to a particular extent. The pore size in zeolites limits the diameter of the synthesised nanoparticles to < 2 nm.[10] Different sizes and different shapes of semiconductor nanoparticles can be synthesised in micelles or reverse micelles.[3,10,13-15] The shape and size of the micelles or reverse micelles, which are formed when water, a non-polar solvent and a surfactant are mixed together, can be manipulated depending on a number of factors including water to non-polar solvent ratio, temperature and concentration of surfactant.[15,60] Anodic aluminium oxide is a good polymeric template for the synthesis of nanoparticles as it is characterised with high consistency in pore size.[15]

1.3.2 Hydrothermal/solvothermal method

The hydrothermal and solvothermal methods use water or other polar or nonpolar solvents at high temperatures and pressures to increase the solubility and reactivity of the precursors.[3,10,13,14] In some cases, due to the increased reactivity of the metal salts it is not necessary to bring the solvent to its critical point.[14] The synthesis is carried out in a sealed vessel (autoclave) using three component system: precursor,

solvent and surfactant. Examples of semiconductor nanoparticles prepared using these methods include different metal (Cd,[61] Zn,[61] Cu,[62] Ni[63,64] and Fe[65,66]) sulfides.

1.3.3 Microwave irradiation

In this method the high frequency electromagnetic radiation supply means of rapid heating of the reaction mixtures.[14] The extent of the microwave absorption depends on the materials dielectric constant where molecules which have large permanent dipoles will absorb microwave irradiation over small dipole molecules.[67] Microwave irradiation provides good temperature homogeneity,[67] and short reaction times.[68] It has been used for the synthesis of CdSe,[67] ZnS,[69] CdS[69] and $CuInS_2$[68] semiconductor nanoparticles.

1.3.4 Chemical precipitation

By controlling the factors affecting the precipitation process, such as concentration of the ions, solvent, pH, temperature and the presence of organic molecules, monodispersed semiconductor nanoparticles of controlled size can be obtained.[3,10,14] Brus *et al.*[70] reported the chemical precipitation of CdS nanocrystallites from a diluted solution of $CdSO_4$ and $(NH_4)_2S$ based on the following dynamic equilibrium:

$$(CdS)_{crystal} \leftrightarrow (Cd^{2+})_{solv} + (S^{2-})_{solv} \qquad (1.19)$$

The crystallite size and the dielectric constant of the solvent are the main factors influencing this equilibrium. Large crystallites are more thermodynamically stable and will shift the equilibrium to the left hand side. Small crystallites can be obtained by reducing the stability of the dissolved ions using a solvent of lower dielectric constant. ZnS[71] and CdTe[72] are other examples for semiconductor nanoparticles prepared using the chemical precipitation.

1.3.5 Thermal decomposition method

Thermal decomposition is a major route for nanoparticle synthesis because of its superior control over size and shape of the synthesised nanoparticles.[28] Furthermore, it is a low cost method for the production of high quality material.[73] A general scheme for preparing monodisperse nanoparticles requires a rapid nucleation followed by growth on the existing nuclei. This could be achieved by the hot-

injection method in which the precursor(s) is rapidly injected into a hot, high-boiling, coordinating solvent (capping agent) where the temperature of the solution should be high enough to decompose the precursor(s) (Fig. 1.10).[3,18,19] The rapid injection of a room temperature solution reduces the temperature of the hot solvent and therefore, separation of the nucleation step from the growth step takes place. A non-injection approach in which the precursor(s), capping agents and solvent are mixed at low temperature can also satisfy this requirement through steady heating of the reaction solution.[73]

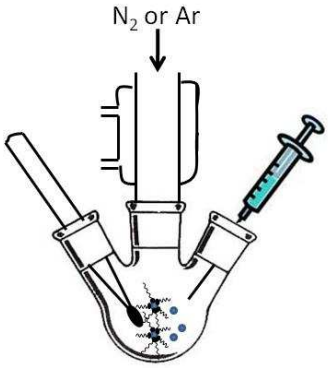

Fig. 1.10 Hot-injection method.

By controlling the reaction conditions such as time, temperature, concentration and the chemistry of precursor(s) and surfactant(s), nanoparticles of different sizes and/or shapes can be obtained. Generally, the size of the nanoparticles increase with increasing reaction time, concentration of the precursor(s) or growth temperature; where the increase in reaction time or concentration of the precursor(s) will allow more material to be added to the nanoparticles surfaces, and increasing the growth temperature increases the rate of addition of materials to the existing nuclei.[3,18,28,40] The capping agent also plays a key role in the synthesis of the nanoparticles.[3,28] It adheres to the surface of the nanoparticles forming an organic shell which stabilise the nanoparticles and control their growth. Capping agents that bind more strongly to the nanoparticles surface provide higher steric hindrance which reduces the rate of materials addition to the nanoparticles, leading to the formation of smaller nanoparticles.

At the required size of the nanoparticles, further growth is quenched by removing the heating source and allowing the solution to cool. The nanoparticles are then precipitated by the addition of a suitable solvent followed by centrifugation and

isolation of the nanoparticles. These nanoparticles can be redispersed in a variety of solvents. The capping agent determines which solvents are suitable for precipitation and redispersion.

The preparation of nanoparticles using the molecular precursor method has been described by Murray, Norris and Bawendi;[18] in which a solutions of dimethyl cadmium ($CdMe_2$) and trioctylphosphine selenide (TOPSe) were injected into hot TOPO, to produce TOPO capped CdSe nanoparticles in the temperature range of 120-300 °C. Using $CdMe_2$ is a major limitation for this method, as it is toxic, pyrophoric, expensive and unstable at room temperature.[40]

1.3.6 Single molecular precursor

In the continuing search for new reproducible routes for the synthesis of monodispersed nanoparticles, single source precursors (SSP), a single compound containing all elements required within the nanocrystallite, have shown more advantages over other routes. Some of these advantages include:

- overcoming the need of using hazardous compounds such as $CdMe_2$,
- most of the SSP are air and moisture stable
- lower decomposition temperature
- lower defect material
- maintaining the stoichiometries of metal and chalcogen.[74,75]

The most common SSP are:

1.3.6.1 Dithio/selenoiminophosphinate

In a general synthesis, a phosphorus(III) compound is formed through the condensation of R_2PCl with $NH(SiMe_3)_2$ which is followed by an oxidation reaction with S or Se forming $R_2P(E)NHP(E)R_2$ (E=S or Se) as illustrated in equations 1.20 and 1.21.[76] Complexes of the dithio/selenoiminophosphinate are then formed by the deprotonation of the N-H (equation 1.22). Imino-bis(di-*iso*-propylphosphine selenide)cadmium(II) $[Cd(N(SeP^iPr_2)_2)_2]$ (Fig. 1.11) was successfully used for the synthesis of TOPO-capped CdSe nanoparticles.[77]

$$2R_2PCl + NH(SiMe_3)_2 \rightarrow R_2PNHPR_2 + ClSiMe_3 \qquad (1.20)$$

$$R_2PNHPR_2 \xrightarrow{E=S \text{ or } Se} R_2P(E)NHP(E)R_2 \qquad (1.21)$$

$$R_2P(E)NHP(E)R_2 + M^{n+} \rightarrow [M(N(SeP^iPr_2)_2)_n] \quad (1.22)$$

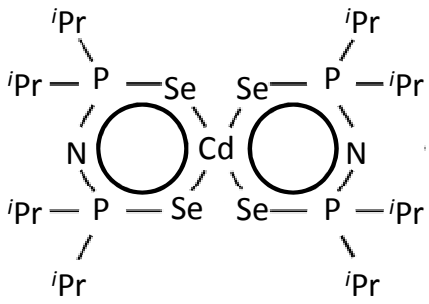

Fig. 1.11 Structure of $[Cd(N(SeP^iPr_2)_2)_2]$.

1.3.6.2 Dithio/selenophosphinate

The dithiophosphinate ligands and have been well explored because of its industrial and agricultural applications.[78] The coordination chemistry of the dithiophosphinato complexes have also been investigated.[79-81] In a simple synthesis of the dithiophosphinato complexes, the metal salt is reacted with sodium dialkyldithiophosphinate forming the neutral complex $[M(S_2PR_2)_n]$. Thin films of CdS and ZnS were prepared from $[Cd(S_2P^iBu_2)_2]_2$ and $[Zn(S_2P^iBu_2)_2]_2$, respectively.[79]

The diselenophosphinate is less explored due to the complicated synthesis procedures. Moreover, the synthesis routes are not always reproducible and the reported selenophosphinates are highly air sensitive.[82] O'Brien *et al.*[83,84] reported a more facile procedure for the synthesis of $[(R_2PSe)_2Se]$ (R = ^{i}Pr or Ph) and their metal complexes $[M(Se_2PR_2)_n]$ (M = Zn, Cd, Pb, Ni, Cu, In, Ga or Bi). The ligand synthesis was carried out by the reaction between R_2PCl, $HSiCl_3$ and NEt_3 in toluene followed by filtration and reflux of the filtrate with Se powder as illustrated in equations 1.23 and 1.24. The complexes were obtained by the reaction of $[(R_2PSe)_2Se]$ with the metal salts in a methanolic solution.

$$R_2PCl + HSiCl_3 + NEt_3 \xrightarrow{\text{toluene,6h,rt}} R_2PSiCl_3 + [HNEt_3]Cl \quad (1.23)$$

$$R_2PSiCl_3 + 3\ Se \xrightarrow{\text{toluene,20h,reflux}} [(R_2PSe)_2Se] + Si_2Cl_6 \quad (1.24)$$

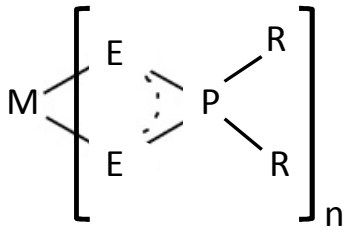

Fig. 1.12 Structure of $[M(R_2PE_2)_n]$.

By more detailed research on the diselenophosphinates ligands, ionic dialkyldiselenophosphinate salts were isolated in the form of alkylammonium salt $[HNEt_3][R_2PSe_2]$ (R= ^{i}Pr, ^{t}Bu or Ph).[82] The ionic ligand was synthesised in the same manner except for using excess $HSiEt_3$ and NEt_3 in the first step and excess Se in the second step. Thermal decomposition of $[Zn(Se_2P^{i}Pr_2)_2]$ in HDA produced ZnSe nanorods.[82]

1.3.6.3 Alkylxanthates

Alkylxanthates complexes can be easily prepared by dropwise addition of the metal salt to potassium alkylxanthate solution. Various metal sulfide nanoparticles and alloyed nanoparticles were prepared from their ethylxanthate complexes including CdS,[85-87] ZnS,[85,86] CuS,[85] NiS,[85] PdS[85] and ZnCdS.[86]

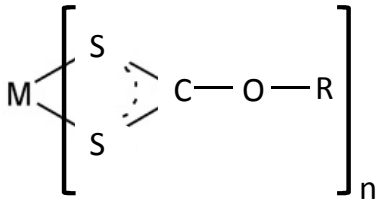

Fig. 1.13 Structure of $[M(S_2COR)_n]$.

1.3.6.4 Dithio/selenocarbamates

These complexes are prepared from the reaction of alkyl/dialkylamine with CS_2 or CSe_2 in the presence of NaOH at 0 °C, followed by the addition of the metal salt solution (equation 1.25 and 1.26).[74]

$$R_2NH + CE_2 \xrightarrow{NaOH} Na(E_2CNR_2) + H_2O \qquad (1.25)$$

$$Na(E_2CNR_2) + M^{n+} \rightarrow [M(E_2CNR_2)] \quad (1.26)$$

The carbamates complexes could be divided into:

- Symmetrical dialkyldithio/selenocarbamates

These symmetrical complexes are air-stable with a general formula of $[M(E_2CNR_2)_n]$ (E = S or Se) (R = Me, Et, ^{n}Pr, ^{i}Pr or ^{n}Bu). O'Brien *et al.*[85,86] found that $[Cd(S_2CNEt_2)]$ produced CdS nanoparticles of low quality and the production of CdSe nanoparticles from the analogues selenium precursor was not very successful. The major product obtained from $[Cd(Se_2CNEt_2)]$ was elemental Se with CdSe nanoparticles as a minor product. Nanowires of hexagonal Cu_2S were synthesised from the thermolysis of $[CuS_2CNEt_2]$.[87] Fe_3S_4 nanoparticles[88] and nanosheets[89] were synthesised using $[Fe(S_2CNEt_2)_3]$.

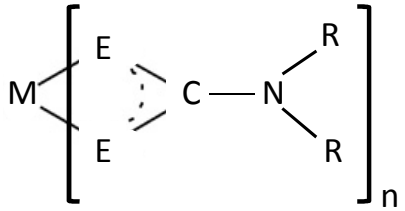

Fig. 1.14 Structure of $[M(E_2CNR_2)_n]$.

- Unsymmetrical dialkyldithio/selenocarbamates

Unsymmetrical dialkyldithio/selenocarbamates complexes have a general formula of $[M(E_2CNRR`)_2]$ (E = S or Se), (R = Me or Et) and (R` = ^{n}Hex or ^{n}Bu). $[Cd(E_2CNMe^nHex)_2]$, in particular, has proven to be the best unsymmetrical dialkyldithio/selenocarbamates for the production of CdS and CdSe monodispersed nanoparticles.[37,90] It has been also used for the synthesis of monodispersed CdSe/CdS core/shell nanoparticles.[91] $[Cu(S_2CNMe^nHex)_2]$ was used as a SSP for the synthesis of Cu_2S nanoparticles.[92]

- Mixed dialkyldithio/selenocarbamates

Compounds with general formula $[RM(E_2CNR`_2)_2]$ (E = S or Se) such as $[MeCd(E_2CNEt_2)]_2$,[93] $[EtCd(E_2CNEt_2)]_2$,[94] and $[EtZn(E_2CNEt_2)]_2$.[95] In spite of their

instability, they produced CdS and CdSe nanoparticles with high quality and close to monodispersed ZnS and ZnSe nanoparticles.

- *N*-alkyldithiocarbamates

This group of dithiocarbamate complexes has received less attention because they are generally not very stable. O'Brien *et al.*[96] prepared a series of $[M(S_2CNHR)_2]$ (M = Cd or Zn) and (R = Et, ^{n}Bu, ^{n}Hex or ^{n}dodecyl) and synthesised CdS nanorods and ZnS nanoparticles from the thermolysis of $[Cd(S_2CNH^n dodecyl)_2]$ and $[Zn(S_2CNH^n hexyl)_2]$, respectively, in HDA.

1.3.6.5 Thio/dithiobiurets

These compounds have been explored for their potential medical and industrial applications.[97,98] Thiobiuret complexes are formed from the reaction of *N,N′*-dialkylcarbamyl chloride, sodium thiocyanate, and dialkylamine followed by the dropwise addition of a methanolic solution of the metal salt.[99] The same procedure is used for the dithiobiurets but replacing *N,N′*-dialkylcarbamyl chloride with *N,N′*-dialkylthiocarbamylchloride (equation 1.27-1.29). Thio/dithiobiuret complexes have not been explored for the deposition of materials until very recently. A series of the thio/dithiobiuret complexes were synthesised and used as a SSP for the deposition of thin films.[99] The synthesised complexes include $[M(SON(CN^iPr_2)_2)_n]$ (n = 2 or 3), (M = Fe, Co, Ni, Cu, Zn, Cd or In), $[M(SON(CNMe_2)_2)_n]$ (n = 2 or 3), (M = Fe or Ni) $[M(N(SCNMe_2)_2)_n]$ (n = 2 or 3), (M = Co, Ni, Zn, Cd or In) and $[M(N(SCNEt_2)_2)_n]$ (n = 2 or 3), (M = Co, Ni, Zn, Cd or In).

$$R_2NCOCl + NaSCN \xrightarrow{acetonitrile} R_2NCONCS + NaCl \quad (1.27)$$

$$R_2NCONCS + R_2NH \rightarrow R_2NCONHCSNR_2 \quad (1.28)$$

$$R_2NCONHCSNR_2 + M^{n+} \rightarrow [M(SON(CNR_2)_2)_n] \quad (1.29)$$

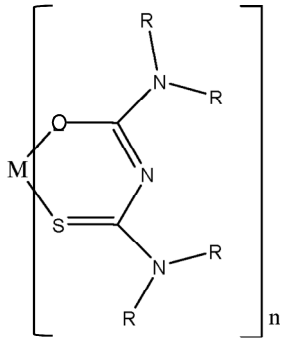

Fig. 1.15 Structure of $[M(SON(CNR_2)_2)_n]$.

1.3.7 Synthesis in microfluidic reactors

Microfluidic reactors are basically systems which operate using microchannels with dimensions between tens to hundreds of micrometers accommodating very small amounts of fluid (10^{-9} to 10^{-18} L).[100] Ever since the first reports of using microfluidic reactors for the synthesis of nanoparticles were published,[101,102] it has been considered to be an attractive method because it offers a number of different advantages including: [103-106]

- superior levels of control
- efficient reagents mixing
- simplicity as some microreactors are composed of only a microtube immersed in an oil bath
- on-line analysis which could give rise to a fully automated process
- efficient heat transfer because of the high surface area to volume ratio of the microchannels.

In spite of these advantages and the ability of the microfluidic reactors to produce high quality nanoparticles, there are still three general issues that should be considered. Firstly, a single-phase laminar flow will result in a broad residence time distribution due to the very slow diffusive mixing.[107-109] At high flow rates, a parabolic velocity profile is created, leading to a non-uniform velocity in the microchannel. Therefore, particles will spend different times inside the channels based on their locations; particles at the stream centre spend less time than the ones at the edge of the stream. Secondly, the deposition of the nanoparticles on the walls

of the microchannels which will lead to their blockage.[103,104] Finally, the choice of solvents and surfactants is very limited. Only solvents and surfactants which are liquids at both room temperature and the temperature required for synthesis are suitable in order to prevent clogging of the microchannels. For example, TOPO can decompose at high temperatures and block the microchannels.[110]

Different types of microreactors have been developed and used for the production of highly monodispersed semiconductor nanoparticles through overcoming the above mentioned limitations. Generally, microreactors can be classified into microcapillary tubes or chips. The most common used microcapillary tubes are made of glass[102,110-113] or polytetrafluoroethylene (PTFE)[114-119] with their inner diameters varying between 100 to 1000 µm.[104] Researchers took advantage of the simplicity, flexibility and the ability of these microcapillary tubes to operate at elevated temperatures for the synthesis of monodispersed nanoparticles using a pre-heated oil bath as a heating source. Maeda *et al.*[111] showed that heating the reaction solution from 20 °C to 300 °C in a silica glass capillary of an inner diameter 200 µm requires only 0.28 seconds. The chip microreactors are formed of a reaction microchannel again with inner diameters varying between 100 to 1000 µm. The microchannel is etched in a microfluidic reactor made of materials with high chemical and thermal durability such as glass or silicon.[104] The chip is normally placed on a hot plate for the heating purposes. Both types of these microreactors offer the same control level over the reaction parameters,[104] except that microcapillaries has been reported to be more flexible than the chip microreactor for the distribution of the residence time in the synthesis of CdSe/ZnS core/shell.[112]

Different attempts towards modifying the microreactor design were made. A microreactor with a temperature gradient was used for the synthesis of CdSe nanoparticles.[115] The main aim of the temperature gradient was the separation of the nucleation step from the growth step. Nucleation took place in a high temperature zone area after which the reaction solution passed through a transition part into a lower temperature zone for the nanoparticles growth. The microfluidic reactor was made of a PTFE capillary with an inner diameter of 300 µm and a tube furnace for the temperature control. It was reported that the PTFE capillary is more flexible than the silica capillary in such microreactor.[115] The broad residence time distribution caused by the parabolic velocity in a single-phase laminar flow can be narrowed by

using serpentine microchannel which compensate the non-uniform velocity through the recirculation around the turns.[120] Experimental comparison between CdSe nanoparticles synthesised in straight and serpentine PTFE microchannels confirmed that serpentine microchannels leads to narrower residence time distribution as the CdSe nanoparticles possess a sharper absorption band edge and narrower full width half maxima (FWHM).[117]

Introducing the idea of segmented flow microreactors (gas-liquid or liquid-liquid) had a profound effect on narrowing the residence time distribution. Gas-liquid segmented flow microreactors can operate at elevated temperatures with possibility of obtaining uniform segmentation over a large range of bubble velocities.[108] Moreover, it is possible to inject or withdraw reaction aliquots in a gas-liquid segmented flow microreactors.[108] Gas-liquid segmentation in microcapillaries was applied but not fully examined.[102] Bawendi *et al.*[108] used gas-liquid segmentation in a silicon chip microreactor with argon as a carrier and squalane as reaction phase. This system showed high efficiency in terms of the rapid mixing of the reagents, achieving uniform segmentation at the high temperatures required for synthesis and narrower residence time distribution particularly at higher flow rates. However, gas-liquid segmentation still encounters some difficulties, specifically, the significant change in volume with the change in pressure or temperature and the physical contact between the liquid or reaction phase and the walls of the channels leading to particles deposition and channel blockage.[104,106] The inevitable deposition of the nanoparticles on the walls of the channels can be overcomed using liquid-liquid segmentation flow microreactors in which the reaction phase is encapsulated in a nanolitre droplet, hence, preventing interaction between the nanoparticles and the walls of the channel.[106] It has been proved experimentally that synthesis in nanolitre droplets is effective for CdSe nanoparticles. Mathies *et al.*[121] used octadecene as droplet phase and perfluorinated polyether as carrier fluid in a glass chip microreactor which produced highly monodispersed CdSe nanoparticles. The main issue concerning the liquid-liquid segmentation microfluidic reactors is the limited options of the available liquids that are immiscible at the elevated synthesis temperatures.[104,108] In the continuing research for the optimum microreactor, a pressurised microreactor was developed in order to keep solvents supercritical at the elevated synthesis temperatures which prevents the vaporisation and therefore, the number of available solvents expanded to include low boiling point solvents.[104]

Comparison of the synthesis of CdSe quantum dots in supercritical hexane and non-supercritical squalane at the same temperature showed that dots prepared in hexane were more monodispersed as indicated by their narrower emission peak.[122]

1.3.8 Seeded growth

Seeded growth can be used to increase the average size of the nanocrystals and more importantly for the synthesis of core/shell structures.[12,14] It is the most efficient method for the separation of the nucleation and growth steps as preformed nanocrystals are used as seed nuclei. In this process heterogeneous nucleation takes place where the preformed nanocrystals acts as nucleation sites and any additional monomer will precipitate on top of the existing nanocrystals.

1.4 Optical properties of nanocrystalline semiconductors

In nanocrystalline semiconductors, there are two factors which interpret the difference in the behaviour of these semiconductors from the bulk ones. The first is the high surface /volume ratio resulting in higher energetic state of surface atoms and the second factor is the band gap of the nanomaterial.[10] The band gap of semiconductor nanoparticles is dependent on a number of factors listed below:

1. Size: once the diameter of the nanocrystals is smaller than the bulk exciton Bohr radius (equation 1.24)[10], quantum confinement takes place and the nanocrystalline semiconductors show an increase in their band gaps and a blue shift in their optical spectra as a result of the decrease in size.[123-127]

$$a_B = \frac{\hbar^2 \epsilon}{e^2}\left[\frac{1}{m_e *} + \frac{1}{m_h *}\right] \qquad (1.24)$$

   Where, ħ is the reduced Planck's constant, ϵ is the bulk optical dielectric coefficient, e is the elementary charge, and m_e* and m_h* are the effective mass of the electron and hole, respectively.
2. Difference in dimensions: nanowires show a weaker quantum confinement compared to quantum dots due to vanishing of one of the dimension of confinement.[128-132]
3. Crystal structure: semiconductors which can exist in a cubic (zinc blende) or hexagonal (wurtzite) phase such as CdS showed a slightly higher band gap in

the hexagonal form.[133-135] However, CdSe showed no crystallographic dependence.[128]

4. Alloying: tuning the band gap in alloyed semiconductor quantum dots such as $Zn_xCd_{1-x}S$ or $CdSe_xS_{1-x}$ ($0 \leq x \leq 1$) can be achieved through altering their constituent stoichiometries.[128,136-144]

Quantum confinement can be divided into three different regimes based on the ratio between the particle radius (r) and the bulk exciton Bohr radius (a_B) which are, weak confinement regime ($r >> a_B$), intermediate confinement regime ($r \sim a_B$) and strong confinement regime ($r << a_B$).[145] Different models have been developed for the band gap determination of nanocrystalline semiconductors. A simple effective mass approximation showed good agreement with the experimental values for large sizes of CdSe nanoparticles, but the model diverts from the experimental results for small sizes, due to the finite potential barrier at the surface of the particles.[18] Tight binding calculations on small CdS and ZnS nanocrystallites have shown better agreement for these smaller sizes as suggested by Lippens and Lannoo.[146] Another model which shows good agreement with the experimental values is based on an empirical pseudopotential method which also includes the spin-orbit coupling and explains the effect of the crystal structure on the optical properties of CdS nanoparticles.[134] Recently, Yang *et al.*[128] provided a general quantitative model for the band gap calculation of strong quantum confined systems (III-V and II-VI semiconductors) with respect to size, dimensionality and composition. The model is based on the nearly free-electron approximation in which the E_g originates from the crystal potential *V*. The model which is represented in equations 1.25 and 1.26 for binary and alloyed semiconductor nanocrystals respectively, showed high accuracy when compared to the experimental results even for nanocrystals with diameter < 3 nm.

$$\frac{E_g(D,d)}{E_g(\infty)} = 2 - \left[1 - \frac{1}{6D/[(3-d)h] - 1}\right] * \exp\left[-\frac{2S_b}{3R}\frac{1}{6D/[(3-d)h] - 1}\right] \quad (1.25)$$

Where, E_g (*D*,*d*) is band gap of nanodots or nanowires, *Eg*(∞) is the band gap of the bulk material, *D* is diameter of nanodots or nanowires, *d* is dimensionality (*d* = 0 for

(1.26)

nanodots and d = 1 for nanowires), h is molecular diameter, S_b is the bulk solid – vapour transition entropy of the crystals and R is the ideal gas constant.

$$1/E_g(x,D,d) = (1-x)/E_g(0,D,d) + x/E_g(1,D,d)$$

Where, x is the constituent stoichiometry, E_g (x,D,d) is the band gap of the nanoalloyed semiconductor which lies in the range between E_g (0,D,d) and E_g (1,D,d).

1.4.1 Absorption spectroscopy

Optical absorption spectroscopy can be used for the observation of the discrete energy levels in the band gap of semiconductor nanoparticles.[3] It is also useful for size determination and calculation of the nanoparticles concentration.[3,127] Peng *et al.*[127] showed that there is a red shift in the absorption spectra of CdS, CdSe and CdTe spherical nanoparticles accompanied with the increase in their sizes. They provided empirical formulas for calculating size of these quantum dots based on the wavelength of the first excitonic absorption peak of each sample. Calculating the concentration of colloidal nanoparticles is very difficult because of the unknown number of the capping agent attached to the surface of the nanoparticles.[127] Optical absorption spectroscopy was found to be valuable method for concentration determination, independent of the capping agent, synthesis procedure and refractive index of the solvent.[127] Using Beer-Lambert's law (equation 1.27) it is possible to find the concentration by determining the absorbance (A) at the first excitonic absorption and extinction coefficient per mole of nanoparticles (ε in L mol^{-1} cm^{-1}).

(1.27)

$$A = \varepsilon CL \qquad (1.27)$$

Where, L is the path length of the beam in cm.

The extinction coefficient per mole of nanoparticles is size-dependent in the strong quantum confinement regime of CdS, CdSe and CdTe quantum dots and can be calculated according to the following equations[127]

$$\varepsilon = 5500\Delta E(D)^{2.5} = 21536(D)^{2.3} \text{ for CdS} \qquad (1.28)$$

$$\varepsilon = 1600\Delta E(D)^{3} = 5857(D)^{2.65} \text{ for CdSe} \qquad (1.29)$$

(1.30)

$$\varepsilon = 3450\Delta E(D)^{2.4} = 10043(D)^{2.12} \text{ for CdTe}$$

Where, ΔE is the first absorption peak transition energy and D is the diameter of the nanoparticle.

1.4.2 Photoluminescence (PL)

After excitation, the exciton goes through intra-band relaxation followed by inter-band exciton recombination which takes place by different routes including: radiative *e-h* recombination at the band edge, non-radiative phonon assisted *e-h* recombination, non-radiative Auger recombination and radiative and/or non-radiative relaxations at the surface defects.[147,148] The radiative *e-h* recombination at the band edge is responsible for the PL colour of the quantum dots.[148] The quality of the emission is determined by the purity of the emission colour, its brightness and the stability of emission.[31] The emission colour and its purity are determined by the emission peak position and its FWHM, respectively, whereas the brightness is determined by the quantum yield (QY) calculations. The emission colour and its purity are size[123] and shape-dependent.[34] PL QY of nanoparticles is calculated according to equation 1.31 by comparison with a standard dye of known QY. In order to avoid re-absorption, low concentrations with an excitonic peak absorbance between 0.01 and 0.05 should be used.[149]

$$QY_x = QY_s \times \frac{A_s}{A_x} \times \frac{S_x}{S_s} \times \left(\frac{n_x}{n_s}\right)^2 \quad (1.31)$$

Where, A is the absorbance at excitation wavelength, S is the integrated emission and n is the refractive index of unknown (x) and standard (s).

1.4.2.1 QY enhancement

Surface and trap states are the main reason for low QY.[31,150] These traps are located in the band gap of the nanoparticles and are created due to the dangling bonds of the surface atoms.[22,31] The probability of a radiative *e-h* recombination at these traps is reduced as a result of the reduction in the overlap between *e* and *h* wave functions.[150] Moreover, the recombination could take a non-radiative pathway and energy is released in the form of heat.[150] Surface states are also responsible for the broad tail observed in the PL peak which is known as deep-trap emission.[151] QY

enhancement can be achieved through surface passivation by organic ligands, photoactivation or shelling with a larger band gap semiconductor *i.e.* formation of a core/shell structure.[31,148, 150]

1.4.2.1.1 Surface passivation by organic ligands

As mentioned earlier, surface ligands or capping agents play a key role in the nucleation, growth and stability of nanoparticles.[28] Furthermore, the surface ligands bind to the dangling orbitals at the nanoparticle surface, hence may partially or completely eliminate the surface traps and prevent the non-radiative exciton recombination. Primary amines such as HDA, have shown to be the most efficient passivating ligands as they can provide higher surface coverage compared to bulky ligands such as secondary and tertiary amines or TOPO.[31,150] For instance, CdSe nanoparticles synthesised in HDA/TOPO/TOP mixture had much higher QY than the ones synthesised in a mixture of TOPO/TOP alone.[152] Significant increase in the QY can also be achieved through a post-preparative ligand exchange in which TOPO can be replaced with primary alkylamines.[152] Furthermore, surface states could be eliminated by redistribution of the electronic density through reorganization of the surface atoms which is known as surface relaxation and reconstruction or self-passivation.[150,153] These reconstructions are size-dependent; for quantum dots with diameters > 4 nm the reconstruction takes place at the surface of the dots only, while reconstruction for quantum dots with diameters < 4 nm extends to the core of the dot as well.[154] The capping agent has an effect on the reconstruction of CdSe nanoparticles surface.[155] Surface atoms bonded to the capping agent show vertical displacement when the tilt angle of the adjacent alkyl chains can vary, whereas for a fixed tilt angle surface reconstruction is not possible.[154] This process is assisted by primary alkylamines but suppressed by bulky ligands such as TOPO.[150] On the other hand, some surfactants may quench the PL by capturing electrons or holes thus preventing the *e-h* radiative recombination. Thiol surfactants are able to quench the PL of CdSe quantum dots by hole trapping, but not CdTe because of the higher energies of CdTe valence band with respect to the oxidation potential of most thiols.[156]

1.4.2.1.2 Photoactivation

Illuminating the quantum dots above their band gap energies for a certain period increases the QY but further illumination will result in a slow decay of the QY because of the photo-oxidation.[157] The illumination wavelength, solvent and concentration of the surfactant are the factors which control the rate and magnitude of the photoactivation.[157]

1.4.2.1.3 Shelling

Shelling the quantum dots with a wider band gap semiconductor provides the most efficient surface passivation. Organic surface ligands are labile and may desorb from the surface[158] whereas, inorganic shelling is more permanent and completely isolate all surface atoms of the core from its environment.[150,159] In addition to eliminating the surface traps, shelling will reduce the probability of other processes such as capturing the charge carriers by redox species and Auger-assisted ionization which leads to a low PL QY.[159]

1.4.3 Blinking

Blinking is the fluctuation between bright and dark states or on and off states even under continuous illumination and is observed in the emission of a single quantum dot.[9,160] The performance of quantum dots in many applications is highly affected by the blinking phenomenon.[150,161,162] Recently, CdZnSe/ZnSe[162] ternary core/shell with a composition gradient from core to shell and CdSe/CdS[163] core/shell with a thick shell (5 nm) have shown to suppress blinking. Initially, blinking was considered to be a result of an extra charge which turns the quantum dot PL temporally to an off state due to the increase of the non-radiative Auger recombination.[164] However, Bawendi *et al.*[161] challenged this charge model with their results on multiexciton blinking of CdSe/CdZnS core/shell.

1.4.4 Multiple exciton generation (MEG)

MEG is the generation of two or more *e-h* pairs from a single absorption event of a photon of at least twice the band gap energy.[6,165] The excess energy, from the non-radiative Auger recombination of an exciton, instead of being released in the form of

heat will be used for the generation of a second exciton thus a biexciton is formed.[6,165] This process is supposed to increase the efficiency of photovoltaic devices.[6,159,165] Klimov *et al.*[166] demonstrated the production of seven excitons from the absorption of a single photon. Recently, a study on CdSe quantum dots showed that the multiplication rate of a photogenerated *e-h* pair is size-dependent for a given photon energy.[167]

1.5 Heteronanoparticles

Heteronanoparticles can be classified into core/shell structures and alloys.

1.5.1 Core/shell

Depending on the band off set alignment of both core and shell and hence the charge carrier wave functions overlap, core/shell structures can be divided into four main types:

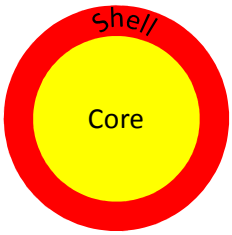

Fig. 1.16 Illustration of core/shell structure.

1.5.1.1 Type I core/shell

In type I core/shell, the shelling material is of a much higher band gap such that both the electron and hole are confined within the core.[150,159,168,169] The advantages of this structure are the complete isolation of the exciton from its environment and the elimination of the dangling bonds thus; high QY and high stability is achieved.[150,159,168,169] Although the optical properties of type I are core-dependent, a small red-shift is observed in the absorption and emission spectra upon shell deposition.[150] This shift is because of the finite energy off set between the core and the shell and therefore the electron wave function could to some extent escape into the shell. The red-shift is more observed in the smaller core sizes.[169]

One of the most explored type I core/shell is CdSe/ZnS[169-172] having a CB off set between CdSe and ZnS of 850 meV.[159] This energy off set difference makes ZnS a suitable choice as a shelling material on top of CdSe core in order to prevent the exciton from the interaction with the surface, yet the partial leakage of the electron into the shell makes thicker ZnS shells a requirement for QY enhancement. Epitaxial growth of thick ZnS shells on top of CdSe core is actually a challenge because of the high lattice mismatch (12%) between the two materials.[168] The difference in bond lengths between the atoms in the core and those in the shell is the main source of the lattice mismatch.[159] The lattice mismatch induces a strain at the interface between the core and the shell which increases as the shell deposition increase, finally leading to defects which opens a non-radiative route for the *e-h* recombination.[159,169] In fact, only 2-3 monolayers (MLs) of ZnS shell can be deposited on top of a CdSe core with the highest QY obtained from about 1.3 ZnS MLs.[169] Despite this, CdSe/ZnS was extensively explored, these quantum dots exhibit strong blinking with no relation between the blinking and the shell thickness being observed.[173] To overcome this problem, one can introduce a material with smaller lattice mismatch in between the core CdSe and the shell ZnS, forming a core/shell/shell such as CdSe/CdS/ZnS.[174] The lattice mismatch between CdS and ZnS[175] is 8% and between CdS and CdSe[176] is only 3.9%.

Another well explored type I core/shell system is the CdSe/CdS[91,171,176-178] although it is sometimes considered as type $I^{1/2}$.[150] The energy off set between the core and the shell decrease as the electron wave function is more extended into the shell and consequently, the electron is less confined into the core. The CB off set between CdSe and CdS is only 200 meV, and there is a continuous red-shift in the absorption and emission spectra of CdSe/CdS during the shell growth that might go up to 60 nm.[159,168] Therefore, in case of CdS shell the electron is more likely to be delocalized over the whole core/shell.[150,168] On the other hand, the small lattice mismatch between CdSe and CdS (3.9%) facilitates the epitaxial growth of thick CdS shells.[176] CdSe/CdS with a thick shell of 5 nm (equivalent to about 14 MLs) was recently reported with 68% emitting continuously for 5 minutes.[163] Using the seeded growth method, CdSe/CdS core/shell nanorods[179,180] and nanotetrapods[180] with high luminescent properties were synthesised. Other type I core/shell structures include CdSe/ZnSe,[181,182] CdS/ZnS[175,183] and InP/ZnS.[184]

1.5.1.2 Inverted type I core/shell (quantum shells)

Both charge carriers are confined in the shell and therefore could be called quantum shells.[185,186] In order to have both charge carriers confined in the shell the diameter of the bulk exciton of the shell should be smaller than the perimeter of the shell.[186] Quantum confinement takes place along the radial direction only as indicated by the dependence of the optical properties on the shell thickness but not the core size where a huge red-shift up to 90 nm was previously observed as a CdSe shell was formed on top of CdS core.[186,187]

1.5.1.3 Type $I^{1/2}$ or *quasi* type II core/shell

In this type, one of the charge carriers is confined in either the core or the shell, whereas the other carrier is delocalized over the whole structure.[150,185] This core/shell type is very sensitive towards the shell thickness; whilst only a thin shell is required to form a type $I^{1/2}$ core/shell material, a thick shell will convert it into a type II core/shell. CdTe/CdSe was reported to form a type $I^{1/2}$ core/shell system with the hole wave function completely confined in the core CdTe and the electron wave function is delocalized over the entire core/shell system.[185] The electron wave function was gradually confined in the CdSe shell as the growth proceed until complete shell confinement of the electron took place forming a type II core/shell. The same trend was observed in the CdS/ZnSe core/shell structure, shifting from a *quasi* type II core/shell to type II core shell along the shell growth.[188] ZnSe/CdSe was also reported as a *quasi* type II core/shell with the electron being shell-confined and the hole delocalized over the entire system.[188] The ZnSe/CdSe core/shell system demonstrated to be a good example of the transition between the different core/shell types depending on the thickness of the shell for a given core size.[189,190] Compared to type I, the red-shift observed in type $I^{1/2}$ is much larger whereas, the *e-h* overlap is reduced.[150]

1.5.1.4 Type II core/shell

In this case, the core and shell energy levels are in a staggered alignment with either the VB edge or the CB edge of the shell placed within the band gap of the core.[150,159,168,185] Type II core/shell mainly target near infra-red emission and can tune the emission to wavelength that is difficult to achieve using other

materials.[168,191] This staggered alignment results in a spatial separation of the charge carriers on the different components of the core/shell system which reduces the *e-h* overlap and lengthens the exciton radiative lifetimes.[185,188,191] Type II core/shell nanoparticles are known to be of low emission and low QY but more useful in photovoltaic applications.[159,188,189,191] Examples of type II core/shell nanoparticles include: CdSe/ZnTe,[191] ZnTe/CdS[192] and ZnTe/CdTe.[192]

1.5.2 Alloy and ternary nanoparticles

Ternary alloyed nanoparticles (solid solution) are formed by mixing two semiconductors of a common anion or a common cation but of different band gaps. The main advantage of the alloyed nanoparticles is tuning the band gap by changing the stoichiometries of its constituents instead of varying the size of the nanoparticles.[136-144] Controlling the stoichiometry to tune the band gap is more beneficial than the size control as very small (< 2 nm) nanoparticles are unstable, hence the alloyed nanoparticles can emit at wavelengths (colours) which cannot be achieved by binary nanoparticles.[136-138] Alloyed nanoparticles could be homogeneous or gradient depending on the distribution of its components (Fig. 1.17).[138-141,150,193] The gradient alloy has different optical behaviour compared to the homogeneous one, it resembles a core/shell structure to some extent.[138,150,193,194] In fact, gradient alloyed CdSeS with Se-rich core and S-rich shell showed a QYs up to 85% across the visible region with fine colour saturation without any inorganic shelling.[195] The high QY could be attributed to the gradual variation in the lattice parameters minimizing the formation of any interface defects and to the reduced non-radiative Auger recombination.[196]

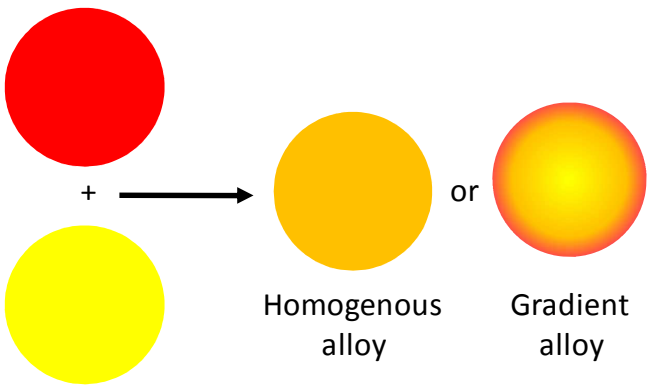

Fig. 1.17 Illustration of homogeneous and gradient alloys.

Végard's Law identify the relationship between the lattice constant of a homogenous alloy and its constituent composition as a linear relationship.[197] The relationship correlating the change in the band gap with the change in the composition can be described in a non-linear quadratic empirical formula;[198] for $A_xB_{1-x}C$

$$E_g(x) = E_g(\mathrm{BC}) + (E_g(\mathrm{AC}) - E_g(\mathrm{BC}) - b)x + bx^2 \qquad (1.32)$$

where, $E_g(x)$ is the band gap of the alloy at x composition, E_g(AC) and E_g(BC) are the band gaps of the two bulk materials AC and BC, respectively and b is the bowing parameter describing the degree of the non-linearity. According to van Vechten and Bergstresser,[198] the bowing is mainly due to disorder effects due to aperiodicity (extrinsic bowing) while the order effects observed in virtual crystal (intrinsic bowing) is very small. This disorder effect was contradicted by Hill and Richardson[199] and they suggested that the disorder effect does not contribute to the bowing parameter as evidenced by the independence of the bowing parameter on the phase change observed in CdS_xTe_{1-x} alloys. Instead, Hill[200] assigned the bowing parameter to the non-linear dependence of the crystal potential on the properties of the constituent ions. Later, Bernard and Zunger[201] reported that the disorder effect on the bowing parameter is small and that the intrinsic bowing is due to three main factors: (i) structural relaxation, (ii) difference in electronegativities and (iii) volume deformation due to difference in the lattice constants of the two binary materials. Wei *et al.*[202] summarized some of the results of the bowing parameter in the following list:

(i) As the chemical and size differences increase as the bowing parameter increase b(S,Se) < b(Se,Te) < b(S,Te). For instance, CdSeS, CdSeTe and CdSTe have b values of 0.28, 0.75 and 1.69 eV, respectively, due to the increase in the lattice mismatch form 3.9% between CdS and CdSe to 11% between CdS and CdTe.

(ii) The bowing parameter for the cadmium chalcogenides alloys is smaller than that of the zinc chalcogenides. For example, b is 0.28 and 0.5 for CdSeS and ZnSeS alloys, respectively.

(iii) The bowing parameter is almost independent of the composition x, except for alloys with large chemical and size differences between its

constituents such as $CdS_{1-x}Te_x$, in which only small amount of Te is sufficient to produce a large shift in the band gap.

(iv) The effect of alloying on the band gap depends on the following equation:

$$dE_g/dx|_{x=0} = [E_g(\text{AC}) - E_g(\text{BC})] - b \qquad (1.33)$$

CdSTe alloy can be used to illustrate the meaning of the above equation. The addition of CdS (E_g = 2.42 eV) to CdTe (E_g = 1.51 eV) results in an alloy with a band gap less than that of both materials because of the small difference in their band gaps and the high bowing parameter.

The effect of particles size on the bowing parameter was studied by Rosenthal *et al.*[139] on a CdSeS alloy. They found that the change in the bowing parameter due to size-dependence is insignificant as both CdSeS nanoparticles and the bulk material show identical bowing. However, CdSeS nanowires did not show any bowing character due to the uniform geometry and the single crystallinity of the nanowires.[203] Finally, the experimental determination of the bowing parameter is difficult therefore, Yang *et al.*[128] provided equation 1.14 (section 1.4) for the determination of the band gap of alloyed nanoparticles without the need for using a bowing parameter. This equation still shows the same bowing and good agreement with the experimental results.

In addition to the II-II-VI alloys mentioned above, well explored ternary nanoparticles are the I-III-VI_2 materials. The size-dependent band gap calculation of chalcopyrite ternary I-III-VI_2 nanoparticles showed that they cover the whole spectrum from ultraviolet to near-infrared. Optical band gaps above 2.5 eV are covered by $CuGaS_2$ and $AgGaS_2$ whereas, $AgGaSe_2$, $CuGaSe_2$, $CuInS_2$ and $CuInSe_2$ show lower optical band gaps (1.5-2.5 eV) which means that they could be a good substitute for the toxic cadmium-based quantum dots.[204] The well-defined exciton absorption peaks are not observed in most of these materials, which could be due to a number of different reasons; firstly, their distinctive electronic properties compared to the II-VI materials, secondly, non-uniform composition distribution and finally, size and shape inhomgeneity.[205] The optical properties of $CuInS_2$ nanoparticles were examined by Castro *et al.*[206] and observed that the broad characteristics of the absorption and emission (FWHM *ca.* 100 nm) peaks are slightly dependent on the size distribution and the nature of the capping agent. Therefore, they concluded that

the origin of the photoluminescence is the unique electronic structure of the $CuInS_2$, in which defects forms an intraband gap levels near the CB and VB edges. Sulfur vacancy and either an indium interstitial or copper indium substitution forms two donor levels below the CB from which electrons can recombine with acceptor states formed above the VB. Maeda *et al.*[207] proved the defect-related photoluminescence in $CuInS_2$ by intentionally introducing copper defects which increased the QY from less than 1% to about 5%. Shelling the $CuInS_2$ nanoparticles with ZnS increased the QY to not more than 60%,[205,208] however, very recently, Klimov *et al.*[209] reported a method for the synthesis of much higher luminescent $CuInS_2$ nanoparticles (QY > 80%) after shelling with few monolayers of CdS or ZnS.

1.6 Characterisation techniques

In addition to the optical spectroscopy techniques (absorption and emission spectroscopy) discussed earlier, other characterisation techniques must be included for the full determination of the nature of the nanoparticles. For heteronanoparticles in particular, more detailed analysis should be carried out to determine the compositional variation and for the determination of diameter and thickness of core and shell, respectively, in a core/shell material.[36,210] The main characterisation techniques are:

1.6.1 Powder X-ray diffraction (p-XRD)

Used for phase identification of the crystalline nanoparticles, based on Bragg's law: $2d\sin\theta = n\lambda$, where, d is spacing between the (*hkl*) planes, θ is the angle between the incident or diffracted beam and the planes, λ is X-ray wavelength and n is an integer. The crystal structure could be identified by analysing the position and intensity of the peaks in the p-XRD pattern. In case of a mixed phase material, the weight fraction of each phase can be obtained from the following equation:

$$W_p = \frac{S_p(ZMV)_p}{\sum_i S_i(ZMV)_i} \tag{1.34}$$

where, *S* is the Rietveld scale factor, *Z* is the number of formula units per unit cell, *M* is the mass of the formula unit, and *V* is the unit cell volume.[211] The increase or decrease in the intensity of a particular peak compared to the standard reference

could give an indication on the preferred growth direction. For example, the formation of hexagonal ZnS[212] and hexagonal CdS[213] nanorods was confirmed by observing a stronger and narrower (002) peak in their p-XRD patterns. The retarded growth direction of ZnS nanowires[214] and In_2S_3 nanoplates[46] was also confirmed by their p-XRD patterns in which certain peaks showed a significant decrease in their intensities. In addition to that, the peak's broadness could be used for the size determination by applying Scherrer equation:

$$D = (k \times \lambda)/(FWHM \times \cos\theta) \quad (1.35)$$

where, *D* is diameter and *k* is a constant.

1.6.2 Transmission electron microscopy (TEM) and high-resolution transmission electron microscopy (HRTEM)

These are the most important techniques for size and shape determination. As its name implies, an electron beam is transmitted through an ultra thin sample forming an image on a fluorescent screen. Theoretical resolution (*r*) in TEM and HRTEM depends on the electron beam wavelength and deflection angle (α): $r = 0.61\lambda/\alpha$ which means that resolutions comparable to the size of a single atom could be achieved.[215] Practically, this resolution cannot be achieved because of lenses aberrations. Contrast in TEM depends on the thickness and composition of the sample; thinner areas or areas with lower atomic number elements will appear brighter than the thicker areas or areas with higher atomic number elements. HRTEM provide good information about the crystallinity of the sample and the crystal defects. The lattice spacing of even small nanoparticles can be observed in HRTEM indicating the high crystallinity of the particles. Crystal defects such as twinning, stacking faults, dislocations and polytypism can also be detected by HRTEM which offer useful understanding for the growth mechanism.[49-51,216]

1.6.3 Selected area electron diffraction (SAED)

SAED *via* TEM is a valuable technique for structure determination. It is more powerful than both X-ray and neutron diffraction due to the very short wavelength of the electron beam, strong atomic scattering, and the ability to investigate small volumes of matter.[217] Similar to X-ray diffraction, electron diffraction follows

Bragg's law but could be simplified into $\lambda=2d\theta$ since, Bragg angle is very small and the integer n is omitted as multiples of Miller indices are used. SAED of a single crystal will be in the form of regular array of spots but would be more complicated for a sample having a number of crystals in different orientations.[215] In case of a sample containing too many randomly oriented crystals, a large number of close spots will be produced such that the SAED will be obtained as continuous rings.

1.6.4 Energy dispersive X-ray analysis (EDAX)

The chemical composition of the nanoparticles can be detected by EDAX, in which, electron beam strike the nanoparticles causing it to emit X-rays that is characteristic to the atoms present in the sample. The energy (or wavelength) of the emitted X-rays depends on the atomic number of each atom, hence, qualitative analysis can be carried out. Quantitative analysis, on the other hand, depends on the frequency of these emissions. EDAX could be done using TEM or scanning electron microscope (SEM).

1.6.5 Electron tomography (ET)

ET is used for reconstructing a 3D projection of the nanocrystal from a series of 2D images taken from different directions by tilting the sample in the electron beam.[218,219] ET combined with HRTEM can provide a higher level of morphological characterisation. Truncations of the corners of Cubic CeO_2[220] nanocrystals and the formation of ZnS[221] nanocrystals with conic heads are examples of the findings based on that combination.

1.7 Applications

Various nanoscale devices have been fabricated based on nanocrystals, including light emitting diodes, photovoltaic cells, optical detectors, quantum dot lasers and memory units. The use of nanocrystals in two of these devices, namely, LEDs and photovoltaic devices are discussed below.

1.7.1 Light emitting diodes (LED)

Since the first report on CdSe-based LEDs,[8] QD-based LEDs became highly competitive with the organic LEDs because of the high colour purity (narrow

FWHM) and the ability to control the emission colour from the UV to the near-IR, by varying the nanoparticles size.[28,222] A typical LED device is formed from a monolayer of the light emitting QDs, sandwiched between an electron transport layer and a hole transport layer. Core/shell nanocrystals (CdSe/CdS and CdSe/ZnS), core/shell/shell (CdSe/CdS/ZnS and ZnSe/CdSe/ZnS) and alloyed nanocrystals (ZnCdSe) were all reported as a good emitting layer with emission colours varying from blue to red.[28] As an example, a recent report used indium tin-oxide/poly(ethylenedioxythiophene):polystyrene sulphonate as an anode, poly(*N*,*N*`-bis(4-butylphenyl)-*N*,*N*`-bis(phenyl)benzidine) as a hole transport layer, tris(8-hydroxyquinoline) aluminium as an electron transport layer, Ca/Al as the cathode and both CdSe/ZnS or CdSe/CdS/ZnS as the QD emitting layer for the fabrication of a green to red emitting QD-LED.[223]

1.7.2 Photovoltaic devices

Owing to the limited reserve of the fossil fuel and its negative impact on the environment, the search for an alternative source of renewable clean energy is attracting the attention. Solar energy provides an endless sustainable energy source. The conversion of the solar energy directly into electricity is done using photovoltaic devices, which is still expensive compared to other technologies. A typical polycrystalline Si photovoltaic device cost more than the double of the average cost of natural gas or wind energy; therefore, economic solar cells with efficient capabilities of both light harvesting and storage are required.[224] Most of the materials reported for photovoltaic use are either toxic or non-abundant materials such as Cd, Pb, In, Se and Te, which means that these materials cannot contribute significantly to a sustainable energy supply.[224,225] Instead, non-toxic, abundant, and thus cheap materials are much more promising and could make an impact even with overall lower efficiencies. Recent estimates of the annual electricity potential as well as material extraction costs and environmental friendliness led to the identification of materials that could be used in photovoltaic applications on a large scale.[224] Most promising materials include iron and copper sulfide.[224,225]

Semiconductor nanocrystals could act as an efficient light absorber material because of their unique optical and electronic properties.[6,28,225] Various nanocrystals were explored for photovoltaic devices including: cadmium and lead chalcogenides,

Cu_2S, $CuIn(S,Se)_2$ and Cu_2ZnSnS_4.[6,28,225] The morphology of the nanocrystals influence the solar cell efficiency as CdSe nanorods allow higher light conversion relative to CdSe QDs.[7] As mentioned earlier, MEG process (section 1.4.4) and type II core/shell materials (section 1.5.1.4) can enhance the photovoltaic applications of the nanocrystals. The disadvantage of the nanocrystals as light absorbers arises from the capping agent. The large organic ligands should be exchanged with smaller ones to decrease the interparticle spacing which affects the electronic properties of the nanocrystals.[225]

1.8 Scope of the present study

The aim of this thesis is to develop novel processes in chemistry for different types of semiconductor nanoparticles. A series of metal complexes of thiobiuret $[M(SON(CN^iPr_2)_2)_n]$ has been used for the first time as single source precursors for the colloidal synthesis of the corresponding metal sulfide nanoparticles. Copper, nickel, iron, zinc, cadmium and indium sulfide nanoparticles, as well as ZnCdS and $CuInS_2$ nanoparticles were selected because of their technological importance. Moreover, this thesis explores the use of single source precursor(s) in the synthesis of CdSe, CdS, CdSe/CdS core/shell, CdSeS alloys and $Cu_{2-x}S$ nanoparticles in microfluidic reactors.

1.9 References

1. M. Auffan, J. Rose, J-Y. Bottero, G. V. Lowry, J-P. Jolivet, M. R. Wiesner, *Nature Nanotech,* 2009, **4**, 634.
2. M. Faraday, *Philos. Trans. R. Soc.* 1857, **147**, 145.
3. C. Burda, X. Chen, R. Narayanan, M. A. El-Sayed, *Chem. Rev.* 2005, **105**, 1025.
4. M. Bruchez Jr., M. Moronne, P. Gin, S. Weiss, A. P. Alivisatos, *Science*, 1998, **281**, 2013.
5. W. C. W. Chan, S. M. Nie, *Science*, 1998, **281**, 2016.
6. A. J. Nozik, *Nano Lett.*, 2010, **10**, 2735.
7. W. U. Huynh, J. J. Dittmer, A. P. Alivisatos, *Science*, 2002, **295**, 2425.
8. V. L. Colvin, M. C. Schlamp, A. P. Alivisatos, *Nature*, 1994, **370**, 354.
9. M. Nirmal, L. Brus, *Acc. Chem. Res.* 1999, **32**, 407.
10. T. Trindade, P. O'Brien, N. L. Pickett, *Chem. Mater.*, 2001, **13**, 3843.
11. J. Tauc, R. Grigorovici, A. Vancu, *Phys. Status Solidi*, 1966, **15**, 627.
12. J. Park, J. Joo, S. G. Kwon, Y. Jang, T. Hyeon, Angew. *Chem. Int. Ed.*, 2007, **46**, 4630.
13. S. Kumar, T. Nann, *Small,* 2006, **3**, 316.
14. B. L. Cushing, V. L. Kolesnichenko, C. J. O'Connor, *Chem. Rev.*, 2004, **104**, 3893.
15. P. D. Cozzoli, T. Pellegrino, L. Manna, *Chem. Soc. Rev.,* 2006, **35**, 1195.
16. C. B. Murray, C. R. Kagan, M. G. Bawendi, *Annu. Rev. Mater. Sci.,* 2000, **30**, 545.
17. Y. Yin, A. P. Alivisatos, *Nature*, 2005, **437**, 664.
18. C. B. Murray, D. J. Noms, M. G. Bawendi, *J. Am. Chem. Soc.*, 1993, **115**, 8706.
19. C. de Mello Donega, P. Liljeroth, D. Vanmaekelbergh, *Small,* 2005, **1**, 1152.
20. Z. A. Peng, X. Peng, *J. Am. Chem. Soc.*, 2002, **124**, 3343.
21. X. Peng, J. Wickham, A. P. Alivisatos, *J. Am. Chem. Soc.*, 1998, **120**, 5343.
22. A. P. Alivisatos, *J. Phys. Chem.*, 1996, **100**, 13226.
23. H. Zhang, J. F. Banfield, *J. Phys. Chem. B* 2000, **104**, 3481.
24. D. V. Talapin, A. L. Rogach, M. Haase, H. Weller, *J. Phys. Chem. B,* 2001, **105**, 12278.

25. P. Dagtepe, V. Chikan, *J. Phys. Chem. C*, 2010, **114**, 16263.
26. H. Reiss, *J. Chem. Phys.* 1951, **19**, 482.
27. P. W. Voorhees, *J. Stat. Phys.*, 1985, **38**, 231.
28. D. V. Talapin, J. S. Lee, M. V. Kovalenko, E. V. Shevchenko, *Chem. Rev.*, 2010, **110**, 389.
29. J. Huang, M. V. Kovalenko, D. V. Talapin, *J. Am. Chem. Soc.*, 2010, **132**, 15866.
30. L. Manna, E. C. Scher, A. P. Alivisatos, *J. Am. Chem. Soc.* 2000, **122**, 12700.
31. L. Qu, X. Peng, *J. Am. Chem. Soc.*, 2002, **124**, 2049.
32. Y. Xia, P. Yang, *Adv. Mater*. 2003, **15**, 351.
33. J. Hu, T. W. Odom, C. M. Lieber, *Acc. Chem. Res.* 1999, **32**, 435.
34. X. Peng, L. Manna, W. Yang, J. Wickham, E. Scher, A. Kadavanich, *Nature*, 2000, **404**, 59.
35. Z. A. Peng, X. G. Peng, *J. Am. Chem. Soc.*, 2001, **123**, 1389.
36. P. K. Santra, R. Viswanatha, S. M. Daniels, N. L. Pickett, J. M. Smith, P. O'Brien, D. D. Sarma, *J. Am. Chem. Soc.* 2009, **131**, 470.
37. M. A. Malik, N. Revaprasadu, P. O'Brien, *Chem. Mater*. 2001, **13**, 913.
38. Mark Green, Paul O'Brien, *Chem. Commun.*, 1999, 2235.
39. A. Ghezelbash, B. A. Korgel, *Langmuir* 2005, **21**, 9451.
40. Z. A. Peng, X. Peng, *J. Am. Chem. Soc.* 2001, **123**, 183.
41. X. Peng, *Adv. Mater.*, 2003, **15**, 459.
42. M. A. Franzman, R. L. Brutchey, *Chem. Mater.*, 2009, **21**, 1790.
43. L. Cademartiri, G. A. Ozin, *Adv. Mater.*, 2009, **21**, 1013.
44. A. Ghezelbash, M. B. Sigman, Jr., B. A. Korgel, *Nano Lett.*, 2004, **4**, 537.
45. M. Sigman, A. Ghezelbash, T. Hanrath, A. E. Saunders, F. Lee, B. A. Korgel, *J. Am. Chem. Soc.*, 2003, **125**, 16050.
46. K. H. Park, K. Jang, S. U. Son, *Angew. Chem. Int. Ed.*, 2006, **45**, 4608.
47. J. W. Mullin, Crystallization, 4th Ed., Butterworth Heinemann, Boston, 2001.
48. N. N. Maseko, N. Revaprasadu, V. S. R. R. Pullabhotla, R. Karthik, P. O'Brien, *Mater. Lett.*, 2010, **64**, 1037.
49. R. L. Penn, J. F. Banfield, *Am. Mineral.*, 1998, **83**, 1077.
50. R. L. Penn, J. F. Banfield, *Science*, 1998, **281**, 969.
51. R. L. Penn, J. F. Banfield, *Geochim. Cosmochim. Acta*, 1999, **63**, 1549.

52. J. H. Yu, J. Joo, H. M. Park, S. I. Baik, Y. W. Kim, S. C. Kim, and T. Hyeon, *J. Am. Chem. Soc.*, 2005, **127**, 5662.
53. Z. Y. Tang, N. A. Kotov, M. Giersig, *Science*, 2002, **297**, 237.
54. K. S. Cho, D. V. Talapin, W. Gaschler and C. B. Murray, *J. Am. Chem. Soc.*, 2005, **127**, 7140.
55. D. Zitoun, N. Pinna, N. Frolet and C. Belin, *J. Am. Chem. Soc.*, 2005, **127**, 15034.
56. R. L. Penn, *J. Phys. Chem. B*, 2004, **108**, 1270.
57. Y. Wang, N. J. Herron, *Phys. Chem.*, 1987, **91**, 257.
58. M. P. Pileni, *Catal. Today*, 2000, **58**, 151.
59. M. Moffitt, A. Eisenberg, *Chem. Mater.*, 1995, **7**, 1178.
60. J. Liu, A. Y. Kim, L. Q. Wang, B. J. Palmer, Y. L. Chen, P. Bruinsma, B. C. Bunker, G. J. Exarhos, G. L. Graff, P. C. Rieke, G. E. Fryxell, J. W. Virden, B. J. Tarasevich, L. A. Chick, *Adv. Colloid Interface Sci.*, 1996, **69**, 131.
61. H. Ohde, M. Ohde, F. Bailey, H. Kim, C. M. Wai, *Nano Lett.*, 2002, **2**, 721.
62. Q. Lu, F. Gao, D. Zhao, Process. *Nano Lett.* 2002, **2**, 725.
63. W. Zhang, L. Xu, K. Tang, F. Li, Y. Qian, *Eur. J. Inorg. Chem*. 2005, **4**, 653.
64. F. Xu, Y. Xie, X. Zhang, C. Wu, W. Xi, J. Hong, X. Tian, *New J. Chem.*, 2003, **27**, 1331.
65. Z. He, S. H. Yu, X. Zhou, X. Li, J. Qu, *Adv. Funct. Mater*. 2006, **16**, 1105.
66. F. Cao, W. Hu, L. Zhou, W. Shi, S. Song, Y. Lei, S. Wang, H. Zhang, *Dalton Trans.*, 2009, 9246.
67. J. A. Gerbec, D. Magana, A. Washington, G. F. Strouse, *J. Am. Chem. Soc.*, 2005, **127**, 15791.
68. J. S. Gardner, E. Shurdha, C. Wang, L. D. Lau, R. G. Rodriguez, J. J. Pak, *J. Nanopart. Res.*, 2008, **10**, 633.
69. J. Zhu, M. Zhou, J. Xu, X. Liao, *Mater. Lett.*, 2001, **47**, 25.
70. R. Rossetti, J. L. Ellison, J. M. Gibson, L. E. Brus, *J. Chem. Phys.*, 1984, **80**, 4464.
71. R. Rossetti, R. Hull, J. M. Gibson, L. E. Brus, *J. Chem. Phys.*, 1985, **82**, 552.
72. M. Gao, B. Richter, S. Kirstein, H. Moehwald, *J. Phys. Chem. B*, 1998, **102**, 8360.
73. S. G. Kwon, Y. Piao, J. Park, S. Angappane, Y. Jo, N. M. Hwang, J. G. Park, T. Hyeon, *J. Am. Chem. Soc.*, 2007, **129**, 12571.

74. D. Fan, M. Afzaal, M. A. Mallik, C. Q. Nguyen, P. O'Brien, P. J. Thomas, *Coord. Chem. Rev.*, 2007, **251**, 1878.
75. N. L. Pickett, P. O'Brien, *The Chem. Rec.*, 2001, **1**, 467.
76. D. Cupertino, D. J. Birdsall, A. M. Z. Slawin, J. D. Woollins, *Inorg. Chim. Acta*, 1999, **290**, 1.
77. D. J. Crouch, P. O'Brien, M. A. Malik, P. J. Skabara, S. P. Wright, *Chem. Commun.*, 2003, 1454.
78. W. Rickelton, R. Boyle, *Solvent Extr. Ion Exch.*, 1990, **8**, 783.
79. C. Byrom, M. A. Malik, P. O'Brien, A. J. P. White, D. J. Williams, *Polyhedron*, 2000, **19**, 211.
80. M. Azad Malik, C. Byrom, P. O'Brien, M. Motevalli, *Inorg. Chimica Acta*, 2002, **338**, 245.
81. C. C. Landry, A. Hynes, A. R. Barron, *Polyhedron*, 1996, **15**, 391.
82. C. Q. Nguyen, M. Afzaal, M. A. Malik, M. Helliwell, J. Raftery, P. O'Brien, *J. Organomet. Chem.*, 2007, **692**, 2669.
83. C. Q. Nguyen, A. Adeogun, M. Afzaal, M. A. Malik, P. O'Brien, *Chem. Commun.*, 2006, 2179.
84. C. Q. Nguyen, A. Adeogun, M. Afzaal, M. A. Malik, P. O'Brien, *Chem. Commun.*, 2006, 2182.
85. T. Trindade, P. O'Brien, *Chem. Mater*. 1997**, 9**, 523.
86. T. Trindade, P. O'Brien, *J. Mater. Chem.*, 1996, **6**, 343.
87. Z. Liu, D. Xu, J. Liang, J. Shen, S. Zhang, Y. Qian, *J. Phys. Chem. B*, 2005, **109**, 10699.
88. Y. Zhang, Y. Du, H. Xu, Q, Wang, *CrystEngComm.*, 2010, **12**, 3658.
89. W. Han, M. Gao, *Cryst. Growth Des.*, 2008, **8**, 1023.
90. B. Ludolph, M. A. Malik, P. O'Brien, N. Revaprasadu, *Chem. Commun*., 1998, 1849.
91. N. Revaprasadu, M. A. Malik, P. O'Brien, G. Wakefield, *Chem. Commun.*, 1999, 1573.
92. N. Revaprasadu, M. Malik, P. O'Brien, *S. Afr. J. Chem.*, 2004, **57**, 40.
93. T. Trindade and P. O'Brien, *Adv. Mater.*, 1996, **8**, 161.
94. N. Revaprasadu, M. A. Malik, P. O' Brien, M. M. Zulu, G. Wakefield, *J. Mater. Chem.*, 1998, **8**, 1885.
95. M. A. Malik, M. Motevalli, P. O' Brien, *Acta Crystallogr.*, 1996, **C25**, 1931.

96. A. A. Memon, M. Afzaal, M. A. Malik, C. Q. Nguyen, P. O'Brien, J. Raftery, *Dalton Trans.,* 2006, 4499.
97. J. E. Oliver, S. C. Chang, R. T. Brown, A. B. Borkovec, *J. Med. Chem.,* 1971, **14**, 773.
98. F. Kurzer, *Chem. Rev.,* 1956, **56**, 95.
99. K. Ramasamy, M. A. Malik, P. O'Brien, J. Raftery, *Dalton Trans.,* 2010, **39**, 1460.
100. G. M. Whitesides, *Nature,* 2006, **442**, 368.
101. J. B. Edel, R. Fortt, J. C. deMello, A. J. deMello, *Chem. Commun.,* 2002, 1136.
102. H. Nakamura, Y. Yamaguchi, M. Miyazaki, H. Maeda, M. Uehara, P. Mulvaney, *Chem. Comm.* 2002, 2844.
103. C. X. Zhao, L. He, S. Z. Qiao, A. P. J. Middelberg, *Chem. Eng. Sci.,* 2011, **66**, 1463.
104. A. M. Nightingale, J. C. de Mello, *J. Mater. Chem.,* 2010, **20**, 8454.
105. A. Abou-Hassan, O. Sandre, V. Cabuil, *Angew. Chem. Int. Ed.,* 2010, **49**, 6268.
106. Y. Song, J. Hormes, C. S. S. R. Kumar, *Small,* 2008, **4**, 689.
107. J. D. Winterton, D. R. Myers, J. M. Lippmann, A. P. Pisano, F. M. Doyle, *J. Nanopart. Res.,* 2008, **10**, 893.
108. B. K. H. Yen, A. Günther, M. A. Schmidt, K. F. Jensen, M. G. Bawendi, *Angew. Chem. Int. Ed.,* 2005, **44**, 5447.
109. S. Krishnadasan, J. Tovilla, R. Vilar, A. J. deMello, J. C. deMello, *J. Mater. Chem.,* 2004, **14**, 2655.
110. B. K. H. Yen, N. E. Stott, K. F. Jensen, M. G. Bawendi, *Adv. Mater.,* 2003, **15**, 1858.
111. H. Nakamura, A. Tashiro, Y. Yamaguchi, M. Miyazaki, T. Watari, H. Shimizu, H. Maeda, *Lap Chip,* 2004, **4**, 237.
112. H. Wang, X. Li, M. Uehara, Y. Yamaguchi, H. Nakamura, M. Miyazaki, H. Shimizu, H. Maeda, *Chem. Commun.,* 2004, 48.
113. H. Wang, H. Nakamura, M. Uehara, Y. Yamaguchi, M. Miyazaki, H. Maeda, *Adv. Funct. Mater.,* 2005, **15**, 603.
114. W. Luan, H. Yang, S-T. Tu, Z. Wang, *Nanotechnology,* 2007, **18**, 175603.
115. H. Yang, W. Luan, S-T. Tu, Z. M. Wang, *Lap Chip,* 2008, **8**, 451.

116. W. Luan, H. Yang, N. Fan, S-T. Tu, *Nanoscale Res. Lett.*, 2008, **3**, 134.
117. H. Yang, W. Luan, S-T. Tu, Z. M. Wang, *Cryst. Growth Des.*, 2009, **9**, 1569.
118. H. Yang, N. Fan, W. Luan, S. T. Tu, *Nanoscale Res. Lett.*, 2009, **4**, 344.
119. H. Yang, W. Luan, Z. Wan, S-T. Tu, W-K. Yuan, Z. M. Wang, *Cryst. Growth Des.*, 2009, **9**, 4807.
120. A. J. deMello, Nature, 2006, **442**, 394.
121. E. M. Chan, A. P. Alivisatos, R. A. Mathies, *J. Am. Chem. Soc.*, 2005, **127**, 13854.
122. S. Marre, J. Park, J. Rempel, J. Guan, M. G. Bawendi, K. F. Jensen, *Adv. Mater.*, 2008, **20**, 4830.
123. L. E. Brus, *J. Chem. Phys.*, 1986, **90**, 2555.
124. M. L. Steigerwald, L. E. Brus, *Acc. Chem. Res*. 1990, **23**, 183.
125. Y. Wang, N. Herron, *J. Phys. Chem.*, 1991, **95**, 525.
126. A. M. Smith, S. Nie, *Acc. Chem. Res.*, 2010, **43**, 190.
127. W. W. Yu, L. Qu, W. Guo, X. Peng, *Chem. Mater.*, 2003, **15**, 2854.
128. C. C. Yang, S. Li, *J. Phys. Chem. C*, 2008, **112**, 2851.
129. H. Yu, J. Li, R. A. Loomis, L-W. Wang, W. E. Buhro, *Nat. Mater.*, 2003, **2**, 517.
130. L-S. Li, J. Hu, W. Yang, A. P. Alivisatos, *Nano Lett.*, 2001, **1**, 349.
131. H. Yu, J. Li, R. A. Loomis, P. C. Gibbons, L-W. Wang, W. E. Buhro, *J. Am. Chem. Soc.*, 2003, **125**, 16168.
132. J. Li, L-W. Wang, *Phys. Rev. B*, 2005, **72**, 125325.
133. M. V. Ramakrishna, R. A. Friesner, *Phys. Rev. Lett.*, 1991, **67**, 629.
134. A. Tomasulo, M. V. Ramakrishna, *J. Chem. Phys.*, 1996, **105**, 3612.
135. P. Lukashev, W. R. L. Lambrecht, T. Kotani, M. van Schilfgaarde, *Phys. Rev. B.*, 2007, **76**, 195202.
136. M. R. Kim, S-Y. Park, D-J. Jang, *J. Phys. Chem. C*, 2010, **114**, 6452.
137. X. Zhong, Y. Feng, W. Knoll, M. Han, *J. Am. Chem. Soc.*, 2003, **125**, 13559.
138. M. D. Regulacio, M. Han, *Acc. Chem. Res.*, 2010, **43**, 621.
139. L. A. Swafford, L. A. Weigand, M. J. Bowers, J. R. McBride, J. L. Rapaport, T. L. Watt, S. K. Dixit, L. C. Feldman, S. J. Rosenthal, *J. Am. Chem. Soc.*, 2006, **128**, 12299.
140. D. D. Lovingood, R. E. Oyler, G. F. Strouse, *J. Am. Chem. Soc.*, 2008, **130**, 17004.

141. J. Ouyang, M. Vincent, D. Kingston, P. Descours, T. Boivineau, Md. B. Zaman, X. Wu, K. Yu, *J. Phys. Chem. C*, 2009, **113**, 5193.
142. J. Ouyang, C. I. Ratcliffe, D. Kingston, B. Wilkinson, J. Kuijper, X. Wu, J. A. Ripmeester, K. Yu., *J. Phys. Chem. C*, 2008, **112**, 4908.
143. M. W. DeGroot, K. M. Atkins, A. Borecki, H. Rösner, J. F. Corrigan, *J. Mater. Chem.*, 2008, **18**, 1123.
144. W. Wang, I. Germanenko, M. S. El-Shall, *Chem. Mater.*, 2002, **14**, 3028.
145. Al. L. Efros and M. Rosen, *Annu. Rev. Mater. Sci.*, 2000, **30**, 475.
146. P. E. Lippens, M. Lannoo, *Phys. Rev. B*, 1989, **39**, 10935.
147. V. I. Klimov, D. W. McBranch, C. A. Leatherdale, M. G. Bawendi, *Phys. Rev. B*, 1999, **60**, 13740.
148. V. Biju, T. Itoh, A. Anas, A. Sujith, M. Ishikawa, *Anal. Bioanal. Chem.*, 2008, **391**, 2469.
149. S. Xu, C. Wang, Q. Xu, R. Li, H. Shao, H. Zhang, M. Fang, W. Lei, Y. Cui, *J. Phys. Chem., C*, 2010, **114**, 14319.
150. C. de M. Donegá, *Chem. Soc. Rev.*, 2011, **40**, 1512.
151. M. Kuno, J. K. Lee, B. O. Dabbousi, F. V. Mikulec, and M. G. Bawendi, J. Chem. Phys., 1997, **106**, 9869.
152. D. V. Talapin, A. L. Rogach, A. Kornowski, M. Haase, H. Weller, *Nano Lett.*, 2001, **1**, 207.
153. K. Leung, K. B. Whaley, *J. Chem. Phys.* 1999, **110**, 11012.
154. S. F. Wuister, A. van Houselt, C. de Mello Doneg, D. Vanmaekelbergh, A. Meijerink, *Angew. Chem. Int. Ed.*, 2004, **43**, 3029.
155. S. F. Wuister, C. de Mello Donega´, A. Meijerink, *J. Phys. Chem. B* 2004, **108**, 17393.
156. D. D. Lovingood, R. Achey, A. K. Paravastu, G. F. Strouse, *J. Am. Chem. Soc.*, 2010, **132**, 3344.
157. M. Jones, J. Nedeljkovic, R. J. Ellingson, A. J. Nozik, G. Rumbles, *J. Phys. Chem. B*, 2003, **107**, 11346.
158. C. Bullen, P. Mulvaney, *Langmuir* 2006, **22**, 3007.
159. J. van Embden, J. Jasieniak, D. E. Gómez, P. Mulvaney, M. Giersig, *Aust. J. Chem.*, 2007, **60**, 457.
160. M. Nirmal, B. O. Dabbousi, M. G. Bawendi, J. J. Macklin, J. K. Trautman, T. D. Harris, L. E. Brus, *Nature*, 1996, **383**, 802.

161. J. Zhao, G. Nair, B. R. Fisher, M. G. Bawendi, *Phys. Rev. Lett.*, **2010**, 104, 157403.
162. X. Wang, X. Ren, K. Kahen, M. A. Hahn, M. Rajeswaran, S. Maccagnano-Zacher, J. Silcox, G. E. Cragg, A. L. Efros, T. D. Krauss, *Nature*, 2009, **459**, 686.
163. B. Mahler, P. Spinicelli, S. Buil, X. Quelin, J-P. Hermier, B. Dubertret, *Nature Mater.*, 2008, **7**, 659.
164. Al. L. Efros and M. Rosen, *Phys. Rev. Lett.*, 1997, **78**, 1110.
165. V. I. Klimov, *Annu. Rev. Phys. Chem.*, 2007, **58**, 635.
166. R. D. Schaller, M. Sykora, J. M. Pietryga, V. I. Klimov, *Nano Lett.*, 2006, **6**, 424.
167. Z. Lin, A. Franceschetti, M. T. Lusk, *ACS Nano*, 2011, **5**, 2503.
168. P. Reiss, M. Protière, L. Li, *Small* 2009, **5**, 154.
169. B. O. Dabbousi, J. Rodriguez-Viejo, F. V. Mikulec, J. R. Heine, H. Mattoussi, R. Ober, K. F. Jensen, M. G. Bawendi, *J. Phys. Chem. B*, 1997, **101**, 9463.
170. M. A. Hines, P. Guyot-Sionnest, *J. Phys. Chem.*, 1996, **100**, 468.
171. M. A. Malik, P. O'Brien, N. Revaprasadu, *Chem. Mater.*, 2002, **14**, 2004.
172. J. R. Dethlefsen, A. Døssing, *Nano Lett.*, 2011, **11**, 1964.
173. C. D. Heyes, A. Yu. Kobitski, V. V. Breus, G. U. Nienhaus, *Phys. Rev. B*, 2007, **75**, 125431.
174. X. Wang, W. Li, K. Sun, *J. Mater. Chem.*, 2011, **21**, 8558.
175. J. S. Steckel, J. P. Zimmer, S. Coe-Sullivan, N. E. Stott, V. Bulovic´, M. G. Bawendi, *Angew. Chem. Int. Ed.*, 2004, **43**, 2154.
176. X. Peng, M. C. Schlamp, A. V. Kadavanich, A. P. Alivisatos, *J. Am. Chem. Soc.*, 1997, **119**, 7019.
177. J. J. Li, Y. A. Wang, W. Guo, J. C. Keay, T. D. Mishima, M. B. Johnson, X. Peng, *J. Am. Chem. Soc.*, 2003, **125**, 12567.
178. J. van Embden, J. Jasieniak, P. Mulvaney, *J. Am. Chem. Soc.*, 2009, **131**, 14299.
179. L. Carbone, C. Nobile, M. De Giorgi, F. D. Sala, G. Morello, P. Pompa, M. Hytch, E. Snoeck, A. Fiore, I. R. Franchini, M. Nadasan, A. F. Silvestre, L. Chiodo, S. Kudera, R. Cingolani, R. Krahne, L. Manna, *Nano Lett.*, 2007, **7**, 2942.

180. D. V. Talapin, J. H. Nelson, E. V. Shevchenko, S. Aloni, B. Sadtler, A. P. Alivisatos, *Nano Lett.*, 2007, **7**, 2951.
181. P. Reiss, J. Bleuse, A. Pron, *Nano Lett.*, 2002, **2**, 781.
182. P. Reissa, S. Carayonb, J. Bleuse, *Physica E*, 2003, **17**, 95.
183. D. Chen, F. Zhao, H. Qi, M. Rutherford, X. Peng, *Chem. Mater.*, 2010, **22**, 1437.
184. A. Narayanaswamy, L. F. Feiner, A. Meijerink, P. J. van der Zaag, *ACS Nano*, 2009, **3**, 2539.
185. C. de Mello Donegá, *Phys. Rev. B*, 2010, **81**, 165303.
186. D. Battaglia, J. J. Li, Y. Wang, X. Peng, *Angew. Chem. Int. Ed.*, 2003, **42**, 5035.
187. D. Pan, Q. Wang, J. Pang, S. Jiang, X. Ji, L. An, *Chem. Mater.* 2006, **18**, 4253.
188. S. A. Ivanov, A. Piryatinski, J. Nanda, S. Tretiak, K. R. Zavadil, W. O. Wallace, D. Werder, V. I. Klimov, *J. Am. Chem. Soc.*, 2007, **129**, 11708.
189. L. P. Balet, S. A. Ivanov, A. Piryatinski, M. Achermann, V. I. Klimov, *Nano Lett.*, 2004, **4**, 1485.
190. S. A. Ivanov, J. Nanda, A. Piryatinski, M. Achermann, L. P. Balet, I. V. Bezel, P. O. Anikeeva, S. Tretiak, V. I. Klimov, *J. Phys. Chem. B* 2004, **108**, 10625.
191. S. Kim, B. Fisher, H-J. Eisler, M. Bawendi, *J. Am. Chem. Soc.*, 2003, **125**, 11466.
192. R. Xie, X. Zhong, T. Basché, *Adv. Mater.*, 2005, **17**, 2741.
193. R. E. Bailey, S. Nie, *J. Am. Chem. Soc.*, 2003, **125**, 7100.
194. N. P. Gurusinghe, N. N. Hewa-Kasakarage, M. Zamkov, *J. Phys. Chem. C* 2008, **112**, 12795.
195. E. Jang, S. Jun, L. Pu, *Chem. Commun.*, 2003, 2964.
196. D. D. Sarma, A. Nag, P. K. Santra, A. Kumar, S. Sapra, P. Mahadevan, *J. Phys. Chem. Lett.*, 2010, **1**, 2149.
197. L. Z. Végard, Phys., 1921, **5**, 17.
198. J. A. van Vechten, T. K. Bergstresser, *Phys. Rev. B*, 1970, **1**, 3351.
199. R. Hill, D. Richardson, *Thin Solid Films*, 1973, **18**, 25.
200. R. Hill, *J. Phys. C: Solid State Phys.*, 1974, **7**, 521.
201. J. E. Bernard, A. Zunger, *Phys. Rev. B*, 1987, **36**, 3199.

202. S. Wei, S. B. Zhang, A. Zunger, *J. Appl. Phys.*, 2000, **87**, 1304.
203. S. J. Kwon, Y. Choi, J. Park, I. Hwang, J. Park, *Phys. Rev. B,* 2005, **72**, 205312.
204. T. Omata, K. Nose, S. O. Y. Matsuo, *J. Appl. Phys.*, 2009, **105**, 073106.
205. R. Xie, M. Rutherford, X. Peng, *J. Am. Chem. Soc.*, 2009, **131**, 5691.
206. S. L. Castro, S. G. Bailey, R. P. Raffaelle, K. K. Banger, A. F. Hepp *J. Phys. Chem. B* 2004, **108**, 12429.
207. M. Uehara, K. Watanabe, Y. Tajiri, H. Nakamura, H. Maeda, *J. Chem. Phys.* 2008, **129,** 134709.
208. L. Li, T. J. Daou, I. Texier, T. T. K. Chi, N. Q. Liem, P. Reiss, *Chem. Mater.* 2009, **21**, 2422.
209. L. Li, A. Pandey, D. J. Werder, B. P. Khanal, J. M. Pietryga, V. I. Klimov, *J. Am. Chem. Soc.*, 2011, **133**, 1176.
210. G. Zorn, S. R. Dave, X. Gao, D. G. Castner, *Anal. Chem.*, 2011, **83**, 866.
211. R. J. Hill, C. J. Howard, J. *Appl. Crystallogr.* 1987, **20**, 467.
212. Y. Li, X. Li, C. Yang, Y. Li, *J. Phys. Chem. B*, 2004, **108**, 16002.
213. Z. Li, J. Sui, X. Li, W. Cai, *Langmuir*, 2011, **27**, 2258.
214. Z. Deng, H. Yan, Y. Liu, *Angew. Chem. Int. Ed.*, 2010, **49**, 8695.
215. D. B. Williams, C. B. Carter, Transmission Electron Microscopy A Textbook for Materials Science, Springer, 2009.
216. M. Seyring, X. Song, M. Rettenmayr, *ACS Nano*, 2011, **5**, 2580.
217. L. A. Bendersky, F. W. Gayle, *J. Res. Natl. Inst. Stand. Technol.*, 2001, **106**, 997.
218. P. A. Midgley, E. P. W. Ward, A. B. Hungría, J. M. Thomas, *Chem. Soc. Rev.*, 2007, **36**, 1477.
219. H. Friedrich, P. E. de Jongh, A. J. Verkleij, K. P. de Jong, *Chem. Rev.*, 2009, **109**, 1613.
220. K. Kaneko, K. Inoke, B. Freitag, A. B. Hungria, P. A. Midgley, T. W. Hansen, J. Zhang, S. Ohara and T. Adschiri, *Nano Lett.*, 2007, **7**, 421.
221. M. Uehara, Y. Nakamura, S. Sasaki, H. Nakamura, H. Maeda, *CrystEngComm*, 2011, DOI: 10.1039/C1CE05168G.
222. A. L. Rogach, N. Gaponik, J. M. Lupton, C. Bertoni, D. E. Gallardo, S. Dunn, N. L. Pira, M. Paderi, P. Repetto, S. G. Romanov, C. O'Dwyer, C. M. S. Torres, A. Eychmüller, *Angew. Chem. Int. Ed.* 2008, **47**, 6538.

223. Q. Sun, Y. A. Wang, L. S. Li, D. Wang, T. Zhu, J. Xu, C. Yang, Y. Li, *Nat. Photon*, 2007, **1**, 717.

224. C. Wadia, A. P. Alivisatos, D. M. Kammen, *Environ. Sci.& Technol.* 2009**, 43**, 2072.

225. S. E. Habas, H. A. S. Platt, M. F. A. M. van Hest, D. S. Ginley, *Chem. Rev.,* 2010, **110**, 6571.

Chapter 2

Metal Sulfide Nanostructured Semiconductors

2.1 Summary

The copper(II), nickel(II), iron(III), zinc(II), cadmium(II) and indium(III) complexes of 1,1,5,5-tetra-*iso*-propyl-2-thiobiuret [$M(SON(CN^{i}Pr_2)_2)_n$], were used as single source precursors for the preparation of the corresponding metal sulfide nanoparticles by solution thermolysis in different solvent/capping agent combinations. Thermolysis experiments of [$Cu(SON(CN^{i}Pr_2)_2)_2$] (CuBT) using only oleylamine produced Cu_7S_4 nanoparticles as a mixture of roxbyite (monoclinic) and anilite (orthorhombic) phases. Pure anilite Cu_7S_4 nanoparticles were obtained when a solution of precursor in octadecene was injected into hot oleylamine whereas, djurleite $Cu_{1.94}S$ nanoparticles were obtained when a solution of the precursor in oleylamine was injected into hot dodecanethiol. The thermolysis of nickel precursor (NiBT) gave Ni_3S_4 in all cases except when precursor solution in oleylamine was injected into hot octadecene which produced NiS nanoparticles. Thermal decomposition of iron complex (FeBT) in oleylamine/oleylamine produced Fe_7S_8 nanoparticles but other combinations, in most cases, gave amorphous material. Injecting a solution of [$Zn(SON(CN^{i}Pr_2)_2)_2$] (ZnBT) into hot oleylamine produced spherical ZnS nanoparticles. Particles with size smaller than 4.3 nm had a cubic phase, whereas the particles with size larger than 4.3 nm had a hexagonal crystal structure as suggested by the selected area electron diffraction (SAED). Powder X-Ray diffraction (p-XRD) showed that the CdS nanoparticles obtained from the thermolysis of [$Cd(SON(CN^{i}Pr_2)_2)_2$] (CdBT) in oleylamine were cubic under all reaction conditions except when dodecanethiol was used as an injection solvent which produced hexagonal CdS. β-In_2S_3 were synthesized from the thermolysis of the indium(III) complex (InTB). Transmission Electron Microscopy (TEM) showed that the copper, nickel and iron sulfide nanoparticles had various morphologies such as spherical, hexagonal disks, trigonal disks, rods or wires; depending on the reaction temperature, concentration of the precursor, the growth time and the solvent/capping agent combination. The zinc and cadmium sulfide nanoparticles were mostly spherical whereas the indium sulfide nanoparticles were produced in the form of ultra-thin (< 1.0 nm) nanorods or nanowires.

2.2 Introduction

Transition metal chalcogenide nanocrystals have been extensively explored because of their interesting physical and chemical properties.[1-5] These properties are shape-dependant and hence good control is required over the synthetic method.[6-8] Zero-dimensional (OD) or quantum dots have been extensively studied and can be synthesised by different chemical methods.[9-13] Various nanoscale devices have been fabricated based on quantum dots, including light emitting diodes,[14] sensors,[15] optical detectors,[16] quantum dot lasers[17] and memory units.[18] One-dimensional (1D) nanostructures such as wires, rods and tubes are considered to be an enhanced system to explore the relation between electrical or thermal transport or mechanical properties and the size confinement.[6,19] These structures are involved in the fabrication of electronic, optoelectronic and electrochemical devices.[19] Although two-dimensional (2D)[20-22] nanostructures (disks and plates) have achieved slightly less attention compared to both OD and 1D nanostructures, different 2D semiconductor nanocrystals have been successfully synthesised.[22]

Copper sulfide nanoparticles have been investigated for many uses including: p-type semiconductors in solar cells,[23-25] nanoscale switches[26] and cathodic materials for lithium rechargeable batteries.[27] Vaughan[28] reported that in 1940 only the end member (Cu_2S) and CuS were known in the Cu-S system. By 1974 nine more copper sulfide phases had been identified[28,29] and by 2006 a total of fourteen copper sulfide phases were recognized.[29] Some known forms of copper sulfide include: chalcocite (Cu_2S), djurleite ($Cu_{31}S_{16}$ or $Cu_{1.94}S$), digenite (Cu_9S_5 or $Cu_{1.8}S$), anilite (Cu_7S_4 or $Cu_{1.75}S$), covellite (CuS) and villamaninite (CuS_2).[28-30] Various methods have been used to synthesis copper sulfide nanoparticles. A hydrothermal method gave digenite nanowires and djurleite nanotubes from CuCl and thiourea.[31] Nanocrystalline Cu_9S_8, Cu_7S_4 and CuS were formed in autoclaves using $[Cu(NH_3)_4]^{2+}$ and thiourea.[32] In a solvothermal method in toluene CuS nanoplatelets were synthesised from copper acetate and CS_2.[33] Korgel *et al.*[20,34] synthesised nanorods, nanodisks, and nanoplatelets of Cu_2S by the solventless thermolysis of a copper alkylthiolate molecular precursor. Chen *et al.* prepared nanoplates of Cu_2S[35] and nanoflakes of CuS[36] by thermal decomposition of $[Cu(acac)_2]$ (acac = acetylacetonate) with elemental sulfur in oleylamine (OLA). Thermal decomposition

of different precursors such as [$Cu(acac)_2$] or $CuCl_2$ and elemental sulfur or dodecanethiol (DDT), produced hexagonal nanodisks of CuS,[3,37] Cu_7S_4,[37] and Cu_2S.[4,38,39] Nanocrystals of CuS,[1,4] Cu_7S_4,[40] and Cu_2S[40-43] were synthesised by the thermolysis of single source precursors including alkyl xanthates,[4] mercaptobenzothiazole,[1] thiobenzoates,[40] dithiocarbamates[41,42] and dithiolates[43] in hot coordinating solvents.

Nickel sulfide is known to have various stoichiometries: Ni_3S_2, $Ni_{3+x}S_2$, Ni_4S_{3+x}, Ni_6S_5, Ni_7S_6, Ni_9S_8, Ni_3S_4, and NiS.[44-48] These differing stoichiometries make nickel sulfide attractive and interesting but complicated to study. Nickel sulfide has wide range of applications, such in electrodes, battery materials, hydrogenation catalysts and transformation toughening for complex ceramics.[49-52] Various methods have been used to synthesis nickel sulfide nanostructures. A solvothermal method was used to synthesise urchin-like NiS.[53,54] NiS hollow nanospheres were synthesised *via* gamma-irradiation.[55] Sonochemical method[56] and microemulsion system[57] produced NiS nanoparticles. Korgel *et al.*[3] synthesised Ni_3S_4 nanocrystal by the thermal decomposition of $NiCl_2$ and elemental sulfur in OLA. The same group reported the solventless thermolysis of a nickel alkylthiolate molecular precursor producing nanorods and triangular nanoprisms of NiS.[21] Thermal decomposition of single source precursors such as, mercaptobenzothiazole,[1] alkyl xanthates,[4] $[\{(CH_3)_2NCH_2\}_2Ni(SCOC_6H_5)_2]$[58] and polysulfide [Ni(*N*-methylimidazole)$_6$]S_8[59] in a hot coordinating solvent formed a mixture of rods and spheres of NiS, ellipsoidal NiS nanoparticles, alpha or beta NiS nanocrystals and NiS_2 or $Ni_{1-x}S$ nanocrystals, respectively.

Iron sulfide also exist in different forms including, pyrite (cubic-FeS_2), marcasite (calciumchloride structure-FeS_2), troilite (FeS), mackinawite ($Fe_{1+x}S$), pyrrhotite ($Fe_{1-x}S$), smythite (hexagonal- Fe_3S_4), and greigite (cubic spinel-Fe_3S_4).[60-62] Pyrrhotite ($Fe_{1-x}S$, x = 0-0.125) is a non-stoichiometric iron sulfide of numerous known superstructures based on the different arrangement of the iron vacancies.[62-66] Fe_7S_8 (x = 0.125) exist in a monoclinic, trigonal or a hexagonal phase.[63-66] Monoclinic and trigonal Fe_7S_8 are ferrimagnetic and stable below 254 and 262 ºC, respectively, while the hexagonal phase is antiferromagnetic and stable below 315 ºC.[63-66] Fe_9S_{10}, $Fe_{10}S_{11}$ and $Fe_{11}S_{12}$ are antiferromagnetic, stable below 209 ºC and

are generally known as hexagonal pyrrhotite.[63-66] Most of the materials reported for photovoltaic use are either toxic or not very abundant elements such as cadmium, lead or indium, *etc* which means that these materials cannot contribute significantly to a future energy supply. Cheap non-toxic and abundant materials are much more promising and could make a significant impact even with lower efficiencies. Recent estimates of the annual electricity potential as well as material extraction costs and environmental friendliness led to the identification of materials that could be used in photovoltaic applications on a large scale.[67] The most promising materials include iron and copper sulfides. Very recently, Law *et al.*[68] reported the synthesis of colloidal FeS_2 nanocrystals inks for thin film photovoltaics. Hydrothermal and solvothermal routes have been widely investigated for the synthesis of iron sulfide in different phases and shapes, including microrods of Fe_3S_4 and FeS_2,[69] Fe_3S_4 flower-like microspheres,[70] FeS_2 crystallites with cubic and octahedral shapes,[71] Fe_3S_4 nanosheets and nanoparticles in mixed solvents of ethylene glycol and H_2O,[72] $Fe_{0.985}S$ necklace-like chains with no surfactant added[73] and cubic FeS_2 *via* a single-source approach using iron(III) diethyldithiophosphate[74] or iron diethyldithiocarbamate.[75] Fe_7S_8 nanowire array have been prepared by electrodeposition with anodic aluminum oxide (AAO) films.[76] Distinctive nanostructure with dumbbell-like shape formed of hexagonal plates and nanowires with compositions of Fe_9S_8 and Fe_7S_8, respectively, have been synthesized by a chemical evaporation method.[77] Various iron sulfide forms ($Fe_{1-x}S$,[59,78] Fe_7S_8[79-81] and Fe_3S_4[79-82]) have been prepared by the thermal decomposition of different single source precursors, such as alkylthiolate,[78] dithiocarbamates,[79,82] bis(tetra-n-butylammonium)tetrakis[benezenethiolato-μ3-sulfidoiron][81] and [Fe(*N*-methylimidazole)$_6$]S_8.[59]

Among the different II-VI binary metal chalcogenide semiconductor nanoparticles, ZnS[83-88] and CdS[87-92] have been extensively investigated, mainly due to their nonlinear optical properties and the ability to tune their band gaps by controlling the nanoparticles size. Bulk ZnS exist as zinc blende (cubic) at room temperature while at elevated temperatures the wurtzitic (hexagonal) phase becomes more dominant.[93-96] The cubic ZnS undergo a phase transformation into the hexagonal phase at about 1020 °C, however, in the nanoscale the hexagonal phase could be stabilised at lower temperatures.[94,95] The properties, *e.g.* electronic structures and band gaps, of both

phases are different from each other; therefore, a good control over the synthetic procedure is required. Bulk ZnS has a direct and large band gap (3.72 eV for cubic phase[97] and 3.77 eV for hexagonal phase[98] at room temperature) and a small Bohr radius[99] (2.5 nm). ZnS is considered as a basic material in cathode-ray tube luminescence,[100] a good phosphor host material in flat panel displays and in infrared windows.[101-102] Moreover, ZnS is effectively used as a shelling material in core/shell structures such as CdSe/ZnS which can be used in bio-imaging and bio-sensors.[103,104]

ZnS nanocrystals have been synthesised by different methods. El-Shall and co-workers prepared nanocrystalline ZnS by reacting anhydrous $ZnCl_2$, sulfur and KBH_4 at room temperature.[105] Reaction of $ZnCl_2$ and sulfur in OLA in the presence of TOPO produced uniform spherical ZnS nanoparticles.[5] Hyeon *et al.*[2] reported the synthesis of tetrahedron-shaped ZnS nanocrystals from the thermal reaction of zinc-oleate complex in DDT. The same group prepared ZnS nanorods from the oriented attachment of quasi-spherical nanocrystals by aging reaction mixtures containing diethylzinc, sulfur, and hexadecylamine.[106] Nanowires of ZnS with diameters down to 1.2 nm were synthesised from zinc-OLA, sulfur in OLA in the presence of DDT.[93] Hexagonal ZnS nanodots were obtained at low temperature (150 °C) using anhydrous $ZnCl_2$ and thiourea in ethylene glycol.[94] Nanorods[95] and different nanostructures[107] of the hexagonal phase synthesised at low temperatures were also reported using the hydrothermal method. Very recently, a solvothermal method was reported for the synthesis of phase and shape controlled ZnS nanocrystals.[108] Nanodots,[4,10,109,110] Nanorods[109] and nanowires[99,111] of ZnS were synthesised through thermal decomposition of single source precursor such as alkylxanthates[4,109] and dithiocarbamtes.[10,110,111]

Bulk CdS is a direct band gap material (2.42 eV)[112] as well. It has shown to be an important component in various devices including: solar cells,[113] and light emitting diodes.[114] Unlike bulk ZnS, the stability phase for the bulk CdS is the wurtzitic form.[115,116] There are two main concerns about the cubic phase in CdS nanoparticles. Firstly, whether it is a metastable (non-equilibrium) phase or an equilibrium phase for CdS nanoparticles due to the surface effects? Secondly, if it is an equilibrium surface effect, what is the minimum size for the formation of the hexagonal phase? CdS nanoparticles showed structural transitions from the cubic phase to the hexagonal phase at annealing temperatures between 300 °C and 400 °C, supporting a

metastable cubic phase.[115] Recently, Yang *et al.*[116] described, on the basis of the total Gibb's free energy as a function of size, the cubic phase as the metastable phase with no influence for the decrease in size on the phase transition. However, a number of different researchers showed that the hexagonal-cubic phase transition is size-dependent with a critical transformation size varying from 4 nm to 15 nm.[115,117-119] Moreover, differently sized pure hexagonal and cubic phases were obtained at the same growth temperature.[119] It was also suggested that metastable phase could be more preferred if it has lower interfacial energy than that of the stable phase, therefore, the nucleation kinetics may control the phase formation.[117,118] In addition to that, the formation of cubic or hexagonal CdS nanoparticles from a thiourea-cadmium complex was found to be dependent on the thiourea/cadmium ratio; ratios < 1.0 favoured the formation of the cubic phase, while ratios between 3.0 and 4.5 produced hexagonal CdS nanoparticles.[119]

Thermal decomposition of precursor(s) in a hot coordinating solvent has been widely explored for the production of monodispersed CdS nanoparticles. Initially, highly toxic precursors such as dimethylcadmium,[12] bis(trimethylsilyl)sulfur[12] or trioctylphosphine sulfide[120,121] were the main source of cadmium and sulfur. Later, less harmful precursors such as $CdCl_2$,[5,121] Cd-oleate[2] or CdO[120,122] as cadmium precursors and DDT[122] or a solution of elemental sulfur in OLA[5] or in octadecene (ODE)[122] as sulfur precursors were found to be good candidates for the synthesis of monodispersed CdS nanoparticles. Since Trindade and O'Brien reported the use of single source precursors for the synthesis of monodispersed nanoparticles, it has captured the attention of different research groups.[123,124] Dithiocarbamates,[10,111,124-127] xanthates,[4,128,129] thioureas,[119,130-135] thiosemicarbazides,[130,134,135] dithiocarbazates,[136] dithiophosphates[137] and clusters[138,139] are some examples for the single source precursors used for the synthesis of monodispersed CdS nanoparticles.

Group III-VI semiconductors are considered as derivatives of group II-VI, where the divalent cation is replaced with a trivalent cation forming a defect structure.[140] Although group III-VI semiconductors have received less attention compared to group II-VI, indium sulfide as a III-VI material is presently being widely investigated for its potential use in different applications. Indium sulfide is a semiconductor which exists in different stable forms, specifically, InS, In_2S_3, In_6S_7.[141] InS is orthorhombic and In_6S_7 is monoclinic, whereas, In_2S_3 has three

different structures: a defect cubic (α-In_2S_3), cubic or tetragonal defect spinel (β-In_2S_3) and layered structure (γ-In_2S_3).[141-143] β-In_2S_3 is stable at room temperature and up to 420 °C, with a high degree of vacancies ordering.[143,144] Above 420 °C the In atoms becomes randomly distributed as the α-In_2S_3 is formed and above 754 °C the trigonal layered structure γ-In_2S_3 become the stable phase.[143,144] The beta form has been used in green or red phosphors for colour televisions,[145] as a buffer layer instead of toxic CdS in $CuInSe_2$-based solar cells[146,147] and as an electrode material in lithium ion batteries[148] because of its high defects and band gap (2.0-2.3 eV).[149]

Various synthetic methods were used for the production of indium sulfide nanostructures including: hydrothermal,[150-152] solvothermal,[153-155] arrested precipitation,[156] sonochemical[157] and thermal decomposition in hot coordinating solvent.[22,158-160] Very few reports are available on the use of single source precursor for the synthesis of monodispersed indium sulfide nanostructures although O'Brien *et al.*[161,162] have previously used single source precursors for the deposition of indium sulfide thin films. Examples of the single source precursor explored for the synthesis of indium sulfide nanoparticles include: $[In(S_2CNEt_2)_3]$[159] and the polymeric complex $[MeIn(SCH_2CH_2S)]_n$[163] which produced InS and In_2S_3, respectively.

In this chapter we explore the use of the thiobiuret complexes $[M(SON(CN^iPr_2)_2)_n]$[164] (M = Cu, Ni, Fe, Zn, Cd or In) as novel single source precursor for the synthesis of metal sulfide nanocrystals.

2.3 Experimental

2.3.1 Synthesis of precursors

All precursors were synthesised according to the following reaction scheme:

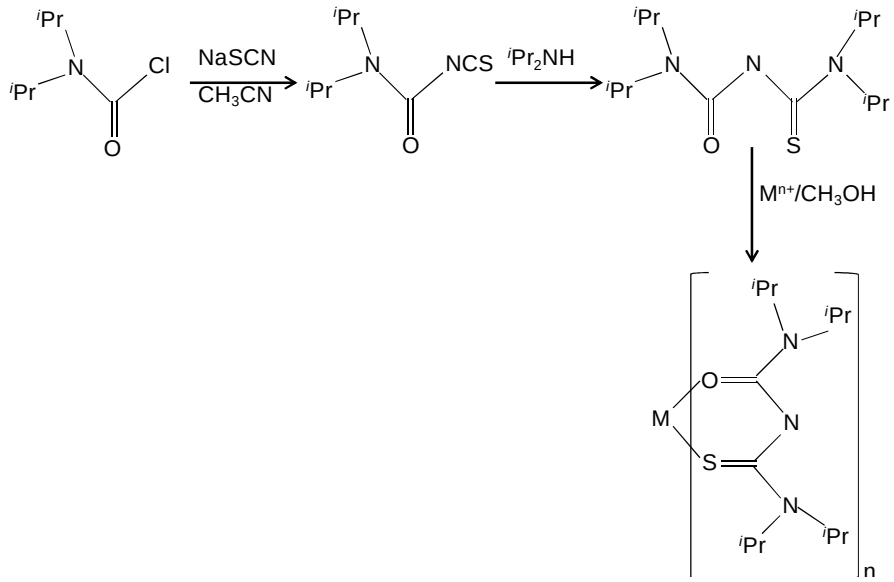

Scheme 2.1: Reaction scheme for the synthesis of $[M(SON(CN^{i}Pr_2)_2)_n]$

2.3.1.1 $[Cu(SON(CN^{i}Pr_2)_2)_2]$ (1)

As described in literature,[164] a solution of di-*iso*-propylcarbamoyl chloride (1.0 g, 6 mmol) and sodium thiocyanate (0.49 g, 6 mmol) in acetonitrile (25 mL) were heated to reflux with continuous stirring for 1 h, during which time a fine precipitate of sodium chloride formed. To the cooled reaction filtrate was added di-*iso*-propylamine (1.49 mL, 12 mmol) followed by stirring for 30 min and addition of copper(II) nitrate (0.76 g, 3 mmol). The product was isolated as green powder.

2.3.1.2 $[Ni(SON(CN^{i}Pr_2)_2)_2]$

The same method as for (**1**) but using nickel(II) acetate (0.74 g, 3 mmol). The product was isolated as violet crystals.[164]

2.3.1.3 $[Fe(SON(CN^{i}Pr_2)_2)_3]$

The same method as for (**1**) but using iron(III) nitrate (0.82g, 2mmol). The product was isolated as a red powder.[164]

2.3.1.4 $[Zn(SON(CN^{i}Pr_2)_2)_2]$

The same method as for (**1**) but using zinc(II) acetate dihydrate (0.67 g, 3 mmol). The product was isolated as a white powder.[164]

2.3.1.5 [Cd(SON(CN^{i}Pr$_2$)$_2$)$_2$]

The same method as for (**1**) but using cadmium(II) acetate dihydrate (0.8 g, 3 mmol) (0.67 g, 3 mmol). The product was isolated as a white powder.[164]

2.3.1.6 [In(SON(CN^{i}Pr$_2$)$_2$)$_3$]

The same method as for (**1**) but using indium(III) chloride (0.45 g, 2 mmol). The product was isolated as a white powder.[164]

2.3.2 Synthesis of nanoparticles

All the nanoparticles were synthesized by thermal decomposition of the single source precursor. In a typical experiment, OLA (15 mL) was degassed under reduced pressure at 100 °C for 30 minutes and then heated to the desired temperature under nitrogen. The required amount of the precursor [M(SON(CN^{i}Pr$_2$)$_2$)$_n$] was dispersed in OLA (5 mL) and injected into the hot OLA solution. The reaction was maintained for 1 h. The solution formed was cooled to approximately 70 °C. After cooling the reaction mixture, an excess of methanol was added and the solid was isolated by centrifugation. The solid was washed several times with methanol then redispersed in toluene. Any insoluble material was removed by centrifugation.

2.3.2.1 Copper sulfide nanoparticles

Nine different thermolysis experiments in OLA were carried out corresponding to three different temperatures (200, 240 and 280 °C) with three different concentrations (5, 10 and 20 mM) at each temperature. Another set of experiments was carried out using different solvent/capping agent combinations at 200 °C and a concentration of 20 mM.

2.3.2.2 Nickel, iron and indium sulfide nanoparticles

Thermolysis experiments in OLA were carried out under different conditions; using three different concentrations (5, 10 and 20 mM) at 200 °C, three different temperatures (200, 240 and 280 °C) at a concentration of 5 mM, and using different solvent/capping agent combinations at a fixed temperature and a fixed concentration.

2.3.2.3 Zinc and cadmium sulfide nanoparticles

Thermolysis experiments in OLA were carried out under different conditions; using three different concentrations (5×10^{-3} M, 1×10^{-2} M and 2×10^{-2} M) at 280 °C, three different temperatures (200, 240 and 280 °C) at a concentration of 5 mM, and using different injection solvents at a 280 °C and a concentration of 5 mM.

2.4 Results and discussion

2.4.1 Copper sulfide nanoparticles

Nanoparticles obtained from the nine different experiments were analysed by p-XRD, TEM and UV-Vis spectroscopy. The p-XRD patterns of the nanoparticles obtained from all experiments correspond to a mixture of the two Cu_7S_4 phases, roxbyite (monoclinic) (ICDD card No. 023-0958) and anilite (orthorhombic) (ICDD card No. 033-0489) as illustrated in Fig. 2.1 for a concentration of 10 mM. Comparing the intensity of the peaks for roxbyite (086) at 46.83° and for anilite (224) at 46.23° it is clear that at higher thermolysis temperatures the orthorhombic form dominates. A quantitative comparison for concentrations of 10 mM and 20 mM is shown in Fig. 2.2. At 280 °C with 20 mM solution of the precursor; the nanoparticles obtained were principally orthorhombic with only minor impurities of the monoclinic phase.

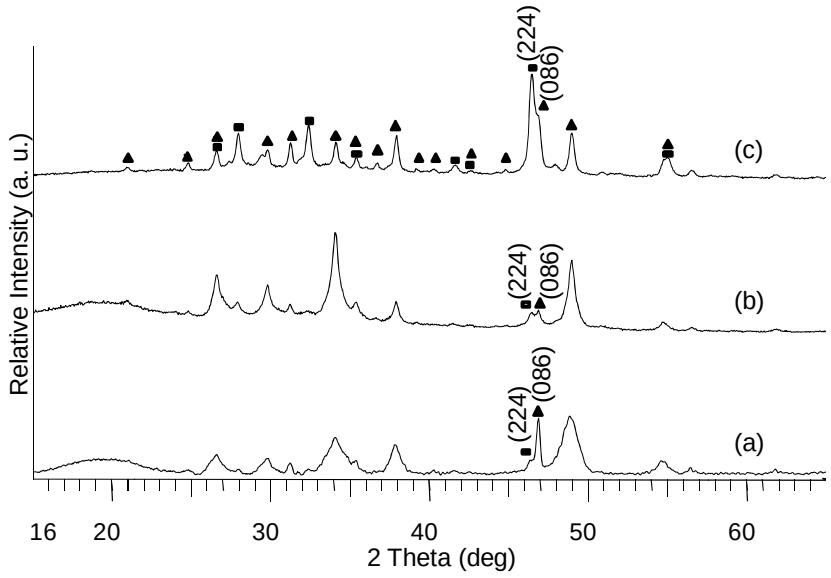

Fig. 2.1 p-XRD patterns of Cu_7S_4 at (a) 200, (b) 240 and (c) 280 °C using 10 mM. (▲) represents roxbyite peaks and (▬) represents anilite peaks.

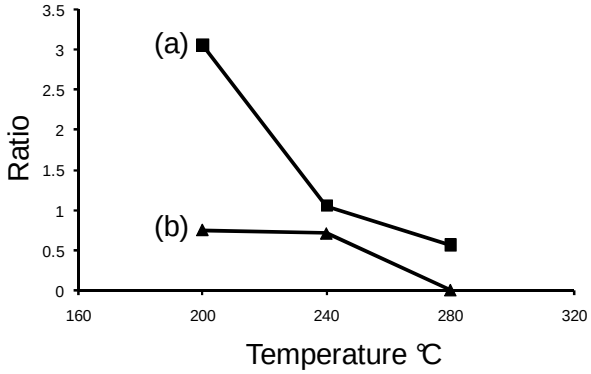

Fig. 2.2 Ratio between the intensity of roxbyite peak to that of the anilite peak at different temperatures, (a) 10 mM (b) 20 mM solutions of the precursor.

TEM images of the nanoparticles grown at different temperatures and concentrations showed remarkable changes in the morphology of crystallites (Fig. 2.3). At 5 mM solution of the precursor and 200 °C, hexagonal nanodisks and spherical nanoparticles with an average diameter of 18.2 ± 2.4 nm were obtained (Fig. 2.3(a)). All the hexagonal particles observed by TEM had large diameter-to-thickness ratios[165] and were therefore oriented parallel to the grid. Hence, in most cases particle thickness had to be obtained using tilting experiments. At 240 and 280 °C, spherical or nearly spherical nanoparticles were formed with an average diameter of 9.4 ± 1.3nm and 9.8 ± 1.6 nm, respectively (Fig. 2.3(b) and 2.3(c)). On increasing the precursor concentration to 10 mM at 200 °C, hexagonal nanodisks lying flat or stacked face-to-face were observed (Fig. 2.3(d)).

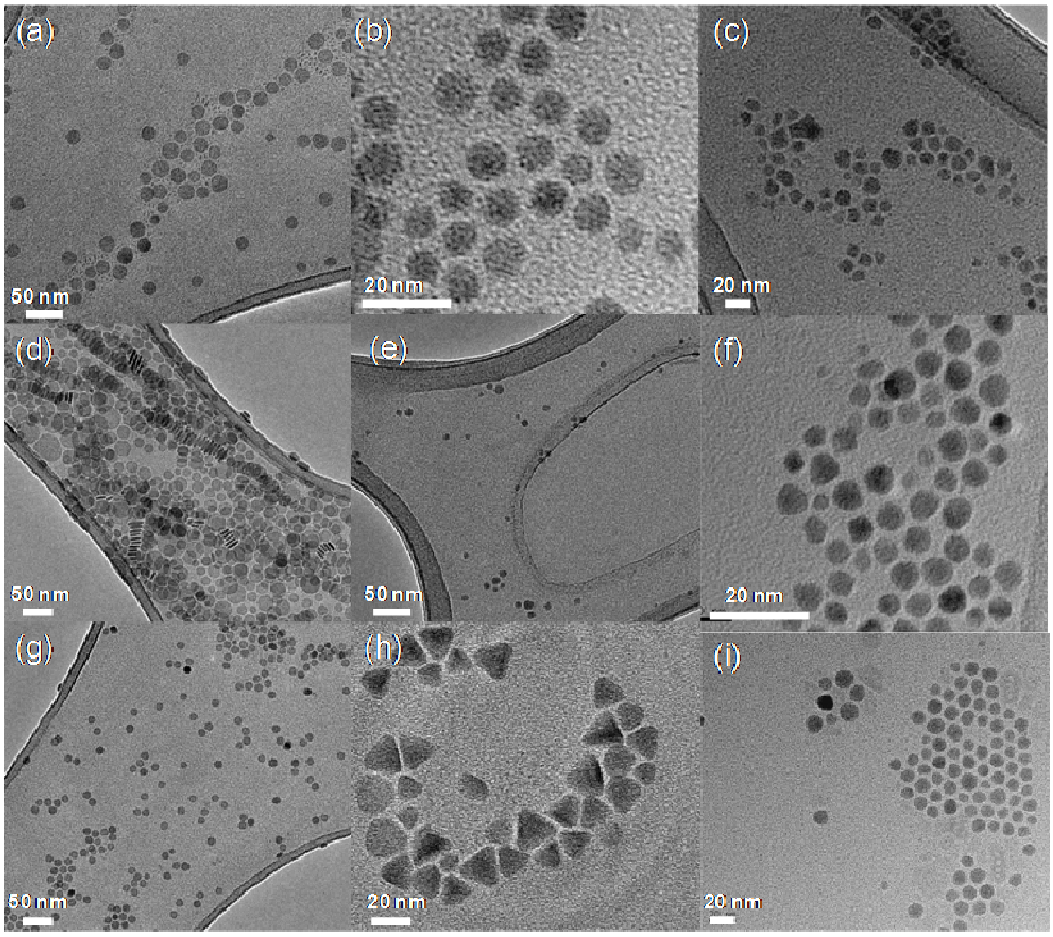

Fig. 2.3 TEM images of Cu_7S_4 after 1 hour. Reactions carried out using 5 mM (a - c), 10 mM (d - f) and 20 mM (g - i) solutions of the precursor at 200 °C (a, d and g), 240 °C (b, e and h) and 280 °C (c, f and i).

The presence of standing and flat oriented disks allowed for the easy measurement of their diameter and thickness by TEM. The average diameter was found to be 22.3 ± 4.6 nm, while the thickness was found to be 4.9 ± 0.35 nm. When nanodisks are standing upright on the grid they resemble rods[38] so the shape of the nanodisks was confirmed using electron tomography (Fig. 2.4). The disk morphology agrees with that described in previous reports.[20] The distance between the face-to-face stacked nanodisks is about 1.2 nm, which is almost equal to the length of OLA,[166] indicating that the nanodisks are covered with a layer of the amine. In some cases the distance was doubled to *ca* 2.4 nm, which is equal to the total length of the two OLA molecules when they are head-to-head as shown in Fig. 2.5. This stacking may minimize the exposed surface area and hence, reduce the surface energy of the structure.[38,165] At higher temperatures the particle morphology changes and disks are not observed. Instead near-spherical or spherical nanoparticles with diameters of 9.3

± 2.2 nm at 240 °C and 12.8 ± 2.2 nm at 280 °C were produced (Fig. 2.3(e) and 2.3(f)). Using a higher precursor concentration (20 mM) lead to parallel oriented hexagonal nanodisks along with some spherical nanoparticles of an average diameter of 12.8 ± 1.9 nm at 200 °C (Fig. 2.3(g)). Trigonal nanodisks were formed at 240 °C (Fig. 2.3(h)), while at 280 °C quasi-close-packed spherical nanoparticles with average diameter of 10.2 ± 2.1 nm were obtained (Fig. 2.3(i)). A spherical structure and not a coin structure was confirmed using tilting experiments.

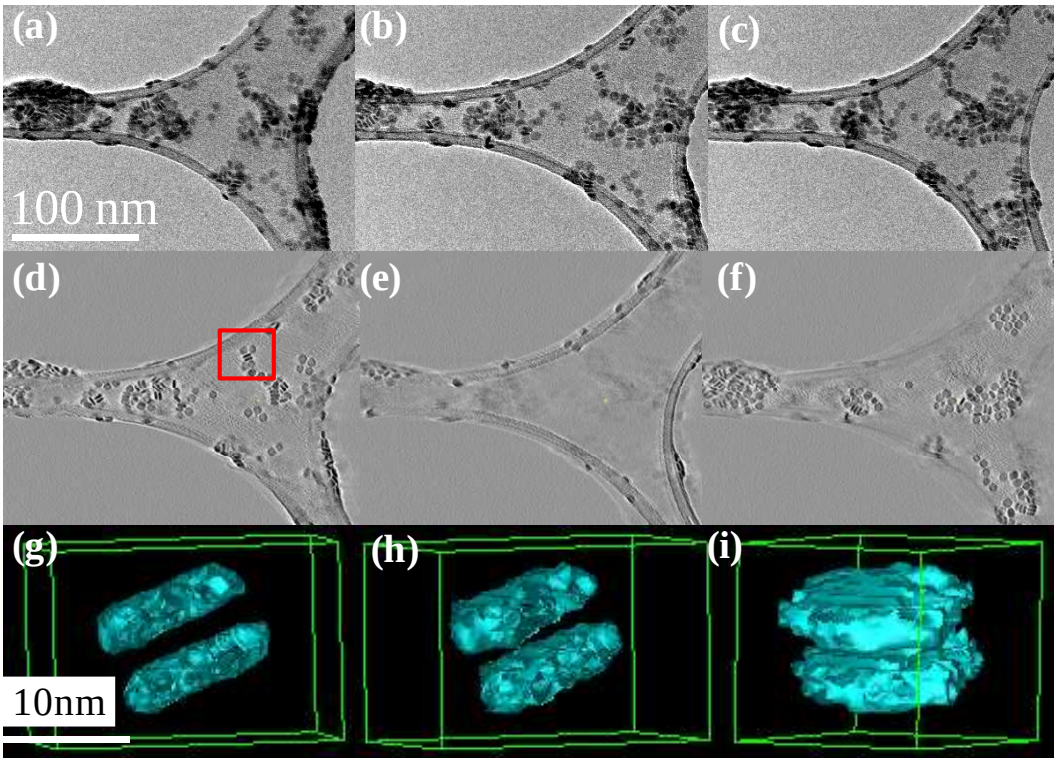

Fig. 2.4 TEM images from a tomographic data series (±60°) at tilt angles of (a)+32°, (b) 0° and (c) -36°. Data slices extracted from the complete tomographic reconstruction are shown for the top surface of the carbon support film (d), the centre of the film (e), and the bottom surface (f). The rendered surface of a pair of representative nanoparticles is shown in for different view directions (g)-(i). The red square in (d) indicates the position of these particles in the full reconstruction.

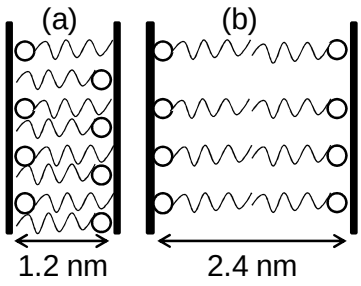

Fig. 2.5 Schematic diagram showing stacked face-to-face nanodisks with (a) 1.2 nm and (b) 2.4 nm spacing.

To study the morphology at an early stage of the reaction time, one or two drops were withdrawn from the reaction mixture after 5 minutes and dispersed in toluene for TEM. The results for all samples are shown in Fig. 2.6. For all thermolysis experiments, trigonal and hexagonal nanodisks were obtained with no evidence of any spherical nanoparticles. Fig. 2.7, shows a study of the effect of reaction time on morphology. The temperature for this reaction was fixed at 280 °C and the highest concentration was used (20 mM). At the beginning of the reaction (2 and 5 minutes) trigonal and hexagonal nanodisks were obtained as shown in Fig. 2.7(a) and 2.7(b). After 30 minutes (Fig. 2.7(c)) the tips of these nanodisks began to erode and at 1 hour (Fig. 2.7(d)) all the nanoparticles became spherical. From these results, it is clear that at the higher temperatures and longer enough growth times, only spherical nanocrystals were obtained.

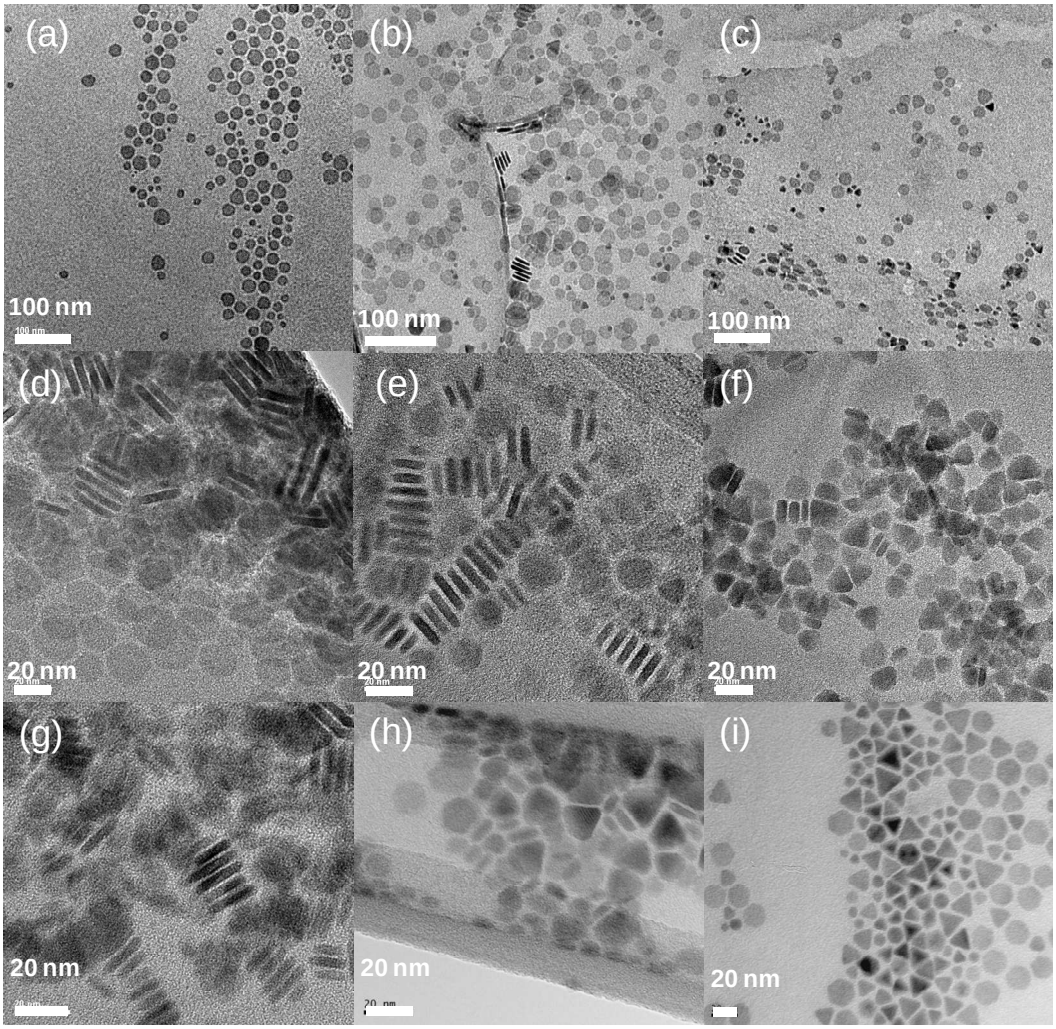

Fig. 2.6 TEM images of Cu_7S_4 after 5 min. Reactions carried out using 5 mM (a - c), 10 mM (d - f) and 20 mM (g - i) solutions of the precursor at 200 °C (a, d and g), 240 °C(b, e and h) and 280 °C (c, f and i).

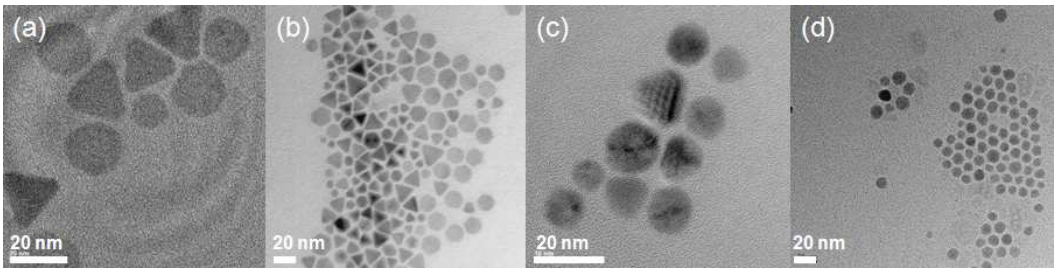

Fig. 2.7 TEM images of Cu_7S_4 produced at (a) 2 min, (b) 5 min, (c) 30 min and (d) 60 min. Reaction carried at 280 °C and using 20 mM solution of the precursor.

Hexagonal Cu_7S_4 nanodisks showed two alignments in TEM studies: parallel alignment to the grid and upright alignment. Interestingly, these alignments were found to depend not only on the diameter-to-thickness ratio of the nanodisk but also

on the concentration of the solution used for preparing the TEM sample. When a concentrated solution was used (~10 mg in 1 mL of toluene) the percentage of the upright nanodisks was very much higher than when the same solution was diluted 10 fold. The upright nanodisks became a minority, as shown in Fig. 2.8. Similar results were previously reported for In_2S_3.[22]

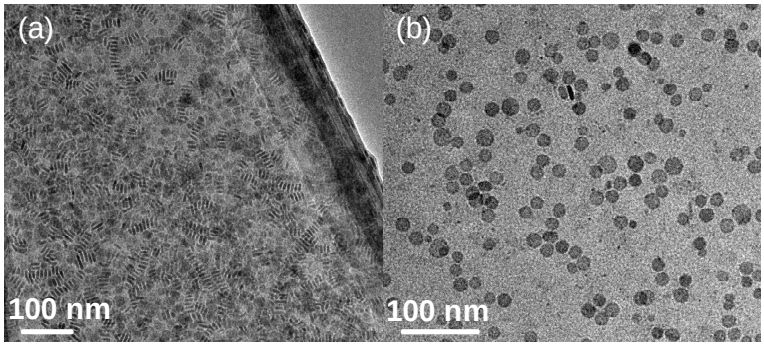

Fig. 2.8 TEM of (a) concentrated and (b) diluted Cu_7S_4 nanodisks samples.

Fig. 2.9 (a-d) shows the High Resolution TEM (HRTEM) images of samples prepared using 20 mM solution of the precursor at 280 °C for 5, 30 and 60 minutes. These images clearly show the transformation of the nanodisks into spherical nanoparticles. The HRTEM images (Fig. 2.9 (e and f)) are for the sample prepared using 10 mM solution of the precursor at 200 °C for 1h. The morphology of the crystallites consists of flat and standing hexagonal nanodisks. The well resolved lattice fringes indicate the highly crystalline nature of the nanocrystals. The d-spacings measured from the lattice fringes of the different crystallites correspond to either the orthorhombic or monoclinic Cu_7S_4 phases. For example, d-spacing of 1.96 Å (Fig. 10(a)) can be indexed to (2 2 4) plane of orthorhombic phase or to (0 16 0) plane of monoclinic phase. The SAED pattern (Fig. 2.9(g)) contains information from a large number of nanoparticles and the polycrystalline diffraction rings at a d-spacing of 1.956 Å (strong ring) and 1.691 Å can be indexed to either orthorhombic or monoclinic Cu_7S_4 phases within measurement errors.

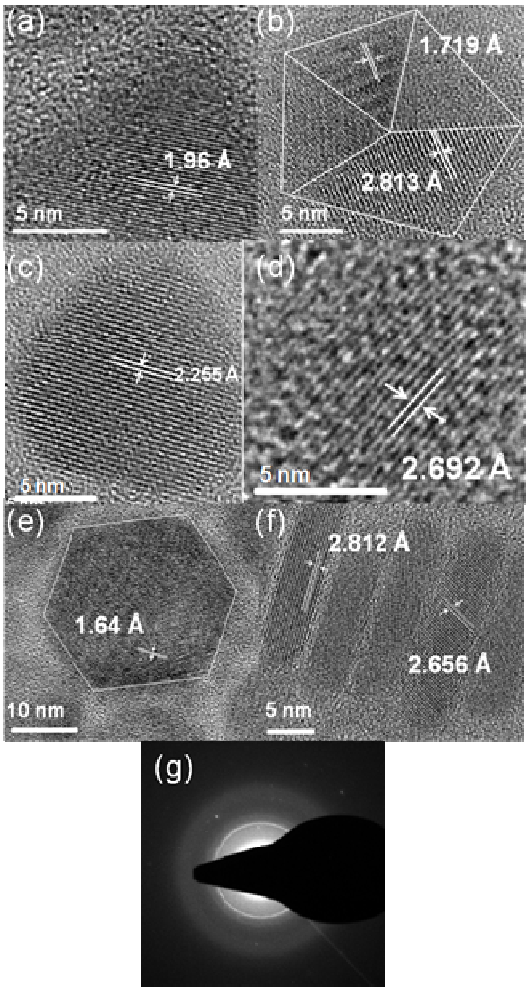

Fig. 2.9 (a-d) are TEM images for sample prepared using 20 mM solution of the precursor at 280 °C for 5, 30 and 60 minutes. (e and f) are for sample prepared using 10 mM solution of the precursor at 200 °C for 1h, showing a flat and standing hexagonal nanodisks, respectively. (g) SAED.

In all previous experiments the precursor was dissolved in OLA and then injected into hot OLA for thermolysis. In order to understand the role of OLA in both size and shape control, two other experiments were carried out. In the first experiment the precursor was dissolved in OLA and then injected into hot DDT and in the other experiment, the precursor was dispersed in ODE and then injected into hot OLA. Reactions were carried out at 200 °C for 1 hour. Using DDT as a capping agent, spherical nanoparticles (Fig. 2.10(b)) of djurleite ($Cu_{1.94}$ S ICDD card No. 23-959) (Fig. 2.11(a)) with an average diameter of 11 nm were formed. In previous reports OLA has been suggested to direct the anisotropic growth of copper sulfide due to preferential absorption on particular planes,[167] whilst DDT was described as a weak

activating agent[40] with weak binding to the copper sulfide.[20] When ODE was used in the injection solution, nonuniform shapes (Fig. 2.10(c)) of anilite (Cu_7S_4 ICDD card No. 33-489) (Fig. 2.12(b)) were obtained. It has been suggested that changing the solvent for precursor injection could change the kinetics of the precursor, leading to a change in the obtained phase of the nanoparticles.[40]

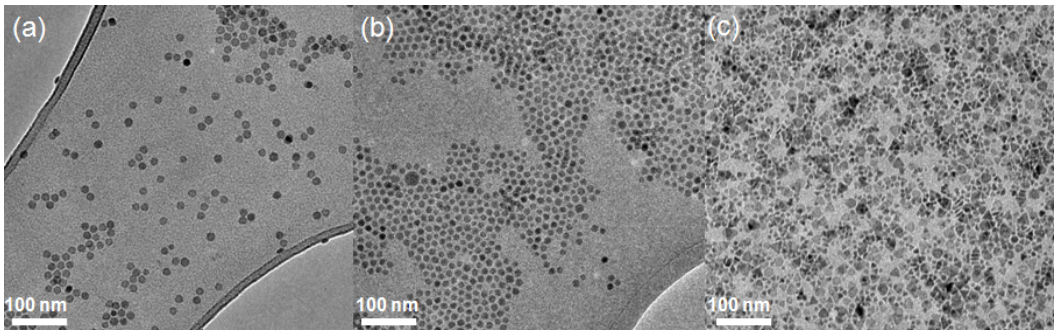

Fig. 2.10 TEM images of (a) only OLA (b) DDT and OLA (c) OLA and ODE.

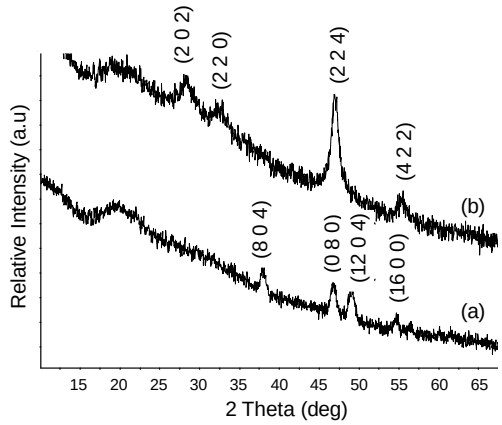

Fig. 2.11 p-XRD of (a) $Cu_{1.94}S$ and (b) Cu_7S_4.

2.4.1.1 Optical properties

All samples showed strong absorption in the UV-blue region and an increase in absorption in the near-IR region (Fig. 2.12), which is consistent with previous reports.[37,168-170] Although $Cu_{2-x}S$ systems have been extremely investigated, there remain uncertainties regarding its electronic structure.[171] The near-IR absorption peak, which corresponds to intraband transition from valence state to unoccupied middle-gap state,[169] was found to depend on both the stoichiometry[169-172] and the structure of the $Cu_{2-x}S$ nanoparticles.[168] Drude-like absorption were subtracted from the data in order to determine the band gap.[172-175] Later it was reported that such correction would make the determination of the nature of the band gap, whether direct or indirect, impossible.[171] Some authors conjectured the possibility of a

mixture of the two types of transition.[172,176] Our results for the two pure samples obtained using DDT or ODE (djurleite ($Cu_{1.94}S$ ICDD card No. 23-959) and anilite (Cu_7S_4 ICDD card No. 33-489)) are shown in Fig. 2.13(a-c). These were used for band gap determination. The best linear fit was obtained on plotting $(\alpha h\nu)^{0.5}$ as a function of photon energy rather than on plotting $(\alpha h\nu)^2$ (where α is the absorption). This observation probably indicates an indirect band gap. The indirect band gap was found to be 1.73 eV for the $Cu_{1.94}S$ and slightly lower (1.70 eV) for the Cu_7S_4. This value is consistent with the value reported by Kuzuya *et al.*[168] for $Cu_{1.72}S$ except that they reported it as a direct transition. Compared to bulk djurleite ($Cu_{1.96}S$) with a band gap of 1.3 eV,[90] a blue shift of 0.43 eV is observed in our $Cu_{1.94}S$ sample, indicating nanometer-sized particles. There is no evidence of any size-dependent character as the absorption of $Cu_{2-x}S$ is size-dependent in the 10 nm particle range only.[171] The near-IR absorption, shows a clear stoichiometric dependence (Fig. 2.13(a)). Moreover, an increase in the orthorhombic composition was associated with an increase in near-IR absorption (Fig. 2.12(c)).

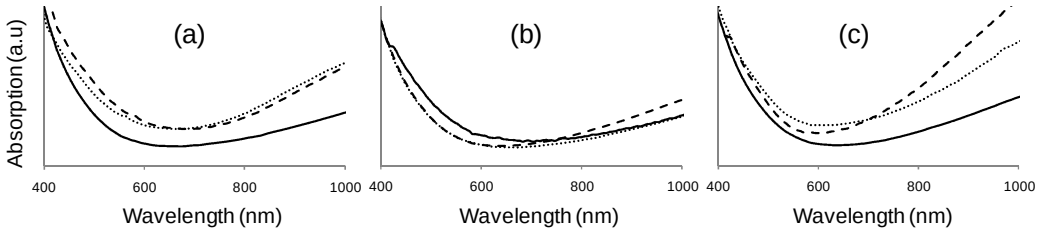

Fig. 2.12 UV-Vis spectra of Cu_7S_4 (a) 200 °C (solid), 240 °C (doted) and 280 °C (dashed), (b) 5 mM (solid), 10 mM (doted) and 20 mM (dashed) and (c) mixture of monoclinic and orthorhombic Cu_7S_4 (solid) orthorhombic Cu_7S_4 with minor monoclinic Cu_7S_4 (doted) and pure orthorhombic Cu_7S_4 (dashed).

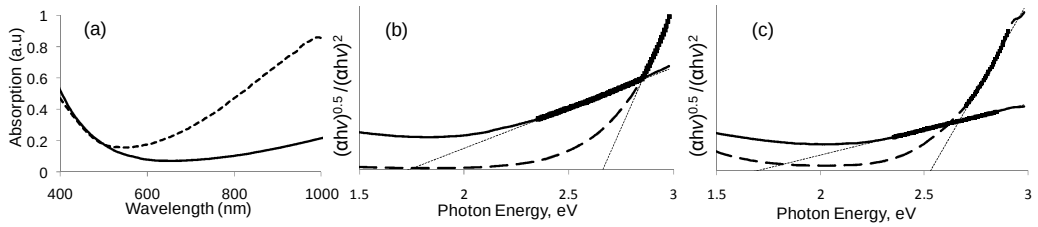

Fig. 2.13 (a) UV-Vis spectra of $Cu_{1.94}S$ (solid) and Cu_7S_4 (dashed), (b) direct (solid) and indirect (dashed) band gap for $Cu_{1.94}S$ and (c) direct (solid) and indirect (dashed) band gap for Cu_7S_4.

2.4.2 Nickel sulfide nanoparticles

Nanoparticles of nickel sulfide were obtained at different thermolysis temperatures and concentrations. The p-XRD patterns of the nickel sulfide nanoparticles obtained from all experiments correspond to cubic Ni_3S_4 (Polydymite) (ICDD card No. 043-1469) with minor impurities of orthorhombic Ni_9S_8 (Godlevskite) (ICDD card No. 022-1193) at higher concentrations, as shown in Fig. 2.14.

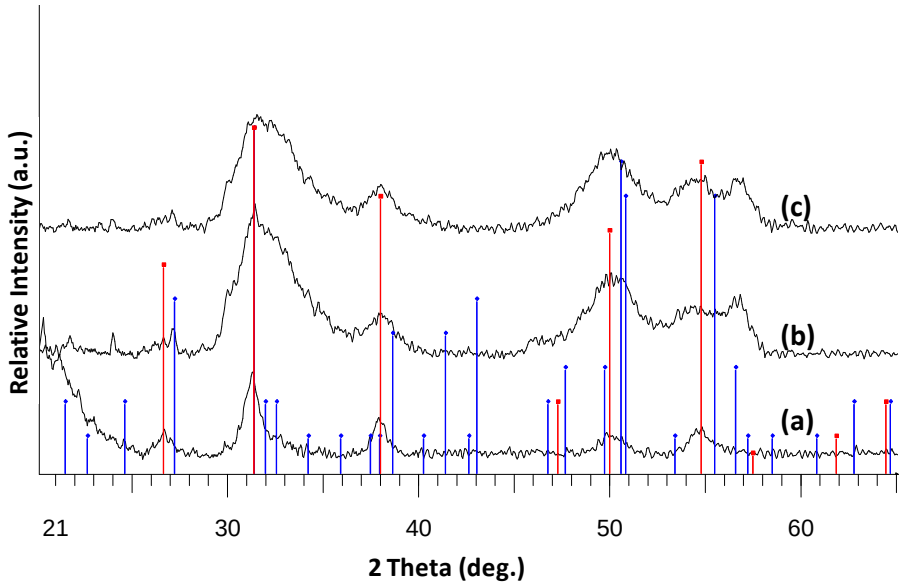

Fig. 2.14 p-XRD patterns of nickel sulfide nanoparticles using (a) 5 mM (b) 10 mM and (c) 20 mM at 200 °C. Red and blue lines represent the Ni_3S_4 (Polydymite) (ICDD card No. 043-1469) and Ni_9S_8 (ICDD card No. 022-1193) peaks, respectively.

TEM images of the nanoparticles grown at different temperatures and concentrations showed remarkable changes in the shape of crystallites (Fig. 2.15). Nanowires (≥ 250 nm) with a diameter between 5 and 10 nm were obtained at 200 °C (Fig. 2.15(a)) when a 5 mM solution of the precursor in OLA was used. Increasing the concentration to 10 mM led to the formation of nanorods 20-65 nm in length and with an average diameter of 8.6 ± 1.7 nm (Fig. 2.15(b)). On using the higher concentration (20 mM), a mixture of spherical nanoparticles and nanorods was produced (Fig. 2.15(c)). The length of the nanorods varied between 24 and 66 nm, whereas the average diameter of nanoparticles was 14.2 ± 1.5 nm. Increasing the growth temperature had the similar effect on the size and shape of nanoparticles. The lengths of nanowires decreased from 250 nm (200 °C) to 140-190 nm (240 °C)

whereas the diameter was almost unaffected (Fig. 2.15(d)). Further increase in thermolysis temperature (280 °C) resulted in the formation of mainly spherical nanoparticles with an average diameter of 13.1 ± 1.2 nm (Fig. 2.15(e)). From these results, it can be suggested that at lower growth temperature or lower precursor concentration, fewer nuclei are formed which favours the growth of elongated nanocrystals.[8,19] By increasing the concentration or temperature more nuclei are formed, due to the presence of more material or increasing the reactivity of the precursor, leaving a lower monomer concentration in solution which directs the nanocrystals growth towards the lowest chemical potential environment and results in the formation of spherical nanocrystals.[8,19]

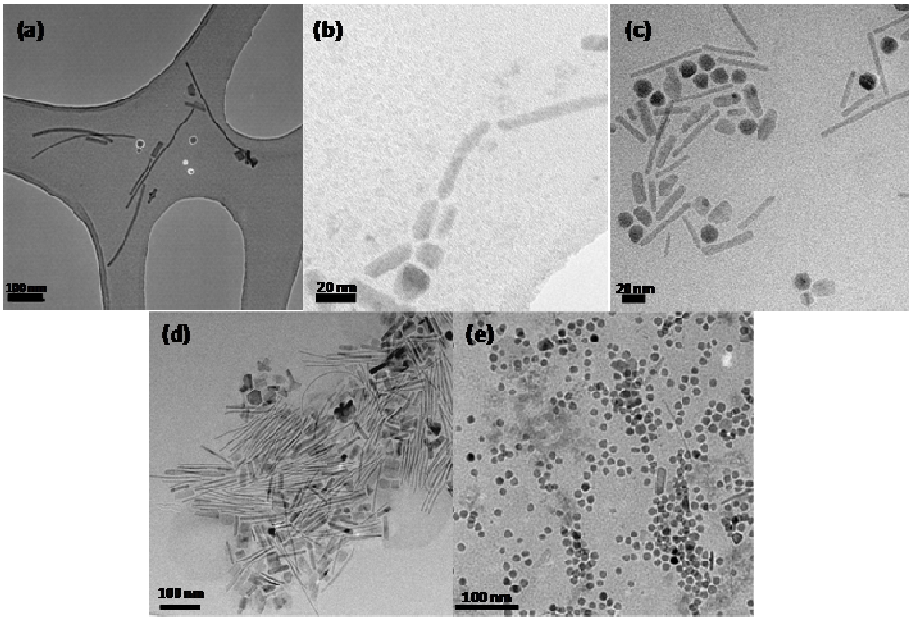

Fig. 2.15 TEM images of nickel sulfide using (a) 5 mM (b) 10 mM and (c) 20 mM at 200 °C and (d and e) using 5 mM at 240 and 280 °C respectively.

At the highest concentration (20 mM) of precursor at 200 °C a mixture of nanorods and spherical nanoparticles were obtained (Fig. 2.15(c)). The reaction mixture was analysed at different time intervals to observe the effect of time on the shape of nanoparticles (Fig. 2.16(a, b and c)). Fig. 2.16(a, b and c) shows that both the nanorods and the spherical nanoparticles are formed from the beginning of the reaction. None of these two morphologies grew at the expense of the other; the rods to spherical nanoparticles ratio roughly remain the same. The nanorods length increased by time from the range of 11-30 nm after 5 minutes to 15-44 nm and 24-66 nm after 30 and 60 minutes, respectively. The average diameter of the spherical

nanoparticles was 9.4 ± 1.2 nm, 13.5 ± 1.5 nm and 14.2 ± 1.5 nm after 5, 30 and 60 minutes respectively.

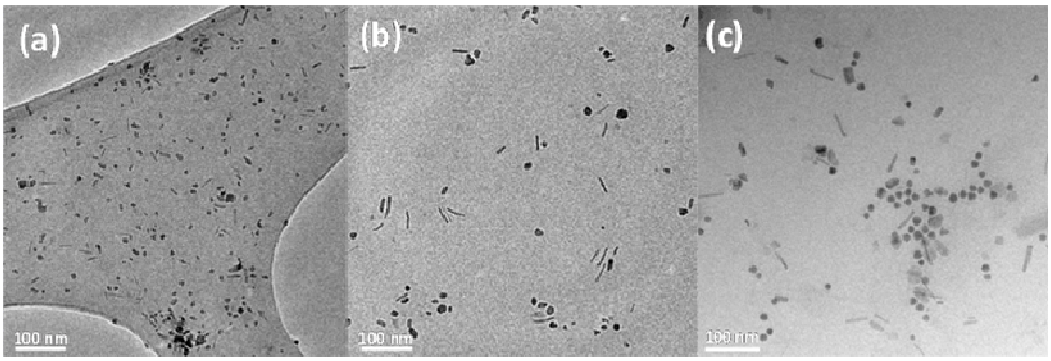

Fig. 2.16 TEM images of nickel sulfide using 20 mM at 200 °C (a) 5 minutes (b) 30 minutes and (c) 1 hour.

The d-spacing obtained for both spherical nanoparticles and the nanorods from HRTEM and fast Fourier transform (FFT) (Fig. 2.17) is about 2.80 Å which corresponds to the (113) planes of the cubic Ni_3S_4 (ICDD card No. 043-1469). An extra pair of spots was observed in the FFT of both spherical nanoparticles and the nanorods that could be indexed to the (004) planes. The two extra spots in the FFT of the spherical nanoparticles originate from the top right part of the crystal which could be due to growth on the (004) planes or due to stacking faults. The source of these extra spots in FFT of the nanorods is a neighbouring crystal growing on the (004) plane. Another HRTEM image (Fig. 2.17(c)) of a nanowire and its FFT (Fig. 2.17(f)) show d-spacing corresponding to the (113) planes and double spacing of the (004) planes.

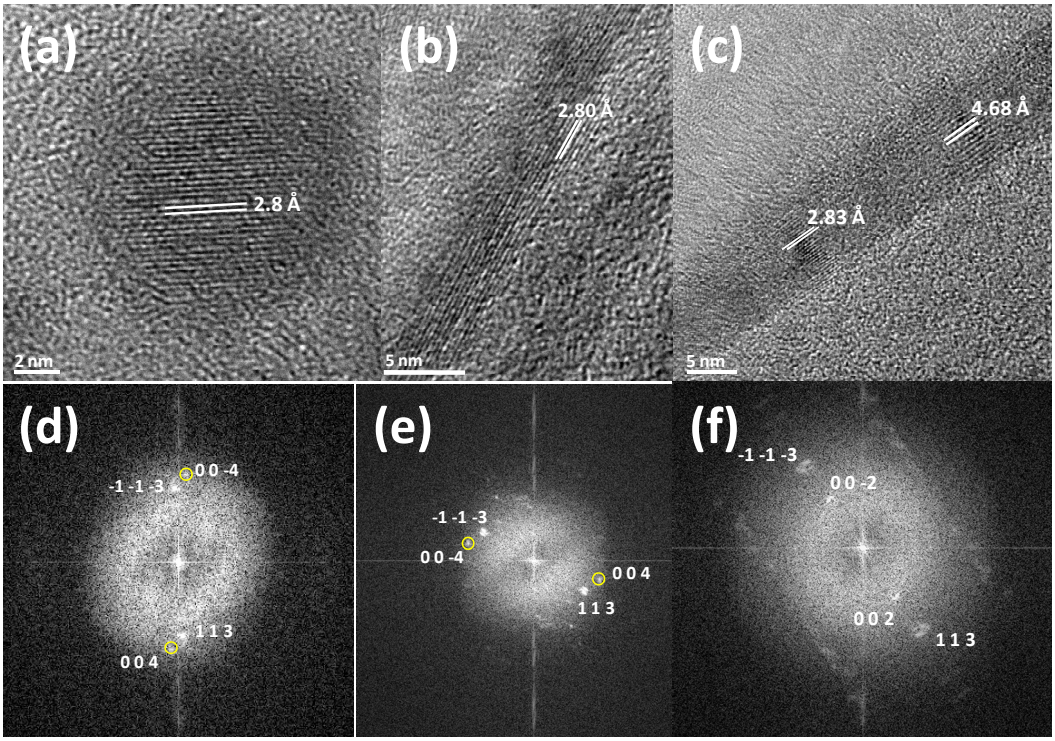

Fig. 2.17 (a) HRTEM of spherical nanoparticles (b and c) HRTEM of nanowires and (d-f) FFT of (a-c) respectively.

The effect of other surfactants or capping agents was investigated using 5 mM solution of the precursor at 240 °C. p-XRD patterns of the as obtained nanoparticles are shown in Fig. 2.18. Replacing OLA from the injection solution with the non-coordinating solvent ODE produced Ni_3S_4 nanorods with average length and diameter of 30 and 7 nm, respectively (Fig 2.19(b)) instead of longer nanowires as observed for OLA as injection solvent and capping agent (Fig. 2.19(a)). When an OLA solution of the precursor was injected into hot ODE, highly aggregated NiS (ICDD card No. 002-1280) nanowires were obtained (Fig. 2.19(c)). DDT showed a great effect on the shape of the nanoparticles. Replacing OLA from the injection solution with DDT produced Ni_3S_4 triangular-based nanostructures (nanoprisms or tetrahedrons) with few nanorods as well (Fig. 2.19(d)). When an OLA solution of the precursor was injected into hot DDT all nanorods disappeared and only the triangular-based nanostructures could be seen in TEM (Fig. 2.19(e)). HRTEM image of the triangular-based nanostructures may suggest a tetrahedral structure as the contrast decrease from the apex to the base indicating a decrease in thickness (Fig. 2.20).[64] Nanorods were again obtained by dissolving the precursor into ODE then injecting the solution into hot DDT (Fig. 2.19(f)).

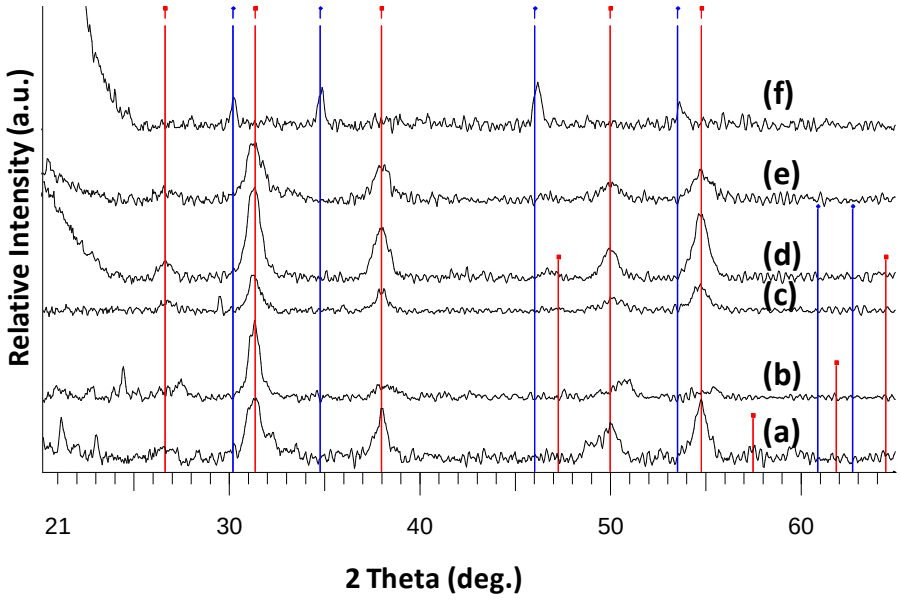

Fig. 2.18 p-XRD patterns of nickel sulfide using different solvent/capping agent (a) OLA/OLA (b) DDT/OLA (c) ODE/OLA (d) OLA/DDT (e) ODE/DDT (f) OLA/ODE. Red and blue lines represent the Ni_3S_4 (Polydymite) (ICDD card No. 043-1469) and NiS (ICDD card No. 002-1280).

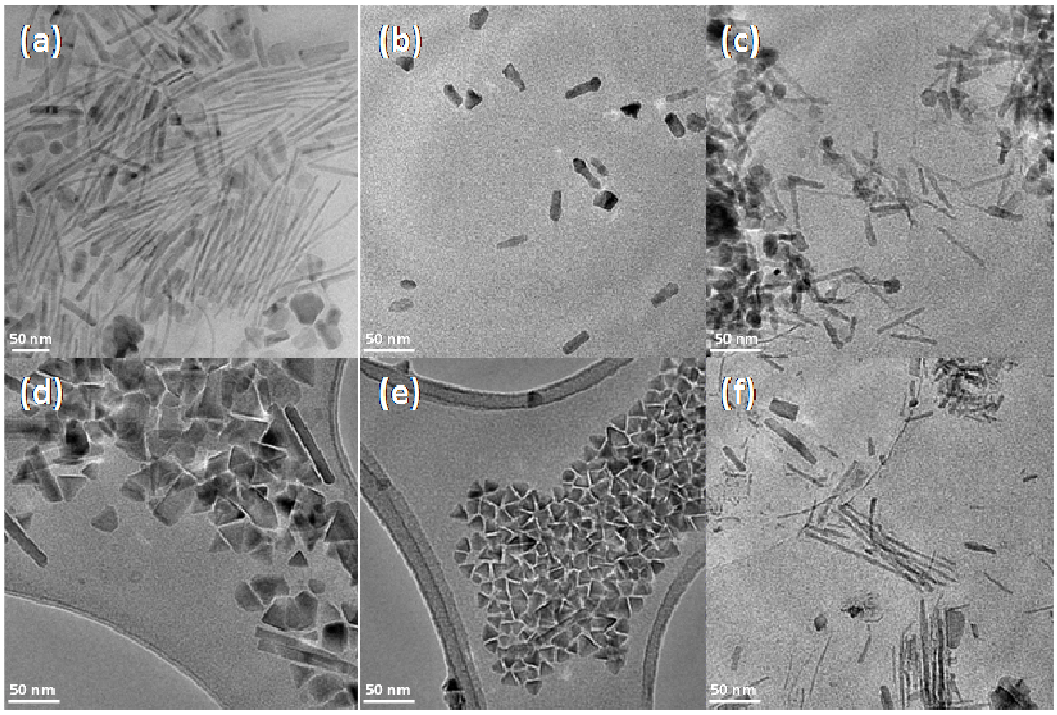

Fig. 2.19 TEM images of nickel sulfide using different solvent/capping agents (a) OLA/OLA (b) ODE/OLA (c) OLA/ODE (d) DDT/OLA (e) OLA/DDT (f) ODE/DDT.

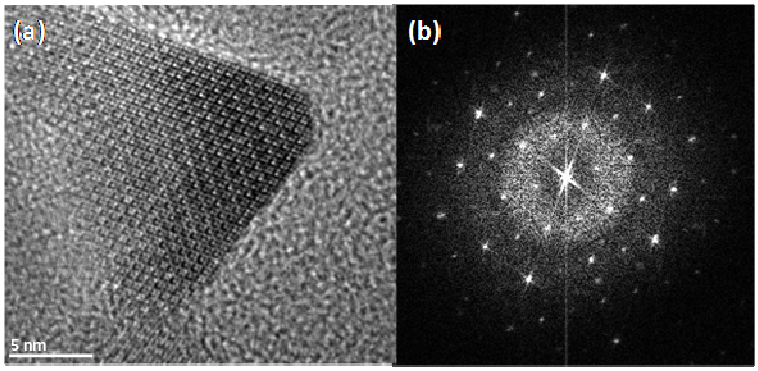

Fig. 2.20 (a) HRTEM of triangular nanoprism and (b) FFT of (a).

2.4.3 Iron sulfide nanoparticles

Nanoparticles obtained from all different experiments were analysed by p-XRD and TEM. All samples produced Fe_7S_8 (Pyrrhotite-4M ICDD card No. 029-0723) (Fig. 2.21) except at high concentration (20 mM) which gave only amorphous material.

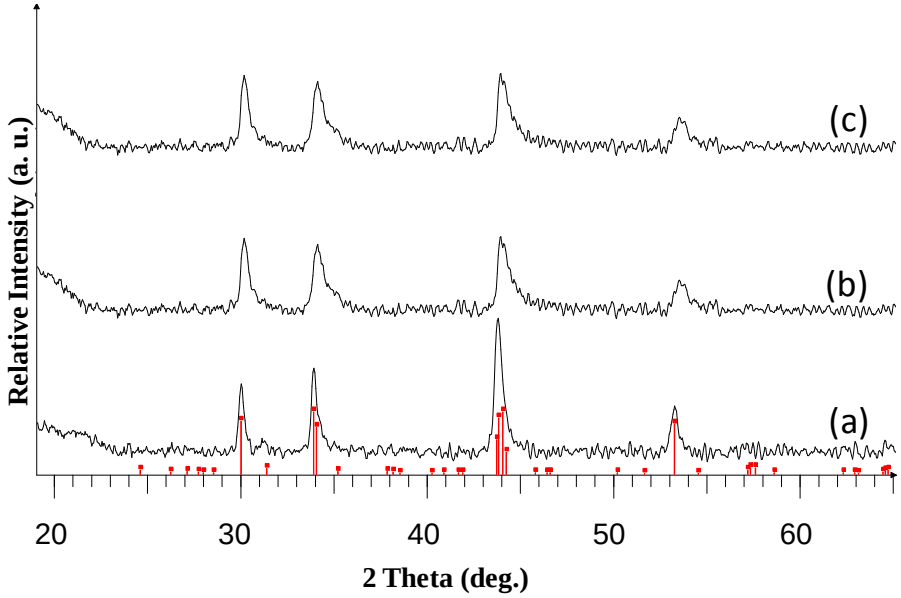

Fig. 2.21 p-XRD patterns of iron sulfide nanoparticles at (a) 200 °C (b) 240 °C and (c) 280 °C using 5 mM solution.

TEM images of the nanomaterials grown at different temperatures and concentrations showed remarkable changes in the morphology of crystallites (Fig. 2.22). At 5 mM solution of the precursor and 200 °C growth temperature, good quality nanoparticles with an average diameter of 5.1 ± 1.0 nm were obtained (Fig. 2.22(a)). Increasing the concentration to 10 mM allowed the nanoparticles to grow

bigger and resulted in average diameter of 6.1 ± 0.9 nm (Fig. 2.22(b)) whereas at higher concentration of 20 mM only amorphous material is observed (Fig. 2.22(c)). Significant change in the morphology of obtained nanomaterials was observed on increasing the growth temperature from 200 to 240 or 280 ºC. At 240 ºC, irregular nanocrystals were formed (Fig. 2.22(d)). At the higher temperature (280 ºC), hexagonal nanoplates and nanorods were obtained (Fig. 2.22(e)). Both structures had a wide range of size distribution as the width of the hexagonal nanoplates varied from 20 nm to 120 nm, and the nanorods lengths were between 37 to 95 nm.

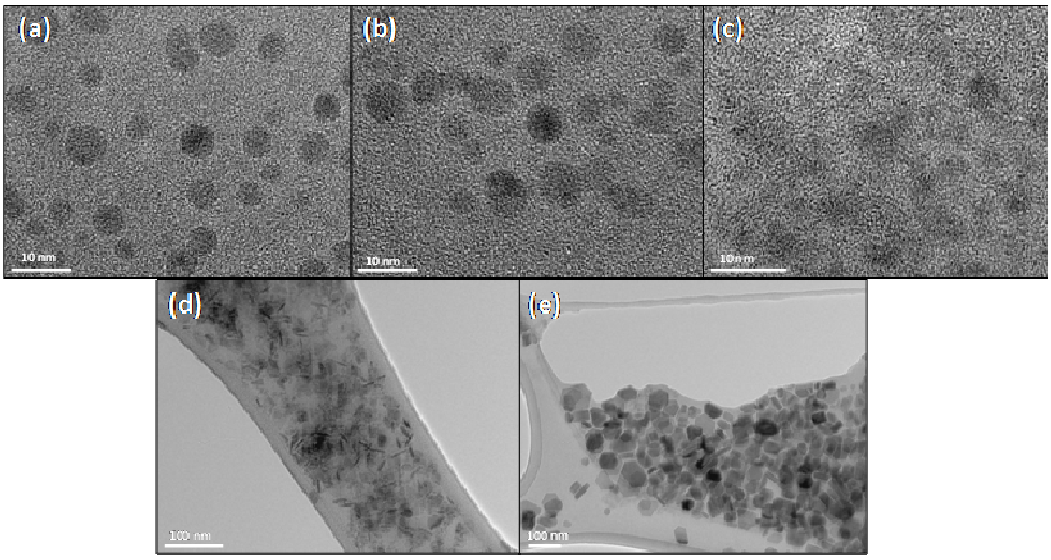

Fig. 2.22 TEM images of iron sulfide using (a) 5 mM (b) 10 mM and (c) 20 mM at 200 °C and (d and e) using 5 mM at 240 and 280 °C respectively.

Fig. 2.23, shows a study of the effect of reaction time at 280 °C and 5 mM concentration. Samples analysed by TEM after 5 minutes of the start of reaction showed hexagonal nanoplates and nanorods (Fig. 2.23(a)). After 30 minutes, a mixture of well defined hexagonal nanoplates with width range between 20 and 60 nm and nanorods with length range of 25 to 60 nm was obtained (Fig. 2.23(b)). After 1 hour these structures grew bigger and reached 120 nm for the hexagonal nanoplates width, and 95 nm for the nanorods length (Fig. 2.23(c)).

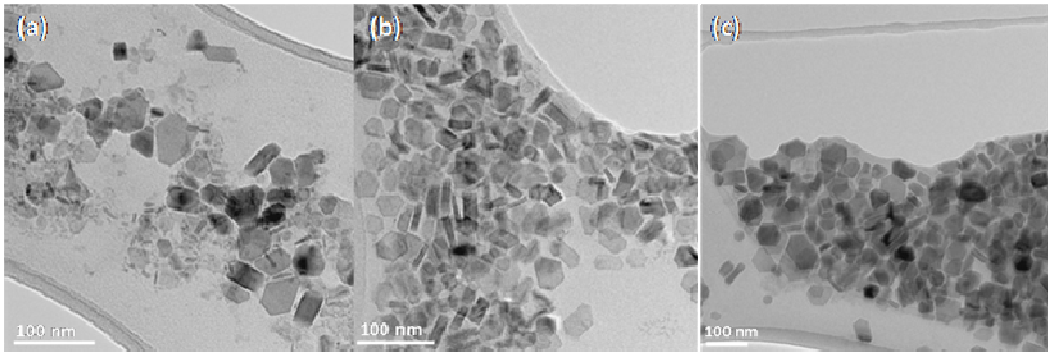

Fig. 2.23 TEM images of iron sulfide using 5 mM at 280 °C (a) 5 minutes (b) 30 minutes and (c) 1 hour.

Lattice fringes observed in the HRTEM images indicates the high crystallinity of the nanoparticles. The spherical nanoparticles showed a d-spacing of 2.08 and 2.67 Å corresponding to the (322) and (004) planes respectively (Fig. 2.24(a, c)). HRTEM revealed that some of the spherical nanoparticles are actually polyhedral (Fig 2.24(d)). The d-spacing calculated from the hexagonal nanoparticles was found to be 3.03 Å corresponding to the (-122) plane (Fig 2.24(e)). Selected area diffraction pattern confirmed the formation of Fe_7S_8 (Pyrrhotite-4M ICDD card No. 029-0723) (Fig. 2.24(f)).

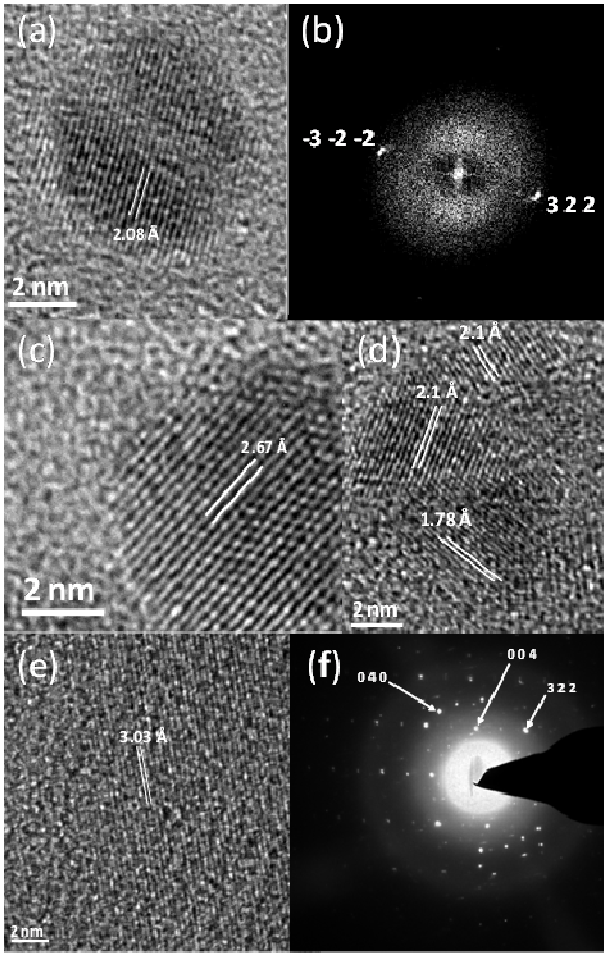

Fig. 2.24 (a and c) HRTEM of spherical Fe_7S_8 nanoparticles, (b) FFT of (a), (d) HRTEM of a polyhedral Fe_7S_8 nanoparticle, (e) HRTEM of hexagonal Fe_7S_8 nanoparticle and (f) SAED of Fe_7S_8 obtained from mixture of hexagonal nanoplates and nanorods.

The effect of other surfactants or capping agents was investigated using 5 mM solution of the precursor at 200 °C. Injecting an ODE solution of the precursor into hot OLA or vice versa produced nanowires of varying length and orientation (Fig. 2.25(a, c)), whereas injecting a DDT solution of the precursor into hot OLA produced monodispersed nanowires with length up to 90 nm and average diameter of 1.5 nm (Fig. 2.25(b)). Injection of OLA solution of the precursor into hot DDT produced cluster of nanowires (Fig. 2.25(d)). p-XRD pattern of the wires showed the growth of Fe_7S_8 (Fig. 2.26(a)). A d-spacing corresponding to the (-122) and (004) planes where calculated from both HRTEM and FFT images (Fig. 2.26(b, c)).

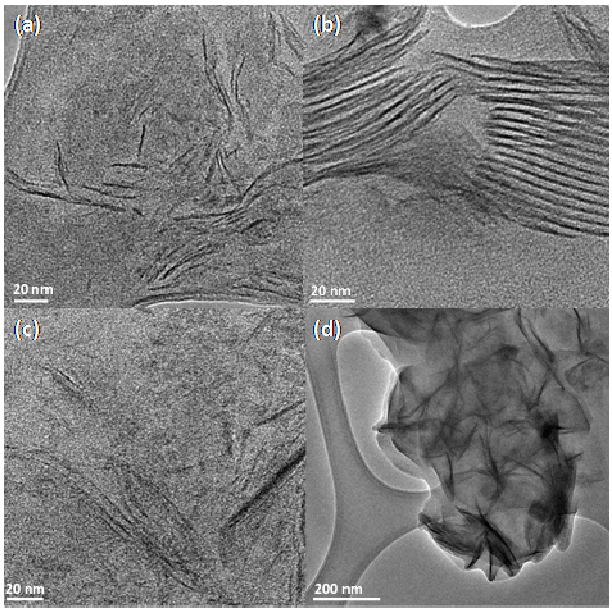

Fig. 2.25 TEM images of iron sulfide using different solvent/capping agents (a) ODE/OLA (b) DDT/OLA (c) OLA/ODE (d) OLA/DDT.

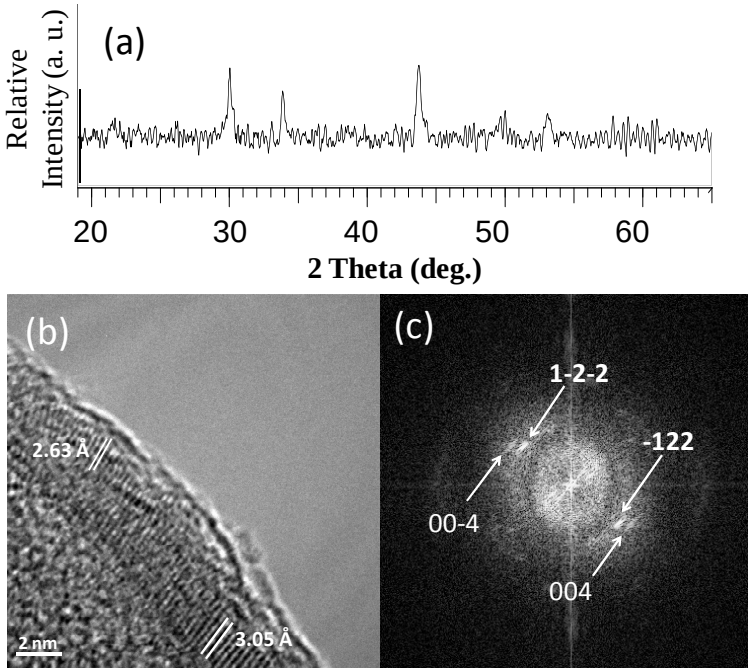

Fig. 2.26 (a) p-XRD pattern of Fe_7S_8 from OLA/DDT (b) HRTEM of Fe_7S_8 from OLA/DDT and (c) FFT of (b).

2.4.4 Zinc sulfide nanoparticles

Nanoparticles obtained from the all different experiments were analysed by p-XRD, TEM, and UV-Vis. The p-XRD patterns (Fig. 2.27-2.29) of the ZnS

nanoparticles obtained from all reactions correspond to the cubic ZnS (ICDD card No. 005-0566). However, the broad peaks in the p-XRD patterns, indicating the small particles size, make the distinction between the cubic and hexagonal phases difficult as peaks may overlap.

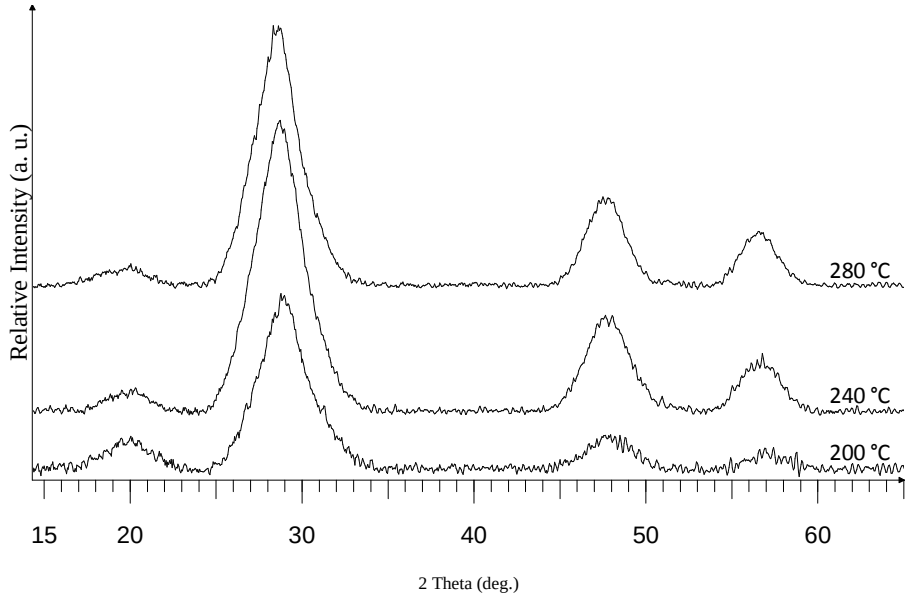

Fig. 2.27 p-XRD patterns of ZnS nanoparticles synthesised at different temperatures.

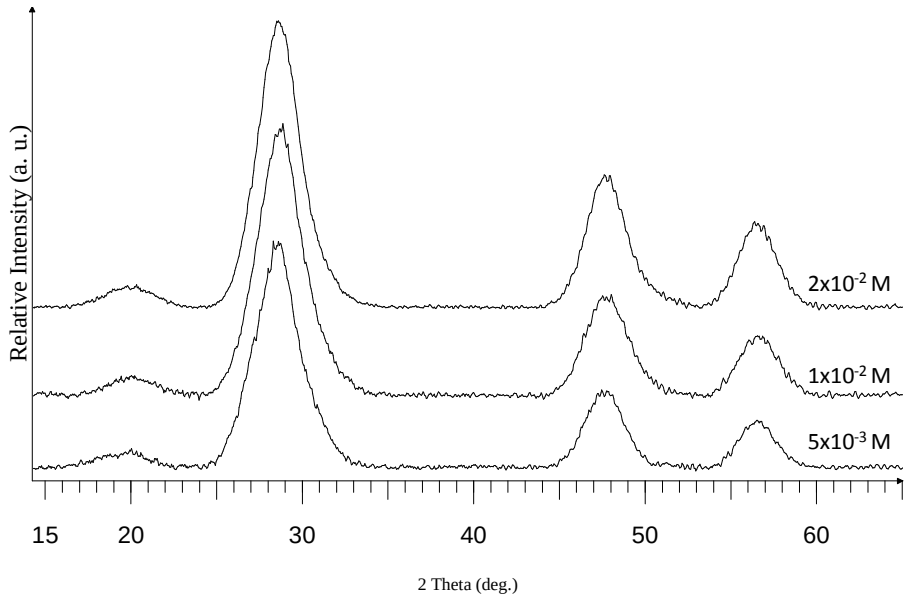

Fig. 2.28 p-XRD patterns of ZnS nanoparticles synthesised from different precursor concentrations.

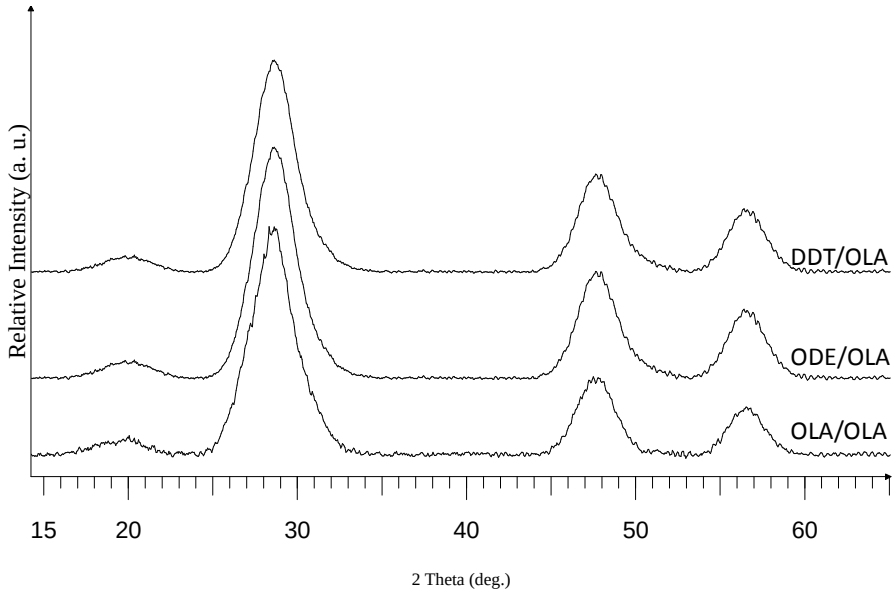

Fig. 2.29 p-XRD patterns of ZnS nanoparticles synthesised from different precursor solutions.

TEM images of the obtained ZnS nanoparticles show that the particles are spherical or close-to-spherical with a slight variation in the average diameter between 3.9 nm and 4.9 nm depending on the reaction conditions. It was found that increasing the growth temperature or precursor concentration resulted in a small increase in the average diameter of the ZnS nanoparticles, whereas the size distribution became broader at higher growth temperatures but narrower at higher precursor concentrations. The average size of the as obtained ZnS nanoparticles was as follows: 3.9 ± 0.5 nm, 4.1 ± 0.6 nm and 4.2 ± 0.8 nm, at growth temperatures of 200 °C, 240 °C and 280 °C, respectively, using 5×10^{-3} M solution of the precursor (Fig. 2.30), and 4.2 ± 0.8 nm, 4.3 ± 0.5 nm and 4.5 ± 0.5 nm using a precursor concentrations of 5×10^{-3} M, 1×10^{-2} M and 2×10^{-2} M, respectively, at a growth temperature of 280 °C (Fig. 2.31). An interesting observation was the formation of few ZnS nanorods at the highest temperature (280 °C). At 280 °C, using ODE or DDT to dissolve the precursor, instead of the OLA, produced spherical or semi-spherical ZnS nanoparticles with no sign of nanorods formation. Both ODE and DDT resulted in a larger average diameter and a broader size distribution (4.9 ± 0.8 nm and 4.8 ± 1.1 nm, respectively) (Fig. 2.32).

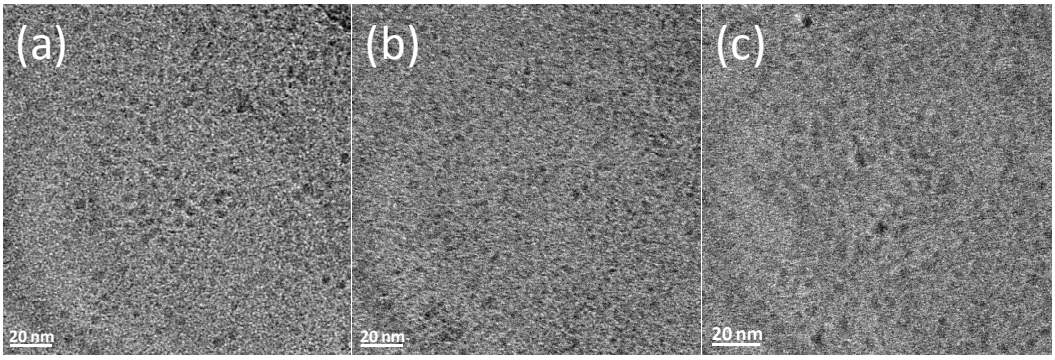

Fig. 2.30 TEM images of ZnS nanoparticles using 5×10^{-3} M solution at (a) 200 °C (b) 240 °C and (c) 280 °C.

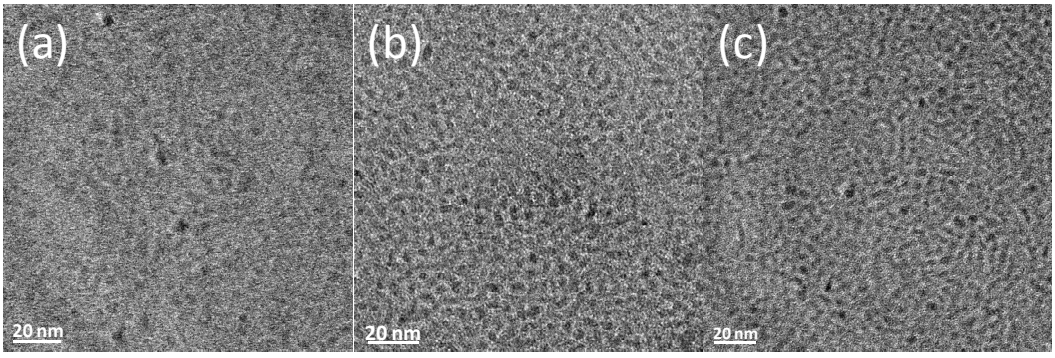

Fig. 2.31 TEM images of ZnS nanoparticles at 280 °C using (a) 5×10^{-3} M, (b) 1×10^{-2} M and (c) 2×10^{-2} M solutions of the precursor.

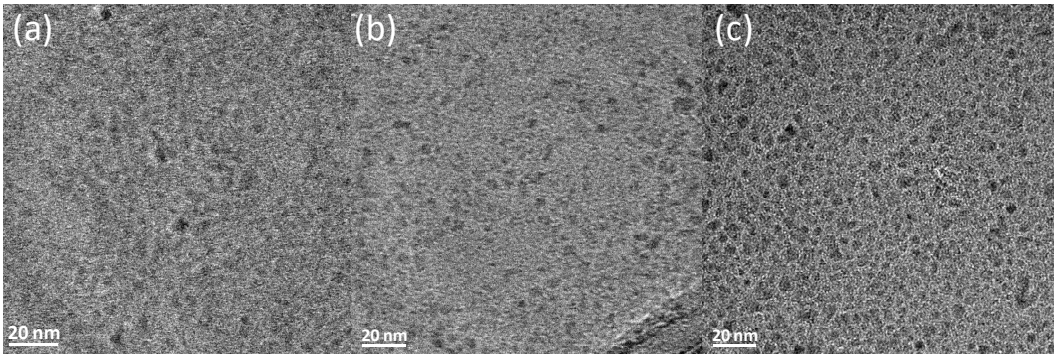

Fig. 2.32 TEM images of ZnS nanoparticles obtained using different solvents: (a) OLA (b) ODE and (c) DDT.

The HRTEM images (Fig. 2.33(a,b)) of the semi-spherical nanoparticles and the nanorods showed a d-spacing of 3.07 Å and 3.1 Å, respectively, which is in a good agreement with the lattice spacing of the (111) plane of the cubic ZnS. The SAED of ZnS nanoparticles with an average size $\geq$ 4.3 nm also confirms the formation of the

cubic ZnS with diffraction rings matching the (111), (220) and (311) planes (Fig. 2.33(c)), whereas particles having an average diameter < 4.3 nm showed two extra weak rings at a lattice spacing of 2.22 Å and 1.72 Å which could be indexed to the (102) and (103) planes of the hexagonal ZnS phase, respectively (Fig. 2.33(d)). Although the hexagonal phase of bulk ZnS is a metastable phase, at a size of 7.02 nm or less it becomes thermodynamically stable.[116]

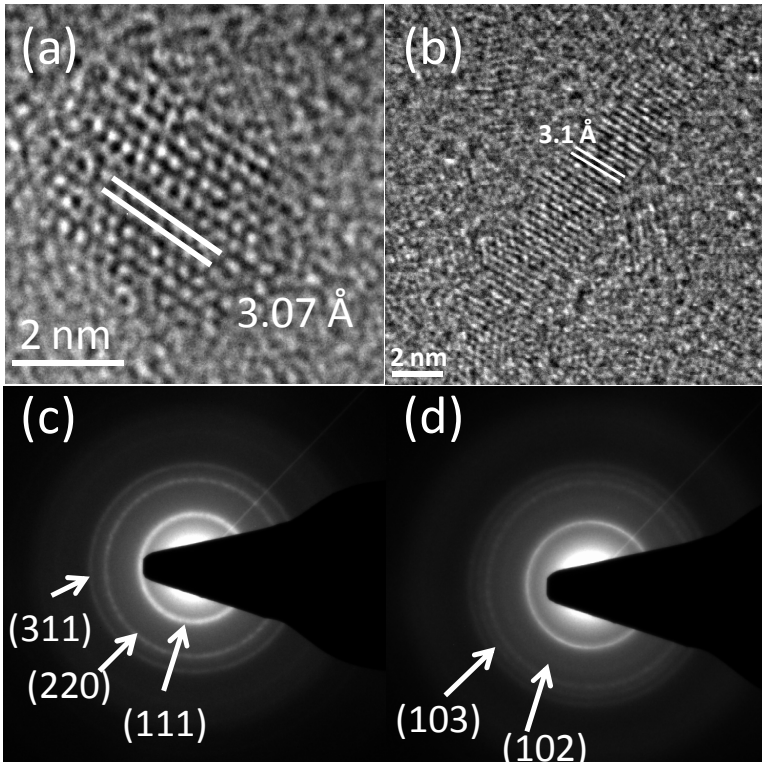

Fig. 2.33 (a) TEM image of ZnS nanorods, (b and c) HRTEM images of ZnS nanorods and nanoparticles respectively and (d) SAED of ZnS.

2.4.4.1 Optical properties

A slight red shift was observed in the absorption spectra of the ZnS nanoparticles with increase in the growth temperature or precursor concentration (Fig. 2.34). The small red-shift is consistent with the slight increase in the average diameter observed by TEM. Using ODE or DDT to dissolve the precursor before injection into hot OLA also resulted in a slight red-shift. The band gaps of the ZnS nanoparticles were larger than that of bulk cubic ZnS (3.72 ev), due to quantum confinement. The band gaps were found to increase from 3.77 eV for the largest particles (4.8, 4.9 nm) to

3.93 eV for the smallest one (3.9 nm). All samples were blue shifted compared to the bulk ZnS as expected.

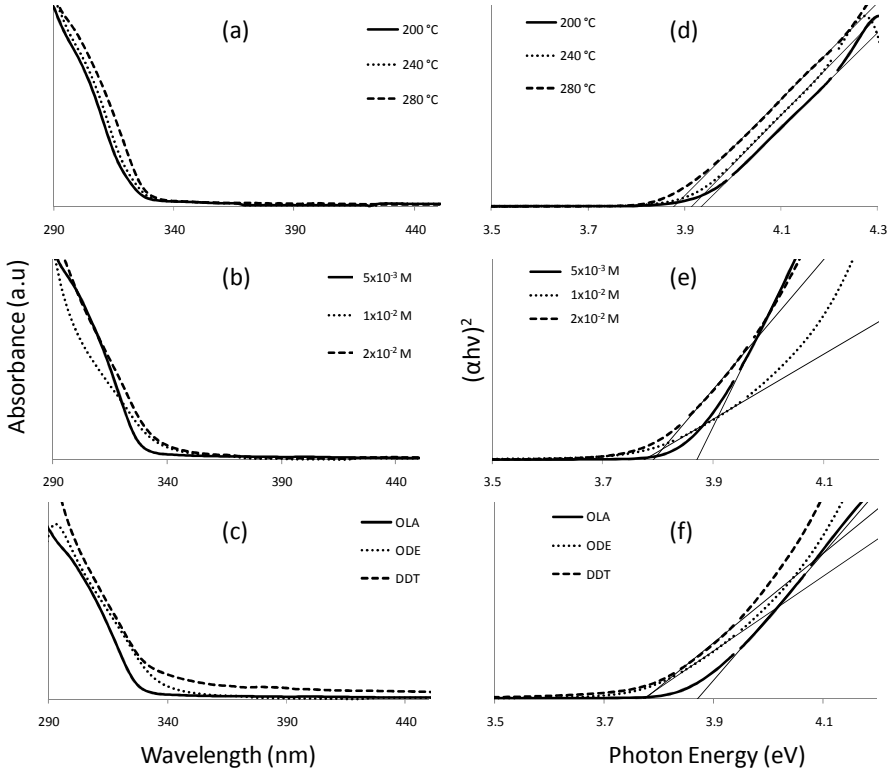

Fig. 2.34 Absorption spectra of ZnS nanoparticles obtained from different (a) growth temperatures, (b) precursor concentration and (c) precursor solutions. (d-f) are their corresponding Tauc plots.

2.4.5 Cadmium sulfide nanoparticles

Nanoparticles obtained from all different experiments were analysed by p-XRD, TEM, UV-Vis and PL spectroscopy. Samples prepared at the lower growth temperatures (200 °C or 240°C) were not highly crystalline as they did not show well defined p-XRD patterns, which might be due the extremely small size of the particles (Fig. 2.35). The p-XRD patterns of the CdS nanoparticles obtained using only OLA from all three different concentrations at a growth temperature of 280 °C correspond to cubic CdS (ICDD card No. 010-0454) (Fig. 2.36). Injecting a solution of the precursor in ODE into hot OLA did not show a significant change in the p-XRD pattern, whereas, DDT resulted in the evolution of the hexagonal phase (ICDD card No. 01-077-2306) (Fig. 2.37). Changing the injection solvent may alter the nucleation and/or growth kinetics which control phase and size of the produced

nanoparticles.[40] In our results it could be suggested that OLA stabilise the precursor more than ODE or DDT resulting in a slower growth rate and smaller particles which favour the cubic structure, supporting the idea of an equilibrium cubic phase at smaller sizes.[117]

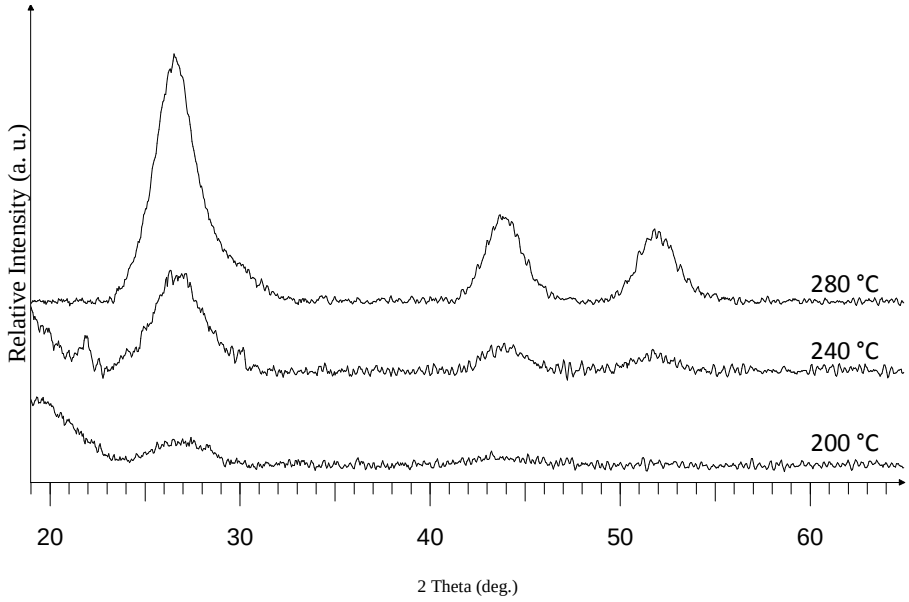

Fig. 2.35 p-XRD patterns of CdS nanoparticles synthesised at different temperatures.

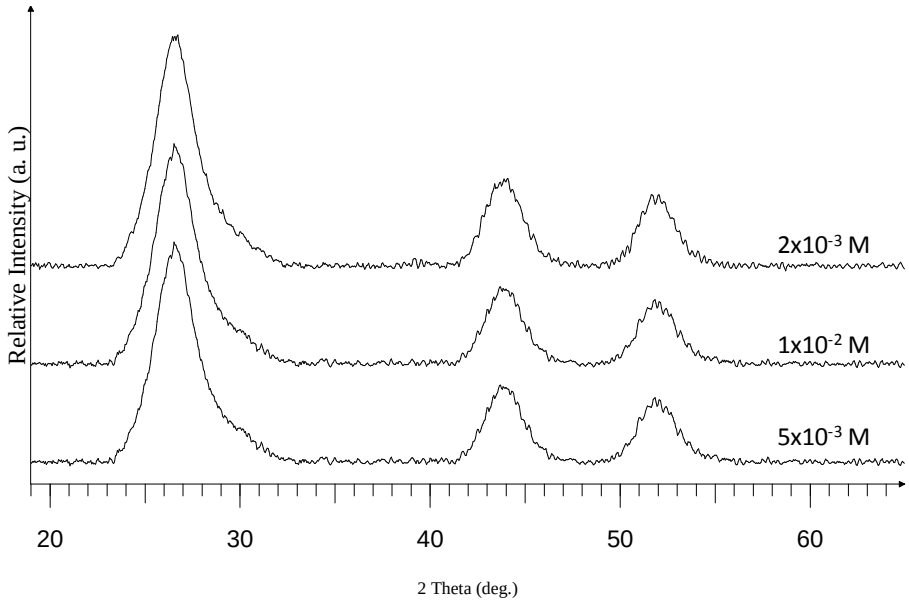

Fig. 2.36 p-XRD patterns of CdS nanoparticles synthesised from different precursor concentrations.

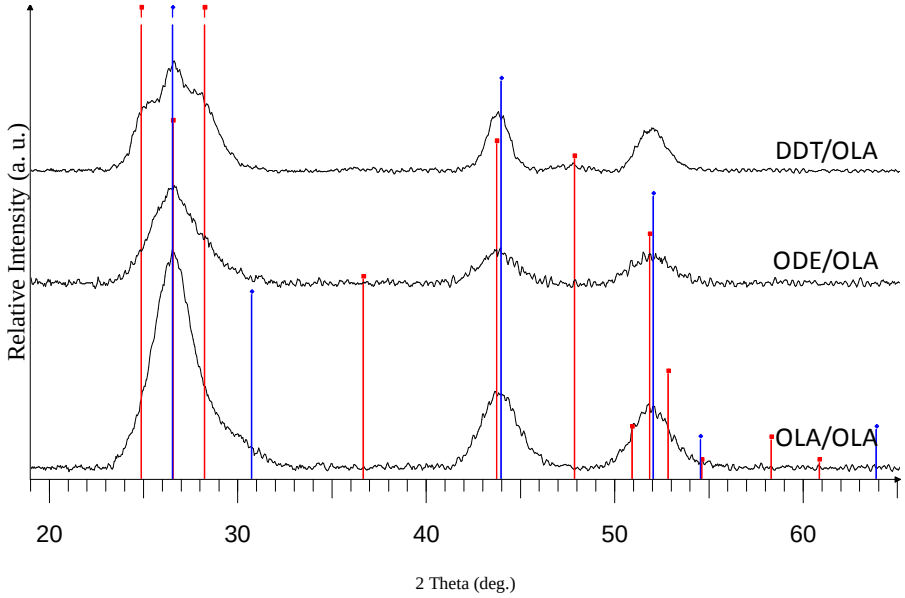

Fig. 2.37 p-XRD patterns of CdS nanoparticles synthesised from different precursor solutions. The blue and red lines represent the standard cubic (ICDD card No. 010-0454) and hexagonal (ICDD card No. 01-077-2306) CdS p-XRD patterns.

TEM showed that samples prepared from only OLA were spherical or close-to-spherical. The diameter of the particles prepared from a 5×10^{-3} M solution at 200 °C or 240 °C was roughly determined from the TEM images and was found to be about 2.8 nm and 3.4 nm, respectively (Fig. 2.38(a,b)). At the higher growth temperature (280 °C), the size of the particles increased and the average diameter was more accurately determined (4.1 ± 0.6 nm) (Fig. 2.38 (c)). Increasing the concentration of the precursor produced particles with larger average diameter (4.7 ± 0.6 nm and 4.9 ± 0.4 nm for 1×10^{-2} M and 2×10^{-2} M, respectively) (Fig. 2.39(b & c)). When ODE replaced OLA in the injection solution the particles were slightly elongated with an average length and average diameter of 4.6 ± 0.7 nm and 3.9 ± 0.6 nm, respectively (Fig. 2.40(b)). On the contrary, DDT resulted in a complete change in the morphology of the nanoparticles as triangular-based structures were observed (Fig. 2.40(c)). Cadmium atoms (soft Lewis acid) prefer larger and more polarisable ligand atoms (soft Lewis bases) *e.g.* sulfur,[178] as a result, DDT can bind more strongly to certain planes reducing their growth rate. It has been previously reported that using OLA as a capping agent produced spherical CdS nanoparticles while in the presence of small amounts of DDT anisotropic CdS structures were obtained.[130] During the nucleation, a spherical nucleus favours the cubic crystal structure[39] and

therefore, this change in morphology (from spherical to triangular-based structures) could be a confirmation for the formation of hexagonal CdS when DDT is used as an injection solvent.

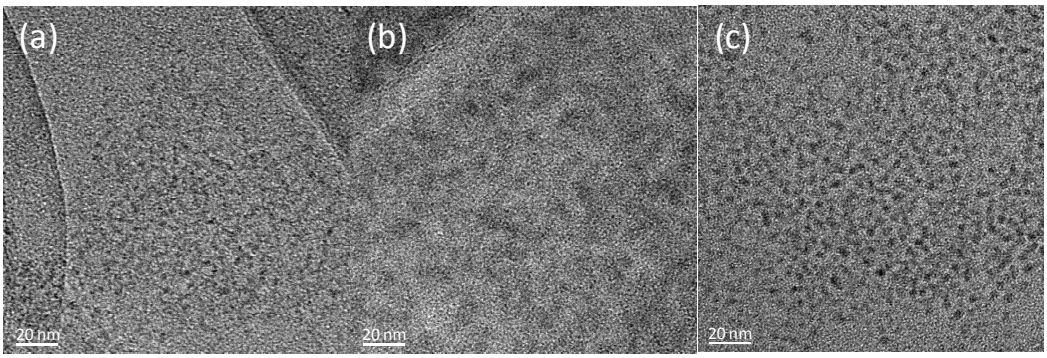

Fig. 2.38 TEM images of CdS nanoparticles prepared using 5×10^{-3} M solution at growth temperatures of (a) 200 °C (b) 240 °C and (c) 280 °C.

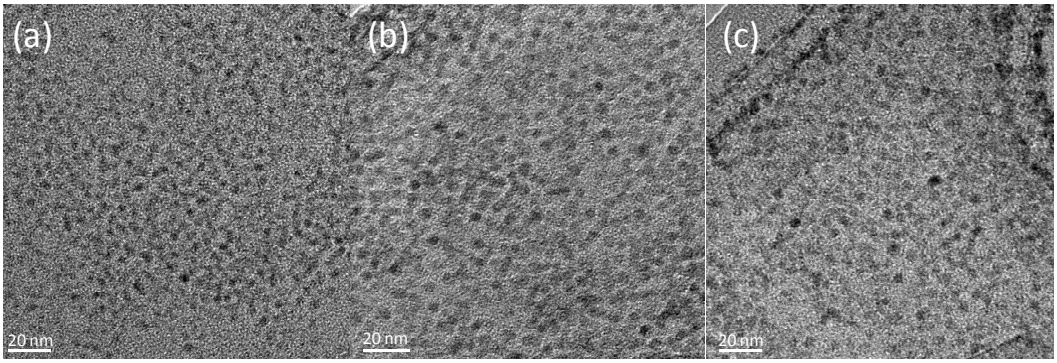

Fig. 2.39 TEM images of CdS nanoparticles prepared a growth temperature of 280 °C using (a) 5×10^{-3} M, (b) 1×10^{-2} M and (c) 2×10^{-2} M solutions of the precursor.

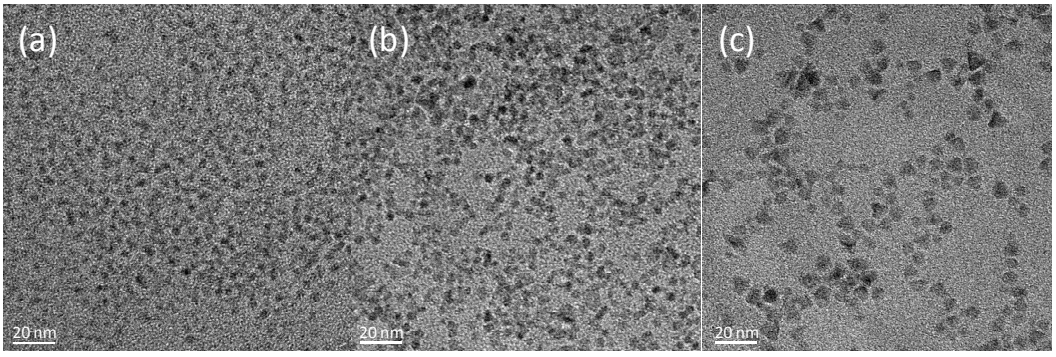

Fig. 2.40 TEM images of CdS nanoparticles obtained using different solvents: (a) OLA (b) ODE and (c) DDT.

The d-spacing calculated from the HRTEM images for samples prepared from only OLA was 3.34 Å which could be indexed to the (111) plane of the cubic CdS phase (Fig. 2.41(a)). SAED of all samples prepared using only OLA confirms a pure cubic structure with diffraction rings matching the (111), (220) and (311) planes of the cubic phase (Fig. 2.41(b)), whilst the diffraction rings characteristic to the hexagonal phase ((100) and (103)) were not observed. When ODE was used for injection, in addition to the d-spacing of 3.38 Å (Fig. 2.41(c)) which correspond to either the (111) plane of the cubic phase or the (002) plane of the hexagonal phase, few nanoparticles showed a d-spacing of 1.86 Å (Fig. 2.41(d)) corresponding to the (103) plane of the hexagonal phase. The (103) plane of the hexagonal phase was also recognized in the SAED, suggesting a mixture of both phases (Fig. 2.41(e)). HRTEM, fast Fourier transform (FFT) and SAED (Fig. 2.41(f-h)) of the triangular-based CdS confirm its hexagonal structure with lattice spacing matching characteristic planes of the hexagonal phase.

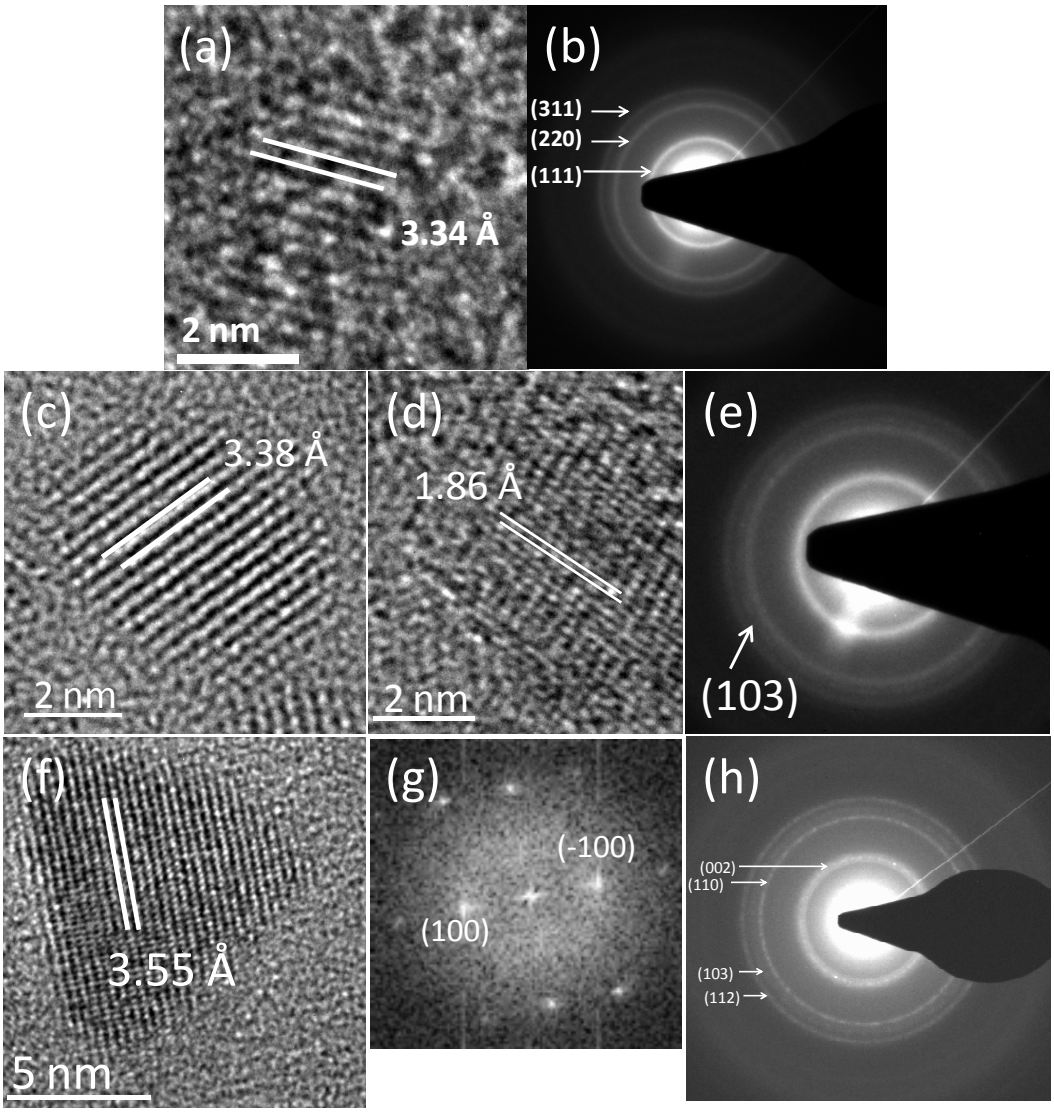

Fig. 2.41 (a,b) HRTEM and SAED of CdS nanoparticles prepared using OLA as an injection solvent, (c,d) HRTEM and (e) SAED of CdS nanoparticles prepared using ODE as an injection solvent (f) HRTEM, (g) FFT and (h) SAED CdS nanoparticles prepared using DDT as an injection solvent.

2.4.5.1 Optical properties

Increasing the growth temperature resulted in a large red-shift in the absorption spectra of the CdS nanoparticles (Fig. 2.42(a)), whereas increasing the concentration of the precursor resulted in only a slight red-shift (Fig. 2.42(b)). A red-shift was also observed on replacing the OLA in the injection solution with ODE or DDT; the shift was very small for ODE and much larger in case of DDT (Fig. 2.42(c)). The red-shift matched with the increase in the particles average diameters as shown in TEM. The band gaps of the CdS nanoparticles calculated from the absorption spectra were

found to be, as expected, size-dependent. The smallest particles (*ca.* 2.8 nm) had the largest band gap (2.72 eV) due to size confinement whilst, the biggest particles showed a band gap of (2.52 eV) (Fig. 2.42(d-f)). All particles were blue shifted compared to bulk CdS (2.42 eV).

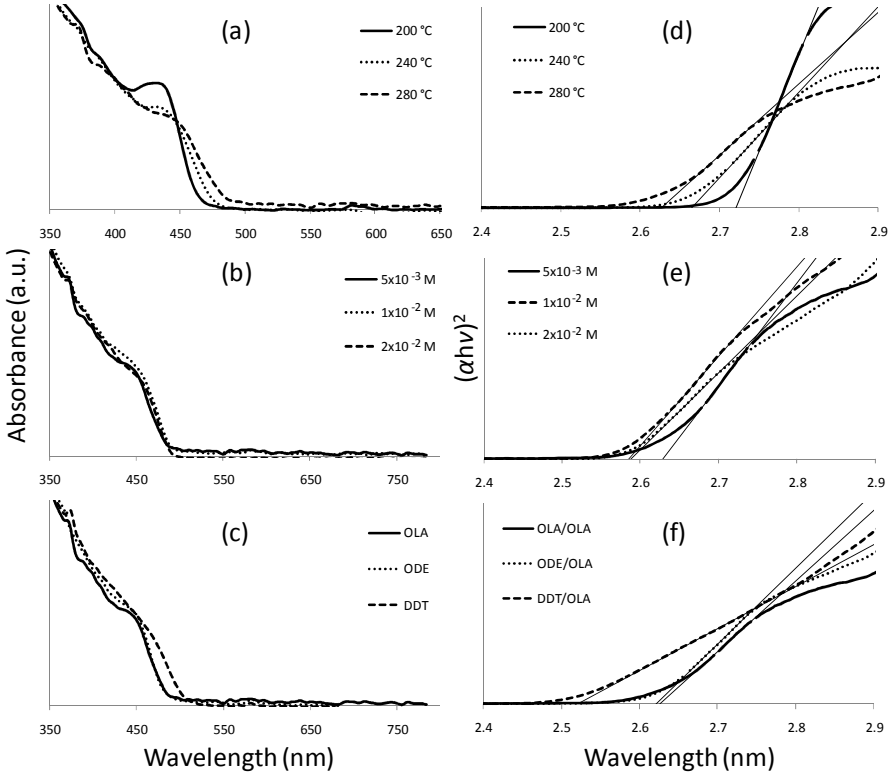

Fig. 2.42 Absorption spectra of CdS nanoparticles obtained from different (a) growth temperatures, (b) precursor concentration and (c) precursor solutions. (d-f) are their corresponding Tauc plots.

Samples prepared at a growth temperature of 200 °C or 240 °C showed very poor luminescence, probably due to their poor crystallinity. At a growth temperature of 280 °C a remarkable increase in the emission spectra was observed (Fig. 2.43(a)). This emission was red-shifted from 464 nm to 480 nm by increasing the precursor concentration from 5×10^{-3} M to 1×10^{-2} M, respectively. Although, no further shift took place on increasing the precursor concentration to 2×10^{-2} M, a drop in the emission intensity was observed (Fig. 2.43(b)). Using ODE resulted in a slight red shift (470 nm) and slightly higher emission intensity. On the other hand, using DDT produced almost non-luminescent particles (Fig. 2.43(c)). Thiols as capping agents were previously reported to quench the photoluminescence of CdSe nanoparticles by hole trapping which reduces the electron-hole radiative recombination.[179]

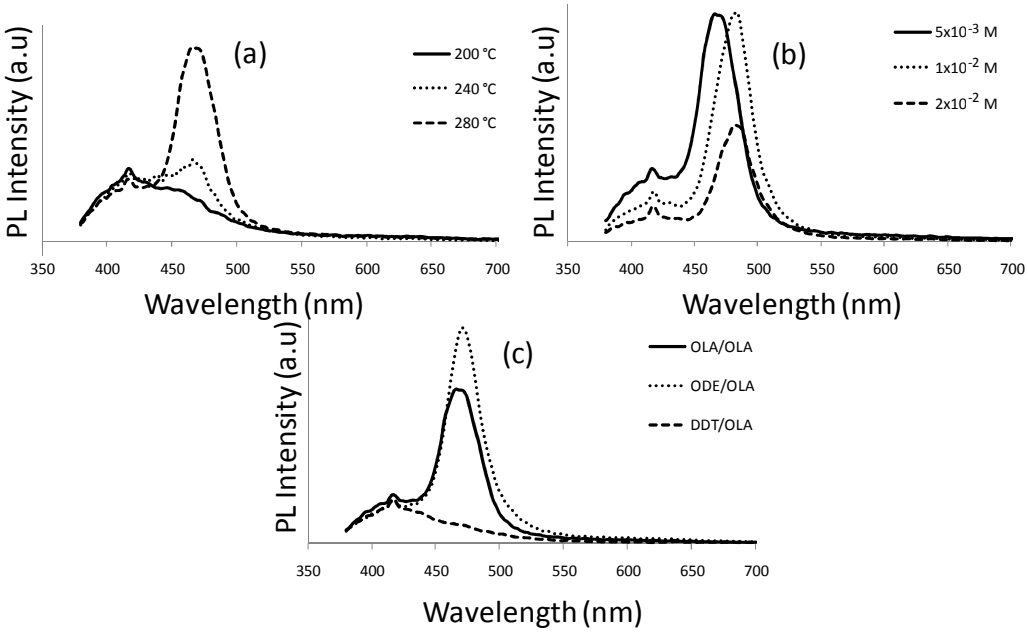

Fig. 2.43 Emission spectra of CdS nanoparticles obtained from different (a) growth temperatures, (b) precursor concentration and (c) precursor solutions.

2.4.6 Indium sulfide nanoparticles

The p-XRD pattern of the as prepared indium sulfide nanocrystals (Fig. 2.44) correspond to β-In_2S_3 (ICDD card No. 32-0456). The broad peaks in the pattern are consistent with the very small diameter of nanorods or the nanowires as confirmed by TEM images (Fig. 2.45). The absence of the (220), (422) and (511) peaks indicates a preferred growth direction.

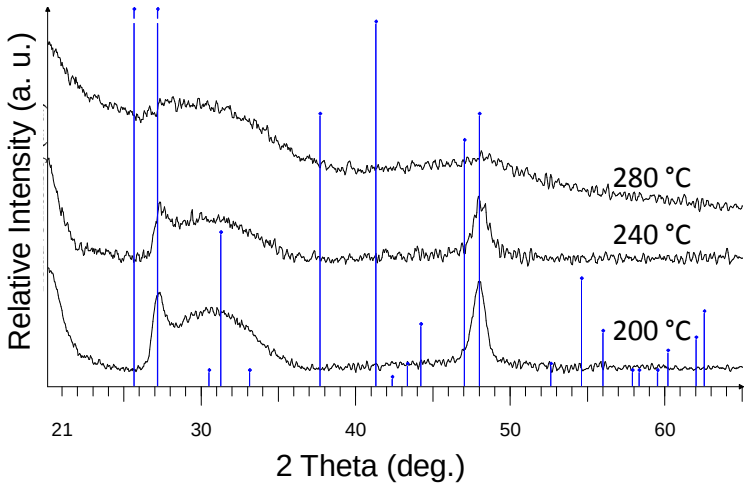

Fig. 2.44 p-XRD pattern of β-In_2S_3 prepared using 5 × 10^{-3} M at different growth temperatures. Blue lines represent β-In_2S_3 (ICDD card No. 32-0456).

TEM images revealed that the material synthesised at 200 °C, is composed of very thin nanorods. The width and length of the nanorods decreased on increasing the concentration of precursor. The nanorods prepared using 5×10^{-3} M solution had dimensions of 0.9 ± 0.1 nm and 11.8 ± 3.5 nm, which decreased to 0.7 ± 0.1 nm and 7.1 ± 2.6 nm using 1×10^{-2} M solution. A further decrease in dimensions to 0.6 ± 0.1 nm and 5.8 ± 1.6 nm was observed with a 2×10^{-2} M solution (Fig. 2.45(a-c)). Increasing the growth temperature from 200 °C, at the lowest concentration (5×10^{-3} M), to 240 °C produced nanowires without change in the average width (0.9 ± 0.1 nm) but with a significant change in the length (Fig. 2.45(d)). A further increase (280 °C) in the growth temperature resulted in a considerable increase in the diameter of the nanowires with a broader distribution (1.4 ± 0.4 nm) (Fig. 2.45(e)). Ultra-thin indium sulfide nanowires[160] and nanotubes[180] were previously reported as oriented nanoplates. In our results, there was no evidence of the formation of any plates, which makes our indium sulfide nanorods/nanowires, to the best of our knowledge, the thinnest prepared. SAED of the nanowires confirmed the formation of β-In_2S_3 with strong diffraction rings matching the (311) and the (440) planes (Fig. 2.45(f)). Unfortunately, due to the ultra-thinness of the nanorods/nanowires, HRTEM could not produce images to determine their lattice spacing or the growth direction.[160]

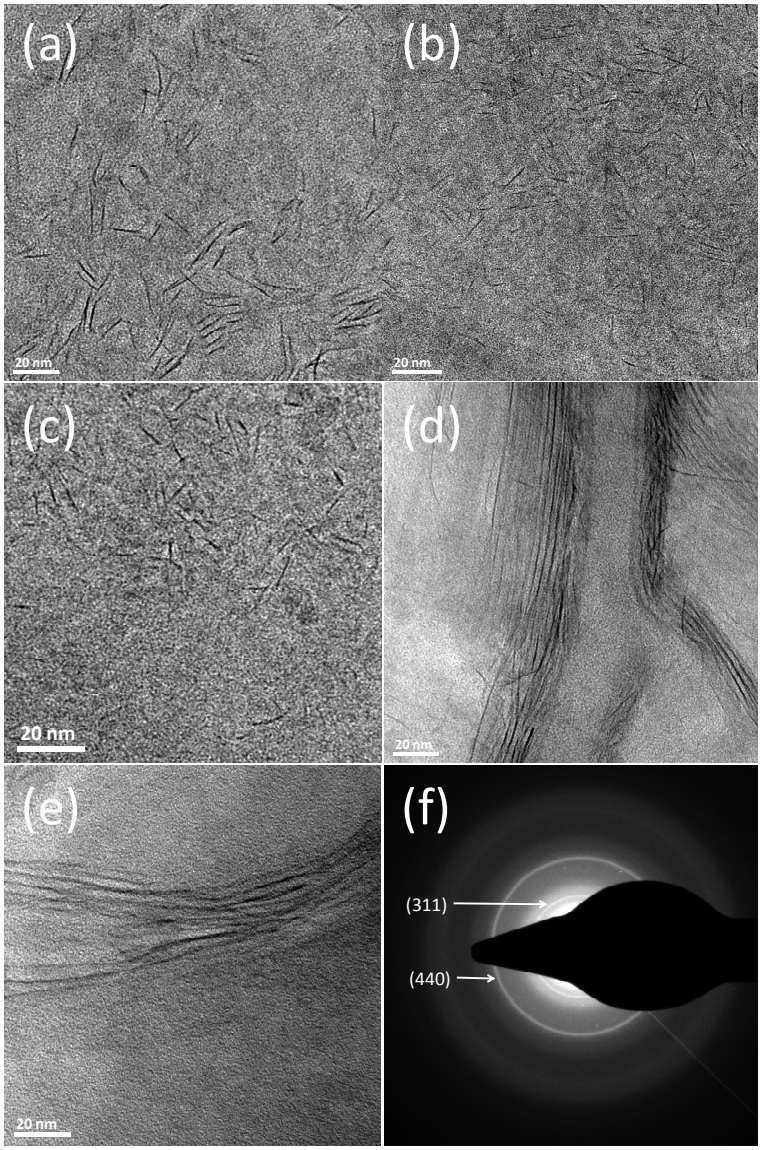

Fig. 2.45 (a-c) TEM of In_2S_3 nanorods synthesised at 200 °C using 5×10^{-3} M, 1×10^{-2} M and 2×10^{-2} M respectively. (d & e) TEM of In_2S_3 nanowires synthesised using 5×10^{-3} M at 240 °C and at 280 °C respectively. (f) SAED of (d).

Progress of the reaction time was investigated by withdrawing a couple of drops from the reaction solution at different time intervals (5, 30 and 60 minutes) for the sample prepared at 200 °C using the lowest concentration (5×10^{-3} M) of precursor. The width of the nanorods increased slightly from 0.6 ± 0.2 nm to 0.7 ± 0.1 and finally 0.9 ± 0.1 nm, whilst the nanorods length showed a more rapid growth from 7.7 ± 2.3 nm to 10.2 ± 2.6 nm and 11.8 ± 3.5 nm after 5, 30 and 60 minutes from the injection, respectively (Fig. 2.46).

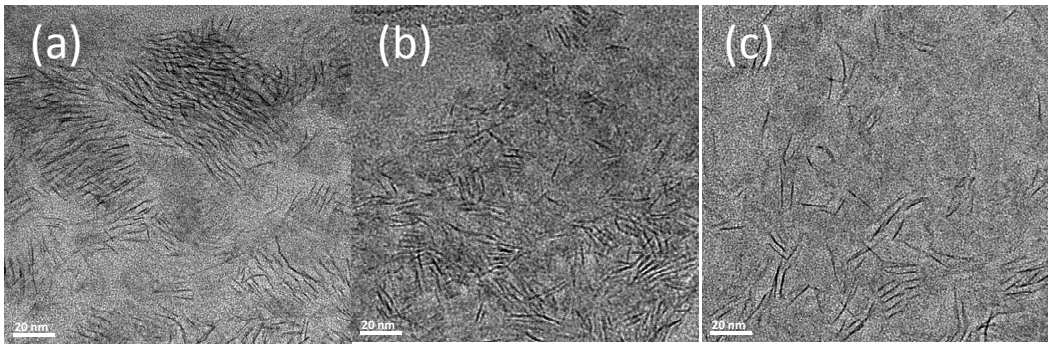

Fig. 2.46 (a-c) TEM of In_2S_3 nanorods after 5, 30 and 60 minutes, respectively.

Injecting an ODE solution of the precursor into hot OLA or an OLA solution into hot DDT also produced ultra-thin nanorods of β-In_2S_3 (Fig. 2.47).

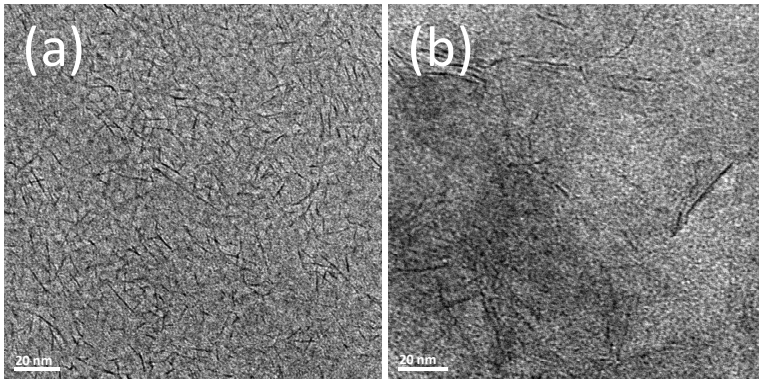

Fig. 2.47 TEM images of In_2S_3 nanorods prepared in (a) ODE/OLA and (b) OLA/DDT.

2.4.6.1 Optical properties

The absorption spectra of all In_2S_3 nanorods or nanowires dispersed in toluene showed almost no difference in the band edge, as can be seen in Fig. 2.48(a), for samples prepared for different times. The insignificant difference in the absorption spectra could be due to the very slight change in the width of the rods/wires. The step like shape of the absorption spectra is because of the conduction to valence band transition as observed previously.[22,160,181] The band gap of the rods, calculated from the Tauc plot (Fig. 2.48(b)), was found to be 3.26 eV which is much larger than that of the bulk material due to the massive reduction in the nanorods width.

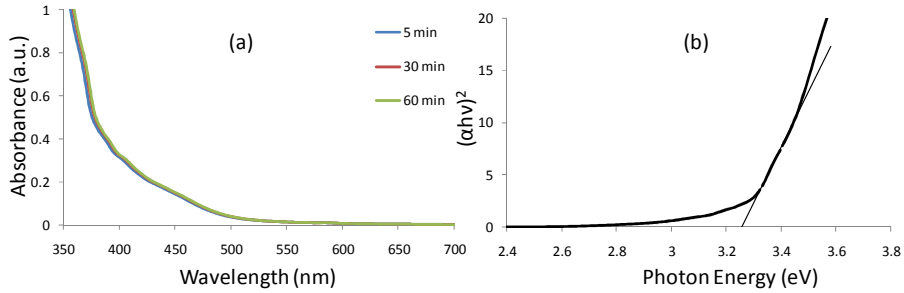

Fig. 2.48 (a) Absorption spectra of In_2S_3 nanorods produced at different time intervals (b) Tauc Plot for sample obtained after 1 hour.

2.5 Conclusion

Solution thermolysis of 1,1,5,5-tetra-*iso*-propyl-4-thiobiuret complex of copper(II) in OLA produced a mixture of orthorhombic and monoclinic phases of Cu_7S_4 nanoparticles. The morphology of the crystalline nanoparticles obtained by thermolysis varied as a function of the reaction temperature, precursor concentration, reaction time and capping agent used. Shorter reaction times produced hexagonal and trigonal nanodisks whereas, longer reaction times at high temperatures yielded spherical nanoparticles. Different phases and different morphologies were also obtained by changing the solvent or the capping agent. The distinction between direct or indirect band gap for this material is complicated, however, our results supports an indirect band gap as the best linear fit was obtained on plotting $(\alpha h\nu)^{0.5}$ as a function of photon energy rather than on plotting $(\alpha h\nu)^2$.

Colloidal thermolysis of nickel(II) and iron(III) complexes of 1,1,5,5-tetra-*iso*-propyl-2-thiobiurets in OLA produced Ni_3S_4 and Fe_7S_8 respectively. Ni_3S_4 was obtained from all reactions except when precursor solution in OLA was injected into hot ODE which produced NiS nanoparticles. Fe_7S_8 was produced from the thermolysis of the iron complex in OLA/OLA or OLA/DDT only. All other combinations of injection solvent/capping agent gave amorphous material. The morphology of the obtained nanoparticles was highly dependent on the reaction parameters (growth temperature, precursor concentration and injection solvent/capping agent mixture).

Fig. 2.49 shows a plot similar to that developed by our group[182] and by Vaughan and Lennie,[60] representing the relative stabilities of the various phases of iron sulfide nanoparticles obtained from the thermolysis of different single source precursors in OLA at different temperatures. The height of the pyramid on the negative z-axis

represents the free energy of formation of each phase. The solid line represents the thermodynamic stability and connects the stable phases FeS (troilite) and FeS_2 (pyrite).[38] Our work produced Fe_7S_8 as the only phase (shown in orange) at all temperatures which suggests that the reaction product was kinetically controlled.

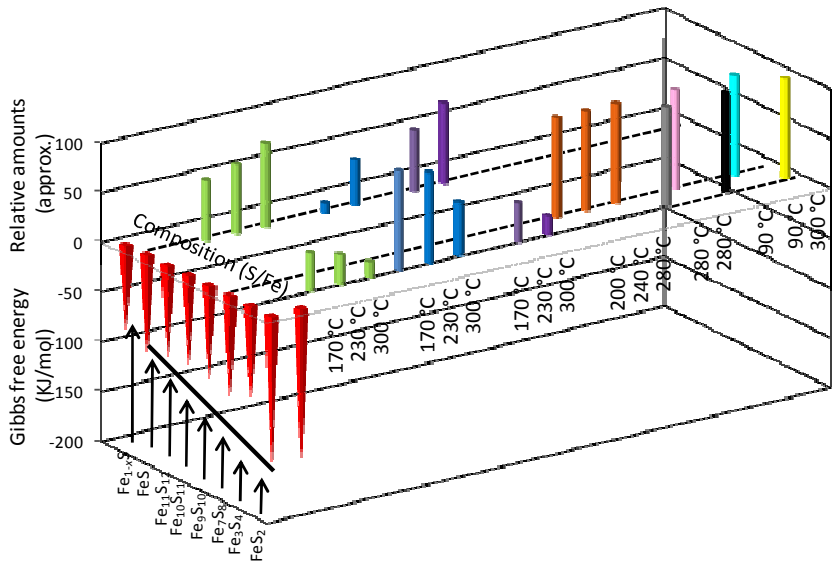

Fig. 2.49 Graphical representation of iron sulfide nanoparticles showing different phases as reported in the literature by the thermolysis of different single source precursors in OLA at different temperatures, compared to the relative thermodynamic stabilities of the various phases of iron sulfide after Vaughan.[38] $[Fe(S_2CNEt^iPr)_3]$ (green),[82] $[Fe(S_2CN(Hex)_2)_3]$ (blue),[82] $[Fe(S_2CNEtMe)_3]$ (violet),[82] $[Fe(SON(CN^iPr_2)_2)_3]$ (orange) this work, $[Fe(S_2CNEt_2)_3]$ (grey[79] and black[80]), $[Fe(S_2CNEt_2)_2(phenanthroline)]$ (pink[79] and light blue[80]), and [Fe(*N*-methylimidazole)$_6$]S_8 (yellow).[59]

$[Zn(SON(CN^iPr_2)_2)_2]$ and $[Cd(SON(CN^iPr_2)_2)_2]$ were used as precursors for the colloidal synthesis of ZnS and CdS nanoparticles respectively. Both materials were cubic except for ZnS nanoparticles with average diameter > 4.3 nm and CdS nanoparticles prepared using DDT as injection solvent; both had a hexagonal structure. The ZnS nanoparticles had a spherical morphology, apart from samples prepared at 280 °C, where few nanorods were observed as well. Cubic CdS nanoparticles also were spherical, whereas the hexagonal CdS had a triangular morphology.

β-In_2S_3 nanorods or nanowires of extreme thinness (< 1.0 nm) were synthesised from the thermolysis of the single source precursor $[In(SON(CN^iPr_2)_2)_3]$ in hot OLA.

The nanorods had a direct band gap of 3.26 eV which is much larger than that of the bulk material (2.0-2.3eV).

Schematic illustrations of thermolysis experiments of $[M(SON(CN^{i}Pr_2)_2)_n]$ are shown in Scheme 2.1-2.6.

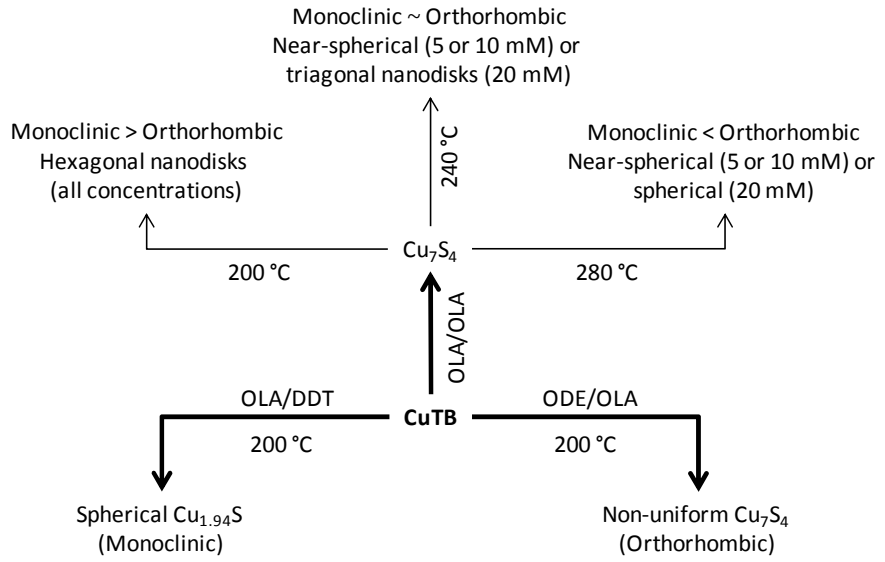

Scheme 2.1 A schematic illustration of thermolysis experiments of $[Cu(SON(CN^{i}Pr_2)_2)_2]$.

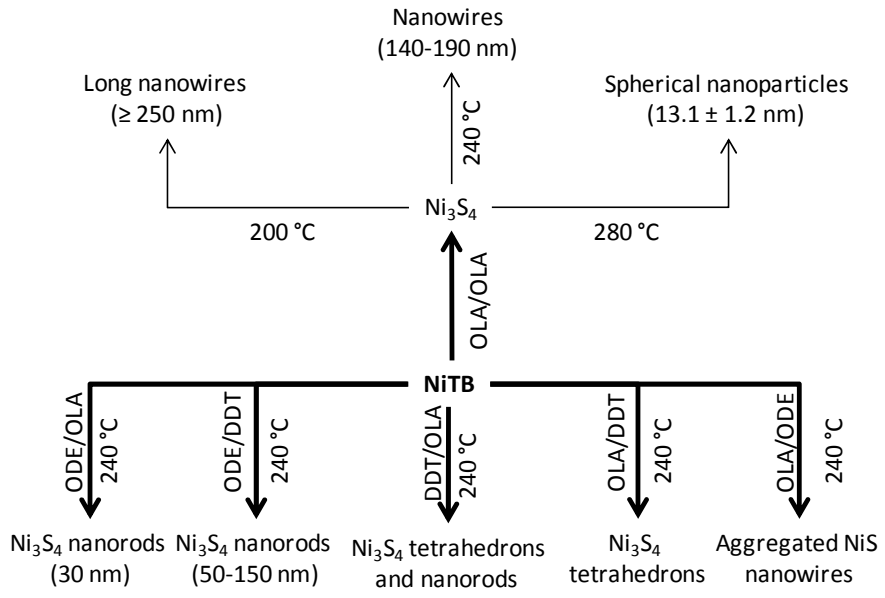

Scheme 2.2 A schematic illustration of thermolysis experiments of $[Ni(SON(CN^{i}Pr_2)_2)_2]$.

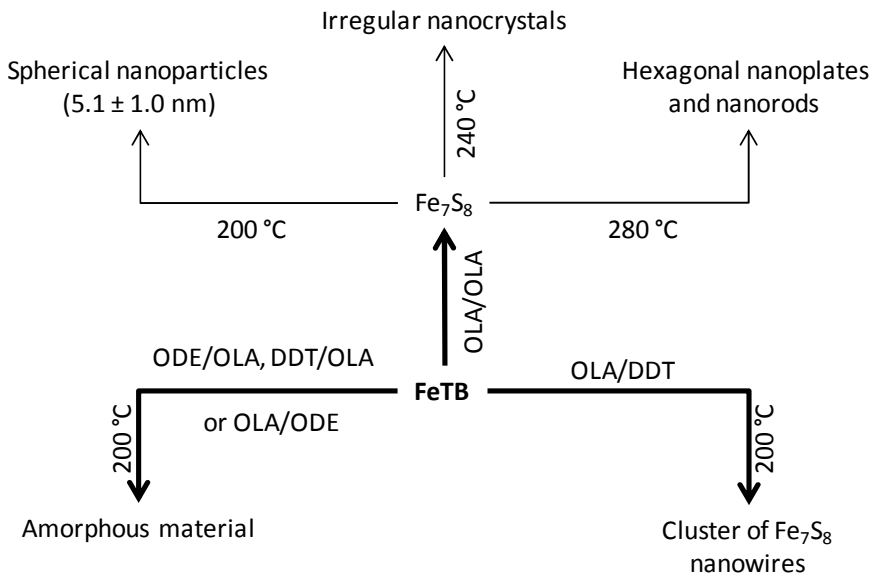

Scheme 2.3 A schematic illustration of thermolysis experiments of $[Fe(SON(CN^{i}Pr_2)_2)_3]$.

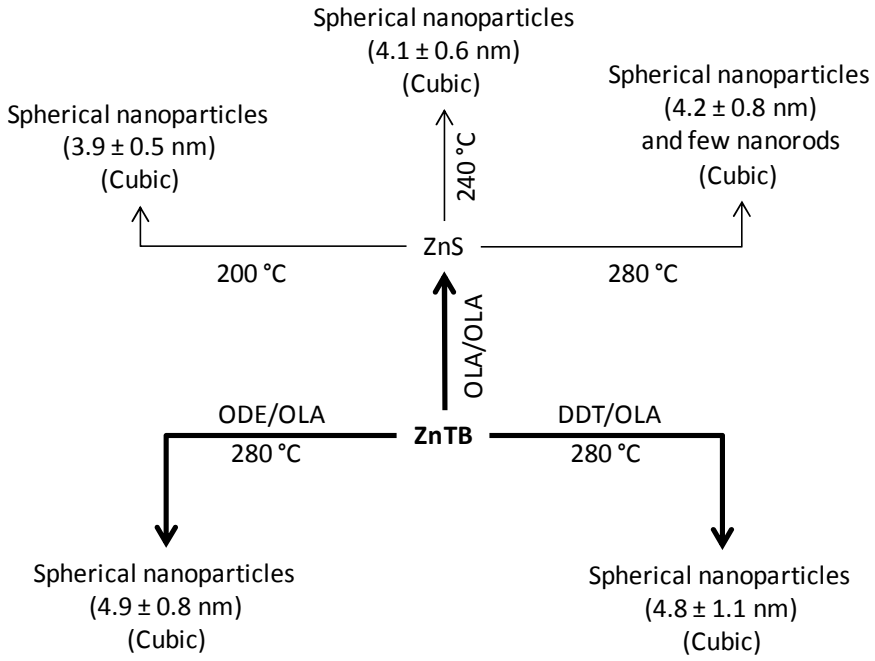

Scheme 2.4 A schematic illustration of thermolysis experiments of $[Zn(SON(CN^{i}Pr_2)_2)_2]$.

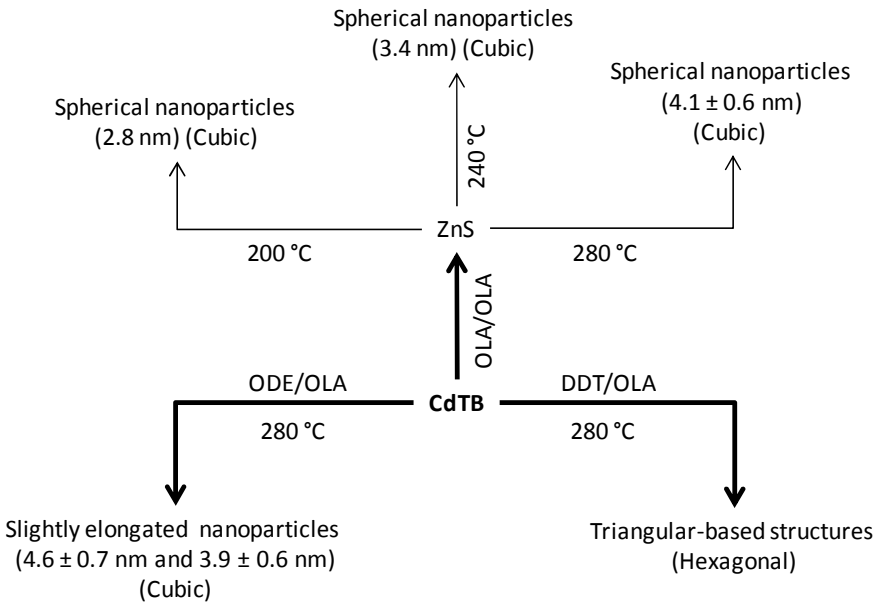

Scheme 2.5 A schematic illustration of thermolysis experiments of $[Cd(SON(CN^{i}Pr_2)_2)_2]$.

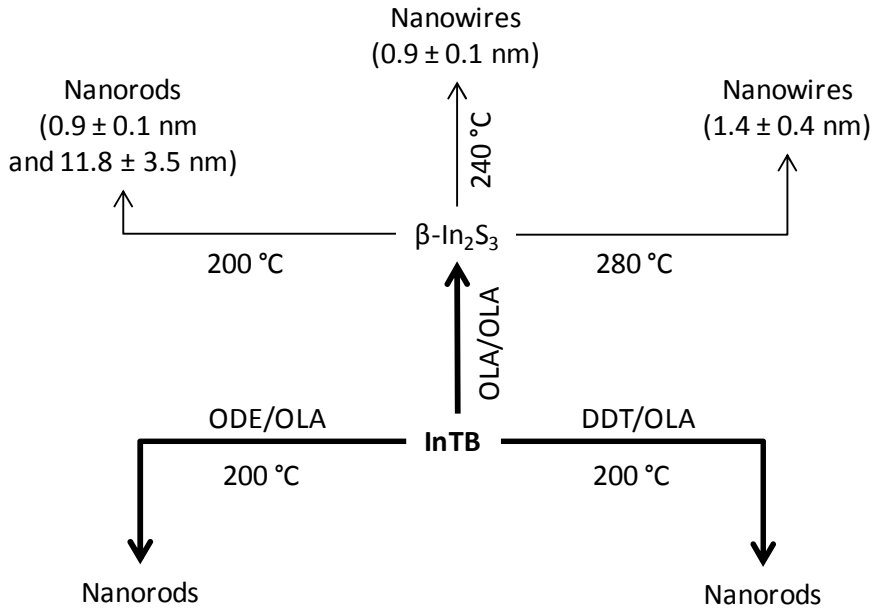

Scheme 2.6 A schematic illustration of thermolysis experiments of $[In(SON(CN^{i}Pr_2)_2)_3]$.

2.6 References

1. B. Geng, X. Liu, J. Ma, Q. Du, *Mater. Sci. Eng. B* 2007, **145**, 17.
2. S.H. Choi, K. An, E. G. Kim, J. H. Yu, J. H. Kim, T. Hyeon, *Adv. Funct. Mater.* 2009, **19**, 1645.
3. A. Ghezelbash, B. A. Korgel, *Langmuir* 2005, **21**, 9451.
4. N. Pradhan, B. Katz, S. Efrima, *J. Phys. Chem. B* 2003, **107**, 13843.
5. J. Joo, H. B. Na, T. Yu, J. H. Yu, Y. W. Kim, F. Wu, J. Z. Zhang, T. Hyeon *J. Am. Chem. Soc.* 2003, **125**, 11100.
6. Y. Xia, P. Yang, *Adv. Mater*. 2003, **15**, 351.
7. J. Hu, T. W. Odom, C. M. Lieber, *Acc. Chem. Res.* 1999, **32**, 435.
8. C. Burda, X. Chen, R. Narayanan, M. A. El-Sayed, *Chem. Rev.* 2005, **105**, 1025.
9. P. K. Santra, R. Viswanatha, S. M. Daniels, N. L. Pickett, J. M. Smith, P. O'Brien, D. D. Sarma, *J. Am. Chem. Soc.* 2009, **131**, 470.
10. M. A. Malik, N. Revaprasadu, P. O'Brien, *Chem. Mater*. 2001, **13**, 913.
11. Mark Green, Paul O'Brien, *Chem. Commun.,* 1999, 2235.
12. C. B. Murray, D. J. Noms, M. G. Bawendi, *J. Am. Chem. Soc.* 1993, **115**, 8706.
13. B. O. Dabbousi, J. Rodriguez-Viejo, F. V. Mikulec, J. R. Heine, H. Mattoussi, R. Ober, K. F. Jensen, M. G. Bawendi, *J. Phys. Chem. B* 1997, **101**, 9463.
14. S. Coe, W. K. Woo, M. Bawendi, V. Bulovic, *Nature* 2002, **420**, 800.
15. A. N. Shipway, E. Katz, I. Willener, *Chem. Phys. Chem.,* 2000, **1**, 18.
16. J. Phillips, *J. Appl. Phys.*, 2002, **91**, 4590.
17. V. I. Klimov, A. A. Mikhailovsky, S. Xu, A. Malko, J. A. Hollingsworth, C. A. Leatherdale, H. J. Eisler, M. G. Bawendi, *Science* 2000, **314**, 290.
18. H. Pettersson, L. Baath, N. Carlsson, W. Seifert, L. Samuelson, *Appl. Phys. Lett.* 2001, **79**, 78.
19. Y. Xia, P. Yang, Y. Sun, Y. Wu, B. Mayers, B. Gates, Y. Yin, F. Kim, H. Yan, *Adv. Mater.,* 2003, **15**, 353.
20. M. Sigman, A. Ghezelbash, T. Hanrath, A. E. Saunders, F. Lee, B. A. Korgel, *J. Am. Chem. Soc.,* 2003, **125**, 16050.
21. A. Ghezelbash, M. B. Sigman, Jr., B. A. Korgel, *Nano Lett.,* 2004, **4**, 537.
22. K. H. Park, K. Jang, S. U. Son, *Angew. Chem. Int. Ed.* 2006, **45**, 4608.

23. H. Lee, S. W. Yoon, E. J. Kim, J. Park, *Nano Lett*., 2007, **7**, 778.
24. Y. Wu, C. Wadia, W. Ma, B. Sadtler, A. P. Alivisatos, *Nano Lett.*, 2008**, 8**, 2551.
25. C. Wadia, A. P. Alivisatos, D. M. Kammen, *Environ. Sci. Technol.*, 2009, **43**, 2072.
26. T. Sakamoto, H. Sunamura, H. Kawaura, *Appl. Phys. Lett.*, *2*003**, 82**, 3032.
27. J. S. Chung, H. J. Sohn, *J. Power Sources*, 2002**, 108**, 226.
28. D. J., Vaughan, J. R. Craig, Mineral Chemistry of Metal Sulfides; Harland, W. B., Agrell, S. O., Cook, A. H., Hughes, N. F., Eds; Cambridge University Press, Cambridge, 1978; pp 290-292.
29. M. E. Fleet, *Rev. Mineral Geochem.*, 2006, **61**, 365.
30. D. F. A. Koch, R. McIntyre, *J. Electroanal. Chem.* 1976, **71**, 285.
31. Q. Lu, F. Gao, D. Zhao, Process. *Nano Lett*. 2002, **2**, 725.
32. X. Jiang, Y. Xie, J. Lu, W. He, L. Zhu, Y. Qian, *J. Mater. Chem.*, 2000, **10**, 2193.
33. W. Du, X. Qian, X. Ma, Q. Gong, H. Cao, J. Yin, *Chem. Eur. J.* 2007, **13**, 3241.
34. T. H. Larsen, M. Sigman, A. Ghezelbash, R. C. Doty, B. A. Korgel, *J. Am. Chem. Soc*., 2003, **125**, 5638.
35. H. T. Zhang, G. Wu, X. H. Chen, *Langmuir* 2005, **21**, 4281.
36. H. T. Zhang, G. Wu, X. H. Chen, *Mater. Chem. Phys.* 2006, **98**, 298.
37. H. Zhang, Y. Zhang, J. Yu, D. Yang, *J. Phys. Chem. C* 2008, **112**, 13390.
38. Y. Wang, Y. Hu, Q. Zhang, J. Ge, Z. Lu, Y. Hou, Y. Yin, *Inorg. Chem.* 2010, **49**, 6601.
39. A. Tang, S. Qu, K. Li, Y. Hou, F. Teng, J. Cao, Y. Wang, Z. Wang, *Nanotechnology* 2010, **21**, 285602.
40. W. P. Lim, C. T. Wong, S. L. Ang, H. Y. Low, W. S. Chin, *Chem. Mater.* 2006, **18**, 6170.
41. Z. Liu, D. Xu, J. Liang, J. Shen, S. Zhang, Y. Qian, *J. Phys. Chem. B* 2005, **109**, 10699.
42. N. Revaprasadu, M. Malik, P. O'Brien, *S. Afr. J. Chem.*, 2004, **57**, 40.
43. X. S. Du, Z. Z. Yu, A. Dasari, J. Ma, Y. Z. Meng, Y. W. Mai, *Chem. Mater.* 2006, **18**, 5156.
44. A. G. Andersen , P. Kofstad, *Oxid. Met.* 1995, **43**, 173.

45. R. D. Tilley, D. A. Jefferson, *J. Phys. Chem. B* 2002, **106**, 10895.
46. A. Manthiram, Y. U. Jeong, *J. Solid State Chem.* 1999, **147**, 679.
47. H. T. Zhang, G. Wu, X. H. Chen, *Mater. Lett.* 2005, **59**, 3728.
48. K. Anuar, Z. Zainal, N. Saravanan, S. Nor Hamizi, *J. Indian Chem. Soc.* 2005, **82**, 526.
49. H. Vandenborre, P. Vermeiren, R. Leysen, *Electrochim. Acta* 1984, **29**, 297.
50. J.Z. Wang, S.L. Chou, S.Y. Chew, J. Z. Sun, M. Forsyth, D. R. MacFarlane, H. K. Liu, *Solid State Ionics* 2008, **179**, 237.
51. G. Kishan, L. Coulier, V. H. J. de Beer, J. A. R. van Veen, J. W. Niemantsverdriet, *J. Catal.* 2000, **196**, 180.
52. W. M. Kriven, *J. Am. Ceram. Soc.* 1988, **71**, 1021.
53. W. Zhang, L. Xu, K. Tang, F. Li, Y. Qian, *Eur. J. Inorg. Chem*. 2005, 653.
54. F. Xu, Y. Xie, X. Zhang, C. Wu, W. Xi, J. Hong, X. Tian, *New J. Chem.*, 2003, **27**, 1331.
55. Y. Hu, J. Chen, W. Chen, X. Lin, X. Li, *Adv. Mater.* 2003, **15**, 726.
56. H. Wang, J. R. Zhang, X. N. Zhao, S. Xu, J. J. Zhu, *Mater. Lett.*, 2002, **55,** 253.
57. P. S. Khiew, N. M. Huang, S. Radiman, Md. S. Ahmad, *Mater. Lett.,* 2004, **58,** 762.
58. L. Tian, L. Y. Yep, T. T. Ong, J. Yi, J. Ding, J. J. Vittal, *Cryst. Growth Des.,* 2009, **9**, 352.
59. J. H. L. Beal, P. G. Etchegoin, R. D. Tilley, *J. Phys. Chem. C* 2010, **114**, 3817.
60. D. J. Vaughan, A. R. Lennie, *Sci. Prog. (Edinburgh)* 1991, **75**, 371.
61. J. B. Goodenough, *Mater. Res. Bull.*, 1978, **13**, 1305.
62. C. N. R. Rao, K. P. R. Pisharody, *Prog. Solid State Chem.*, 1975, **10**, 207.
63. H.Wang, A. Pring, F.Wu, G. Chen, J. Jiang, F. Xia, J. Zhang, Y. Ngothai, B. O'Neill, *J. Sulfur Chem.*, 2006, **27**, 27.
64. H. Wang, I. Salveson, *Phase Transitions*, 2005, **78**, 547.
65. H. Nakazawa, N. Morimoto, *Mat. Res. Bull.*, 1971, **6**, 345.
66. F. Li, H. F. Franzen, *J. Solid State Chem.*, 1996, **126**, 108.
67. A. Wadia, A. P. Alivisatos, D. M. Kammen, *Environ. Sci. Technol.,* 2009, **43**, 2072.

68. J. Puthussery, S. Seefeld, N. Berry, M. Gibbs, M. Law, *J. Am. Chem. Soc.*, 2011, **133**, 716.
69. Z. He, S. H. Yu, X. Zhou, X. Li, J. Qu, *Adv. Funct. Mater.*, 2006, **16**, 1105.
70. F. Cao, W. Hu, L. Zhou, W. Shi, S. Song, Y. Lei, S. Wang, H. Zhang, *Dalton Trans.*, 2009, 9246.
71. D. W. Wang, Q. H. Wang, T. M. Wang, *CrystEngComm*, 2010, **12**, 755.
72. Z. J. Zhanga, X. Y. Chenb, *J. Alloy Compd.*, 2009, **488**, 339.
73. Y. Min, L. Hu, Y. Chen, Y. Zhang, Y. Zhao, *Mater. chem. phys.*, 2009, **114**, 518.
74. C. Wadia, Y. Wu, S. Gul, S. K. Volkman, J. Guo, A. P. Alivisatos, *Chem. Mater.* 2009, **21**, 2568.
75. X. Chen, Z. Wang, X. Wang, J. Wan, J. Liu, Y. Qian, *Inorg. Chem.*, 2005, **44**, 951.
76. G. H. Yue, P. X. Yan, L. S. Wang, W. Wang, Y. Z. Chen, D. L. Peng, *Nanotechnology*, 2008, **19**, 195706.
77. X. L. Yu, Y. Wang, R. K. Zheng, J. F. Qu, H. L. W. Chan, C. B. Cao, *Cryst. Growth Des.*, 2009, **9**, 1293.
78. H. Y. Lai, C. J. Chen, *J. Cryst. Growth*, 2009, **311**, 4698.
79. Y. Zhang, Y. Du, H. Xu, Q, Wang, *CrystEngComm.*, 2010, **12**, 3658.
80. W. Han, M. Gao, *Cryst. Growth Des.*, 2008, **8**, 1023.
81. P. V. Vanitha, P. O'Brien, *J. Am. Chem. Soc.*, 2008, **130**, 17256.
82. M. Akhtar, J. Akhter, M. A. Malik, P. O'Brien, F. Tuna, J. Raftery, M. Helliwell, *J. Mater. Chem.*, 2011, **21**, 9737.
83. X. Fang, T. Zhai, U. K. Gautam, L. Li, L. Wu, Y. Bando, D. Golberg, *Prog. Mater. Sci.*, 2011, **56**, 175.
84. M. Afzaal, M. A. Malik, P. O'Brien, *New J. Chem.*, 2007, **31**, 2029.
85. D. Moore, Z. L. Wang, *J. Mater. Chem.*, 2006, **16**, 3898.
86. X. Fang, L. Zhang, *J. Mater. Sci. Technol.*, 2006, **22**, 721.
87. M. Afzaal, M. A. Malik, P. O'Brien, *J. Mater. Chem.*, 2010, **20**, 4031.
88. T. Trindade, P. O'Brien, N. L. Pickett, *Chem. Mater.*, 2001, **13**, 3843.
89. Z. Li, J. Sui, X. Li, W. Cai, *Langmuir*, 2011, **27**, 2258.
90. K. Ramasamy, M. A. Malik, P. O'Brien, J. Raftery, *Dalton Trans.*, 2009, 2196.
91. Y. Cheng, Y. Wang, F. Bao, D. Chen, *J. Phys. Chem. B*, 2006, **110**, 9448.

92. W. W. Yu, L. Qu, W. Guo, X. Peng, *Chem. Mater.*, 2003, **15**, 2854.
93. Z. Deng, H. Yan, Y. Liu, *Angew. Chem. Int. Ed.*, 2010, **49**, 8695.
94. Y. Zhao, Y. Zhang, H. Zhu, G. C. Hadjipanayis, J. Q. Xiao, *J. Am. Chem. Soc.*, 2004, **126**, 6874.
95. X. Chen, H. Xu, N. Xu, F. Zhao, W. Lin, G. Lin, Y. Fu, Z. Huang, H. Wang, M. Wu, *Inorg. Chem.*, 2003, **42**, 3100.
96. C. Y. Yeh, Z. W. Lu, S. Froyen, A. Zunger, *Phys. Rev. B*, 1992, **46**, 10086.
97. T. K. Tran, W. Park, W. Tong, M. M. Kyi, B. K. Wagner, C. J. Summers, *J. Appl. Phys.*, 1997, **81**, 2803.
98. H. C. Ong, R. P. H. Chang, *Appl. Phys. Lett.*, 2001, **79**, 3612.
99. Y. Zhang, H. Xu, Q. Wang, *Chem. Commun.*, 2010, **46**, 8941.
100. M. Bredol, J. Merikhi, *J. Mater. Sci.*, 1998, **33**, 471.
101. R. Vacassy, S. M. Scholz, J. Dutta, H. Hofmann, C. J. G. Plummer, G. Carrot, J. Hilborn, M. Akine, *Mater. Res. Soc. Symp. Proc.*, 1998, **501**, 369.
102. P. Calandra, M. Goffredi, V. T. Liveri, *Colloids Surf. A*, 1999, **160**, 9.
103. P. T. Tran, E. R. Goldman, G. P. Anderson, J. M. Mauro, H. Mattoussi, *Phys. Status Solidi G*, 2002, **229**, 427.
104. E. R. Goldman, E. D. Balighian, H. Mattoussi, M. K. Kuno, J. M. Mauro, P. T. Tran G. P. Anderson, *J. Am. Chem. Soc.*, 2002, **124**, 6378.
105. W. Wang, I. Germanenko, M. S. El-Shall, *Chem. Mater.*, 2002, **14**, 3028.
106. J. H. Yu, J. Joo, H. M. Park, S. Baik, Y. W. Kim, S. C. Kim, T. Hyeon, *J. Am. Chem. Soc.*, 2005, **127**, 5662.
107. S. Xiong, B. Xi, C. Wang, D. Xu, X. Feng, Z. Zhu, Y. Qian, *Adv. Funct. Mater.*, 2007, **17**, 2728.
108. L. Hou, F. Gao, *Mater. Lett.*, 2011, **65**, 500.
109. Y. Li, X. Li, C. Yang, Y. Li, *J. Phys. Chem. B*, 2004, **108**, 16002.
110. N. Revaprasadu, M. A. Malik, P. O'Brien, G. Wakefield, *J. Mater. Res.*, 1999, **14**, 3237.
111. C. J. Barrelet, Y. Wu, D. C. Bell, C. M. Lieber, *J. Am. Chem. Soc.*, 2003, **125**, 11498.
112. K. Rajeshwar, N. R. de Tacconi, C. R. Chenthamarakshan, *Chem. Mater.*, 2001, **13**, 2765.
113. Y. Kashiwaba, H. Kirita, H. Abe, T. Ikeda, Jap. J. App. Phys., 1990, **29**, 1733.

114. H. Murai, T. Abe, J. Matsuda, H. Sato, S. Chiba, Y. Kashiwaba, *Appl. Surf. Sci.*, 2005, **244**, 351.
115. R. J. Bandaranayake, G. W. Wen, J. Y. Lin, H. X. Jiang, C. M. Sorensen, *Appl. Phys. Lett.*, 1995, **67**, 831.
116. S. Li, G. W. Yang, *J. Phys. Chem. C*, 2010, **114**, 15054.
117. R. Banerjee, R. Jayakrishnan, P. Ayyub, *J. Phys.: Condens. Matter*., 2000, **12**, 10647.
118. C. Ricolleau, L. Audinet, M. Gandais, T. Gacoin, J.P. Boilot, M. Chamarro, *J. Cryst. Growth*, 1996, **159**, 861.
119. N. Bao, L. Shen, T. Takata, K. Domen, A. Gupta, K. Yanagisawa, C. A. Grimes, *J. Phys. Chem. C*, 2007, **111**, 17527.
120. Z. A. Peng, X. Peng, *J. Am. Chem. Soc.*, 2001, **123**, 183.
121. M. Lazell, P. O'Brien, *J. Mater. Chem.*, 1999, **9**, 1381.
122. W. W. Yu, X. Peng, *Angew. Chem. Int. Ed.*, 2002, **41**, 2368.
123. T. Trindade, P. O'Brien, *Adv. Mater.*, 1996, **8**, 161.
124. T. Trindade, P. O'Brien, X. Zhang, *Chem. Mater.*, 1997, **9**, 523.
125. T. Mthethwa, V. S. R. Pullabhotla, P. S. Mdluli, J. W. Smith, N. Revaprasadu, *Polyhedron*, 2009, **28**, 2977.
126. B. Ludolph, M. A. Malik, P. O'Brien, N. Revaprasadu, *Chem. Commun.*, 1998, 1849.
127. A. A. Memon, M. Afzaal, M. A. Malik, C. Q. Nguyen, P. O'Brien, J. Raftery, *Dalton Trans.*, 2006, 4499.
128. P. S. Nair, T. Radhakrishnan, N. Revaprasadu, G. A. Kolawole, P. O'Brien, *J. Mater. Chem.*, 2002, **12**, 2722.
129. Y. Li, X. Li, C. Yang, Y. Li, *J. Mater. Chem.*, 2003, **13**, 2641.
130. T. Mandal, V. Stavila, I. Rusakova, S. Ghosh, K. H. Whitmire, *Chem. Mater.*, 2009, **21**, 5617.
131. J. C. Bruce, N. Revaprasadu, K. R. Koch, *New J. Chem.*, 2007, **31**, 1647.
132. M. J. Moloto, N. Revaprasadu, P. O'Brien, M. A. Malik, *J. Mater. Sci. Mater. Electron*, 2004, **15**, 313.
133. P. S. Nair, T. Radhakrishnan, N. Revaprasadu, G. A. Kolawole, P. O'Brien, *Chem. Commun.*, 2002, 564.
134. P. S. Nair, G. D. Scholes, *J. Mater. Chem.*, 2006, **16**, 467.

135. S. N. Mlondo, N. Revaprasadu, P. Christian, M. Helliwell, P. O'Brien, *Polyhedron*, 2009, **28**, 2097.
136. P. Bera, C-H. Kim, S. Seok, *Solid State Sci.*, 2010, **12**, 1741.
137. W. Lou, M. Chen, X. Wang, W. Liu, *Mater. Lett.*, 2007, **61**, 3612.
138. Z. Li, W. Cai, J. Sui, *Nanotechnology.*, 2008, **19**, 35602.
139. W. Cai, Z. Li, J. Sui, *Nanotechnology*., 2008, **19**, 465606.
140. W. Rehwald, G. Harbeke, *J. Phys. Chem. Solids*, 1965, **26**, 1309.
141. H. G. Ansell, R. S. Boorman, *J. Electrochem. Soc.*, 1971, **118**, 133.
142. M. Ueda, H. Suzuki, O. Kido, M. Shintaku, M. Kurumada, T. Sato, Y. Saito, C. Kaito, *J. Phys. Soc. Jpn.*, 2005, **74**, 1621.
143. R. Diehl, R. Nitsche, *J. Cryst. Growth*, 1975, **28**, 306.
144. K. Kambas, J. Spyridelis, M. Balkanski, *Phys. Stat. Sol. (b)*, 1981, **105**, 291.
145. T. Asikainen, M. Ritala, M. Leskela, *Appl. Surf. Sci.*, 1994, **82/83**, 122.
146. S. Yu, L. Shu, Y. Qian, Y. Xie, J. Yang, L. Yang, *Mater. Res. Bull.*, 1998, **33**, 717.
147. J. Sterner, J. Malmström, L. Stolt, *Prog. Photovolt: Res. Appl.*, 2005, **13**, 179.
148. N. Naghavi, S. Spiering, M. Powalla, B. Cavana, D. Lincot, *Prog. Photovolt: Res. Appl.*, 2003, **11**, 437.
149. Y. Liu, H. Xu, Y. Qian, *Cryst. Growth Des.*, 2006, **6**, 1304.
150. X. Fu, X. Wang, Z. Chen, Z. Zhang, Z. Li, D. Y. C. Leung, L. Wu, X. Fu, *Appl. Catal. B: Environ.*, 2010, **95**, 393.
151. Y. Xing, H. Zhang, S. Song, J. Feng, Y. Lei, L. Zhao, M. Li, *Chem. Commun.*, 2008, 1476.
152. L-Y. Chen, Z-D. Zhang, W-Z. Wang, *J. Phys. Chem. C*, 2008, **112**, 4117.
153. Y. Liu, H. Xu, Y. Qian, *Cryst. Growth Des.*, 2006, **6**, 1304.
154. W. Du, J. Zhu, S. Li, X. Qian, *Cryst. Growth Des.*, 2008, **8**, 2130.
155. L. Liu, H. Liu, H-Z. Kou, Y. Wang, Z. Zhou, M. Ren, M. Ge, X. He, *Cryst. Growth Des.*, 2009, **9**, 113.
156. D. K. Nagesha, X. Liang, A. A. Mamedov, G. Gainer, M. A. Eastman, M. Giersig, J-J. Song, T. Ni, N. A. Kotov, *J. Phys. Chem. B*, 2001, **105**, 7490.
157. Z. Li, X. Tao, Z. Wu, P. Zhang, Z. Zhang, *Ultrason. Sonochem.*, 2009, **16**, 221.
158. J. Tabernor, P. Christian, P. O'Brien, *J. Mater. Chem.*, 2006, **16**, 2082.

159. N. Revaprasadu, M. A. Malik, J. Carstens, P. O'Brien, *J. Mater. Chem.*, 1999, **9**, 2885.
160. M. A. Franzman, R. L. Brutchey, *Chem. Mater.*, 2009, **21**, 1790.
161. S. W. Haggata, M. A. Malik, M. Motevalli, P. O'Brien, J. C. Knowles, *Chem. Mater.*, 1995, **7**, 716.
162. M. Afzaal, M. A. Malik, P. O'Brien, *Chem. Commun.*, 2004, 334.
163. D. P. Dutta, G. Sharma, A. K. Tyagi, S. K. Kulshreshtha, *Mater. Sci. Eng. B*, 2007, **138**, 60.
164. K. Ramasamy, M. A. Malik, P. O'Brien, J. Raftery, *Dalton Trans.*, 2010, **39**, 1460.
165. Y. Chen, L. Chen, L. Wu, *Chem. Eur. J.* 2008, **14**, 11069.
166. S. Yamamuro, D. F. Farrell, S. A., Majetich, *Phys. Rev. B* 2002, **65**, 224431.
167. R. Si, Y. W. Zhang, H. P. Zhou, L. D. Sun, C. H. Yan, *Chem. Mater.* 2007, **19**, 18.
168. T. Kuzuya, K. Itoh, K. Sumiyama, *J. Colloid Interface Sci. 2*008, **319**, 565.
169. M. C. Brelle, C. L. Torres-Martinez, J. C. McNulty, R. K. Mehra, J. Z. Zhang, *Pure Appl. Chem.*, 2000, **72**, 101.
170. Y. Zhao, H. Pan, Y. Lou, X. Qiu, J. Zhu, C. Burda, *J. Am. Chem. Soc.* 2009, **131**, 4253.
171. P. Lukashev, W. R. L. Lambrecht, T. Kotani, M. van Schilfgaarde, *Phys. Rev. B*, 2007, **76**, 195202.
172. L. D. Partain, P. S. Mcleod, J. A. Duisman, T. M. Peterson, D. E. Sawyer, C. S. Dean, *J. Appl. Phys.* 1983, **54**, 6708.
173. B. J. Mulder, *Phys. Status Solidi A*, 1973, **15**, 409.
174. B. J. Mulder, *Phys. Status Solidi A*, 1972, **13**, 79.
175. B. J. Mulder, *Phys. Status Solidi A*, 1972, **13**, 569.
176. E. Eser, J. A. Cambridge, *Solar Cells, 1*982, **5**, 343.
177. B. J. Mulder, *Phys. Stat. Sol. A* 1973, **18**, 633.
178. C. de Mello Donegá, *Chem. Soc. Rev.*, 2011, **40**, 1512.
179. M. Jones, J. Nedeljkovic, R. J. Ellingson, A. J. Nozik, G. Rumbles, *J. Phys. Chem. B*, 2003, **107**, 11346.
180. Y. H. Kim, J. H. Lee, D-W. Shin, S. M. Park, J. S. Moon, J. G. Nam, J-B. Yoo, *Chem. Commun.*, 2010, **46**, 2292.

181. J. Ning, K. Men, G. Xiao, L. Zhao, L. Wang, B. Liu, B. Zou, *J. Colloid Interface Sci.*, 2010, **347**, 172.
182. K. Ramasamy, M. A. Malik, M. Helliwell, F. Tuna, P. O'Brien, *Inorg. Chem.*, 2010, **49**, 8495.

Chapter 3

Alloy and Ternary Nanoparticles

3.1 Summary

This chapter describes the synthesis of $Zn_xCd_{1-x}S$ and $CuInS_2$ nanoparticles from the 1,1,5,5-tetra-*iso*-propyl-4-thiobiureto complexes of Zn, Cd and Cu, In, respectively. The influence of the different reaction parameters (precursor concentration, growth temperature, reaction time and solvent/capping agent combination) on the size, morphology and optical properties of the produced nanoparticles were studied. Powder X-ray diffraction (p-XRD) showed that the obtained $Zn_xCd_{1-x}S$ nanoparticles were cubic under all reaction conditions. The $Zn_xCd_{1-x}S$ nanoparticles had an average diameter between 3.5 to 6.4 nm as shown by transmission electron microscopy (TEM). The optical properties of the $Zn_xCd_{1-x}S$ nanoparticles were highly dependent on the ZnS to CdS precursor ratio and the solvent/capping agent combination. Chalcopyrite (tetragonal), wurtzite (hexagonal) or a mixture of both $CuInS_2$ nanoparticles were obtained depending on the reaction conditions. TEM showed that the $CuInS_2$ nanoparticles could be synthesised with different morphologies (spherical, hexagonal, trigonal or cone). Luminescent $CuInS_2$ nanoparticles were obtained only in the absence of oleylamine. Wurtzite-chalcopyrite polytypism was observed in one of the samples by high-resolution transmission electron microscopy (HRTEM).

3.2 Introduction

Quantum dots have been extensively studied and can be synthesised by different chemical methods.[1-5] Various nanoscale devices have been fabricated based on quantum dots, including light emitting diodes,[6] sensors,[7] optical detectors,[8] quantum dot lasers[9] and memory units.[10] The main factor controlling the properties of the quantum dots and their exploit in such a wide variety of different fields is the band gap. Quantum confinement can be achieved by reducing the dimensions of the semiconductor quantum dots to a size smaller than their exciton Bohr radius and hence, changing the size of quantum dots is a profound way of tuning their band gap. However, the synthesis of extremely small quantum dots (< 2 nm), which are essential for various applications, has encountered problems due to their instability.[11-13] Ternary semiconductor quantum dots pose an advantage over the binary ones as tuning their band gaps can be achieved through altering their constituent stoichiometries.[11-24] Ternary alloys are formed from two quantum dots with either a common cation or a common anion but of different band gaps. An alloyed semiconductor quantum dot can provide a wide range of emission colours independently of their size and can achieve emission colours which are difficult to get using a single component material.[11-13, 18-24] A possible increase in the multiple exciton generation through altering the lattice or tuning the electronic properties of the excited state is another advantage of the alloyed semiconductor quantum dots.[23] This constituent stoichiometry effect has been considered as a result of the dependence of the electronic energy of the quantum dots on the effective exciton mass.[12,22,24] It is worth noting that ternary semiconductor quantum dots can be classified into, homogenous, gradient or core/shell. The formation of these different types may depend on the order of the addition of the precursors and their reactivity. Han *et al.*[24] synthesised CdSe/ZnSe core/shell through alternative addition of Zn and Se precursors into pre-prepared CdSe quantum dots. This core/shell structure transformed into an alloyed quantum dot at higher temperatures due to the dissociation of the Zn and Se bond followed by the diffusion of the Zn into the core CdSe. Smith *et al.*[23] prepared a compositionally controlled lead chalcogenide alloys by the selection of different anions precursors and balancing their reactivity.

$Zn_xCd_{1-x}S$ alloy is a promising candidate for optoelectronic devices such as blue laser diodes,[12,21] optical recording devices,[12,21] biomedical tags,[12] and visible light photocatalyst.[14,17] Wurtzite $Zn_xCd_{1-x}S$ alloy nanoparticles,[11] nanowires[15] and nanorods[16] have been prepared using a ethylenediamine assisted solvothermal method. Nanorods of this hexagonal alloy were also synthesised by a microwave method.[14] Thermal decomposition of the precursors in a hot coordinating solvent for the production of $Zn_xCd_{1-x}S$ alloys has been investigated as well. Cubic $Zn_xCd_{1-x}S$ gradient alloy nanoparticles with Cd-rich inner cores and Zn-rich outer cores were synthesised through a non-injection approach.[19] Injecting a solution of sulfur in octadecene (ODE) into a hot mixture of CdO, ZnO, oleic acid and ODE produced wurtzite nanoparticles of $Zn_xCd_{1-x}S$.[12] Another injection approach involves the injection of the molecular precursors, zinc and cadmium ethylxanthates into hot capping agent to produce $Zn_xCd_{1-x}S$ with different phases and different morphologies depending on the reaction conditions.[20] Other examples illustrating the use of molecular precursors for the synthesis of $Zn_xCd_{1-x}S$ alloys include the silylated metal chalcogenolate complexes $[\{(CH_3)_2NCH_2\}_2M(SSiMe_3)_2]$ (M = Zn or Cd)[19] and the single source precursor (cadmium zinc bis(*N*,*N*-diethyldithiocarbamate)).[16]

Ternary I-III-VI_2 semiconductors have been extensively explored as they are promising candidates in: solar cells, light emitting diodes, and non-linear optical devices.[25-31] These materials favour ionic bonding similar to the II–VI semiconductors.[32] $CuInS_2$ (CIS) is a direct transition semiconductor with a bulk band gap of 1.53 eV.[33] It is a promising material for solar cells,[34-36] a good emitter in the near-infrared region,[37] and may be a good material for photocatalytic H_2 evolution from water under visible light.[38] Chalcopyrite, sphalerite and wurtzite are the three different forms of CIS which are the dominant phases at <980, 980-1050 and >1050 ^oC, respectively.[39] In the wurtzitic form, copper and indium share a lattice site, giving more flexibility of stoichiometry as compared to the chalcopyrite phase.[40,41] Thermal decomposition of multiple precursors such as metal oleates/dodecanethiol (DDT),[41,42] metal acetates/DDT,[43] metal iodides/elemental sulphur[32] and metal chlorides/thiourea,[44] has been used for the synthesis of CIS with different morphologies including as: nanorods[41] spherical nanoparticles,[32,43] nanodisks,[44] and other unique shapes (acron, bottle and larva).[42] Metal-organic precursors used include: copper and indium diethyldithiocarbamates: $[Cu(S_2CNEt_2)_2]$ and

$[In(S_2CNEt_2)_3]$,[45] copper and indium S-methyldithiocarbazates: $Cu(MeSCSNHNH_2)Cl_2$ and $[In(MeSCSNHNH_2)_2Cl_2]Cl$[40] and $[Cu(SC\{O\}Ph)]/[In(bipy)\text{-}(SC\{O\}Ph)_3]$.[46] Vittal *et al.*[46] reported the thermal decomposition of the single source precursor $[(Ph_3P)CuIn(SC\{O\}Ph)_4]$ in a mixture of DDT and trioctylphosphine oxide to give wurtzite or zinc blende CIS depending on the growth temperature and the ratio of the capping agents. Thermal decomposition of another single source precursor $[(PPh_3)_2CuIn(SEt)_4]$ in the non-coordinating solvent dioctylphthalate has been reported by Castro *et al*.[47]

We discussed the use of $[M(SON(CN^iPr_2)_2)_n]$[48] as a single source precursor for the synthesis of metal sulfide nanocrystals in the previous chapter. In this chapter the use of thiobiureat complexes of zinc, cadmium, copper and indium for the synthesis of zinc cadmium sulfide and copper indium disulfide nanocrystals and their characterisation is described.

3.3 Experimental

3.3.1 Synthesis of precursors: $[Zn(SON(CN^iPr_2)_2)_2]$, $[Cd(SON(CN^iPr_2)_2)_2]$, $[Cu(SON(CN^iPr_2)_2)_2]$ and $[In(SON(CN^iPr_2)_2)_3]$

For the synthesis of these precursors please see section 2.3.

3.3.2 Synthesis of nanoparticles

3.3.2.1 Zinc cadmium sulfide nanoparticles

All nanoparticles were synthesized by thermal decomposition of a mixture of zinc and cadmium precursors. Thermolysis experiments were carried out under different conditions:

(i) Using three different thermolysis temperatures (200, 240 and 280 °C) at a ratio of 1:1 of cadmium precursor to zinc precursor in oleylamine (OLA).

(ii) Using three different ratios of cadmium precursor to zinc precursor (2:1, 1:1 and 1:2) at 280 °C in OLA.

(iii) Using different solvent/capping agent combinations at 280 °C and a ratio of 1:1 of cadmium precursor to zinc precursor.

In a typical experiment, OLA (capping agent) (15 mL, 46.6 mmol) was degassed under reduced pressure at 100 °C for 30 minutes and then heated to the desired

temperature under nitrogen. The required amount of the zinc sulfide precursor [$Zn(SON(CN^{i}Pr_2)_2)_2$] (0.127 g, 0.2 mmol) and cadmium sulfide precursor [$Cd(SON(CN^{i}Pr_2)_2)_2$] (0.137 g, 0.2 mmol) were dispersed in OLA (solvent) (5 mL, 15.5 mmol) and injected into the hot OLA. The reaction was maintained for 1 h. The mixture was allowed to cool then at around 50 °C an excess of methanol was added to give a yellow or yellowish precipitate which was isolated by centrifugation. The solid was washed several times with methanol then redispersed in toluene. Any insoluble material was removed by centrifugation.

3.3.2.2 Copper indium disulfide nanoparticles

All nanoparticles were synthesized by thermal decomposition of the 1:1 mixture of copper and indium precursors. Thermolysis experiments were carried out under different conditions:

(i) Using three different molar ratios of precursors to OLA (1:300, 1:150 and 1:75) at 240 °C.

(ii) Using three different thermolysis temperatures (200, 240 and 280 °C) at a ratio of 1:150 of precursors to OLA.

(iii) Using three different thermolysis solvent/capping agents (OLA, DDT, ODE) at a thermolysis temperature of 240 °C and precursors to capping agent ratio of 1:150.

Reactions were carried out using the same method used for the synthesis of the $Zn_xCd_{1-x}S$ nanoparticles.

3.4 Results and discussion

3.4.1 Zinc cadmium sulfide

Nanoparticles obtained from the all different experiments were analysed by p-XRD, TEM, UV-Vis and PL spectroscopy and all results are summarised in Table 3.1.

Table 3.1. Summary of the synthesis conditions and the structure characterisation of the alloyed $Zn_xCd_{1-x}S$ nanoparticles.

	Precursors Molar Ratio Cd:Zn	Thermoly-sis Temp., °C	Solvent /Capping agent mixture	Average Size (TEM), nm	EDAX Cd:Zn	Band gap, eV	Emission, nm	FWHM, nm (PL)
1	1:1	200	OLA/OLA	3.3±0.5	0.44:0.56	2.94	414	39
2	1:1	240	OLA/OLA	4.2±0.6	0.49:0.51	2.91	424	30
3	1:1	280	OLA/OLA	4.7±0.7	0.48:0.52	2.88	426	30
4	2:1	280	OLA/OLA	6.0±0.9	0.65:0.35	2.72	452	28
5	1:2	280	OLA/OLA	4.4±0.9	0.32:0.68	3.09	418	47
6	1:1	280	ODE/OLA	4.6±0.7	0.52:0.48	2.79	440	37
7	1:1	280	OLA/ODE	5.1±0.8	0.47:0.53	2.9	436	48
8	1:1	280	DDT/OLA	6.1±1.0	0.52:0.48	2.96	418	-
9	1:1	270	OLA/DDT	6.4±1.5	0.53:0.47	3.05	415	-

3.4.1.1 p-XRD

The p-XRD patterns of the nanocrystals obtained from a 1:1 ratio between ZnS precursor and CdS precursor at all temperatures are shown in Fig. 3.1 with the red and blue lines representing the cubic CdS (ICDD card No. 010-0454) and the cubic ZnS (ICDD card No. 003-0570), respectively. Compared to the cubic CdS and the cubic ZnS, the p-XRD of the alloyed $Zn_xCd_{1-x}S$ lies almost at halfway between the two reference materials, indicating an almost 1:1 ratio of Zn to Cd. Changing the ratio between the ZnS and CdS precursors had an effect on the Zn and Cd ratio in the produced alloy (Fig. 3.2) (Table 3.2). The peaks in the p-XRD pattern of the $Zn_xCd_{1-x}S$ alloy prepared using a ratio of 2:1 of CdS precursor to ZnS precursor are shifted to lower angles, towards the position of CdS, suggesting that more Cd is incorporated into the nanocrystal. On the other hand, higher ratio of the ZnS precursor to the CdS precursor (2:1) resulted in a shift in the p-XRD peaks to higher

angles, towards the position of ZnS (Table 3.2). Changing the solvent/capping agent did not change the phase of the produced nanoparticles. Cubic $Zn_xCd_{1-x}S$ alloys were obtained using OLA only, ODE/OLA or DDT/OLA mixtures (Fig. 3.3).

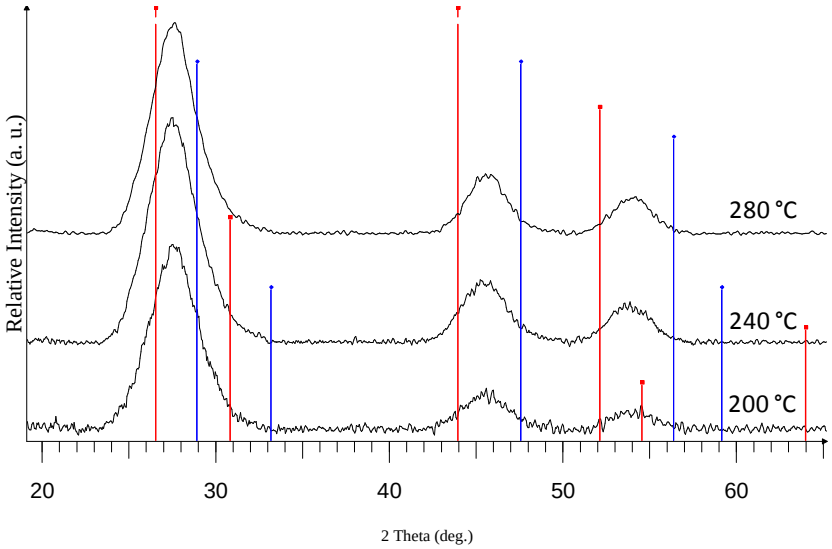

Fig. 3.1 p-XRD pattern of $Zn_xCd_{1-x}S$ nanoparticles prepared at different growth temperatures in OLA from a 1:1 molar ratio of CdS precursor to ZnS precursor. Red and blue lines represent the cubic CdS (ICDD card No. 010-0454) and the cubic ZnS (ICDD card No. 003-0570), respectively.

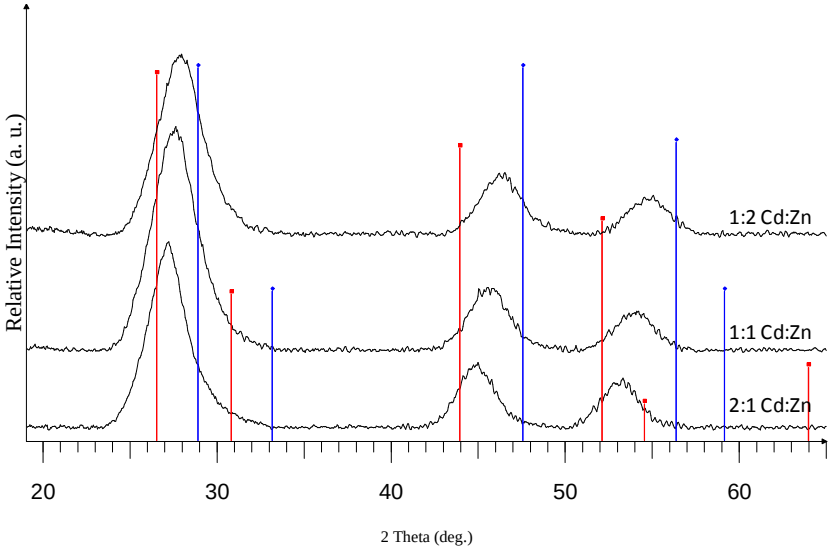

Fig. 3.2 p-XRD pattern of $Zn_xCd_{1-x}S$ nanoparticles prepared using different ratios of CdS precursor to ZnS precursor in OLA at 280 °C. Red and blue lines represent the cubic CdS (ICDD card No. 010-0454) and the cubic ZnS (ICDD card No. 003-0570), respectively.

Table 3.2. Average 2θ and d-spacing of the alloyed $Zn_xCd_{1-x}S$ nanoparticles prepared from different CdS precursor to ZnS precursor ratios and the standard values for cubic CdS (ICDD card No. 010-0454) and cubic ZnS (ICDD card No. 003-0570).

(111) plane	Cubic CdS (ICDD card No. 010-0454)	$Zn_xCd_{1-x}S$			Cubic ZnS (ICDD card No. 003-0570)
		2:1 Cd:Zn	1:1 Cd:Zn	1:2 Cd:Zn	
2θ in deg.	26.50	27.1	27.3	27.9	28.87
d-spacing in Å (TEM)	3.36	3.29	3.26	3.19	3.09

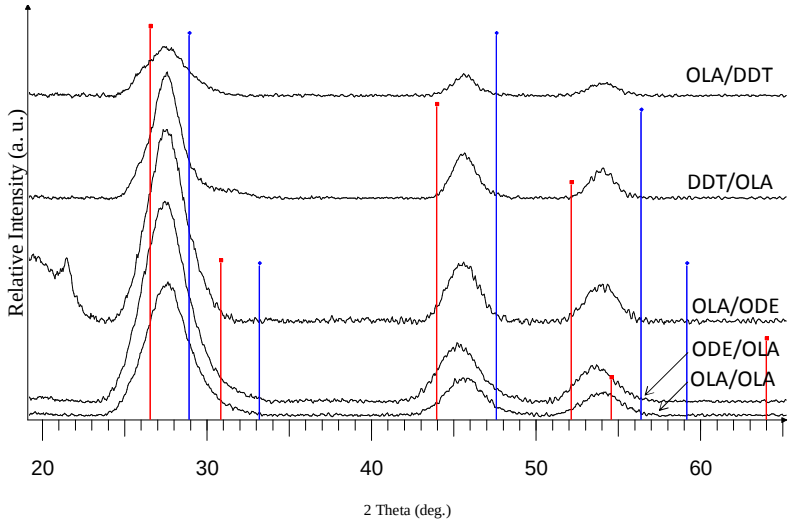

Fig. 3.3 p-XRD pattern of $Zn_xCd_{1-x}S$ nanoparticles prepared from a 1:1 molar ratio of CdS precursor to ZnS precursor at 280 °C using different solvents/capping agents. Red and blue lines represent the cubic CdS (ICDD card No. 010-0454) and the cubic ZnS (ICDD card No. 003-0570), respectively.

3.4.1.2 TEM

TEM images (Fig. 3.4) showed that the size of the nanoparticles increased as the growth temperature increased. At 200 °C, the average size of the spherical $Zn_xCd_{1-x}S$ nanoparticles was 3.3 ± 0.5 nm (Fig. 3.4(a)) which increased to 4.2 ± 0.6 nm and 4.7 ± 0.6 nm at 240 °C (Fig. 3.4(b)) and 280 °C (Fig. 3.4(c)), respectively. The size of

the $Zn_xCd_{1-x}S$ nanoparticles also increased as the Cd content in the alloy increased, which could be due to the larger size of the Cd atoms compared to the Zn atoms (Fig. 3.5). Stoichiometric ratio of ZnS precursor to CdS precursor produced $Zn_xCd_{1-x}S$ alloy with an average diameter of 4.7 ± 0.6 nm (Fig. 3.5(b)). Higher ratio of the CdS precursor to the ZnS precursor enlarged the average diameter to 6.0 ± 0.9 nm (Fig. 3.5(a)) whereas; the higher ratio of the ZnS precursor to the CdS precursor caused a slight reduction in the average diameter (4.4 ± 0.9 nm) (Fig. 3.5(c)). TEM images of $Zn_xCd_{1-x}S$ nanoparticles obtained from different solvent/capping agents are shown in Fig. 3.6. Using ODE as a solvent instead of the OLA had no significant effect on the size or size distribution of the nanoparticles (4.6 ± 0.7 nm) (Fig. 3.6(b)), whereas, dissolving the precursors into OLA followed by injection into hot ODE produced nanoparticles with larger average diameter (5.1 ± 0.8 nm) (Fig. 3.6(c)). On the other hand, DDT as a solvent or capping agent had a remarkable effect on the size and size distribution of the produced nanoparticles as the average size grew to 6.1 ± 1.0 nm (Fig. 3.6(d)) and 6.4 ± 1.5 nm (Fig. 3.6(e)), respectively.

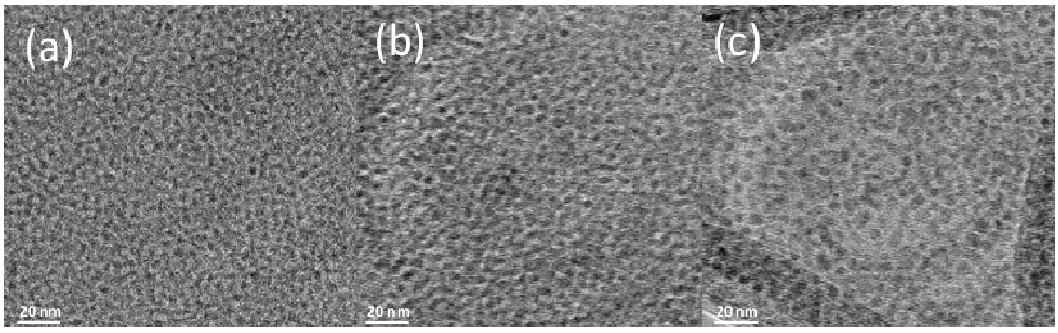

Fig. 3.4 TEM of $Zn_xCd_{1-x}S$ nanoparticles prepared from a 1:1 molar ratio of CdS precursor to ZnS precursor in OLA at (a) 200 °C, (b) 240 °C and (c) 280 °C.

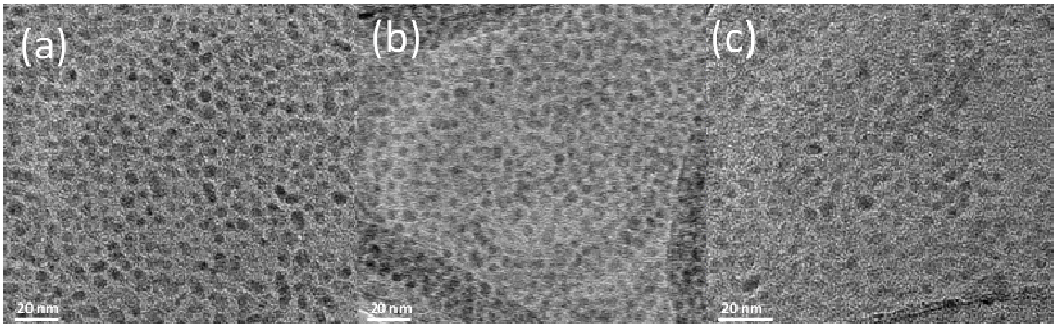

Fig. 3.5 TEM of $Zn_xCd_{1-x}S$ nanoparticles prepared in OLA at 280 °C using (a) 2:1, (b) 1:1 and (c) 1:2 molar ratios of CdS to ZnS precursors.

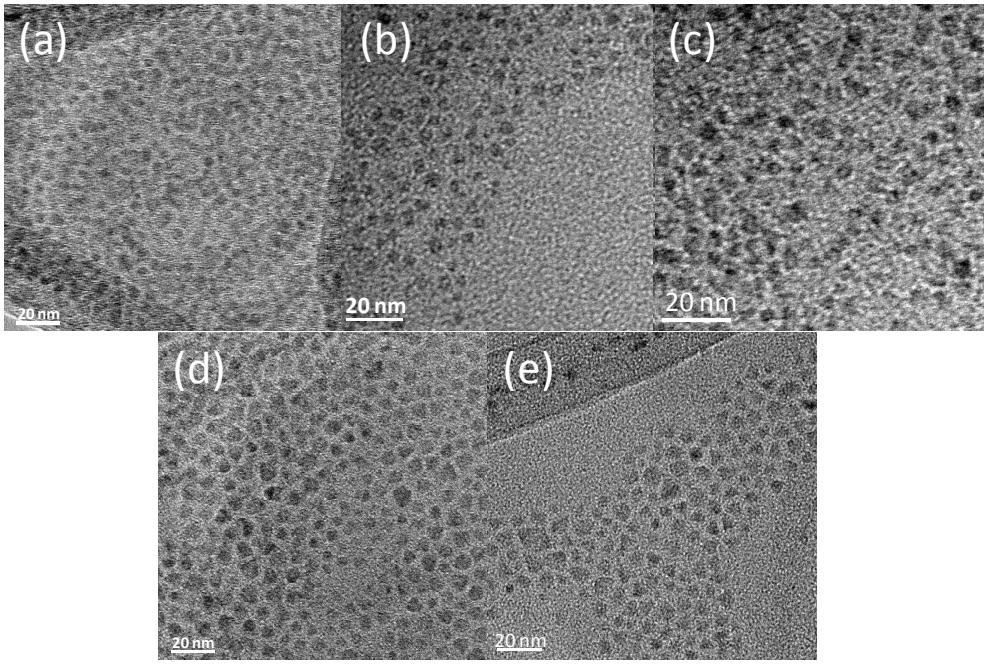

Fig. 3.6 TEM of $Zn_xCd_{1-x}S$ nanoparticles prepared from a 1:1 molar ratio of CdS precursor to ZnS precursor using different solvents/capping agents (a) OLA/OLA, (b) ODE/OLA, (c) OLA/ODE, (d) DDT/OLA and (e) OLA/DDT.

3.4.1.3 HRTEM

The high crystalline nature of the alloys was confirmed by the well-resolved lattice fringes in the HRTEM. The shape of the nanoparticles was more accurately determined from the HRTEM. Spherical or semi-spherical nanoparticles were obtained at the lowest growth temperature (Fig. 3.7(a)). As the temperature increased the obtained nanoparticles became slightly elongated, having an ellipsoid shape (Fig. 3.7(b & c)). The nanoparticles maintained the ellipsoid shape when the amount of ZnS precursor in the feed solution was twice as the CdS precursor whereas; the higher ratio of the CdS precursor to ZnS precursor (2:1) resulted in more spherical nanoparticles (Fig. 3.8). Introducing ODE into the reaction converted the ellipsoid nanoparticles into spherical ones (Fig. 3.9(a & b)), whereas, using DDT as a solvent produced a slightly pointed nanoparticles, like a petal shape (Fig. 3.9(c)). The lattice spacing was calculated from the HRTEM images. $Zn_xCd_{1-x}S$ alloys prepared at different temperatures, from a (1:1) molar ratio, showed a d-spacing of about 3.25 Å, which is almost the average value of the lattice spacing of the (111) plane in the reference cubic CdS and ZnS (Fig. 3.7). This result confirms the p-XRD result suggesting that the nanoparticles obtained at all three temperatures are

homogenously alloyed. The composition of the as obtained nanoparticles is highly dependent on the mole fraction of the precursors in the feed solution as the calculated d-spacing of the nanoparticles was 3.29 Å for a 2:1 ratio, 3.26 Å for a 1:1 ratio and 3.19 Å for a 1:2 ratio of the CdS precursor to the ZnS precursor (Fig. 3.8) (Table 3.2). It is worth mentioning that the average d-spacing of the nanoparticles were calculated from a number of lattice fringes by considering some randomly aligned nanoparticles in each case. These d-spacing are in a good agreement with Vegard's law (Fig. 3.10), which states that the lattice spacing change linearly with the composition of the alloy.[49]

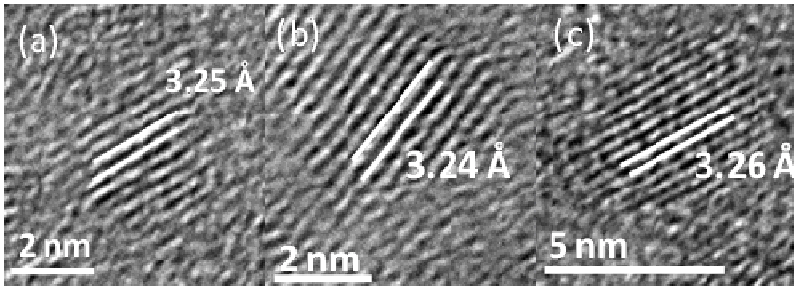

Fig. 3.7 HRTEM images of $Zn_xCd_{1-x}S$ nanoparticles prepared at (a) 200 °C, (b) 240 °C and (c) 280 °C.

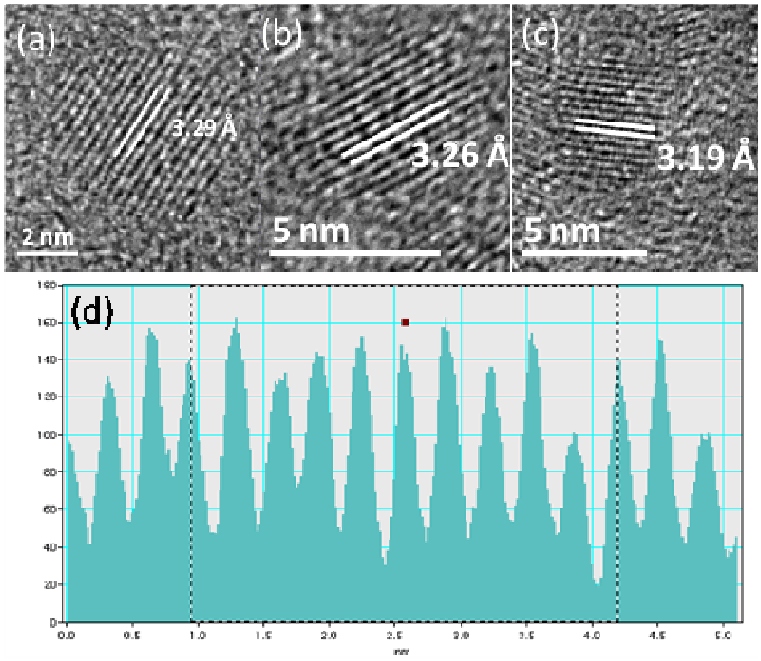

Fig. 3.8 (a-c) HRTEM of $Zn_xCd_{1-x}S$ nanoparticles prepared using 2:1, 1:1 and 1:2 ratios of CdS to ZnS precursors. (d) Line profile used for calculating d-spacing from (b).

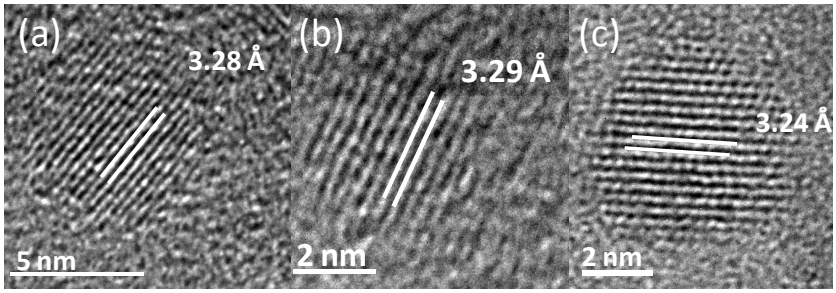

Fig. 3.9 HRTEM images of $Zn_xCd_{1-x}S$ nanoparticles prepared using different solvents/capping agents (a) OLA/ODE, (b) ODE/OLA and (c) DDT/OLA.

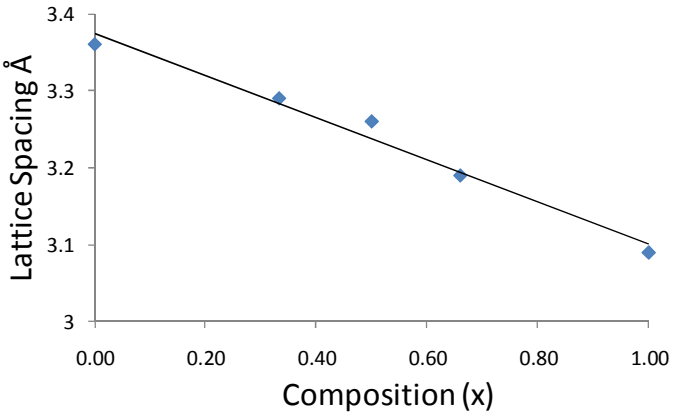

Fig. 3.10 Lattice spacing of $Zn_xCd_{1-x}S$ nanoparticles as a function of mole fraction (x) as determined by EDAX.

3.4.1.4 Energy dispersive analysis of X-Ray (EDAX)

The composition of the nanoparticles was determined using EDAX. The ratio of Zn:Cd was almost 1:1 for all samples prepared using a 1:1 ratio of the CdS precursor to the ZnS precursor. Using excess CdS precursor in the feed solution produced particles with a ratio of 0.35:0.65 Zn:Cd, while excess ZnS precursor resulted in a ratio of 0.68:0.32 Zn:Cd.

3.4.1.5 Optical properties

The absorption and the emission spectra (Fig. 3.11) of the $Zn_xCd_{1-x}S$ nanoparticles obtained at different temperatures showed a slight red shift as the growth temperature increased due to the slight increase in the size of the alloys, as confirmed by TEM. Although the emission peak was slightly red shifted (414 nm at

200 °C to 426 nm at 280 °C), the emission peak became more symmetrical and more intense.

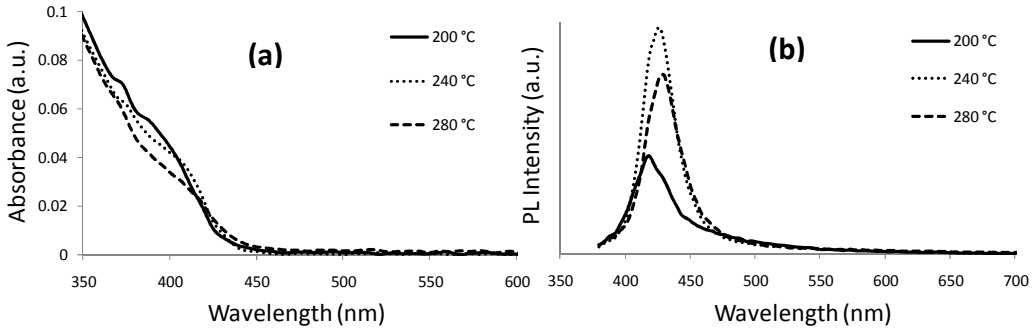

Fig. 3.11 (a) UV-Vis and (b) PL of $Zn_xCd_{1-x}S$ alloys prepared at different temperatures.

A large blue shift in the absorption and the emission spectra (Fig. 3.12) of the alloyed nanoparticles was observed compared to a pure CdS nanoparticles prepared under the same reaction conditions. The blue shift increased as the mole fraction of the ZnS precursor in the feed solution increased. The CdS nanoparticles were emitting at 480 nm which was blue shifted to 452 nm, 426 nm and 418 nm for the $Zn_xCd_{1-x}S$ alloys prepared using a 2:1 ratio, 1:1 ratio and 1:2 ratio of the CdS precursor to the ZnS precursor, respectively. This large blue shift eliminates the formation of a CdS/ZnS core/shell material, as shelling results in a slight red shift or fixing of the absorption and emission peaks.[18] The band gaps of the nanoparticles calculated from the Tauc plot (Fig. 3.13) were 2.58 eV for the pure CdS nanoparticles, 2.72 eV for the Cd rich alloy, 2.88 eV for the homogenous alloy and 3.09 eV for the Zn rich alloy. The increase in the band gap of the pure CdS nanoparticles compared to that of the bulk CdS (2.42 eV), is due to the expected quantum confinement effect where the band gap increase as the particle size decrease. On the other hand, the large increase in the band gap with the increase in the Zn content in the nanoparticles could not be due to the quantum confinement, especially for samples with almost the same average size, but it is consistent with the fact that bulk ZnS has a larger band gap (3.68 eV) than the bulk CdS. The variation of the band gap of the $Zn_xCd_{1-x}S$ alloys with composition is nonlinear and can be illustrated using the empirical equation 3.1:[50]

$$E_g(x) = E_g(\text{CdS}) + (E_g(\text{ZnS}) - E_g(\text{CdS}) - b)x + bx^2 \qquad (3.1)$$

Taking into account bulk band gap of CdS and ZnS are 2.42 and 3.72 eV, respectively, and b is the bowing parameter (Fig. 3.14). Although our results of plotting band gaps as a function of x, (from both input values and EDAX analysis) show a good fit with regression coefficients close to 1, a bowing factor between 0.74 and 0.84 eV was obtained (Table 3.3). This bowing parameter value is slightly higher than the previously reported value of 0.594 eV.20 In terms of the emission intensity, it was found that introducing some amount of Zn into the CdS nanoparticles (2:1 Cd:Zn) enhanced the emission properties (stronger emission intensity and narrower full width half maxima (fwhm)). Further increase in the Zn content in the alloyed nanoparticles resulted in a lower emission intensity and broader fwhm.

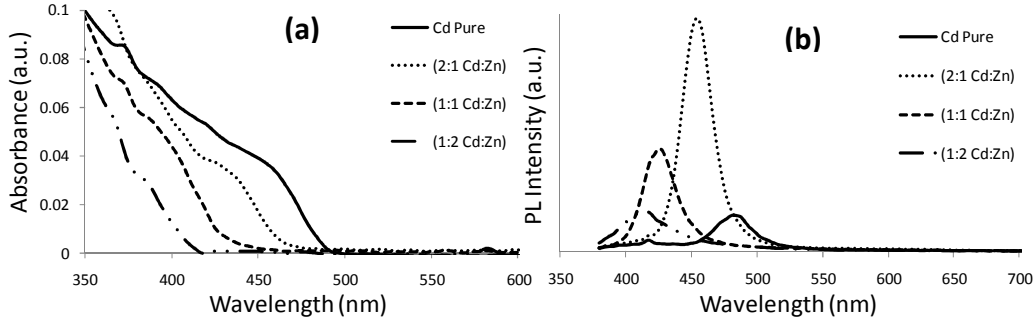

Fig. 3.12 (a) UV-Vis and (b) PL of CdS nanoparticles and $Zn_xCd_{1-x}S$ alloys prepared using different ratios of CdS precursor to ZnS precursor.

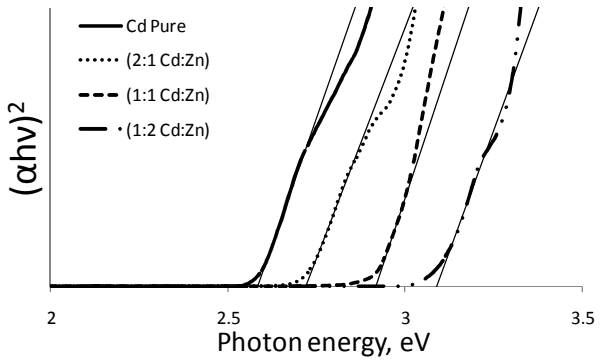

Fig. 3.13 Tauc plot for the CdS nanoparticles and $Zn_xCd_{1-x}S$ alloys prepared using different ratios of CdS precursor to ZnS precursor.

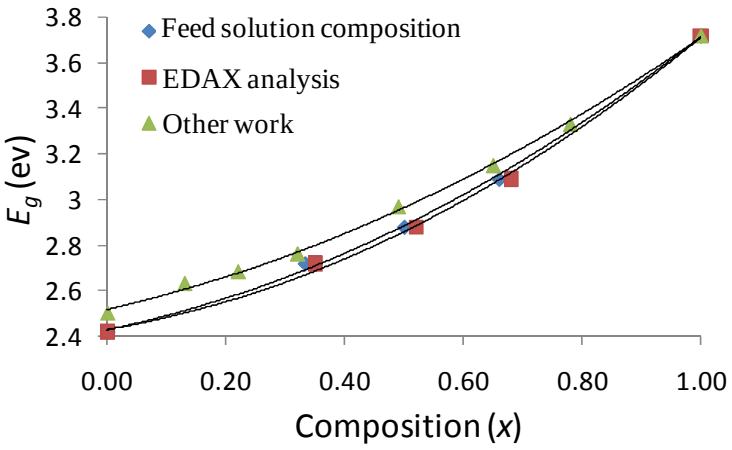

Fig. 3.14 Band gaps of $Zn_xCd_{1-x}S$ nanoparticles as a function of mole fraction (x). (Diamonds) composition in feed solution, (squares) composition from EDAX, (triangles) composition from Ref. 20.

Table 3.3 Bowing parameter (b) and its standard error obtained from the input composition, EDAX analysis and Ref. 20.

	$E_g(x) = E_g(\text{CdS}) + (E_g(\text{ZnS}) - E_g(\text{CdS}) - b)x + bx^2$	
	b	Standard error
Feed solution composition	0.74	0.101
EDAX analysis	0.84	0.127
Other work	0.594	0.069

The effect of the reaction time on the optical properties of the nanoparticles was studied by withdrawing a couple of drops from the reaction solution at different time intervals (5 minutes, 30 minutes and 60 minutes). This reaction was carried out using a 1:1 mole ratio of the CdS precursor to the ZnS precursor at 240 °C. There was no significant change in the absorption or the emission spectra over the course of one hour apart from a slight increase in the emission peak intensity after 60 minutes (Fig. 3.15). This insignificant change could be an indication of a slight change in size

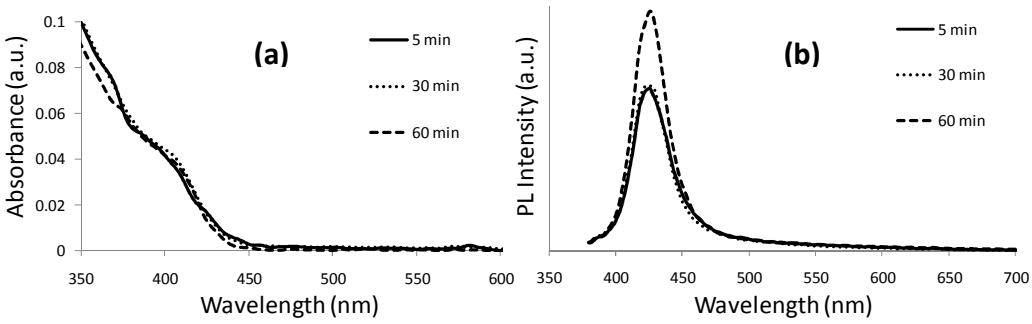

Fig. 3.15 (a) UV-Vis and (b) PL of $Zn_xCd_{1-x}S$ nanoparticles at different time intervals.

The optical properties of the alloyed $Zn_xCd_{1-x}S$ nanoparticles were found to be highly dependant on the solvent and the capping agent as well. Compared to the nanoparticles prepared using only OLA as both solvent and capping agent, using ODE resulted in a slight red shift in the absorption and emission spectra (Fig. 3.16). The emission peak became more intense in particular when ODE was used as a solvent. On the contrary, DDT produced nanoparticles with two emission peaks. A very small emission peak at about 415 nm and a much broader, highly red shifted emission peak (Fig. 3.17). The broad emission peak could be due to the surface traps, which is well-known to be a luminescence quenching sites. Surprisingly, the nanoparticles prepared using DDT had a larger band gap compared to particles prepared in OLA only, although they had a larger size and an almost 1:1 ratio of Zn to Cd, (Fig. 3.18). The quantum yields (QYs) of the Zn_xCd_{1-x} S nanoparticles are between 2-7%, which is about the normal range for the lilac or blue emitting nanoparticles.[20]

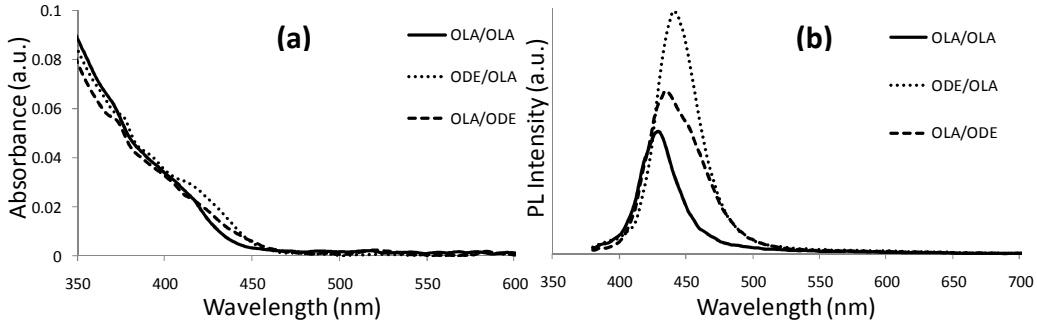

Fig. 3.16 (a) UV-Vis and (b) PL of $Zn_xCd_{1-x}S$ nanoparticles prepared using OLA or ODE/OLA mixture.

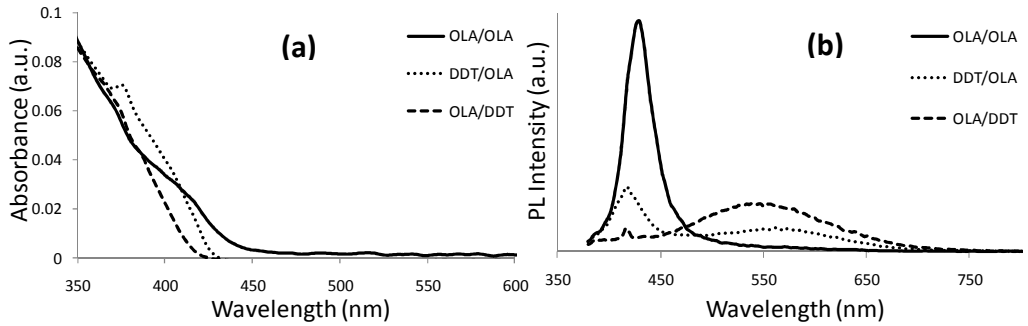

Fig. 3.17 (a) UV-Vis and (b) PL of $Zn_xCd_{1-x}S$ nanoparticles prepared using OLA or DDT/OLA mixture.

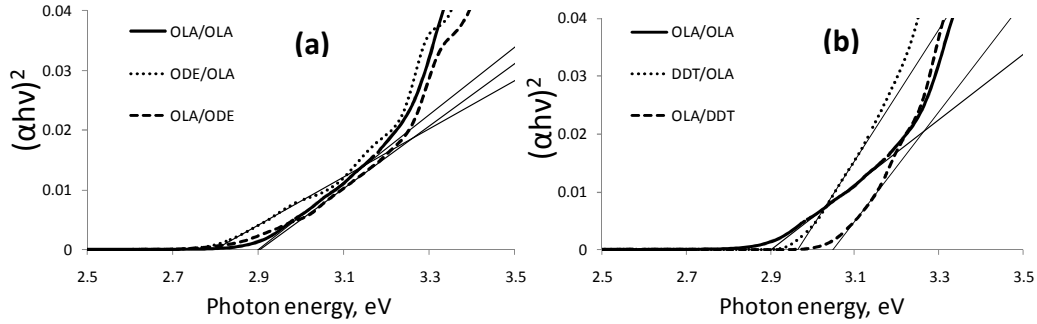

Fig. 3.18 Tauc plot for the $Zn_xCd_{1-x}S$ alloys prepared using different solvents/capping agents.

3.4.2 Copper indium disulfide nanoparticles

Nanoparticles obtained from the all different experiments were analysed by p-XRD, TEM, UV-Vis and PL spectroscopy and the results are summarized in Table 3.4.

Table 3.4 Summary of the synthesis conditions and structure characterisation of the alloyed $CuInS_2$ nanoparticles.

Sample	Ratio	Solvent/Capping agent	Temp, ºC	Phase	Shape	EDX Cu:In:S
CIS**1**	1:300	OLA/OLA	240	Chalcopyrite	Semi-spherical	1.25:1.0:2.5
CIS**2**	1:150	OLA/OLA	240	Chalcopyrite and wurtzite	Trigonal and hexagonal disks	1.1:1.0:1.8
CIS**3**	1:75	OLA/OLA	240	Chalcopyrite and wurtzite	Trigonal and hexagonal disks	1.1:1.0:1.8
CIS**4**	1:150	OLA/OLA	200	Chalcopyrite and wurtzite	Irregular	1.1:1.0:2.1
CIS**5**	1:150	OLA/OLA	280	Chalcopyrite	Spherical	1.4:1.0:2.0
CIS**6**	1:150	ODE/OLA	240	Chalcopyrite and wurtzite	Semi-spherical	1.1:1.0:1.9
CIS**7**	1:150	OLA/ODE	240	Chalcopyrite and wurtzite	Trigonal and hexagonal disks	1.2:1.0:2.0
CIS**8**	1:150	DDT/OLA	240	Wurtzite	Cones	1.1:1.0:2.0
CIS**9**	1:150	OLA/DDT	240	Wurtzite	Cones	1.6:1.0:2.6
CIS**10**	1:150	OLA/DDT	260	Wurtzite	Cones	2.1:1.0:2.3
CIS**11**	1:150	ODE/DDT	240	Chalcopyrite and wurtzite	Spherical	1.1:1.0:2.3

3.4.2.1 p-XRD

The p-XRD patterns of the nanocrystals obtained from the first set of experiments are shown in Fig. 3.19. At the lowest ratio of precursors to OLA (1:300) pure chalcopyrite phase (CIS**1**) was obtained (ICDD card No. 04-001-4943) whereas the nanocrystals obtained at higher ratios (1:150 and 1:75) (CIS**2** and CIS**3**) showed patterns corresponding to the chalcopyrite phase but with a slight mixture of wurtzite (hexagonal) phase. The formation of wurtzitic CIS was only recently reported by Lu and co-workers.[22] In the second set of experiments, the products obtained at thermolysis temperature of 200 ºC (CIS**4**) and 240 ºC (CIS**2**) were a mixture of chalcopyrite and wurtzite, while increasing the thermolysis temperature to 280 ºC (CIS**5**) led to pure chalcopyrite phase (Fig 3.20).The diminution of the wurtzite phase at temperatures above 250 °C has been previously reported.[23] The effect of changing the solvent/capping agent is shown in Fig. 3.21. Dissolving the precursors in ODE then injecting it into hot OLA (CIS**6**) did not change the phase of the nanoparticles produced, similarly when a solution of the precursors dissolved in OLA was injected into hot ODE (CIS**7**). Introducing DDT along with OLA allowed the growth of pure wurtzite CIS nanoparticles even at higher temperature (260 ºC)

(CIS**8**-CIS**10**). Previous reports showed that both OLA[21] or DDT[22,23] could be used to stabilize the wurtzitic phase. When no OLA was used *i.e* the precursors were dissolved in ODE and injected into hot DDT resulted in the production of chalcopyrite with minor wurtzite phase (CIS**11**) which shows in contrary to the previous reports[21-23] that a mixture of both (not one) OLA and DDT is essential for the growth of pure wurtzite phase.

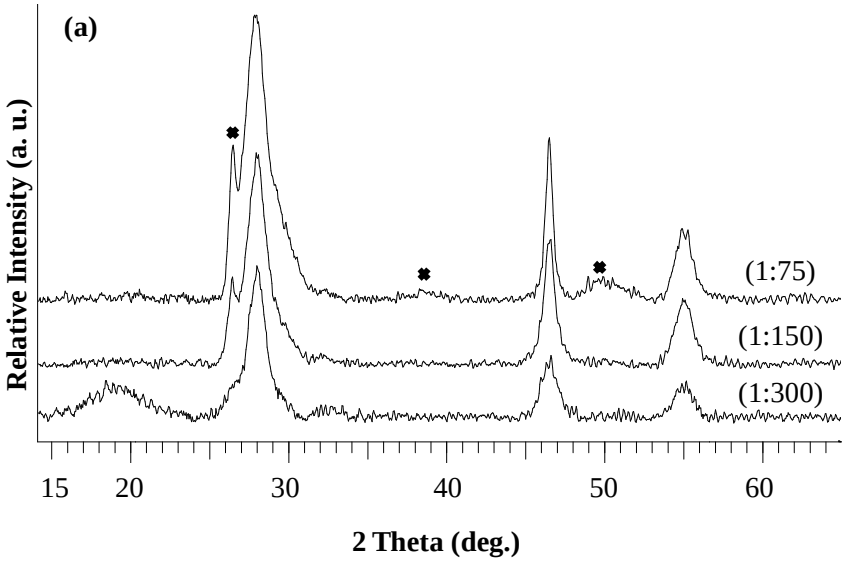

Fig. 3.19 p-XRD patterns of $CuInS_2$ nanoparticles prepared at different ratios, bottom to top CIS**1**, CIS**2** and CIS**3**, respectively. (✱) represents wurtzite peaks.

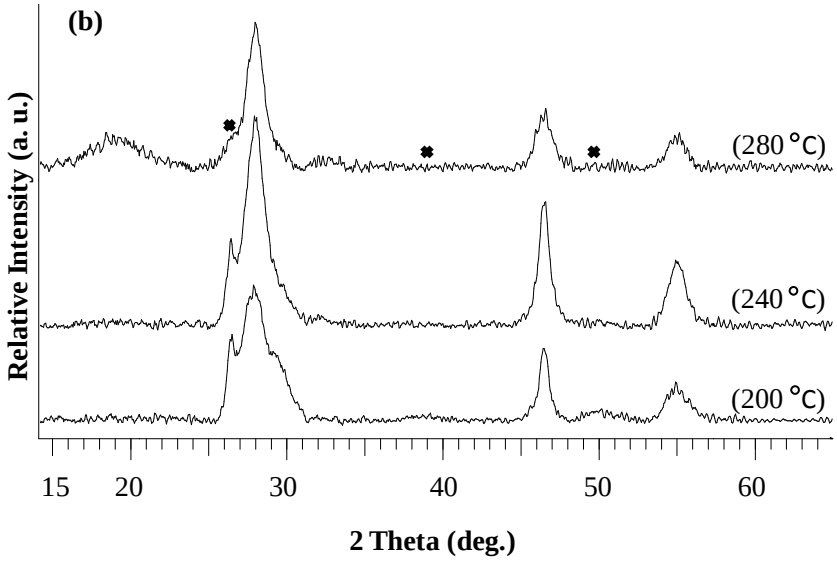

Fig. 3.20 p-XRD patterns of $CuInS_2$ prepared at different growth temperatures, bottom to top CIS**2**, CIS**4** and CIS**5**, respectively. (✱) represents wurtzite peaks.

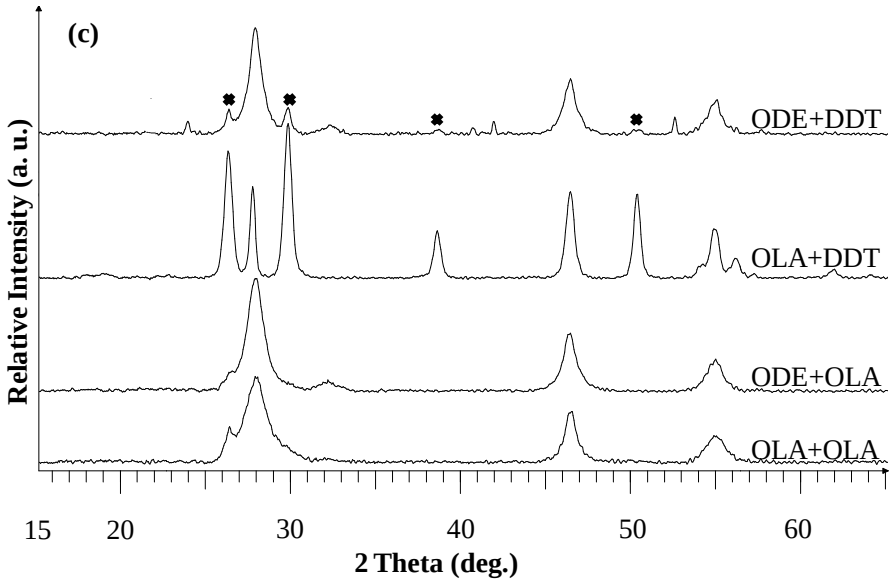

Fig. 3.21 p-XRD patterns of $CuInS_2$ prepared using different solvents/capping agents, bottom to top CIS**2**, CIS**6**, CIS**9** and CIS**11**, respectively. (✱) represents wurtzite peaks.

3.4.2.2 TEM

TEM images of the nanoparticles grown at different concentrations and temperatures showed remarkable changes in the morphology of crystallites (Fig. 3.22). At a temperature of 240 °C and a low ratio of precursors to OLA (1:300) (CIS**1**), close to spherical nanoparticles with an average diameter of 9.5 nm were obtained (Fig. 3.22(a)), whereas, at higher ratios (1:150 and 1:75) (CIS**2** & CIS**3**) trigonal and hexagonal nanodisks were observed (Fig. 3.22(b and c)). At a 1:150 ratio between precursors and OLA and 200 ºC (CIS**4**), small irregular nanoparticles were formed (Fig. 3.22(d)), but at 240 ºC (CIS**2**), trigonal and hexagonal nanodisks were obtained (Fig. 3.22(b)), almost spherical nanoparticles with an average diameter of 10.6 nm were seen at 280 ºC (CIS**5**) (Fig. 3.22(e)). At high temperatures, the reactivity of the precursor is increased and more nuclei are formed, leaving a lower monomer concentration in solution which directs the nanocrystals growth towards the spherical shape.[51] Changing the capping agent had a significant effect on the morphology. When the precursors where dissolved in OLA then injected into hot OLA (CIS**2**) or hot ODE (CIS**7**) trigonal and hexagonal nanodisks were observed (Fig. 3.20(b & f)), whilst on injecting the same solution into hot DDT cones were formed (CIS**9**) (Fig. 3.22(g)). Dispersing the precursors in the non-coordinating

solvent ODE then injecting it into hot OLA (CIS**6**) or hot DDT (CIS**11**) formed semi-spherical or spherical nanoparticles with average diameter of 11.8 nm and 6.7 nm, respectively (Fig. 3.22(h and i)). On using DDT to dissolve the precursors before injecting into hot OLA (CIS**8**) cones were obtained (Fig. 3.22(j)).

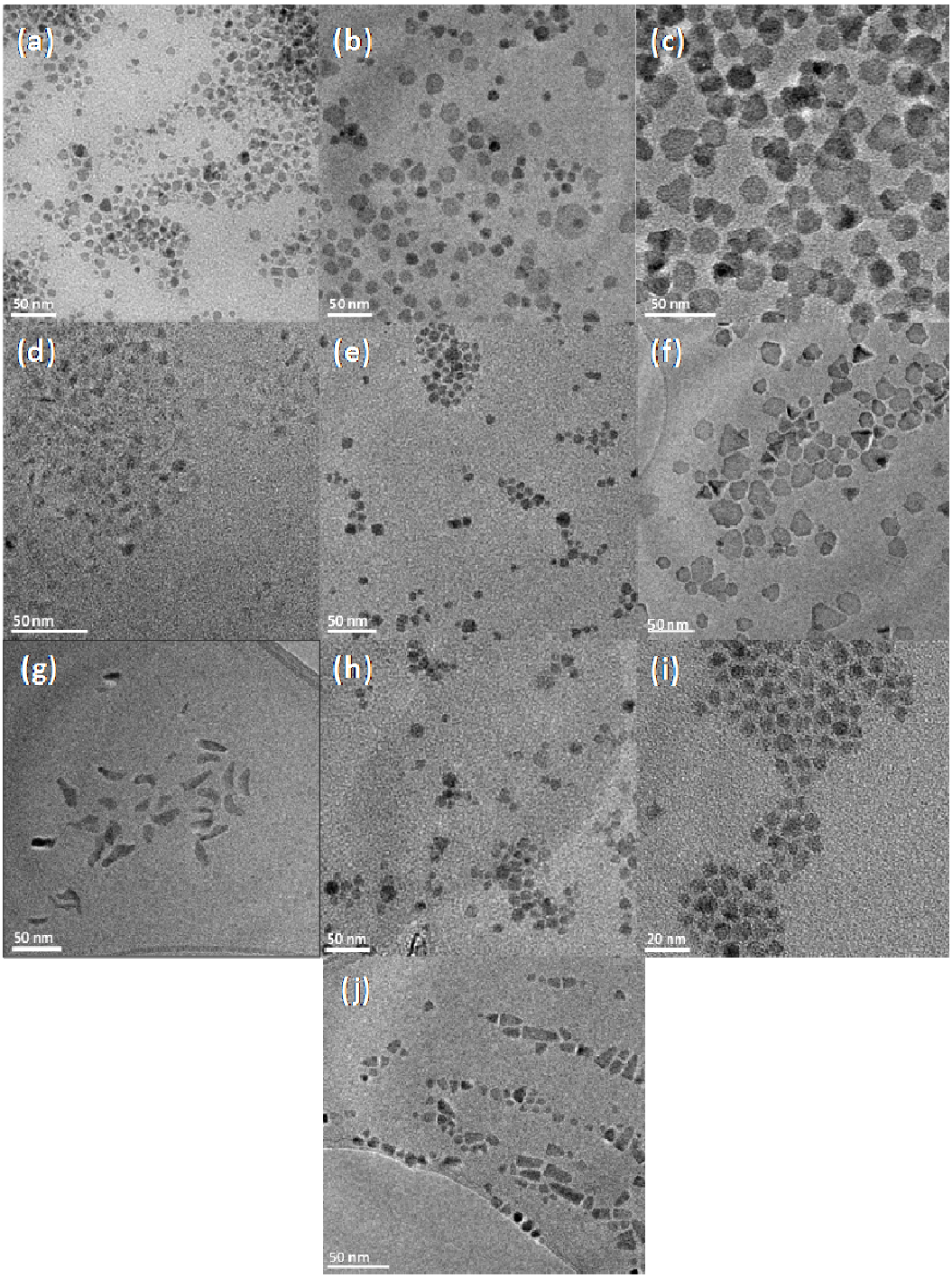

Fig. 3.22 TEM images of (a) CIS**1**, (b) CIS**2**, (c) CIS**3**, (d) CIS**4**, (e) CIS**5**, (f) CIS**7**, (g) CIS**9**, (h) CIS**6**, (i) CIS**11** and (j) CIS**8**.

3.4.2.3 HRTEM

HRTEM images, fast Fourier transform (FFT) and selected area energy diffraction (SAED) of different samples showing different morphologies are shown in Fig. 3.23 The d-spacing calculated from Fig. 3.23(a & b) (CIS**2** & CIS **3**) was 3.35 Å and 1.96 Å, which are matching with the (100) and (110) planes of the wurtzite phase. The angle between the two planes was measured from the FFT (Fig. 3.23(c)) obtained from Fig. 3.23(a) was found to be 30° which is consistent with the theoretical value calculated for these two planes in a hexagonal crystal lattice. The spherical nanoparticle (CIS**5**) (Fig. 3.23(d)) showed a d-spacing of 3.18 Å consistent with the (112) plane of the chalcopyrite phase, whereas the cones (CIS**9**) (Fig. 3.21(e)) showed a d-spacing of 3.23 Å consistent with the (002) plane of the wurtzite phase. The FFT (Fig 3.23(f)) obtained from Fig. 3.21(e) showed two spots perpendicular to the lattice fringes confirming the growth along the (002) direction of the wurtzitic phase. Fig. 3.23(g) is an HRTEM image of the cones (CIS**8**) with d-spacing of 3.23 Å and 3.06 Å, corresponding to the (002) and (101) wurtzite planes, respectively. The FFT (Fig. 3.21(i)) obtained from the circled area in Fig. 3.23(h) (CIS**7**) showed two extra weaker spots than what is expected for a wurtzitic phase imaged down the [001] zone axis. The extra spots are not exactly at half the distance between the bright spots, and hence it could not be due to repeated reflection from superlattice stacking faults or twin planes. The extra spots could be indexed to the (200) planes which is characteristic for chalcopyrite phase indicating a wurtzite-chalcopyrite polytypism. Polytypic CIS nanoparticles were previously reported by Korgel *et al.*[44] The SAED pattern of CIS**7** (Fig. 3.23(j)) could be indexed to match either pure wurtzitic CIS or a mixture of both wurtzite and chalcopyrite CIS. A mixture of both phases would be more consistent with the p-XRD results which showed that the wurtzitic phase exist as a minor component only.

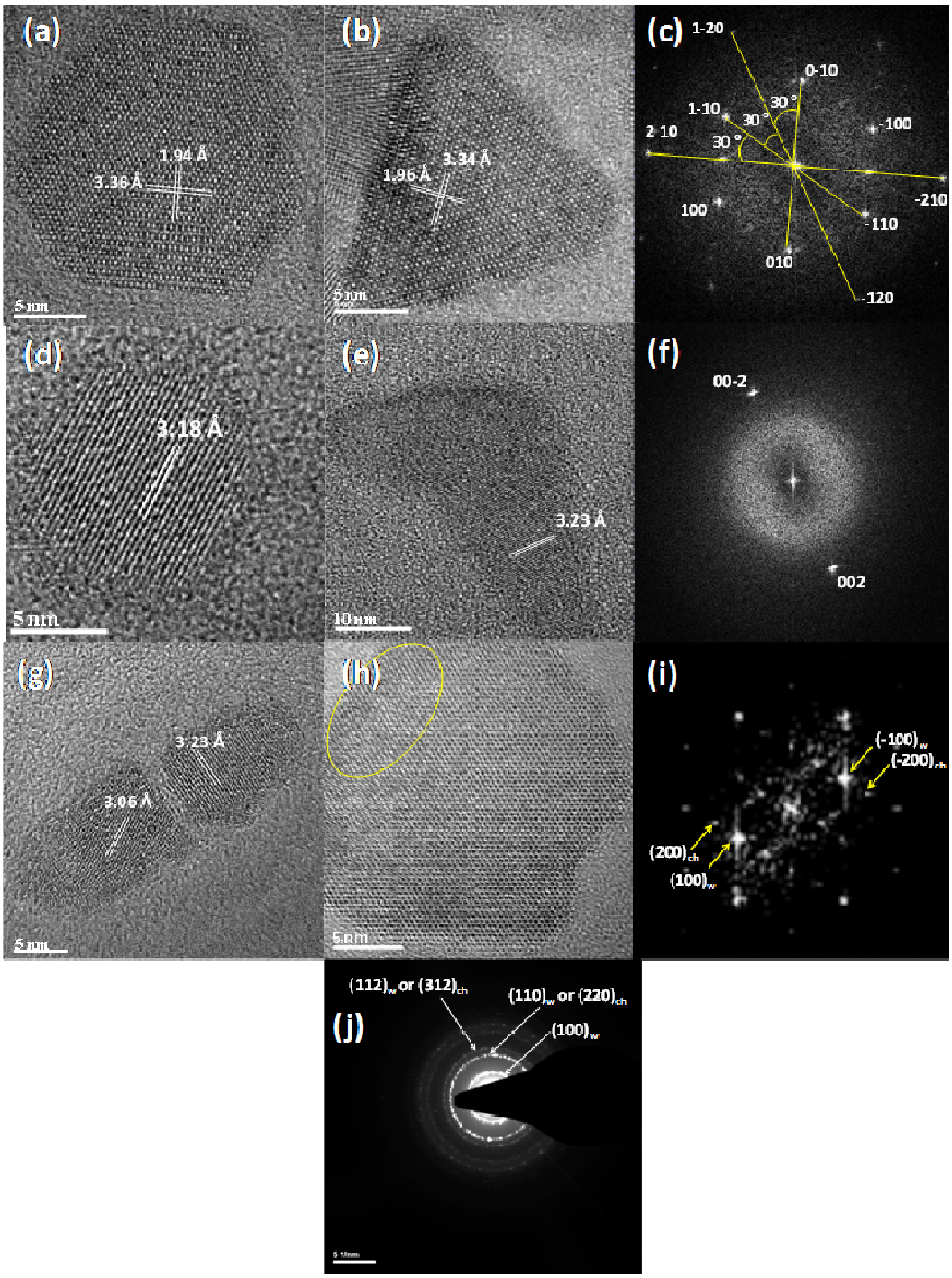

Fig. 3.23 (a, b, d, e, g & h) are HRTEM of CIS2, CIS3, CIS5, CIS9, CIS8 and CIS7, respectively. (c, f & i) are FFT of (a), (e) and the circled area in (h), respectively. (j) SAED of CIS7.

3.4.2.4 EDAX

Fig. 3.24 shows a line scan of EDAX for a sample prepared in OLA at 240 °C. It is quite clear that the sample is well alloyed with homogenous distribution of all three elements in a ratio of Cu:In:S 1:1:2. The EDAX results revealed that higher thermolysis temperature or the presence of DDT along with OLA activates the copper complex resulting in copper rich CIS nanoparticles.

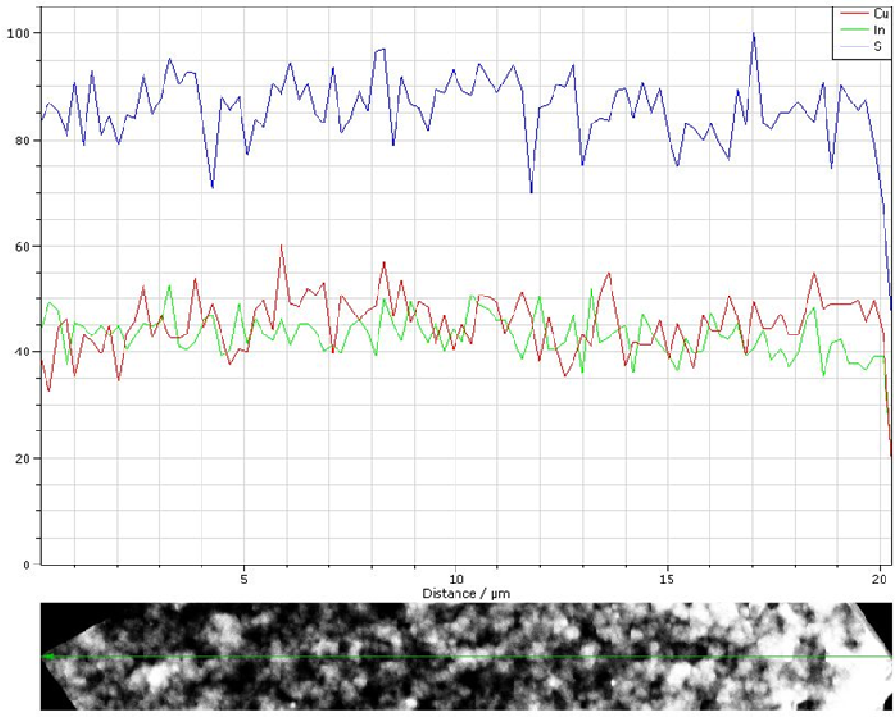

Fig. 3.24 Line scan of Energy-dispersive X-ray spectroscopy (EDAX) of CIS**2.**

3.4.2.5 Optical properties

All the UV-Vis spectra are shown in Fig 3.25. Using only OLA, as both solvent and capping agent, no change was observed on varying the ratios of precursors to OLA, or the temperature (Fig. 3.25(a & b)). UV-Vis was also used to monitor the progress of the reactions. The spectra obtained from reactions in OLA, as both solvent and capping agent again did not show any size dependent character (Fig. 3.25(c)) except at the lowest ratio (1:300) (CIS**1**) or the lowest temperature (200 °C) (CIS **4**) where a slight red shift was observed as the reaction proceeds (Fig. 3.25(d & e)). It has been previously reported that the band edge of CIS nanocrystals with diameters larger than about 10 nm do not show significant shift in the UV-Vis spectra. This observation could be due to the absence of any quantum confinement

as the bulk exciton radius of $CuInS_2$ is around 4.0 nm.[43] Replacing the OLA with ODE (CIS**6** &CIS**7**) caused an insignificant shift, whereas DDT (CIS**8** & CIS**9**) led to a blue shift in the band edge (Fig. 3.25(f)). Fig. 3.25(g & h) show the progress of the reaction when DDT was used as a capping agent and as a solvent, respectively. The red shift in the band edge at the early stages of the reaction (5 min) as well as the absorbance in the near-IR region suggests that $Cu_{2-x}S$[48] may be formed at the beginning of the reaction which gradually changed to the ternary material as shown by a blue shift after 30 min of the reaction. This led to copper rich CIS nanoparticles, which was confirmed by the EDAX analysis (Table 3.4). When no OLA was used (CIS**11**), large blue shift in the band edge was observed compared to other capping agents at the completion of reaction (1 hour). A size-dependant character was confirmed for CIS**11** by the UV-Vis, where the band edge was shifted to higher wavelength as the reaction proceeds (Fig. 3.26(a)). The large blue shift indicates quantum confinement and as a result the particles were luminescent (Fig. 3.26(b)). Although a red shift was observed in the UV-Vis spectra along with the progress of the reaction, no shift was observed in the position of the emission peak (660 nm) (Fig. 3.26(b)). As the reaction proceeds the particles showed an increase in the QY (Fig. 3.26(c)). The absence of any photoluminescence character on using OLA agrees with previous results.[52] A band gap of 1.49 eV was observed for almost all samples obtained without DDT. This value is typical for bulk CIS material.[23] On using DDT with OLA, the band gap increased to 1.54 and 1.59 eV for CIS**8** and CIS**9**, respectively (Fig. 3.27(a)). The nanoparticle sample obtained without using any OLA (CIS**11)** had a size-dependant band gap that decreased from 2.31 eV after 1 minute to 2.07 eV after 1 hour and 2.05 eV after 2 hours (Fig. 3.27(b)).

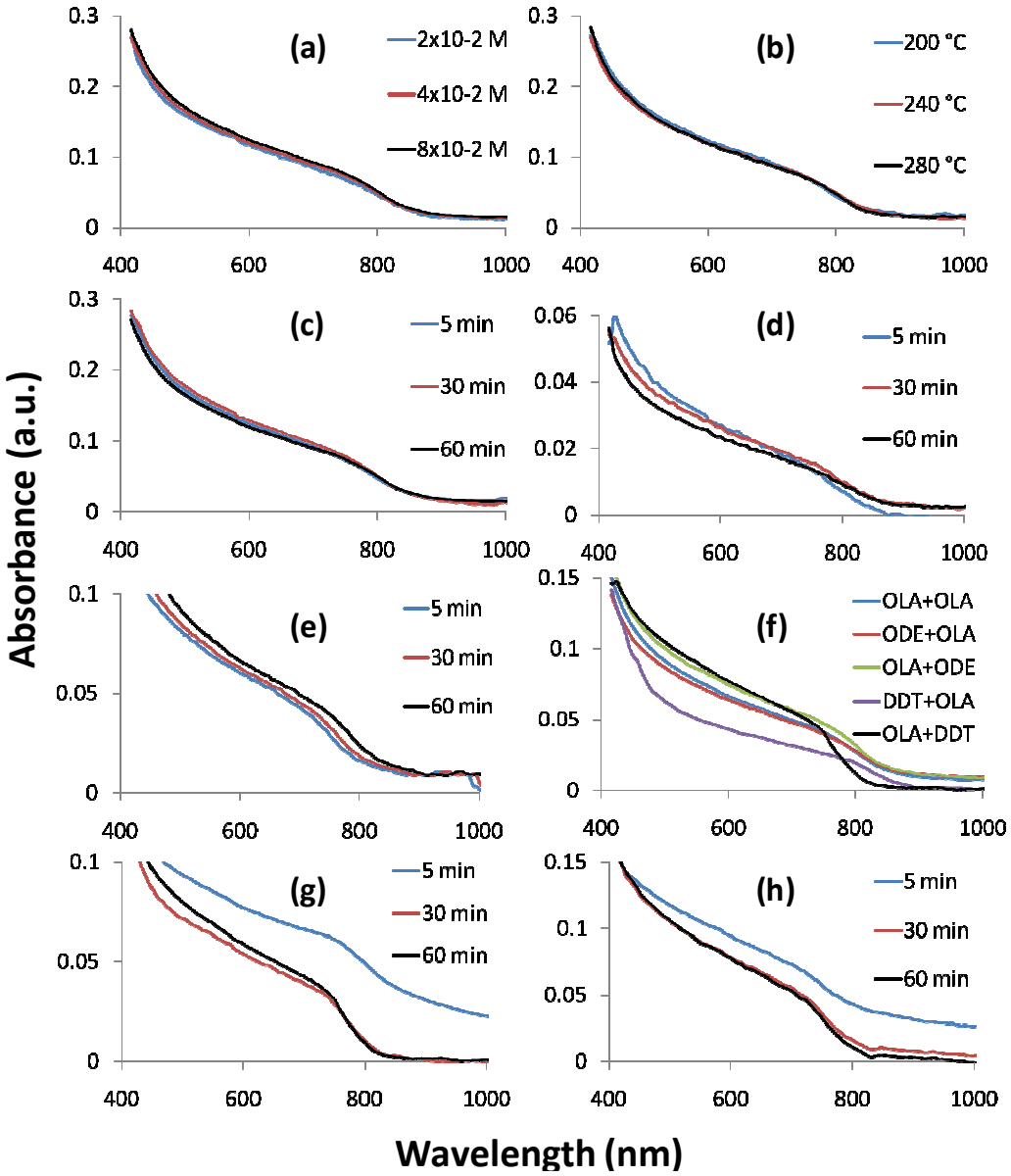

Fig. 3.25 UV-Vis spectra of (a) different precursors to OLA ratios (CIS**1**, CIS**2** & CIS**3**), (b) different growth temperature (CIS**2**, CIS**4** & CIS**5**), (c-e) CIS**2**, CIS**1** & CIS**4** analysed during the reaction at different time intervals to monitor the progress of reaction (f) different capping agents (CIS**2**, CIS**6**, CIS**7**, CIS**8** and CIS**9**), (g & h) CIS**9**, CIS**8** samples analysed at different time intervals during reaction.

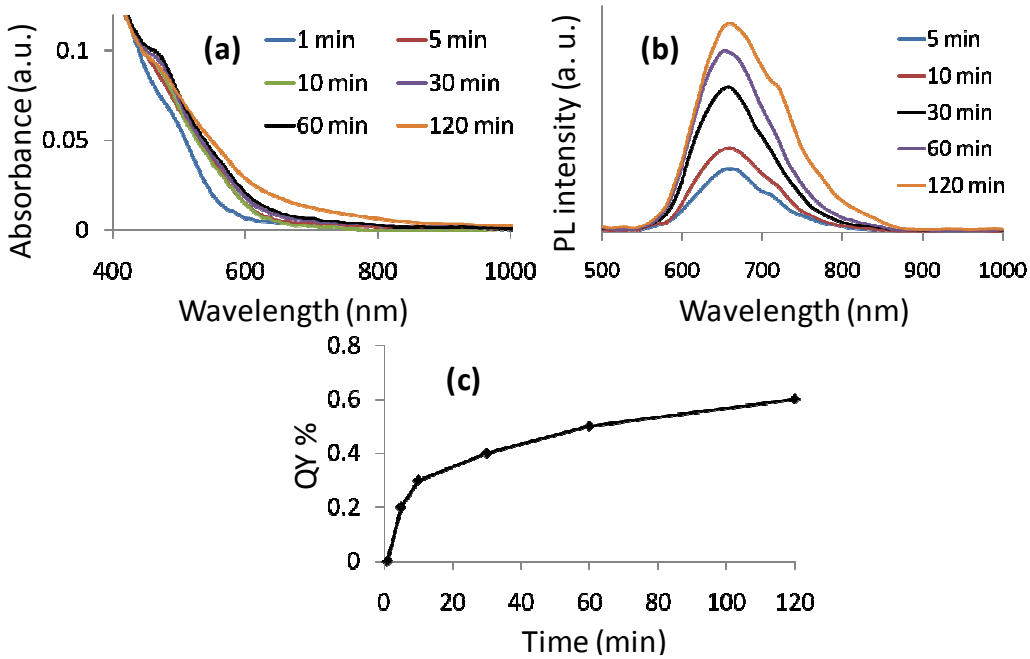

Fig. 3.26 (a) UV-Vis spectra, (b) PL spectra and (c) QY % of CIS**11** at different time intervals during the reaction.

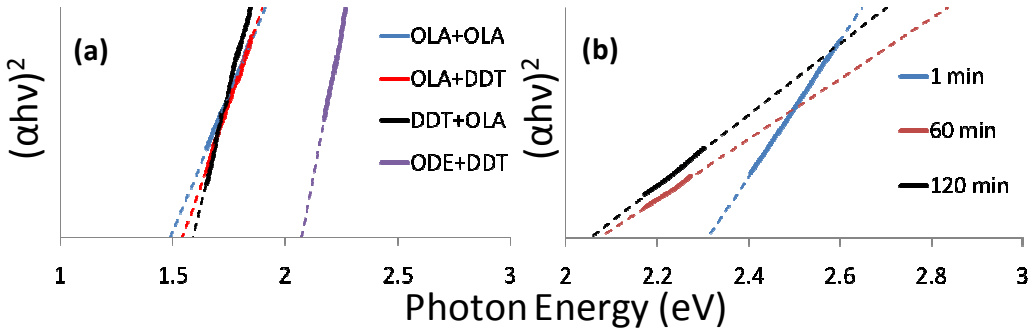

Fig. 3.27 Tauc's plot of (a) direct band gap of CIS**2**, CIS**9**, CIS**8** and CIS**11** and (b) direct band gap of CIS**11** at different time intervals during the reaction.

3.5 Conclusion

$Zn_xCd_{1-x}S$ nanoparticles were synthesised by the thermal decomposition of $[Zn(SON(CN^iPr_2)_2)_2]$ and $[Cd(SON(CN^iPr_2)_2)_2]$ in a hot capping agent. The phase of the obtained nanoparticles was cubic under all reaction conditions. The ratio of the Zn to Cd in the alloyed nanoparticles and hence the optical properties were highly dependent on the ratio of the ZnS to CdS precursor in the feed solution. The emission peak varied between 418 nm and 452, depending on the Zn to Cd ratio. The Zn-rich nanoparticles were ellipsoid, whereas the Cd-rich nanoparticles were more spherical. Using ODE produced spherical nanoparticles with a more intense emission

peak, whilst, DDT produced petal-like nanoparticles with a much lower emission. A mixture of $[Cu(SON(CN^{i}Pr_2)_2)_2]$ and $[In(SON(CN^{i}Pr_2)_2)_3]$ were used as precursors for the synthesis of $CuInS_2$ nanoparticles with different morphologies. The phase of the obtained nanoparticles depends on the reaction conditions. Chalcopyrite $CuInS_2$, wurtzite $CuInS_2$, or chalcopyrite with minor wurtzite phase could be obtained. Using a mixture of OLA and DDT was essential to obtain pure wurtzitic material. Polytypic nanoparticles with the wurtzite phase interfaced with significant chalcopyrite domains were also observed. There were no significant changes observed in band edges of the UV-Vis spectra based on the ratios of precursors to OLA, growth temperature or reaction time, however, noticeable changes were observed in the reactions when OLA was absent as a solvent or capping agent. Nanoparticles grown in the absence of OLA also showed significant luminescence.

3.6 References

1. P. K. Santra, R. Viswanatha, S. M. Daniels, N. L. Pickett, J. M. Smith, P. O'Brien, D. D. Sarma, *J. Am. Chem. Soc.* 2009, **131**, 470.
2. M. A. Malik, N. Revaprasadu, P. O'Brien, *Chem. Mater.* 2001, **13**, 913.
3. Mark Green, Paul O'Brien, *Chem. Commun.*, 1999, 2235.
4. C. B. Murray, D. J. Noms, M. G. Bawendi, *J. Am. Chem. Soc.* 1993, **115**, 8706.
5. B. O. Dabbousi, J. Rodriguez-Viejo, F. V. Mikulec, J. R. Heine, H. Mattoussi, R. Ober, K. F. Jensen, M. G. Bawendi, *J. Phys. Chem. B* 1997, **101**, 9463.
6. S. Coe, W. K. Woo, M. Bawendi, V. Bulovic, *Nature* 2002, **420**, 800.
7. A. N. Shipway, E. Katz, I. Willener, *ChemPhysChem,* 2000, **1**, 18.
8. J. Phillips, *J. Appl. Phys.*, 2002, **91**, 4590.
9. V. I. Klimov, A. A. Mikhailovsky, S. Xu, A. Malko, J. A. Hollingsworth, C. A. Leatherdale, H. J. Eisler, M. G. Bawendi, *Science* 2000, **314**, 290.
10. H. Pettersson, L. Baath, N. Carlsson, W. Seifert, L. Samuelson, *Appl. Phys. Lett.* 2001, **79**, 78.
11. M. R. Kim, S-Y. Park, D-J. Jang, *J. Phys. Chem. C,* 2010, **114**, 6452.
12. X. Zhong, Y. Feng, W. Knoll, M. Han, *J. Am. Chem. Soc.*, 2003, **125**, 13559.
13. M. D. Regulacio, M. Han, *Acc. Chem. Res.*, 2010, **43**, 621.
14. W. Li, D. Li, W. Zhang, Y. Hu, Y. He, X. Fu, *J. Phys. Chem. C,* 2010, **114**, 2154.
15. S. Biswas, S. Kar, S. Santra, Y. Jompol, M. Arif, S. I. Khondaker, *J. Phys. Chem. C,* 2009, **113**, 3617.
16. Y. C. Zhang, W. W. Chen, X. Y. Hu, *Cryst. Growth Des.*, 2007, **7**, 580.
17. W. Wang, W. Zhu, H. Xu, *J. Phys. Chem. C,* 2008, **112**, 16754.
18. J. Ouyang, C. I. Ratcliffe, D. Kingston, B. Wilkinson, J. Kuijper, X. Wu, J. A. Ripmeester, K. Yu., *J. Phys. Chem. C,* 2008, **112**, 4908.
19. M. W. DeGroot, K. M. Atkins, A. Borecki, H. Rösner, J. F. Corrigan, *J. Mater. Chem.*, 2008, **18**, 1123.
20. Y. Li, M. Ye, C. Yang, X. Li, Y. Li, *Adv. Funct. Mater.*, 2005, **15**, 433.
21. W. Wang, I. Germanenko, M. S. El-Shall, *Chem. Mater.*, 2002, **14**, 3028.
22. R. E. Bailey, S. Nie, *J. Am. Chem. Soc.*, 2003, **125**, 7100.

23. D. K. Smith, J. M. Luther, O. E. Semonin, A. J. Nozik, M. C. Beard, *ACS Nano,* 2011, **5**, 183.
24. X. Zhong, M. Han, Z. Dong, T. J. White, W. Knoll, *J. Am. Chem. Soc.,* 2003, **125**, 8589.
25. S. Wagner, P.M. Bridenbugh, *J. Cryst. Growth* 1977, **39**, 151.
26. R. S. Roth, H. S. Parker, W. S. Brower, *Mater. Res. Bull.* 1973, **8**, 333.
27. S. Cattarin, C. Pagura, L. Armelao, R. Bertoncello, N. Dietz, *J. Electrochem. Soc.* 1995, **142**, 2818.
28. J. AbuShama, S. Johnston, T. Moriarty, G. Teeter, K. Ramanathan, R. Noufi, *Prog. Photo*V*oltaics: Res. Appl.* 2004, **12**, 39.
29. M. G. Panthani, V. Akhavan, B. Goodfellow, J. P. Schmidtke, L. Dunn, A. Dodabalapur, P. F. Barbara, B. A. Korgel, *J. Am. Chem. Soc.* 2008, **130**, 16770.
30. I. Aksenov, K. Sato, *Jpn. J. Appl. Phys.* 1992, **31**, 2352.
31. J. L. Shay, B. Tell, H. M. Kasper, L. M. Schiavone, *Phys. Rev. B* 1972, **5**, 5003.
32. M. Uehara, K. Watanabe, Y. Tajiri, H. Nakamura, H. Maeda, *J. Chem. Phys.* 2008, **129,** 134709.
33. B. Tell, J. L. Shay, H. M. Kasper, *Phys. Rev. B* 1971, **4**, 2463
34. C. Guille´na, J. Herreroa, M. T. Gutie´rreza, F. Briones, *Thin Solid Films* 2005, **19**, 480.
35. R. P. Raffaelle, S. L. Castro, A. F. Hepp, S. G. Bailey, *Prog. PhotoVoltaics,* 2002, **10**, 433.
36. M. Nanu, J. Schoonman, A. Goossens, *Nano Lett.* 2005, **5**, 1716
37. R. Xie, M. Rutherford, X. Peng, *J. Am. Chem. Soc*. 2009, **131**, 5691.
38. L. Zheng, Y. Xu, Y. Song, C. Wu, M. Zhang, and Y. Xie, *Inorg. Chem*., 2009, **48**, 4003.
39. J. J. M. Binsma, L. J. Giling, J. Bloem, *J. Cryst. Growth* 1980, **50,** 429.
40. P. Bera, S. Seok, *J. Solid State Chem.,* 2010, **183**, 1872.
41. S. T. Connor, C.M. Hsu, B. D. Weil, S. Aloni, Y. Cui, *J. Am. Chem. Soc.,* 2009, **131**, 4962.
42. S.H. Choi, E.G. Kim, T. Hyeon, *J. Am. Chem. Soc*. 2006, **128**, 2520

43. H. Zhong, Y. Zhou, M. Ye, Y. He, J. Ye, C. He, C. Yang, Y. Li, *Chem. Mater*. 2008, **20**, 6434.
44. B. Koo, R. N. Patel, B. A. Korgel, *Chem. Mater*. 2009, **21**, 1962.
45. D. Pan, L. An, Z. Sun, W. Hou, Y. Yang, Z. Yang, Y. Lu, *J. Am. Chem. Soc.* 2008, **130**, 5620.
46. S. K. Batabyal, L. Tian, N. Venkatram, W. Ji, J. J. Vittal, *J. Phys. Chem. C* 2009, **113**, 15037.
47. S. L. Castro, S. G. Bailey, R. P. Raffaelle, K. K. Banger, A. F. Hepp *J. Phys. Chem. B* 2004, **108**, 12429.
48. K. Ramasamy, M. A. Malik, P. O'Brien, J. Raftery, *Dalton Trans.*, 2010, **39**, 1460.
49. L. Z. Végard, Phys., 1921, **5**, 17-26.
50. J. A. van Vechten, T. K. Bergstresser, Phys. Rev. B, 1970, **1**, 3351.
51. C. Burda, X. Chen, R. Narayanan, M. A. El-Sayed, *Chem. Rev*. 2005, **105**, 1025.
52. L. Li, T. J. Daou, I. Texier, T. T. K. Chi, N. Q. Liem, P. Reiss, *Chem. Mater*. 2009, **21**, 2422.

Chapter 4

Synthesis in Microfluidic Reactors

4.1 Summary

This chapter describes the synthesis of different nanoparticles in microreactors, a chip microreactor and/or microcapillary tubes. Bis(methylhexyldithiocarbamato)cadmium(II) [$Cd(S_2CNMe^nHex)_2$], bis(di-*iso*-propyldiselenophosphinato)cadmium(II) [$Cd(Se_2P(^iPr)_2)_2$] and 1,1,5,5-tetra-*iso*-propyl-4-thiobiuretocopper(II) [$Cu(SON(CN^iPr_2)_2)_2$] were used as single source precursors for CdS, CdSe and $Cu_{2-x}S$, respectively. CdSe/CdS core/shell and CdSeS alloys were investigated as well. The influence of the different reaction parameters (precursor concentration, growth temperature and residence time) on the size and the optical properties of the produced nanoparticles were studied. Oleylamine was used as a capping agent in all experiments. Transmission electron microscopy (TEM) showed that the CdS nanoparticles were in the range of 5.0 to 8.0 nm. The CdSe nanoparticles were ultra small (*ca.* 2 nm) with blue luminescence, whereas, the CdSe/CdS core/shell and the CdSeS alloys were bluish green or green luminescent depending on their size. The phase of the obtained copper sulfide nanoparticles, determined by powder X-Ray diffraction (p-XRD), was found to be monoclinic Cu_7S_4 or monoclinic Cu_7S_4 with minor impurities of rhombohedral Cu_9S_5 depending on the reaction conditions.

4.2 Introduction

Cadmium selenide (CdSe) nanoparticles have been extensively investigated because they are attractive materials for biological labelling[1,2] and solar energy conversion.[3,4] Furthermore, CdSe has a band gap that can be tuned across the visible spectrum. Blue emission (centred at 450 nm) is obtained from small CdSe nanoparticles (< 2 nm), whereas the red emission (centred at 650 nm) requires larger CdSe nanoparticles (> 5 nm). The change in the emission colour as a function of size is due to quantum confinement; the band gap increases as the size of the nanoparticles decrease.[5] The main factors determining the emission quality are: colour, colour purity, brightness and the stability of the emission.[6] The emission colour and the colour purity are not affected only by the nanoparticles size,[5] but also by their shape.[7] Early trials for the colloidal synthesis of CdSe nanoparticles involved the use of highly toxic, pyrophoric and expensive materials such as dimethylcadmium ($CdMe_2$) as a cadmium source.[8,9] Peng *et al.*[10] suggested that in the presence of stong ligands such as hexylphosphonic acid or tetradecylphosphonic acid, the $CdMe_2$ is converted into a Cd-phosphonic acid complex which is the key ingredient for the synthesis of high quality CdSe nanoparticles and not the $CdMe_2$ itself. Cadmium oxide (CdO),[6,10-13] cadmium chloride,[10,14] and cadmium carboxylate salts[15] have been shown to be good cadmium sources for the synthesis of monodispersed CdSe nanoparticles. Our group showed that when cadmium chloride or cadmium sulfate were used spherical particles were formed, whereas cadmium carbonate led to rod shaped CdSe particles.[16] The selenium precursors have been almost limited to phosphine complexes of selenium such as trioctylphosphine selenide (TOPSe). In terms of the photoluminescence (PL) and photostability of the CdSe nanoparticles; the phosphine complex is a good selenium precursor. However, like $CdMe_2$ it is toxic and expensive. 1-octadecene (ODE)[17] and olive oil18 were used as a selenium solvent instead of the phosphine. Although these solvents provide an opportunity to understand the role of the precursor in the nucleation and growth of the nanoparticles, a long heating process is required for the dissolution of the selenium. Recently, another phosphine-free route, in which elemental selenium is reduced by sodium borohydride in the presence of alkylamine forming alkylammonium selenide, has been reported by Ying *et al.*[19] An alternative route for the synthesis of CdSe nanoparticles, involved the use of single source precursors

(SSPs) such as diselenocarbamates[20-23] and imino-di-*iso*-propylphosphine selenide.[24] The cluster $[Cd_{10}Se_4(SPh)_{16}]^{4+}$ has also proved to be an efficient SSP for CdSe nanoparticles.[25] Primary amines were found to be a necessary component for achieving highly luminescent CdSe nanoparticles.[6] However, in most of the synthetic procedures alkylamine has been used as a co-surfactant. Later, Zhong *et al.*[13] reported the synthesis of high quality, red emitting CdSe nanoparticles using oleylamine (OLA) as a sole surfactant. The effect of surfactant or capping agent extends to the phase of the formed CdSe nanoparticles. The use of phosphonic acids with short alkyl chain stabilises the zinc blende phase whereas the wurtzite phase is stabilised by longer chains.[26]

In recent years, continuous flow synthesis in microreactors has emerged as a novel and potentially good route for nanoparticle systems. The main potential advantages of this method are the rapid and continuous screening of reaction parameters, efficient mixing of reagent providing a homogenous reaction environment, varying the composition of the reaction mixture by varying the injection rates, on line analysis, and continuous production. Synthesis of nanoparticles in a microreactor has been reported by different research groups. Alivisatos *et al.*[27] prepared CdSe nanoparticles *via* injecting a mixture of Se/$CdMe_2$/tributylphosphine (2:5:100 molar ratio), dodecylamine, trioctylphosphine (TOP) and ODE into a chip using a syringe pump. Maeda *et al.*[28,29] used cadmium acetate, stearic acid and trioctylphosphine oxide (TOPO) mixed with TOPSe to form a raw material that was loaded to a syringe connected to the capillary channels. CdSe nanoparticles were produced at temperatures from 230 to 300 °C with reaction times of 7 to 150 sec. CdSe nanoparticles were also prepared in microfluidic reactor by deMello *et al.*[30] using a mixture of cadmium acetate, TOPSe and TOPO. Bawendi *et al.*[31] avoided the use of $CdMe_2$ and TOPO in the synthesis of CdSe nanoparticles as $CdMe_2$ causes gas evolution and TOPO can decompose and block the reactor. Instead, they used cadmium hydroxide in a mixture of oleic acid, squalane and olyelamine as a Cd precursor and TOPSe. These precursors were injected in two separate flows using two syringe pumps. Mathies *et al.*[32] reported the synthesis of CdSe nanoparticles in a nanoliter–volume droplets in a microfabricated reactor to overcome the possibility of particles deposition on the channel walls, leading to clogging and unstable microreactor conditions. A gas-liquid segmented flow instead of the liquid-liquid

was investigated by Bawendi *et al.*[33] for the synthesis of CdSe nanoparticles in microreactors. Another method for enhancing the quality of CdSe nanoparticles in microreactors is the use of high pressure.[34] At high pressure and at the required temperature for nanoparticle synthesis, all precursors, ligands and solvents will remain liquid or become supercritical providing high miscibility and fast diffusion rates. In the continuing search for an optimal microreactor, a small tube furnace with distributed temperature zone was used to separate the nucleation and growth steps for the synthesis of more monodispersed CdSe nanoparticles.[35] Serpentine microchannel was also used for the synthesis of CdSe nanoparticles as they offer homogeneous residence time and monomer concentration under fast flow rates.[36] Recently, a combinatorial synthesis system composed of several microreactors and an online detector was reported for the rapid synthesis of CdSe nanoparticles.[37]

Cadmium sulfide (CdS) nanoparticles were also synthesised using the continuous flow method. In 1992, Fischer *et al.*[38] introduced a fast flow technique in which two solutions containing Cd^{2+} and SH^- ions were mixed forming 1.3 nm CdS nanoparticles. deMello *et al.*[39] reported the synthesis of CdS nanoparticles *via* microfludic routes using aqueous solutions of cadmium nitrate and sodium sulfide mixed with an equal amount of sodium polyphosphate. In a different process, CdS nanoparticles with different sizes were produced at a constant temperature and residence time by varying the feed ratio of the cadmium (CdO in oleic acid, OLA and ODE) and sulfur (S in OLA and ODE) precursors.[40]

Surface passivation is critical for the PL and quantum yield (QY) of the nanoparticles.[41] Methods for coating a semiconductor nanoparticle with another semiconductor forming a core/shell material are well developed and different core/shell structures have been reported both in conventional batch method and continuous flow method. CdSe/ZnSe,[12] CdSe/CdS,[42-44] CdSe/ZnS,[25,45] CdS/CdSe[46] and CdS/ZnS,[47] are some examples of core/shell nanoparticles prepared using the batch method. In the continuous flow synthesis, CdSe/ZnS core/shell is the most explored material. Maeda *et al.*[48] prepared CdSe/ZnS core/shell nanoparticles in a multi-step continuous system composed of a CdSe synthesis section, followed by mixing of bis(diethyldithiocarbamato)zinc(II)) $[Zn(S_2CNEt_2)_2]$ as a shelling material. QYs greater than 50% are reported for the CdSe/ZnS nanoparticles.[49] Separate injection of equal volumes of CdSe nanoparticles and $[Zn(S_2CNEt_2)_2]$ into

polytetrafluoroethylene microcapillary tubes produced green luminescent CdSe/ZnS core/shell nanoparticles.[50] Recently, full colour emitting CdS/ZnS and CdSe/ZnS core/shell nanoparticles were prepared in a microreactor using mixtures of CdO in oleic acid, OLA and ODE, elemental sulfur in OLA and ODE, elemental selenium in TOP, OLA and ODE as the cadmium, sulfur and selenium precursors, respectively, and finally $[Zn(S_2CNEt_2)_2]$ in TOP, OLA and ODE as the raw material for the ZnS shell.[40]

Another heterogeneous nanostructure is the alloyed CdSeS nanoparticles. Controlling the composition of the different elements in the alloy provides a good means of tuning the band gap of the nanoparticles. A general route for the synthesis of the CdSeS nanoparticles is the injection of a mixture of the selenium and sulfur precursors into a hot high boiling coordinating solvent containing the cadmium precursor.[51,52] $CdSe_xS_y$ were synthesised by Al-Salim *et al.*[53] in different organic solvents with different coordinating properties. Yu *et al.*[54] reported the synthesis of homogenously alloyed CdSeS nanoparticles *via* a noninjection one-pot method.

Copper sulfides nanoparticles are useful for solar energy conversion applications as well.[55,56] Various methods have been used for the synthesis of copper sulfide nanostructures including: hydrothermal,[57] solvothermal,[58] solventless thermolysis[59] and thermal decomposition of precursor(s) in a hot coordinating solvent(s).[60-69] Alkylxanthates,[64] mercaptobenzothiazole,[65] thiobenzoates,[66] dithiocarbamates[67,68] and dithiolates[69] are examples of the SSPs used for the synthesis of $Cu_{2-x}S$ nanoparticles in the conventional batch method.

To the best of our knowledge there are no reports on the use of single source precursors for the synthesis of CdSe, CdS, CdSe/CdS core/shell, CdSeS alloys or $Cu_{2-x}S$ nanoparticles in microreactors. In this chapter, $[Cd(S_2CNMe^nHex)_2]$, $[Cd(Se_2P(^iPr)_2)_2]$and $[Cu(SON(CN^iPr_2)_2)_2]$ were used as single source precursors for CdS, CdSe and $Cu_{2-x}S$, respectively. The synthesis of these materials was carried out in a chip and/or microcapillary reactor. OLA was chosen as a capping agent because of its good ability, as a primary amine, of achieving high photoluminecense.[6,13] Furthermore, OLA has low melting point, *i.e.* liquid at room temperature, which lowers the probability of the microreactor channels getting clogged. CdS is considered to be a good shelling material for CdSe; it has a larger band gap compared to that of CdSe and the lattice mismatch between CdSe (core) and CdS (shell) is only 3.9%.[9]

4.3 Experimental

4.3.1 Experimental setup

4.3.1.1 Chip microreactor

The chip was formed of reaction microchannel with approximate dimensions of 330 µm width, 160 µm depth and 40 cm length in a glass microfluidic reactor (Fig. 4.1 & 4.2). A hot plate connected to a temperature controller thermocouple was used as a heating source. The reaction solution was loaded to a gastight syringe that was connected to a pump (PHD 2000 Infusion) in order to inject the solution through the chip. The chip had two inlets and as only one was needed the other inlet was sealed with rubber tubing.

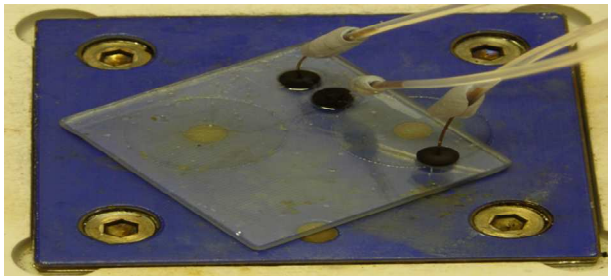

Fig. 4.1 Picture of the chip microreactor.

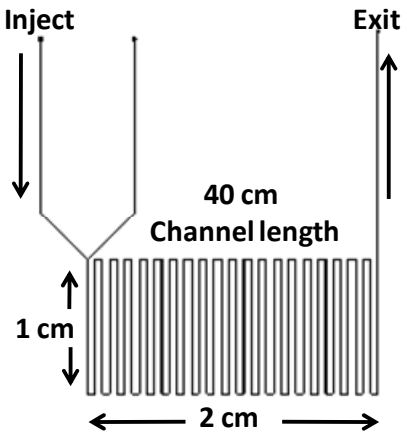

Fig. 4.2 Schematic of the microchannel in the chip.

4.3.1.2 Fused silica microcapillary

Fused silica microcapillary tube of an inner diameter of 150 µm and outer diameter of 360 µm was used as a microreactor (Fig. 4.3). 40 cm of the microcapillary was

immersed in an oil bath for heating purpose. The reaction solution was loaded to a gastight syringe that was connected to a pump (PHD 2000 Infusion) in order to inject the solution through the capillary tube, as shown in Fig. 4.4.

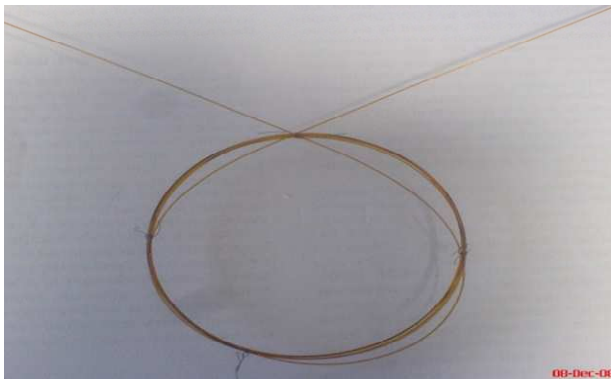

Fig. 4.3 Picture of the microcapillary.

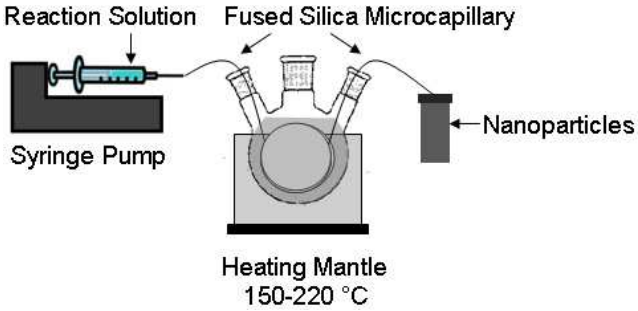

Fig. 4.4 Illustration of experimental setup using the microcapillary reactor.

4.3.2 Cadmium selenide

4.3.2.1 Synthesis of dialkyldiselenophosphinate precursors: $[Cd(Se_2P^iPr_2)_2]$, $[Cd(Se_2P^tBu_2)_2]$ and $[(Cd(Se_2PPh_2)_2)_2]$

4.3.2.1.1 Synthesis of $(HNEt_3)(^iPr_2PSe_2)$ (1)

As described in literature (equation 4.1),[70] $^iPr_2PCl$ (4.8 mL, 30 mmol) and $HSiEt_3$ (9.6 mL, 60 mmol) were dissolved in 150 mL cold dry toluene under nitrogen followed by NEt_3 (8.3 mL, 60 mmol). The mixture was stirred at room temperature for 6 hours forming a white cloudy precipitate. Grey Se powder (4.7g, 60 mmol) was added to the solution and refluxed for 20 hours, leading to a dark red solution and white precipitate. The white precipitate was filtered off. The resulting solution was reduced to ~ 50 mL and kept at 0 °C to produce yellow crystals. The crystals were filtered and washed with cold hexane.

$$^{i}Pr_2PCl + 2HSiEt_3 + 2NEt_3 \xrightarrow{Se/Toluene} (^{i}Pr_2PSe_2)(HNEt_3) + HNEt_3Cl + Si_2Et_6 \quad (4.1)$$

4.3.2.1.2 Synthesis of $(HNEt_3)(^{t}Bu_2PSe_2)$ (2)

Compound (2) was prepared in a similar way to (**1**) but using $^{t}Bu_2PCl$ (5.7 mL, 30 mmol) and obtained yellow crystals.[70]

4.3.2.1.3 Synthesis of $(HNEt_3)(Ph_2PSe_2)$ (3)

Compound (3) was prepared in a similar way to (**1**) but using Ph_2PCl (5.9 mL, 30 mmol) and obtained yellow crystals.[70]

4.3.2.1.4 Synthesis of $[Cd(Se_2P^{i}Pr_2)_2]$ (4)

Solution of $CdCl_2$ (0.915g, 5 mmol) in 5 ml H_2O was added dropwise to solution of $(HNEt_3)(^{i}Pr_2PSe_2)$ (3.77g, 10 mmol) in 100 ml of MeOH. The mixture was stirred for 1 hour at room temperature under atmospheric pressure forming yellow precipitate, which was filtered, washed with hot MeOH and re-crystallized in dichloromethane to obtain yellow crystals of $[Cd(^{i}Pr_2PSe_2)_2]$.[70]

4.3.2.1.5 Synthesis of $[Cd(Se_2P^{t}Bu_2)_2]$ (5)

Compound (5) was prepared in a similar way to (**4**) but using $(HNEt_3)(^{t}Bu_2PSe_2)$ (4.05 g, 10 mmol), and obtained colourless crystals of $[Cd(^{t}Bu_2PSe_2)_2]$.[70]

4.3.2.1.6 Synthesis of $[(Cd(Se_2PPh_2)_2)_2]$ (6)

Compound (6) was prepared in a similar way to (**4**) but using $(HNEt_3)(Ph_2PSe_2)$ (4.45 g, 10 mmol), obtained colourless crystals of $[Cd(Ph_2PSe_2)_2]$.[70]

4.3.2.2 Synthesis of cadmium selenide nanoparticles in chip microreactor

4.3.2.2.1 Effect of concentration

A series of different concentrations were prepared by dissolving $[Cd(Se_2P^{i}Pr_2)_2]$ in 2 mL TOP. The concentrations were as follow 2.27 mM, 7.55 mM and 15.1 mM. Then 8 mL of OLA were added to each solution. The mixtures were loaded into syringe, and injected into the microreactor, separately. The microreactor was pre-heated at 180 °C and the residence time was kept constant at 12.8 sec using a flow rate of 80 µL/min.

4.3.2.2.2 Effect of temperature

Three different temperatures were studied; 160 °C, 180 °C and 200 °C. The concentration of $[Cd(Se_2P^iPr_2)_2]$ used in this study was 2.27 mM and the flow rate was 80 µL/min, (residence time = 12.8 sec).

4.3.2.2.3 Effect of residence time

In order to study the effect of the residence time *i.e.* flow rate, the concentration of $[Cd(Se_2P^iPr_2)_2]$ and the temperature were kept constant at 2.27 mM and 180 °C, respectively. Residence times were studied between 6.8 sec and 20.5 sec.

4.3.2.3 Synthesis of cadmium selenide nanoparticles in microcapillary reactor

4.3.2.3.1 Effect of concentration

A series of different concentrations were prepared by dissolving $[Cd(Se_2P^iPr_2)_2]$ in 2 mL TOP. The concentrations were as follow 5×10^{-3} M, 1×10^{-2} M and 2×10^{-2} M. Then 8 mL of oleyamine were added to each solution. The mixtures were loaded into a syringe, and injected into the fused silica microcapillary tube. The microcapillary tube was pre-heated at 200 °C and the residence time was kept constant at 8.4 sec using a flow rate of 50 µL/min.

4.3.2.3.2 Effect of temperature

Three different temperatures were studied; 180 °C, 200 °C and 220 °C. The concentration of $[Cd(Se_2P^iPr_2)_2]$ used in this study is the 2×10^{-2} M and the flow rate was 50 µL/min, (residence time = 8.4 sec).

4.3.2.3.3 Effect of residence time

In order to study the effect of the residence time, the concentration of $[Cd(Se_2P^iPr_2)_2]$and the temperature were kept constant at 2×10^{-2} M and 200 °C, respectively. Residence times were studied between 4.2 sec and 16.8 sec.

4.3.2.4 Other cadmium selenide precursors

2×10^{-2} M solutions of $[Cd(Se_2P^tBu_2)_2]$ and $[(Cd(Se_2PPh_2)_2)_2]$ were prepared by dissolving 29 mg and 64 mg in TOP (2 mL), respectively. This was then followed by adding OLA (8 mL) to each solution. These solutions were injected into the

microcapillary tube individually, at 200 °C under a flow rate of 50 µL/min, (residence time = 8.4 sec).

4.3.3 Cadmium sulfide

4.3.3.1 Synthesis of precursor: [$Cd(S_2CNMe^nHex)_2$]

As described in literature,[23] a mixture of NaOH (3 g, 75 mmol) and *N*-Hexylmethylamine (11.37 ml, 75 mmol) in methanol (100 ml) was stirred in the ice bath and then CS_2 (4.58 ml, 75 mmol) was slowly added into the reaction mixture and further stirred for 30 min. The aqueous solution of $CdCl_2$ (6.5 g, 37.5 mmol) was added dropwise into the reaction mixture and further stirred for 20 min at room temperature. The white precipitate was recrystallized from chloroform or toluene at room temperature to give [$Cd(S_2CNMe^nHex)_2$].

4.3.3.2 Synthesis of CdS nanoparticles

4.3.3.2.1 Effect of concentration

Three different concentrations were prepared; 0.5 mM, 1.0 mM and 2.0 mM by adding [$Cd(S_2CNMe^nHex)_2$] (2.5 mg, 5×10^{-3} mmol), (5 mg, 1×10^{-2} mmol) and (10 mg, 2×10^{-2} mmol) into OLA (10 mL), respectively. The mixtures were loaded into a syringe and injected into the fused silica microcapillary tube. The microcapillary tube was pre-heated at 200 °C and the residence time was kept constant at 8.4 sec using a flow rate of 50 µL/min.

4.3.3.2.2 Effect of temperature

Three different temperatures were studied; 160 °C, 180 °C and 200 °C. The concentration used in this study is the 2.0 mM and the flow rate was 50 µL/min, (residence time = 8.4 sec).

4.3.3.2.3 Effect of residence time

In order to study the effect of the residence time *i.e.* flow rate, the concentration of the precursor and the temperature were kept constant at 2.0 mM and 200 °C respectively. Residence times were studied between 4.2 and 16.8 sec.

4.3.4 CdSe/CdS core/shell nanoparticles

4.3.4.1 Effect of amount of shelling material

The core CdSe nanoparticles were prepared as mentioned earlier, using a concentration of 2×10^{-2} M of $[Cd(Se_2P^iPr_2)_2]$, at a temperature of 200 °C and under a flow rate of 50 µL/min. Three different solutions were prepared by mixing $[Cd(S_2CNMe^nHex)_2]$ (1 mg, 2×10^{-3} mmol), (2.5 mg, 5×10^{-3} mmol) and (5 mg, 1×10^{-2} mmol) in OLA (2 mL) each with 4 mL of the as-obtained CdSe nanoparticles solution. The mixed solutions were injected into the microcapillary tube, individually, at 200 °C and under a flow rate of 50 µL/min; *i.e.* residence time of 8.4 sec. A control reaction was carried out by re-injecting the as-obtained CdSe nanoparticles into the microcapillary reactor under the exact same conditions without adding any CdS precursor.

4.3.4.2 Effect of shelling residence time

The shelling of the CdSe nanoparticles with CdS layer was carried out at different residence times by varying the flow rate. The flow rate was varied from 50 to 100 µL/min; resulting in a residence time from 8.4 to 4.2 sec. All reactions were done by mixing $[Cd(S_2CNMe^nHex)_2]$ (5 mg, 1×10^{-2} mmol) in OLA (2 mL) with 4 mL of the crude CdSe nanoparticles and injecting the mixture into the microcapillary at 200 °C.

4.3.4.3 Effect of shelling temperature

$[Cd(S_2CNMe^nHex)_2]$ (5 mg, 1×10^{-2} mmol) in OLA (2 mL) were mixed with 4 mL of the crude CdSe nanoparticles and injected into the microcapillary which was pre-heated at 160, 180 or 200 °C under a constant flow rate of 50 µL/min, (residence time = 8.4 sec).

4.3.5 Alloy CdSeS nanoparticles

Three different solutions were prepared by adding three different amounts of $[Cd(S_2CNMe^nHex)_2]$ (5×10^{-3} mmol, 2×10^{-2} mmol and 4×10^{-2} mmol) to a fixed concentration of $[Cd(Se_2P^iPr_2)_2]$ (2×10^{-2} M) in TOP (2 mL). Then 8 mL of OLA were added to each solution. The solutions were loaded into the syringe and injected into the microcapillary reactor at a flow rate between 12.5 µL/min and 100 µL/min, (residence time between 33.6 sec and 4.2 sec, respectively).

4.3.6 Copper sulfide

4.3.6.1 Synthesis of precursor [Cu(SON(CN^{i}Pr$_2$)$_2$)$_2$]

As described in literature,[71] a solution of di-*iso*-propylcarbamoyl chloride (1.0 g, 6 mmol) and sodium thiocyanate (0.49 g, 6 mmol) in acetonitrile (25 mL) was heated to reflux with continuous stirring for 1 h, during which time a fine precipitate of sodium chloride formed. To the cooled reaction mixture was added di-*iso*-propylamine (1.49 mL, 12 mmol) followed by stirring for 30 min and addition of copper(II) nitrate (0.76 g, 3 mmol). The crude product was isolated as green powder and recrystallized from tetrahydrofuran.

4.3.6.2 Synthesis of nanoparticles

4.3.6.2.1 Effect of residence time

1×10^{-2} M solutions of [Cu(SON(CN^{i}Pr$_2$)$_2$)$_2$] in OLA (7.5 mL) was injected into the microcapillary tube. Reaction temperature was kept at 200 °C and the residence time was studied at 2.8 sec, 4.2 sec and 8.4 sec by adjusting the flow rate at 150 µL/min, 100 µL/min and 50 µL/min, respectively.

4.3.6.2.2 Effect of temperature

The same concentration of the precursor 1×10^{-2} M was injected into the microcapillary at a flow rate of 100 µL/min at three different temperatures (170 °C, 200 °C and 230 °C).

4.4 Results and discussion

4.4.1 Cadmium selenide nanoparticles

4.4.1.1 Chip microreactor

Optical absorption is used as it is well known that the absorption spectrum can give a rough idea about the size and the dispersity of nanoparticles. A blue shift and sharper band edge indicates smaller and more monodispersed nanoparticles. The UV-Vis and PL spectra of the OLA capped CdSe nanoparticles prepared at various concentrations, temperatures and residence times are shown in Fig. 4.5-4.7, respectively. Increasing the concentration of [Cd(Se$_2$P^{i}Pr$_2$)$_2$] was accompanied with

a red shift in the UV-Vis spectra, indicating larger particles are formed. Moreover, increasing the concentration of the precursor led to narrower size distribution where at the highest concentration of the precursor (15.1 mM), the absorption spectra became sharper and showed different electronic transition states. The emission peak at 406 nm, obtained from the CdSe nanoparticles prepared using a concentration of 15.1 mM, shows a narrower size distribution and higher emission compared to the lower concentrations. Changing the reaction temperature or the flow rate at a concentration of 2.27 mM of the precursor had almost no effect on the CdSe nanoparticles.

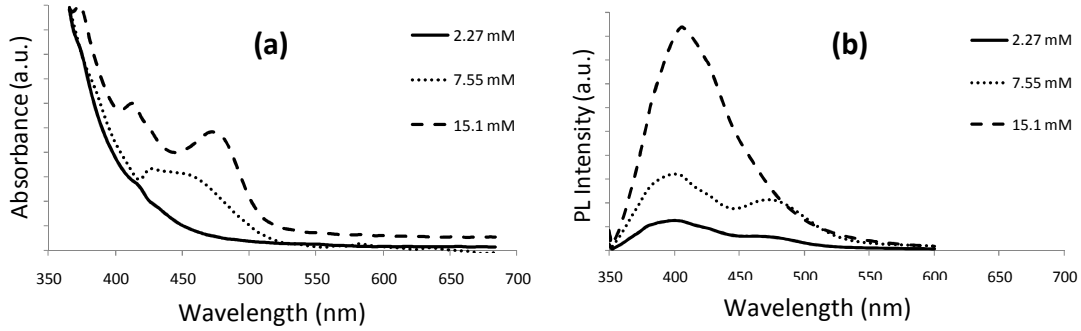

Fig. 4.5 UV-Vis spectra (a) and PL spectra (b) of CdSe nanoparticles prepared at different concentrations.

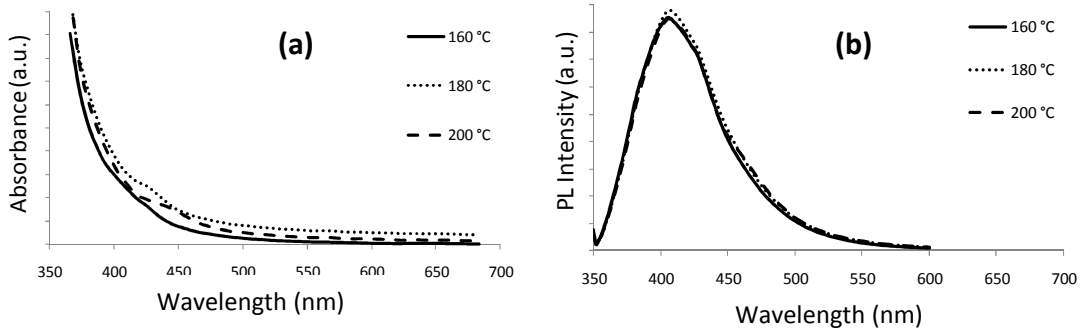

Fig. 4.6 UV-Vis spectra (a) and PL spectra (b) of CdSe nanoparticles prepared at different temperatures.

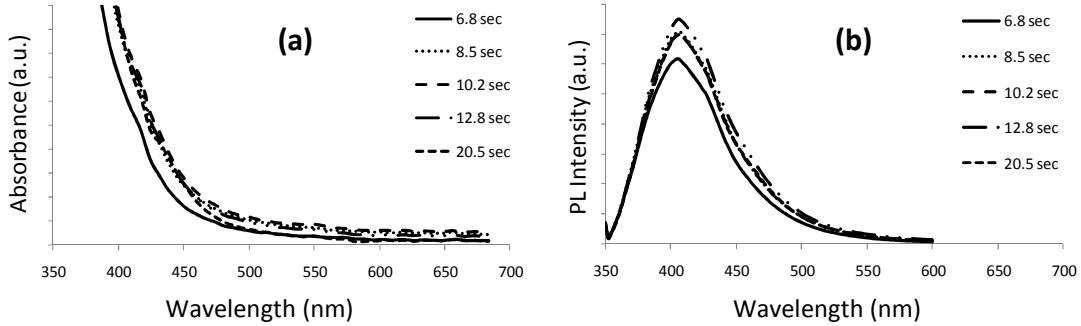

Fig. 4.7 UV-Vis spectra (a) and PL spectra (b) of CdSe nanoparticles prepared at different residence times.

4.4.1.2 Microcapillary reactor

A slight blue shift in both the absorption and the emission spectra was observed on increasing the concentration of the precursor (Fig. 4.8). Increasing the temperature of the oil bath from 180 °C to 200 °C did not cause any significant shift in the band edge of the absorption spectra, whereas at a temperature of 220 °C a large red shift was observed due to the increase in the particles size (Fig. 4.9). The multi-resolved electronic transitions shown in the absorption spectrum of the CdSe nanoparticles grown at 220 °C, indicates a narrow size distribution. An increase in the emission intensity along with a red shift from 464 nm to 470 nm to 480 nm were observed with the increase in temperature from 180 °C to 200 °C to 220 °C. Allowing the particles to spend longer time in the microcapillary, by reducing the flow rate, should permit the particles to grow bigger. A red shift in both absorption and emission spectra was observed only when the flow rate was reduced to 25 µL/min (Fig. 4.10). The observed red shift in the emission spectra was accompanied with an increase in the emission intensity. Calculating the size of the obtained CdSe nanoparticles from their absorption spectra[72] revealed that they are slightly less than 2 nm (1.79 nm to 1.92 nm) except for the samples prepared at the highest temperature (220 °C) or the lowest flow rate (25 µL/min) which were 2.03 nm and 2.1 nm, respectively. The band gaps of these CdSe nanoparticles varied between 2.51 eV (494 nm) to 2.73 eV (454 nm) based on their Tauc plots (Fig. 4.11). An increase between 0.76 eV and 0.98 eV is observed for these blue emitting CdSe nanoparticles when compared to the band gap of the bulk CdSe (1.75 eV). This increase in the band gap is due to the expected quantum confinement effect where the band gap increases as the particle size decreases. The QY ranges from 0.5% to 7% which is similar to the QY obtained

in the batch synthesis. In general, higher concentration, higher temperature or longer residence time produced higher QYs.

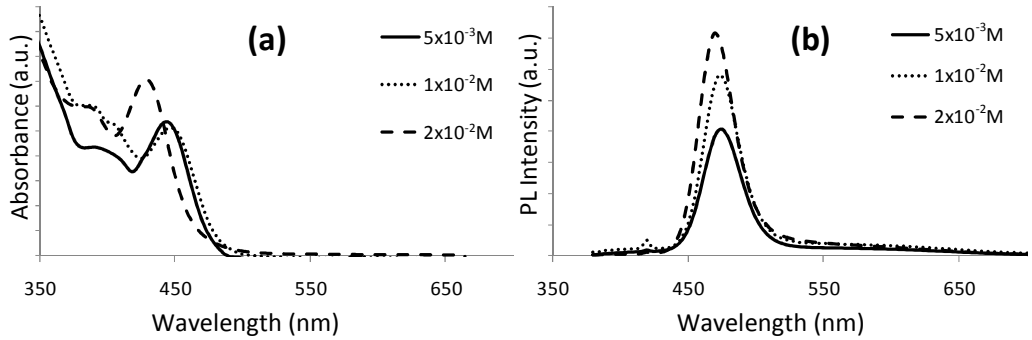

Fig. 4.8 UV-Vis spectra (a) and PL spectra (b) of CdSe nanoparticles prepared at different concentrations.

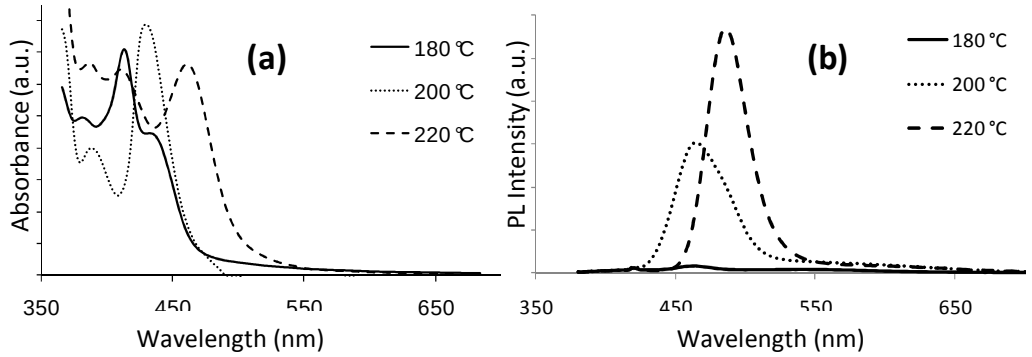

Fig. 4.9 UV-Vis spectra (a) and PL spectra (b) of CdSe nanoparticles prepared at different temperatures.

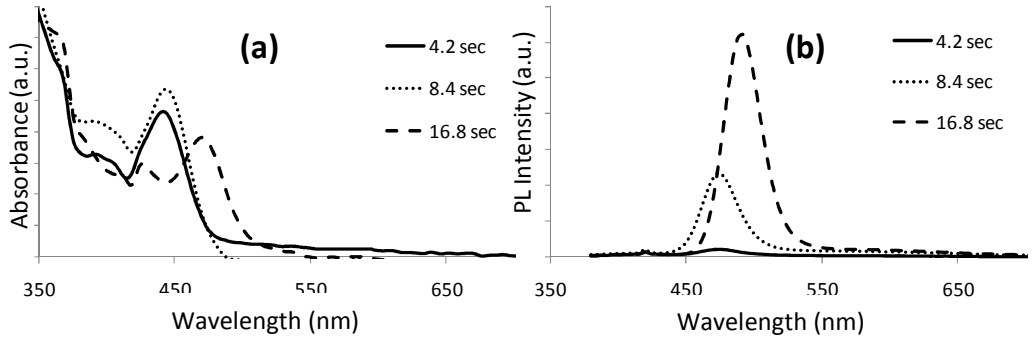

Fig. 4.10 UV-Vis spectra (a) and PL spectra (b) of CdSe nanoparticles prepared at different residence times.

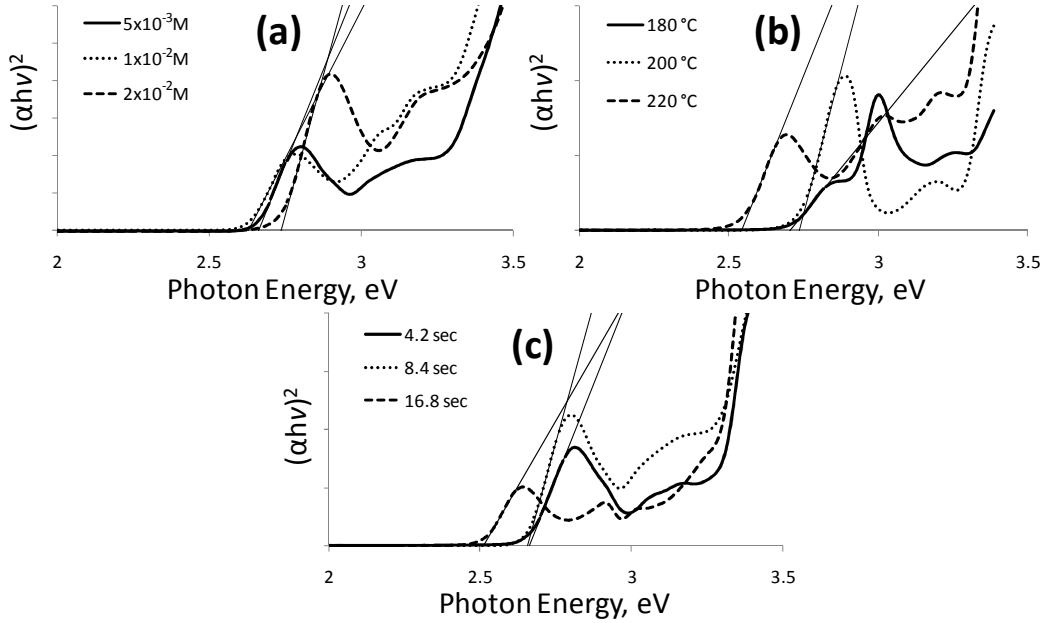

Fig. 4.11 Tauc plots of the CdSe nanoparticles synthesised at different concentration (a), different temperatures (b) and different residence times (c).

4.4.1.2.1 Other cadmium selenide precursors

Replacing the *iso*-propyl substituent with a phenyl substituent in the diselenophosphinate precursor resulted in a red shift in the absorption and the emission spectra, broader absorption spectra, lower and wider PL peak as shown in Fig. 4.12. Using tert-butyl had the same effect of the phenyl but to a larger extent. It has been previously reported that changing the alkyl substituents in the single source precursor affects the properties of the produced nanoparticles. The influence of the alkyl substituents in bis(dialkyldiselenocarbamato)cadmium(II) precursors has been studied by O'Brien *et al.*[73] They found that the thermal decomposition of symmetrical alkyl groups such as $[Cd(Se_2CNEt_2)_2]_2$ gave some elemental selenium as solid phase,[21] whereas, the unsymmetrical alkyl groups such as $[Cd(Se_2CNMe^nHex)_2]$, produced CdSe nanoparticles of good quality.[22,23] Moreover, the unsymmetrical dithiocarbamates of cadmium and bismuth with alkyl groups longer than 6 carbon atoms such as $[Cd\{S_2CNMe(C_{18}H_{37})\}_2]$ and $[Bi\{S_2CNMe(C_{18}H_{37})\}_3]$ produced CdS and Bi_2S_3 nanoparticles, respectively, with the alkyl group acting as the capping agent.[74,75]

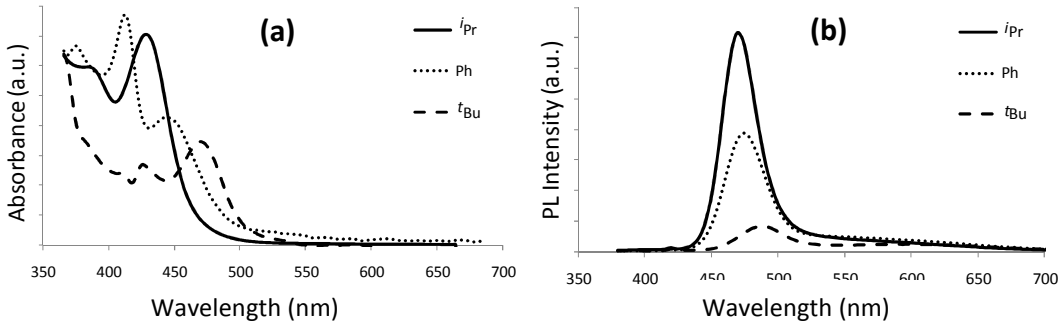

Fig. 4.12 UV-Vis spectra (a) and PL spectra (b) of CdSe nanoparticles prepared from *iso*-propyl, *tert*-butyl and phenyl substituent.

4.4.2 CdS nanoparticles

4.4.2.1 Optical properties

The UV-Vis spectra and the Tauc plots of OLA capped CdS nanoparticles prepared at various concentrations, temperatures and residence times are shown in Fig. 4.13, 4.14 and 4.15, respectively. A red shift was accompanied with the increase in the concentration, temperature or the residence time, indicating the formation of particles of larger size. The direct band gaps of these CdS nanoparticles ranges from 2.47 eV (502 nm) to 2.57 eV (482 nm) as calculated from their Tauc plot. Compared to the band gap of the bulk CdS (2.42 eV) there is a slight blue shift between 0.05 eV and 0.15 eV.

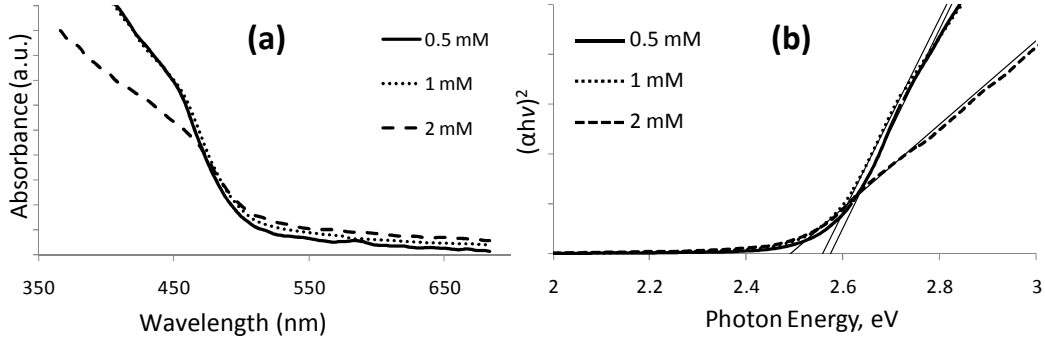

Fig. 4.13 UV-Vis spectra of CdS nanoparticles at different concentrations (a) and their corresponding Tauc plots (b).

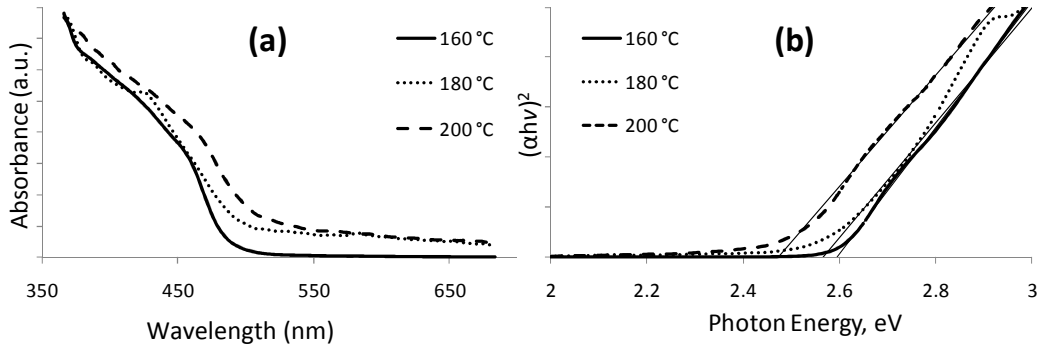

Fig. 4.14 UV-Vis spectra of CdS nanoparticles at different tempretures (a) and their corresponding Tauc plots (b).

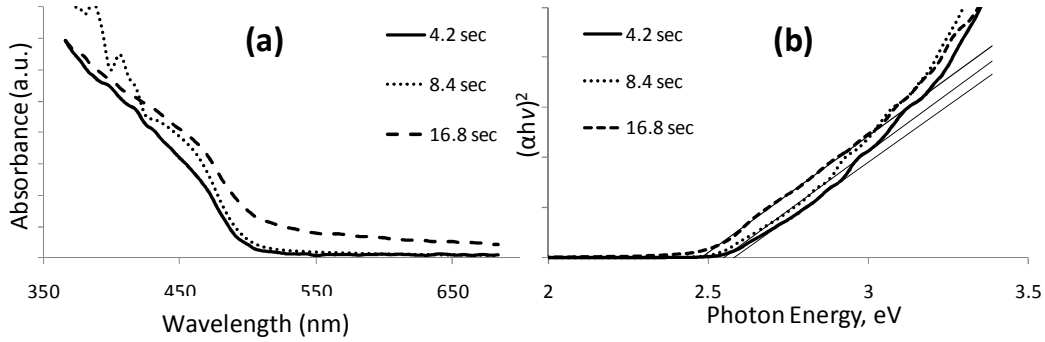

Fig. 4.15 UV-Vis spectra of CdS nanoparticles at different residence time (a) and their corresponding Tauc plots (b).

4.4.2.2 Transmission electron microscopy (TEM)

The TEM images of the CdS nanoparticles prepared from different concentrations (Fig. 4.16) shows well-defined, nearly monodispersed, and spherical CdS nanoparticles. Using the lowest concentration of the CdS precursor (0.5 mM) produced aggregated spherical nanoparticles with an average diameter of 5.8 ± 1.5 nm. Increasing the concentration of the precursor to 1.0 mM resulted in more monodispersed and larger (7.4 ± 0.9 nm) CdS nanoparticles. The size and the monodispersity of the CdS nanoparticles did not change with a further increase in the concentration of the precursor (2.0 mM).

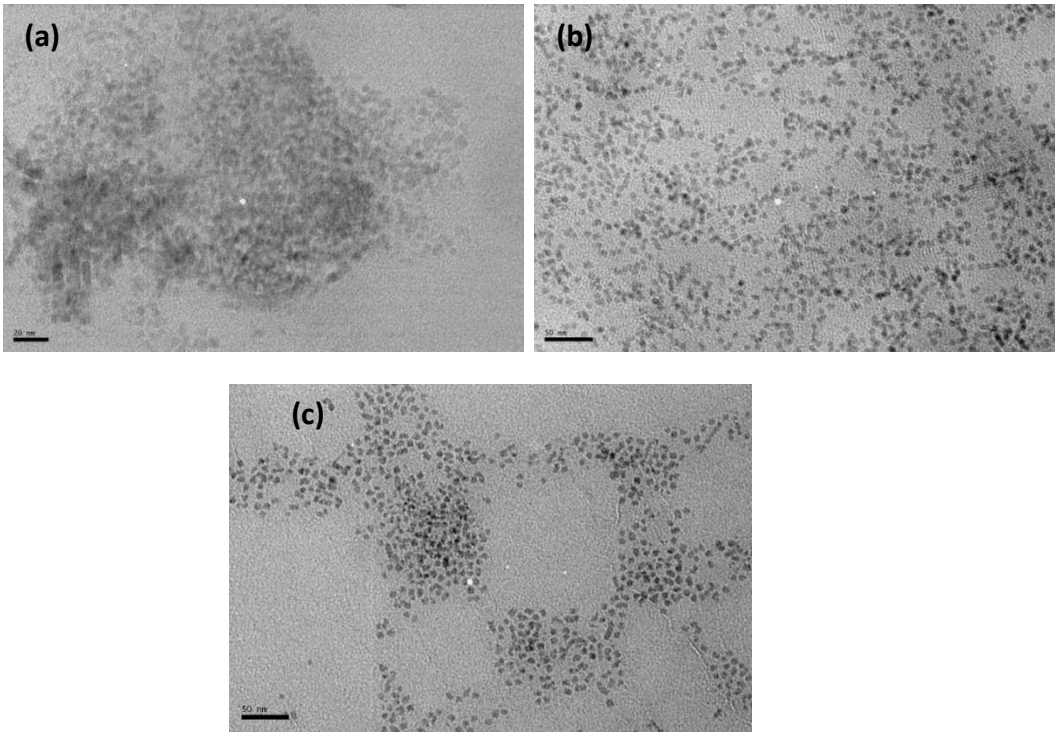

Fig. 4.16 TEM image of CdS nanoparticles prepared from different precursor concentrations: (a) 0.5 mM, (b) 1.0 mM and (c) 2.0 mM. All scale bars are 50 nm.

4.4.3 CdSe/CdS core/shell nanoparticles

As mentioned before, CdS was chosen as a shelling material because it has a larger band gap than CdSe and because the lattice mismatch between CdSe and CdS is only 3.9%.[9] [$Cd(S_2CNMe^nHex)_2$] has previously been demonstrated to be a good precursor for the CdS shell.[43]

4.4.3.1 Optical properties

Fig. 4.17 (a) shows the absorption spectra of the core CdSe and the CdSe/CdS core/shell. A clear difference in the absorption band edge is observed. The core/shell nanoparticles show a red shift of ~ 45 nm (538 nm, 2.30 eV) as compared to the CdSe band edge (492 nm, 2.52 eV) as expected due to their larger size. Fig. 4.16 (b) shows the large difference in the PL intensity of the core and the core/shell as well as a red shift of (52 nm) for the core/shell nanoparticles. The increased QY of the core/shell nanoparticles can be attributed to the elimination of the surface defects/traps and the confinement of the photogenerated exciton in the core due to shelling which is obvious from its symmetrical PL peak. The QY increased from 7% for the core CdSe to 14% for the CdSe/CdS. It is worth noting that there was no

significant change in the UV-Vis or PL peak (Fig. 4.18) observed upon the re-injection of the crude CdSe nanoparticles alone into the microcapillary tube, indicating that the shift observed on injecting a mixture of the as obtained CdSe nanoparticles and $[Cd(S_2CNMe^nHex)_2]$ is due to the shelling of the CdSe core with a shell of CdS. Moreover, the formation of a core/shell structure and not an alloy is confirmed by the red shift in the absorption and emission spectra. Since CdS has a larger band gap than CdSe; a CdSeS alloy nanoparticles will show a blue shift in the absorption and emission spectra compared to pure CdSe nanoparticles.

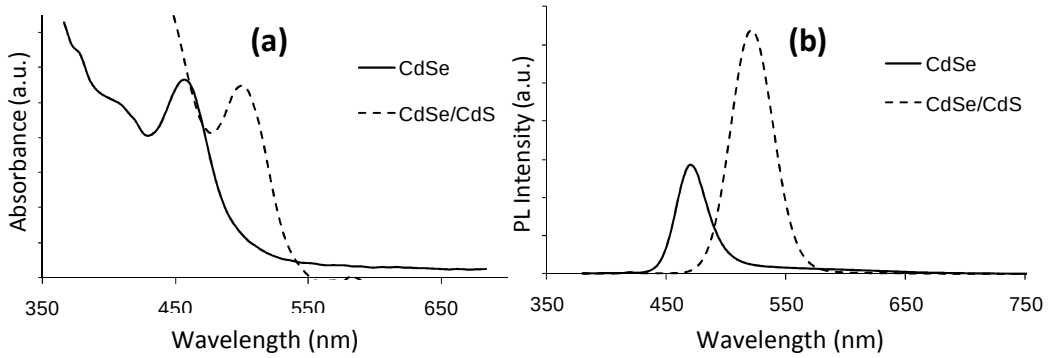

Fig. 4.17 UV-Vis spectra (a) and PL spectra (b) of the core CdSe and the CdSe/CdS core/shell.

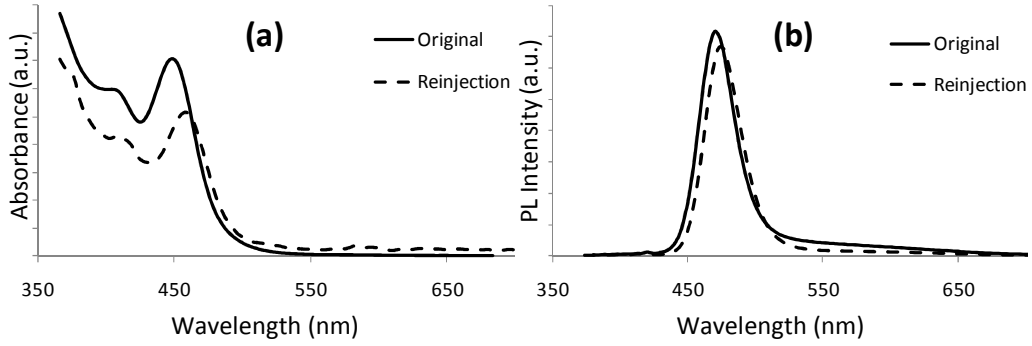

Fig. 4.18 UV-Vis spectra (a) and PL spectra (b) of the original core CdSe and core CdSe upon reinjection.

4.4.3.2 X-Ray diffraction analysis

The p-XRD patterns of CdSe and CdSe/CdS core/shell nanoparticles are shown in Fig. 4.19. The core pattern corresponds to cubic CdSe (ICDD card No. 19-0191) and the broad peaks are a confirmation of the ultra small size. The core/shell nanoparticles gave a pattern with comparatively sharper peaks than that of core pattern as expected. Also the peaks in p-XRD pattern of the CdSe/CdS nanoparticles

are slightly shifted to higher angles, towards the position of CdS suggesting that the shell growth is epitaxial, as the lattice mismatch between CdSe and CdS is only 3.9%.[9]

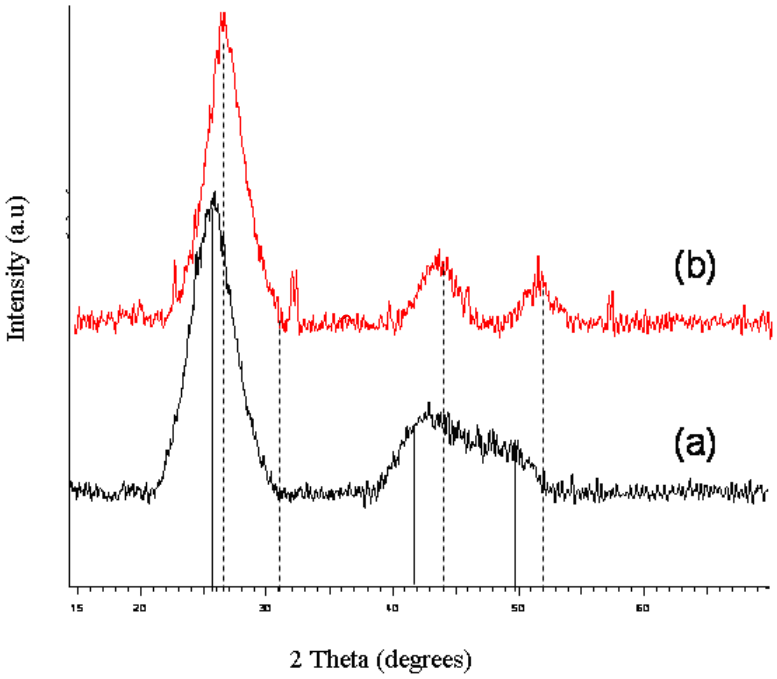

Fig. 4.19 p-XRD pattern of (a) CdSe and (b) CdSe/CdS (solid line) CdSe XRD pattern (dotted) CdS XRD pattern.

4.4.3.3 Transmission electron microscopy (TEM)

The size of the CdSe and CdSe/CdS core/shell nanoparticles measured from their TEM images (Fig. 4.20 (a) and (b)) is 2.1 ± 0.4 nm and 4.2 ± 0.7 nm, respectively. Since a single monolayer (ML) of CdS shell increases the diameter of the nanoparticles by 0.7 nm,[43] then about 3 MLs have been deposited on top of the core CdSe nanoparticles. The clear lattice planes in the HRTEM images confirm the crystalline nature of the dots. The 3.48 Å lattice spacing in CdSe nanoparticles corresponds to the (111) plane of the bulk cubic crystals consistent with the p-XRD data. Energy-dispersive X-ray analysis (EDAX) of the core/shell nanoparticles confirmed the presence of cadmium, selenium and sulfur.

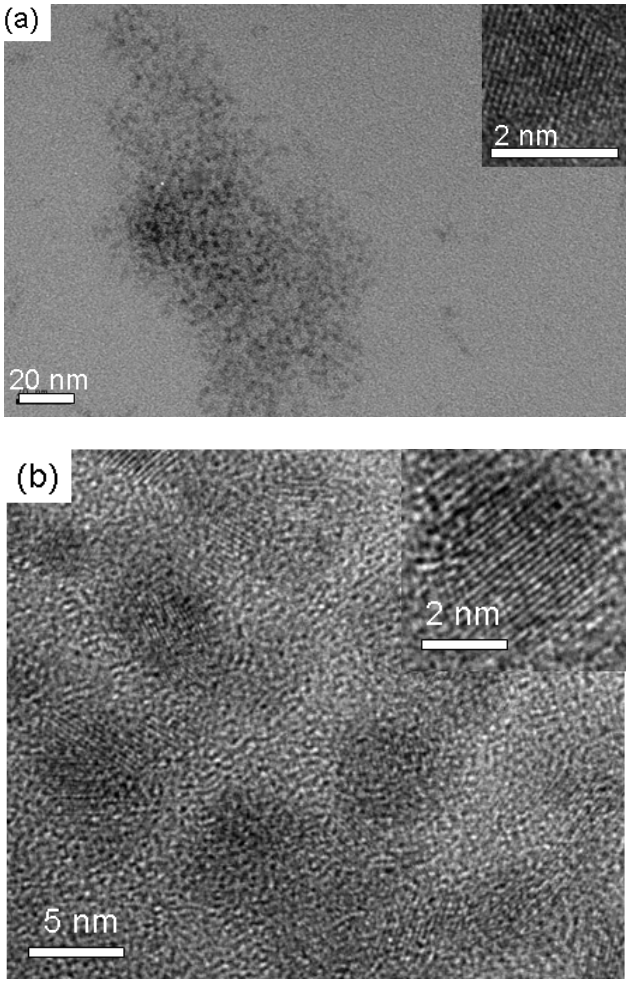

Fig. 4.20 TEM of (a) CdSe and (b) CdSe/CdS.

4.4.3.4 Effect of amount of shelling material

To study the effect of the amount of the CdS precursor, three different concentrations of $[Cd(S_2CNMe^nHex)_2]$ were investigated. From the absorption and emission spectra (Fig. 4.21) it is clear that the more CdS precursor is added the more the red shift is observed, indicating a thicker shell is formed. According to the TEM images (Fig. 4.22), the average shell thickness was 0.7 ± 0.1nm (2 MLs) for the (1 mg, 2×10^{-3} mmol), 0.95 ± 0.14 nm (~ 2.7 MLs) for the (2.5 mg, 5×10^{-3} mmol) and 1.05 ± 0.18 nm (3 MLs) for the (5 mg, 1×10^{-2} mmol) of $[Cd(S_2CNMe^nHex)_2]$. The slight broadening in the size distribution with the growth of the CdS shell is consistent with previous reports.[42] The QYs were 13%, 20% and 14%, for the 2 MLs, 2.7 MLs and 3 MLs, respectively which agrees with the previously reported results suggesting that the maximum QY for a CdSe/CdS core/shell is observed with a CdS shell between 2 and 3 MLs.[9]

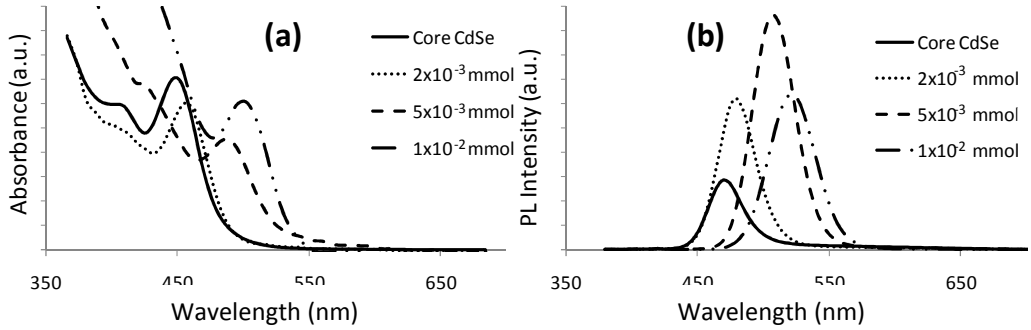

Fig. 4.21 UV-Vis spectra (a) and PL spectra (b) of the core CdSe and the CdSe/CdS core/shell using different concentrations of [$Cd(S_2CNMe^nHex)_2$].

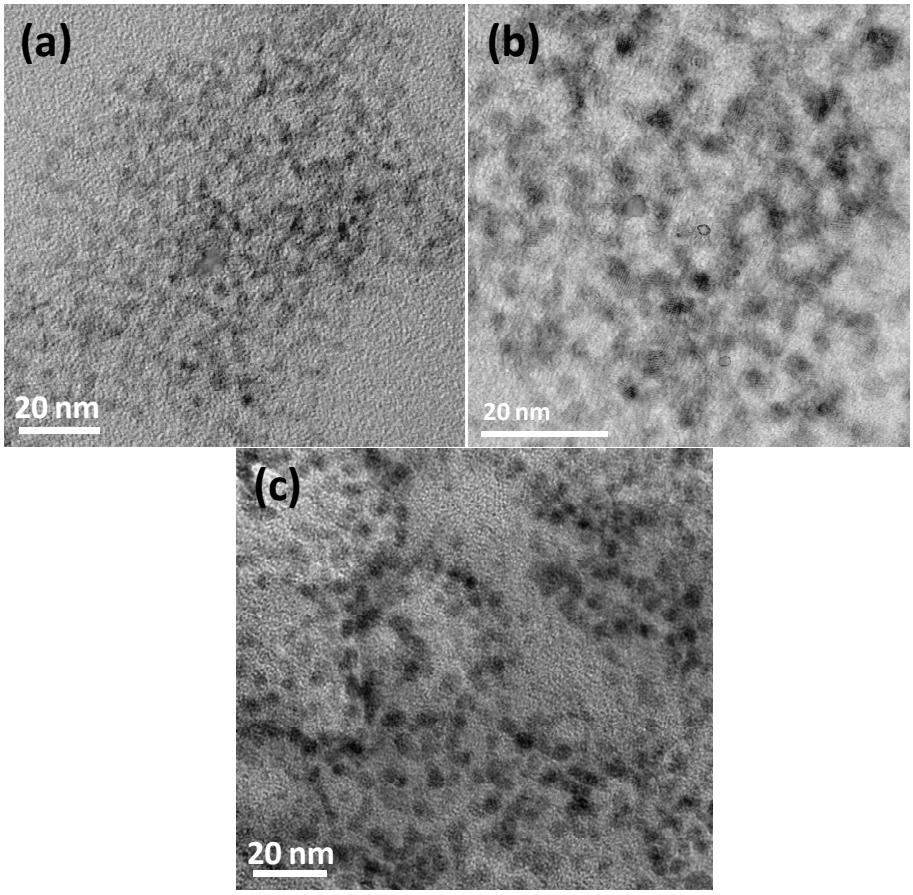

Fig. 4.22 TEM of CdSe/CdS core/shell with shell thickness of 2 MLs (a), 2.7 MLs (b) and 3 MLs (c).

4.4.3.5 Effect of shelling residence time

Using 1 × 10^{-2} mmol of [$Cd(S_2CNMe^nHex)_2$] for the shelling step at shorter residence times lead to a very small blue shift in both absorption and emission

spectra (Fig. 4.23) which refers to the formation of a slightly thinner CdS shell. Similarly, no significant change to the PL intensity was observed.

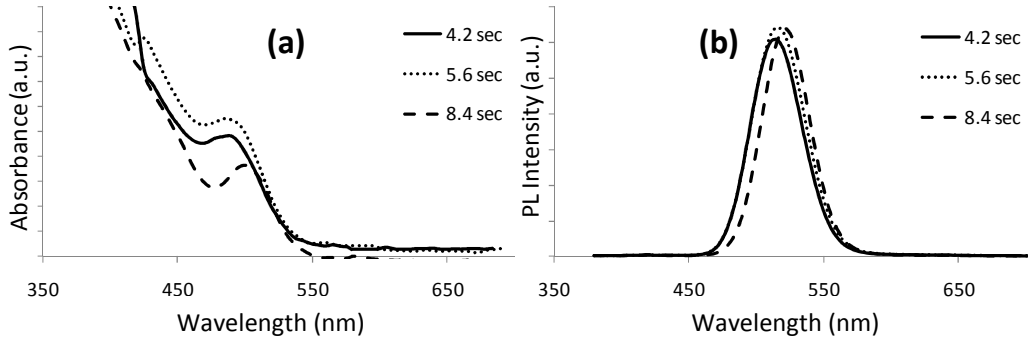

Fig. 4.23 UV-Vis spectra (a) and PL spectra (b) of CdSe/CdS core/shell prepared at different shelling residence times.

4.4.3.6 Effect of shelling temperature

The choice of the shelling temperature is critical as the growth is highly temperature dependant. It was found that for shelling small CdSe nanoparticles (< 2.7 nm) with a CdS shell, temperatures above 200 °C would result in Ostwald ripening of the core CdSe and defocusing of the size distribution, whereas shelling temperatures far below 200 °C leads to great amounts of the CdS precursor remaining unreacted in the solution with no deposition of the CdS on top of the CdSe; instead homogenous nucleation of CdS nanoparticles may take place.[41-43] In our results, shelling the CdSe nanoparticles with CdS at 160 °C did not show any significant effect on the absorption or emission spectra compared to those of the core CdSe nanoparticles (Fig. 4.24). Increasing the shelling temperature to 180 °C led to a red shift in both absorption and emission spectra and an increase in the PL intensity. In terms of QY, a shelling temperature of 200 °C is the most effective.

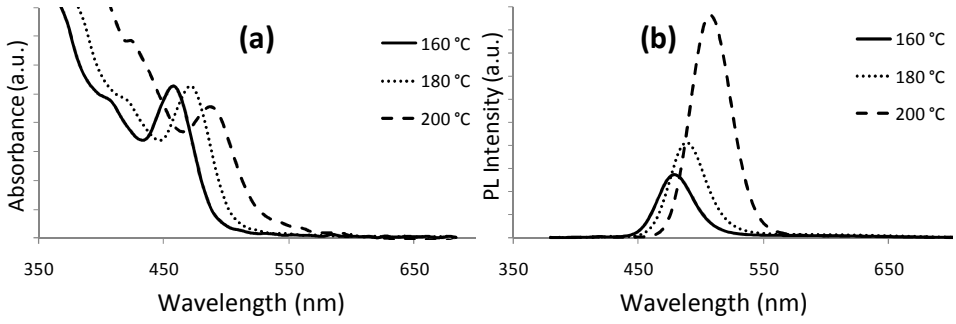

Fig. 4.24 UV-Vis spectra (a) and PL spectra (b) of CdSe/CdS core/shell prepared at 160 °C, 180 °C and 200 °C.

4.4.4 CdSeS alloy

CdSeS alloys were formed by adding three different amounts of the CdS precursor [$Cd(S_2CNMe^nHex)_2$] (5×10^{-3} mmol, 2×10^{-2} mmol and 4×10^{-2} mmol) to a fixed concentration of the CdSe precursor [$Cd(Se_2P^iPr_2)_2$]. Increasing the sulfur content in the CdSeS alloy should result in a blue shift due to its larger band gap compared to that of CdSe. Unfortunately, the total concentration was not kept constant and as a result increasing the amount of the CdS precursor resulted in a red shift (Fig. 4.25) which is probably due to increasing the size of the formed nanoparticles. Increasing the amount of the CdS precursor removed the surface traps created by the dangling bonds at the nanoparticle surface, but produced a broader and less intense emission peak. Changing the residence time had an obvious effect when the lowest amount of the CdS precursor was used (5×10^{-3} mmol) where, both absorption and emission spectra showed a continuous red shift with the increase in the residence time (Fig. 4.26). Using the highest amount of the CdS precursor (4×10^{-2} mmol) a red shift was observed by increasing the residence time from 4.2 sec to 8.4 sec (Fig. 4.27). Further increase in the residence time (16.8 sec or 33.6 sec) did not cause any more red shift. In terms of QY, a residence time between 8.4 sec to 33.6 sec results in almost same efficiency (13-15%) for the lowest CdS amount (5×10^{-3} mmol), whereas, a residence time of 8.4 sec was found to produce the highest QY (*ca.* 4 %) for the highest CdS amount (4×10^{-2} mmol).

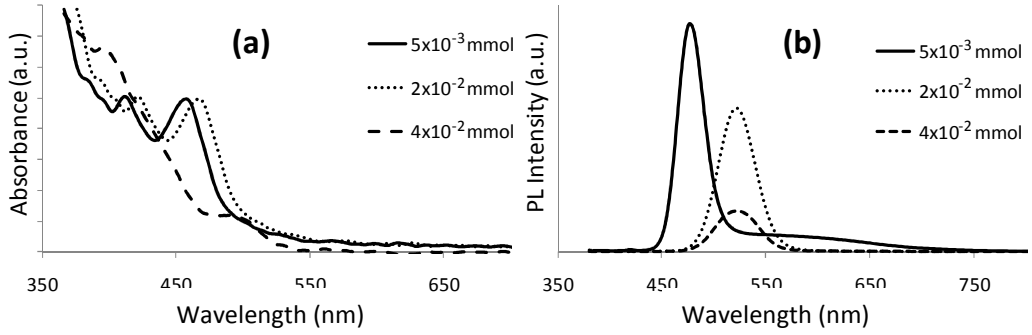

Fig. 4.25 UV-Vis spectra (a) and PL spectra (b) of CdSeS alloy prepared using different amounts of [$Cd(S_2CNMe^nHex)_2$].

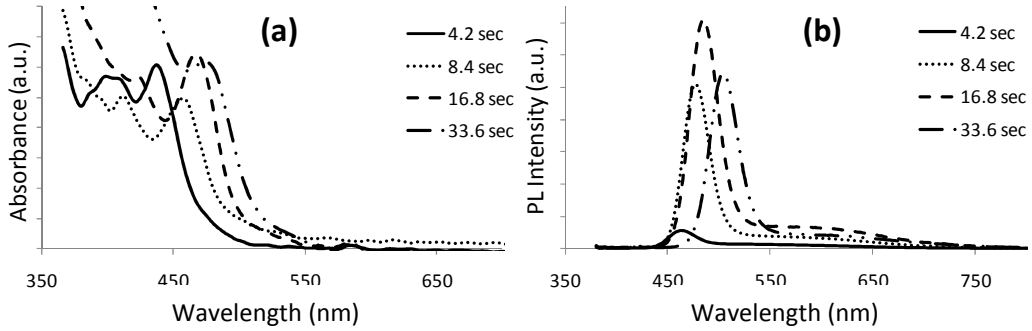

Fig. 4.26 UV-Vis spectra (a) and PL spectra (b) of CdSeS alloy prepared using 5×10^{-3} mmol of $[Cd(S_2CNMe^nHex)_2]$ at different residence times.

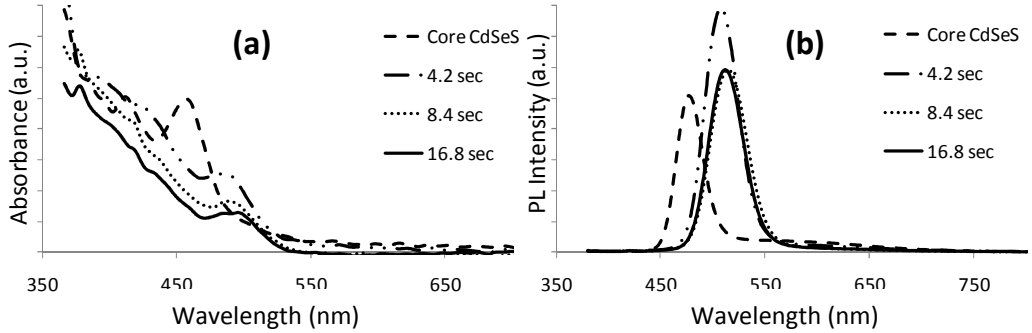

Fig. 4.27 UV-Vis spectra (a) and PL spectra (b) of CdSeS alloy prepared using 4×10^{-2} mmol of $[Cd(S_2CNMe^nHex)_2]$ at different residence times.

TEM images of the CdSeS alloys (Fig. 4.28) prepared at different flow rates using the lowest amount of the CdS precursor (5×10^{-3} mmol) revealed that a residence time of 8.4 sec or 16.8 sec produced the most monodispersed nanoparticles. Shorter (4.2 sec) or longer (33.6 sec) residence times resulted in more polydispersed and aggregated nanoparticles. Comparing the average size and the emission position of the CdSe/CdS core/shell (4.0 ± 0.6 nm emitting at 508 nm) and CdSeS alloy (5.0 ± 0.8 emitting at 476 nm), both prepared using 5×10^{-3} mmol of the CdS precursor, proves the formation of CdSeS alloy. Although the alloy is larger in size, its emission peak is blue shifted because of the incoporation of the sulfur atoms into the core of the lattice (Fig. 4.29). The d-spacing calculated from the HRTEM images (Fig. 4.30) of the samples prepared at a residence time of 8.4 sec and 16.8 sec was 3.42 Å and 3.47 Å, respectively.

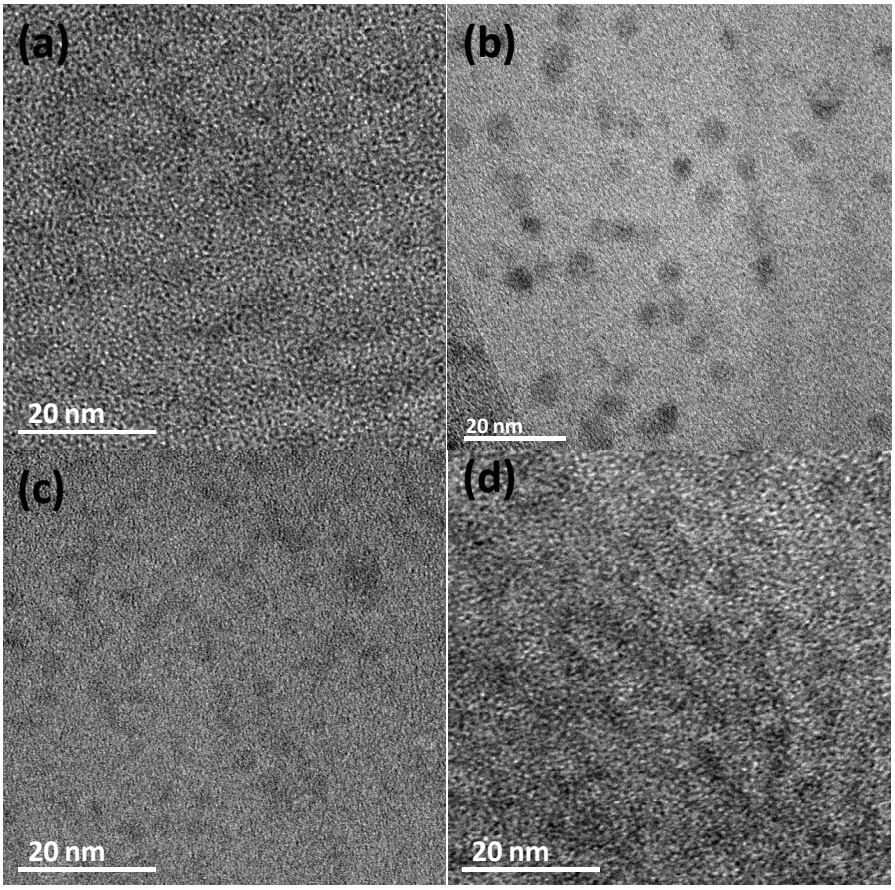

Fig. 4.28 TEM images of CdSeS nanoparticles prepared at 4.2 sec (a), 8.4 sec (b), 16.8 sec (c) and 33.6 sec (d).

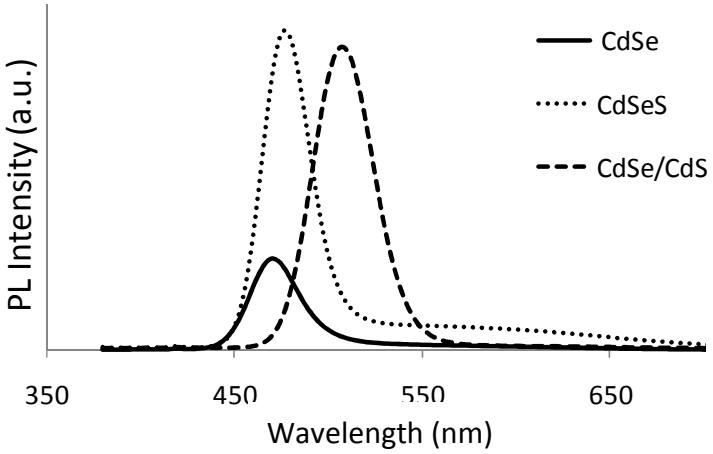

Fig. 4.29 PL spectra of CdSe, CdSeS alloys and CdSe/CdS core/shell nanoparticles.

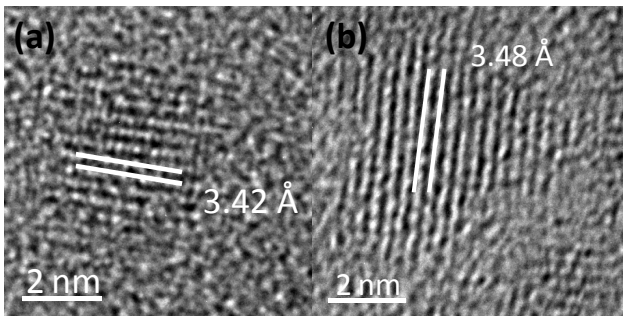

Fig. 4.30 HRTEM images of CdSeS nanoparticles prepared at 8.4 sec (a) and 16.8 sec (b).

4.4.6 Copper sulfide materials

Fig. 4.31 shows the p-XRD of the copper sulfide nanoparticles prepared at different residence times from a 1×10^{-2} M solution at 200 °C. For a residence time of 2.8 sec the p-XRD pattern could be indexed mainly to monoclinic Cu_7S_4 (roxybite) (ICDD card No. 023-0958) with minor impurities of the rhombohedral Cu_9S_5 (ICDD card No. 026-0476). Allowing the particles to spend more time in the microcapillary reactor resulted in the growth of the Cu_9S_5 phase. p-XRD patterns of the nanoparticles grown at different temperature are shown in Fig. 4.32. At a lower growth temperature (170 °C) and a residence time of 4.2 sec, pure monoclinic Cu_7S_4 nanoparticles were obtained. Increasing the temperature to 230 °C did not cause any change to the phase of the nanoparticles compared to the ones obtained at 200 °C.

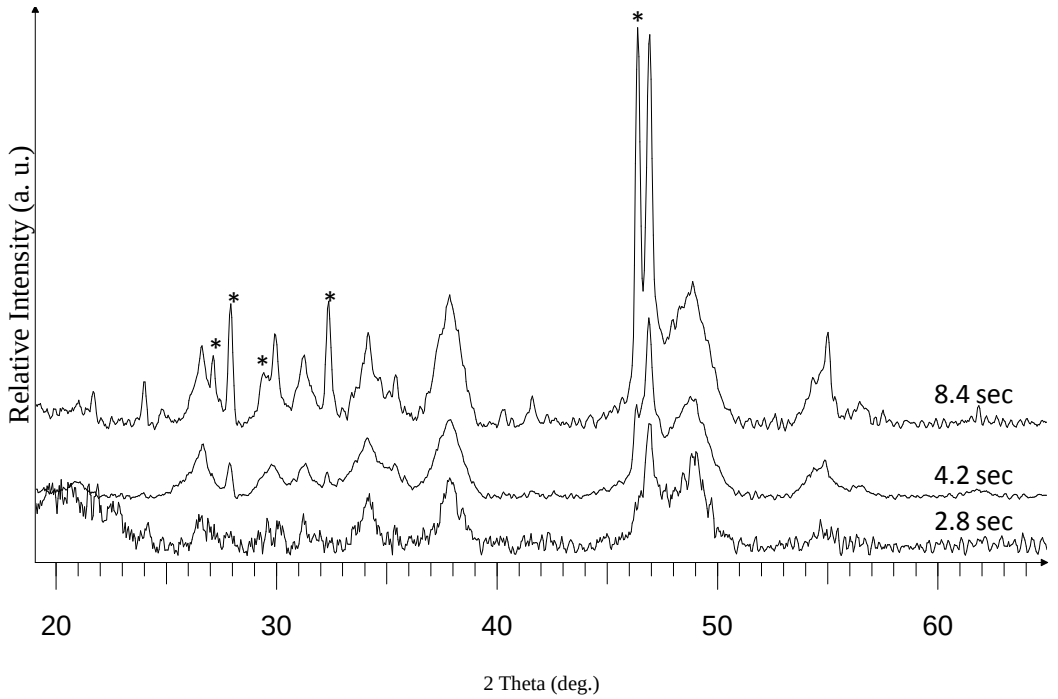

Fig. 4.31 p-XRD pattern of the copper sulfide nanoparticles synthesised at different residence times.

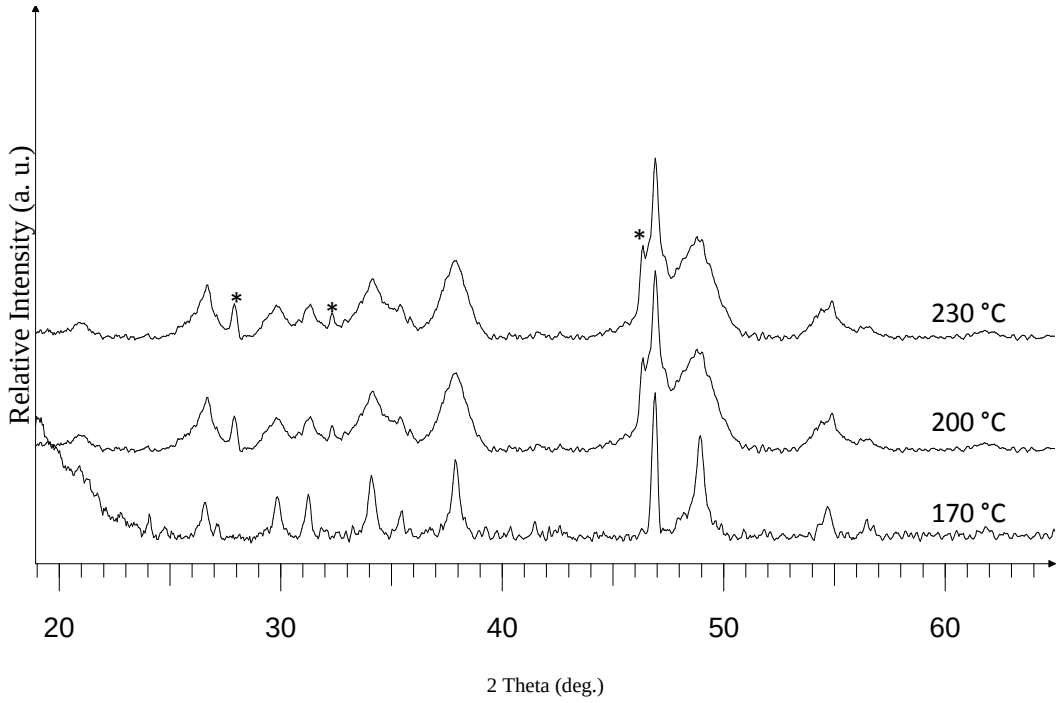

Fig. 4.32 p-XRD pattern of the copper sulfide nanoparticles synthesised at different temperatures.

The average size of the spherical nanoparticles obtained from the TEM images (Fig. 4.33) was 10.7 ± 1.9 nm for a residence time of 2.8 sec or 4.2 sec. Smaller

spherical nanoparticles with a broader size distribution (9.8 ± 2.9 nm) were obtained by increasing the residence time to 8.4 sec. Shorter residence time could probably result in short and rapid nucleation step and the separation of that nucleation step from the growth step. On the other hand, longer residence time could give the nucleation step a chance to take place over a longer period of time which means more nuclei could be formed and hence, smaller and less monodispersed particles are obtained. The defocusing of the size distribution at longer residence time could also be due to Ostwald ripening of the particles.

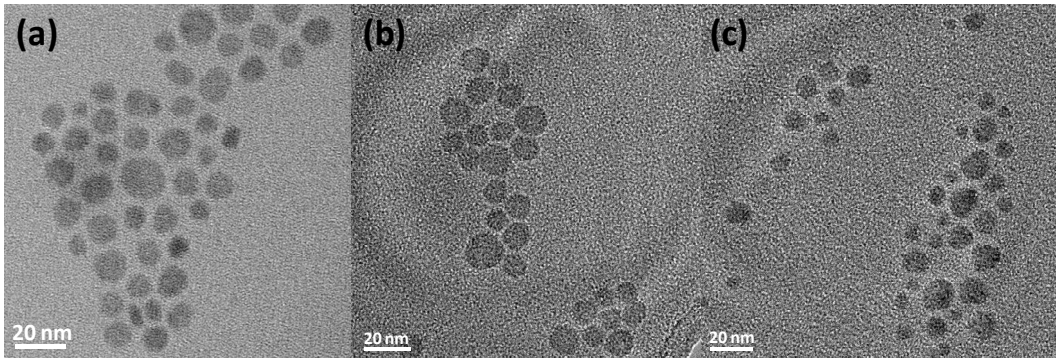

Fig. 4.33 TEM images of copper sulfide nanoparticles at residence time of 2.8 sec (a), 4.2 sec (b) and 8.4 sec (c).

As expected, the average size of the nanoparticles increased by increasing the growth temperature. The increase in the average size was accompanied with a broader size distribution. At 170 °C the obtained nanoparticles were 6.7 ± 1.6 nm in diameter which grew to 10.8 ± 1.9 nm and 11.4 ± 2.4 nm at 200 °C and 230 °C, respectively (Fig. 4.34).

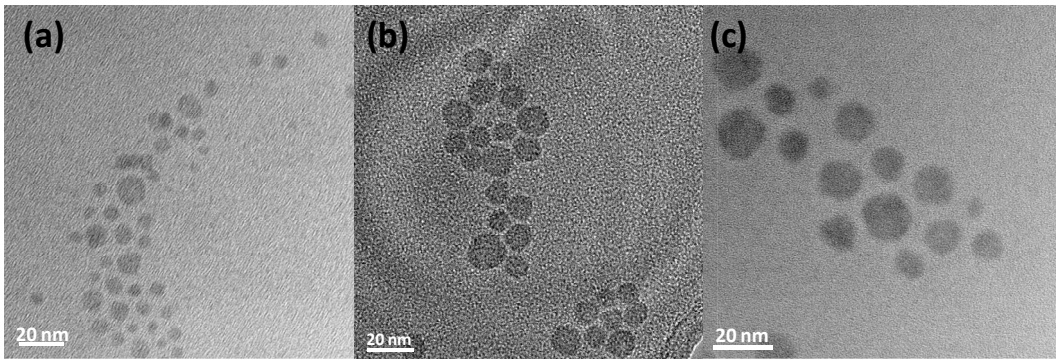

Fig. 4.34 TEM images of copper sulfide nanoparticles at 170 °C (a), 200 °C (b) and 230 °C (c).

The HRTEM images (Fig. 4.35) clearly shows a d-spacings of 1.956 Å and 3.04 Å, which correspond to the (0 16 0) and the (8 0 4) planes of the monoclinic Cu_7S_4, respectively, or to the (1 1 0) and the (1 0 7) planes of the rhombohedral Cu_9S_5, respectively.

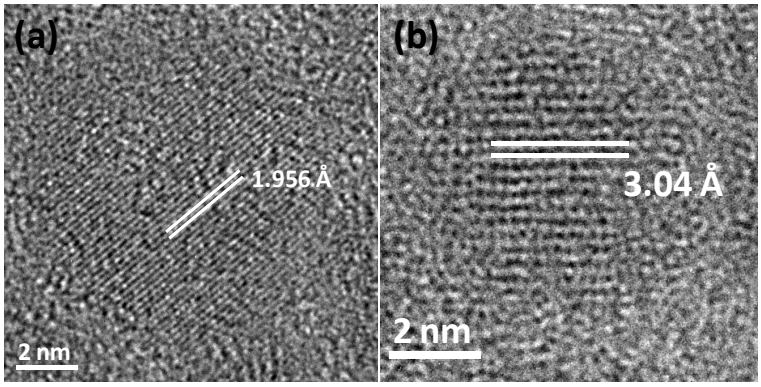

Fig. 4.35 HRTEM images of copper sulfide nanoparticles.

In the batch method synthesis, the Cu_7S_4 nanoparticles had a spherical morphology only at a high temperature (280 ºC) and a long reaction time (1 hour), whereas lower thermolysis temperatures and shorter reaction times produced trigonal and hexagonal nanodisks. As mentioned earlier, synthesis in microcapillary tubes provides efficient heat transfer because of the high surface area to volume ratio of the microchannels and hence, the temperature and reaction time required for the synthesis of spherical nanoparticles can be reduced.

4.5 Conclusion

The synthesis of different nanoparticles (CdSe, CdS, CdSe/CdS core/shell, CdSeS alloy and Cu_7S_4) in chip microreactor and/or microcapillary tubes is reported. The microcapillary tubes were found to be more efficient than the chip microreactor for the synthesis of monodispersed CdSe nanoparticles, hence, it was used for the synthesis of the rest of the above mentioned nanoparticles. Blue emitting, OLA capped CdSe nanoparticles were synthesised from the single source precursor $[Cd(Se_2P^iPr_2)_2]$. $[Cd(S_2CNMe^nHex)_2]$ proved to be a good candidate as a single source precursor for the synthesis of CdS nanoparticles or CdS shell on top of CdSe nanoparticles. CdSeS alloys were synthesised by mixing the two precursors in OLA. Spherical monoclinic Cu_7S_4 nanoparticles, either as a pure phase or with minor impurities of Cu_9S_5, were obtained from a solution of $[Cu(SON(CN^iPr_2)_2)_2]$ in OLA.

Compared to the conventional batch method, continuous flow synthesis in microreactors provides more efficient control on the different reaction parameters. Moreover, it provides an efficient and satisfactory route for the synthesis of small bluish-luminescent nanoparticles with good control over size dustribution.

4.6 References

1. M. Bruchez, M. Moronne, P. Gin, S. Weiss, A. P. Alivisatos, *Science*, 1998, **281**, 2013.
2. M. Y. Han, H. X. Gao, J. Z. Su, S. Nie, *Nat. Biotechnol.*, 2001, **19**, 631.
3. I. Gur, N. A. Fromer, M. L. Geier, A. P. Alivisatos, *Science*, 2005, **310**, 462.
4. W. U. Huynh, J. J. Dittmer, A. P. Alivisatos, *Science*, 2002, **295**, 2425.
5. L. E. Brus, *J. Chem. Phys.*, 1986, **90**, 2555.
6. L. Qu, X. Peng, *J. Am. Chem. Soc.*, 2002, **124**, 2049.
7. X. G. Peng, L. Manna, W. D. Yang, J. Wickham, E. Scher, A. Kadavanich, A. P. Alivisatos, *Nature*, 2000, **404**, 59.
8. C. B. Murray, D. J. Norris, M. G. Bawendi, *J. Am. Chem. Soc.*, 1993, **115**, 8706.
9. X. Peng, M. C. Schlamp, A. V. Kadavanich, A. P. Alivisatos, *J. Am. Chem. Soc.*, 1997, **119**, 7019.
10. Z. A. Peng, X. Peng, *J. Am. Chem. Soc.* 2001, **123**, 183.
11. Z. A. Peng, X. Peng, *J. Am. Chem. Soc.* 2002, **124**, 3343.
12. P. Reiss, J. Bleuse, A. Pron, *Nano Lett.*, 2002, **2**, 781.
13. X. Zhong, Y. Feng, Y. Zhang, *J. Phys. Chem. C*, 2007, **111**, 526.
14. L. Qu, Z. A. Peng, X. Peng, *Nano Lett.*, 2001, **1**, 333.
15. L. Xu, K. Chen, H. M. El-Khair, M. Li, X. Huang, *Appl. Surface Sci.*, 2001, **172**, 84.
16. N. N. Maseko, N. Revaprasadu, V. S. R. R. Pullabhotla, R. Karthik, P. O'Brien, *Mater. Lett.*, 2010, **64**, 1037.
17. J. Jasieniak, C. Bullen, J. van Embden, P. Mulvaney, *J. Phys. Chem. B* 2005, **109**, 20665.
18. S. Sapra, A. L. Rogach, J. Feldmann, *J. Mater. Chem.*, 2006, **16**, 3391.
19. Y. Wei, J. Yang, A. W. H. Lin, J. Y. Ying, *Chem. Mater.*, 2010, **22**, 5672.
20. T. Trindade, P. O'Brien, *Adv. Mater.*, 1996, **8**, 161.
21. T. Trindade, P. O'Brien, *Chem. Mater.* 1997, **9**, 523.
22. B. Ludolph, M. A. Malik, P. O'Brien, N. Revaprasadu, *Chem. Commun.*, 1998, 1849.
23. M. A. Malik, N. Revaprasadu, P. O'Brien, *Chem. Mater.* 2001, **13**, 913.

24. D. J. Crouch, P. O'Brien, M. A. Malik, P. J. Skabara, S. P. Wright, *Chem. Commun.,* 2003, 1454.
25. S. L. Cumberland, K. M. Hanif, A. Javier, G. A. Khitrov, G. F. Strouse, S. M. Woessner, C. S. Yun, *Chem. Mater.,* 2002, **14**, 1576.
26. J. Huang, M. V. Kovalenko, D. V. Talapin, *J. Am. Chem. Soc.,* 2010, **132**, 15866.
27. E. M. Chan, R. A. Mathies, A. P. Alivisatos, *Nano. Lett.,* 2003, **3**,199.
28. H. Nakamura, Y. Yamaguchi, M. Miyazaki, H. Maeda, M. Uehara, P. Mulvaney, *Chem. Comm.* 2002, 2844.
29. H. Nakamura, A. Tashiro, Y. Yamaguchi, M. Miyazaki, T. Watari, H. Shimizu, H. Maeda, *Lap Chip,* 2004, **4**, 237.
30. S. Krishnadasan, J. Tovilla, R. Vilar, A. J. deMello, J. C. deMello, *J. Mater. Chem.,* 2004, **14**, 2655.
31. B. K. H. Yen, N. E. Stott, K. F. Jensen, M. G. Bawendi, *Adv. Mater.,* 2003, **15**, 1858.
32. E. M. Chan, A. P. Alivisatos, R. A. Mathies, *J. Am. Chem. Soc.,* 2005, **127**, 13854.
33. B. K. H. Yen, A. Günther, M. A. Schmidt, K. F. Jensen, M. G. Bawendi, *Angew. Chem. Int. Ed.,* 2005, **44**, 5447.
34. S. Marre, J. Park, J. Rempel, J. Guan, M. G. Bawendi, K. F. Jensen, *Adv. Mater.,* 2008, **20**, 4830.
35. H. Yang, W. Luan, S-T. Tu, Z. M. Wang, *Lap Chip,* 2008, **8**, 451.
36. H. Yang, W. Luan, S-T. Tu, Z. M. Wang, *Cryst. Growth Des.,* 2009, **9**, 1569.
37. A. Toyota, H. Nakamura, H. Ozono, K. Yamashita, M. Uehara, H. Maeda, *J. Phys. Chem. C,* 2010, **114**, 7527.
38. A. H. Fischer, M. Giersig, *Langmuir,* 1992, **8**, 1475.
39. J. B. Edel, R. Fortt, J. C. deMello, A. J. deMello, *Chem. Commun.,* 2002, 1136.
40. H. Yang, W. Luan, Z. Wan, S-T. Tu, W-K. Yuan, Z. M. Wang, *Cryst. Growth Des.,* 2009, **9**, 4807.
41. J. van Embden, J. Jasieniak, D. E. Gomez, P. Mulvaney, M. Giersig, *Aust. J. Chem.,* 2007, **60**, 457.
42. J. van Embden, J. Jasieniak, P. Mulvaney, *J. Am. Chem. Soc.,* 2009, **131**, 14299.

43. J. J. Li, Y. A. Wang, W. Guo, J. C. Keay, T. D. Mishima, M. B. Johnson, X. Peng, *J. Am. Chem. Soc.*, 2003, **125**, 12567.
44. N. Revaprasadu, M. A. Malik, P. O'Brien, G. Wakefield, *Chem. Commun.*, 1999, 1573.
45. V. V. Breus, C. D. Heyes, G. U. Nienhaus, *J. Phys. Chem. C,* 2007, **111**, 18589.
46. D. Battaglia, J. J. Li, Y. Wang, X. Peng, *Angew. Chem. Int. Ed.*, 2003, **42**, 5035.
47. D. Chen, F. Zhao, H. Qi, M. Rutherford, X. Peng, *Chem. Mater.*, 2010, **22**, 1437.
48. H. Wang, X. Li, M. Uehara, Y. Yamaguchi, H. Nakamura, M. Miyazaki, H. Shimizu, H. Maeda, *Chem. Commun.*, 2004, 48.
49. H. Wang, H. Nakamura, M. Uehara, Y. Yamaguchi, M. Miyazaki, H. Maeda, *Adv. Funct. Mater.*, 2005, **15**, 603.
50. W. Luan, H. Yang, N. Fan, S-T. Tu, *Nanoscale Res. Lett.*, 2008, **3**, 134.
51. M. D. Regulacio, M-Y. Han, *Acc. Chem. Res.*, 2010, **43**, 621.
52. L. A. Swafford, L. A. Weigand, M. J. Bowers, J. R. McBride, J. L. Rapaport, T. L. Watt, S. K. Dixit, L. C. Feldman, S. J. Rosenthal, *J. Am. Chem. Soc.*, 2006, **128**, 12299.
53. N. Al-Salim, A. G. Young, R. D. Tilley, A. J. McQuillan, J. Xia, *Chem. Mater.*, 2007, **19**, 5185.
54. J. Ouyang, M. Vincent, D. Kingston, P. Descours, T. Boivineau, Md. B. Zaman, X. Wu, K. Yu, *J. Phys. Chem. C,* 2009, **113**, 5193.
55. H. Lee, S. W. Yoon, E. J. Kim, J. Park, *Nano Lett.*, 2007, **7**, 778.
56. Y. Wu, C. Wadia, W. Ma, B. Sadtler, A. P. Alivisatos, *Nano Lett.*, 2008, **8**, 2551.
57. Q. Lu, F. Gao, D. Zhao, *Nano Lett.* 2002, **2**, 725.
58. W. Du, X. Qian, X. Ma, Q. Gong, H. Cao, J. Yin, *Chem. Eur. J.*, 2007, **13**, 3241.
59. M. Sigman, A. Ghezelbash, T. Hanrath, A. E. Saunders, F. Lee, B. A. Korgel, *J. Am. Chem. Soc.*, 2003, **125**, 16050.
60. A. Ghezelbash, B. A. Korgel, *Langmuir*, 2005, **21**, 9451.
61. H. Zhang, Y. Zhang, J. Yu, D. Yang, *J. Phys. Chem. C,* 2008, **112**, 13390.

62. Y. Wang, Y. Hu, Q. Zhang, J. Ge, Z. Lu, Y. Hou, Y. Yin, *Inorg. Chem.* 2010, **49**, 6601.
63. A. Tang, S. Qu, K. Li, Y. Hou, F. Teng, J. Cao, Y. Wang, Z. Wang, *Nanotechnology*, 2010, **21**, 285602.
64. N. Pradhan, B. Katz, S. Efrima, *J. Phys. Chem. B,* 2003, **107**, 13843.
65. B. Geng, X. Liu, J. Ma, Q. Du, *Mater. Sci. Eng. B,* 2007, **145**, 17.
66. W. P. Lim, C. T. Wong, S. L. Ang, H. Y. Low, W. S. Chin, *Chem. Mater.*, 2006, **18**, 6170.
67. Z. Liu, D. Xu, J. Liang, J. Shen, S. Zhang, Y. Qian, *J. Phys. Chem. B,* 2005, **109**, 10699.
68. N. Revaprasadu, M. Malik, P. O'Brien, *S. Afr. J. Chem.*, 2004, **57**, 40.
69. X. S. Du, Z. Z. Yu, A. Dasari, J. Ma, Y. Z. Meng, Y. W. Mai, *Chem. Mater.*, 2006, **18**, 5156.
70. C. Q. Naguyen, M. Afzaal, M. A. Malik, M. Helliwell, J. Raftery, P. O'Brien, *J.Organomet. Chem.*, 2007, **692**, 2669.
71. K. Ramasamy, M. A. Malik, P. O'Brien, J. Raftery, *Dalton Trans.*, 2010, **39**, 1460.
72. W. W. Yu, L. Qu, W. Guo and X. Peng, *Chem. Mater.*, 2003, **15**, 2854.
73. N. L. Pickett, P. O'Brien, *Chem. Res.*, 2001, **1**, 467.
74. M. Lazell, P. O'Brien, *Chem. Commun.*, 1999, 2041.
75. M. Lazell, S. J. Norager, P. O'Brien, N. Revaprasadu, *Mater. Sci. Eng. C,* 2001, **16**, 129.

Chapter 5

General Experimental

5.1 Chemicals

Dodecanethiol (DDT) was purchased from Fluka. All other reagents were purchased from Sigma-Aldrich chemical company and used as received. Solvents were distilled prior to use.

5.2 Powder X-ray diffraction (p-XRD)

p-XRD studies were performed on a Bruker AXS D8 diffractometer using Cu-Kα radiation. The samples were mounted flat and scanned between 10 to 80° in a step size of 0.05 with a count rate of 9 sec.

5.3 Transmission electron microscopy (TEM), high resolution TEM (HRTEM) and selected area electron diffraction (SAED)

TEM, HRTEM and SAED were performed using Tecnai F30 FEG TEM instrument, operating at 300 kV. Nanoparticle samples (in toluene) were simply drop casted onto lacey carbon copper grids.

5.4 Electron tomography

Electron tomography data was obtained using a JEOL 2100 TEM at 200kV for tilt angles of ±70° and tomographic reconstruction was performed using the IMOD software.[1]

5.5 Energy-dispersive X-ray spectroscopy (EDAX)

EDAX was performed using a SEM Philips XL 30FEG and a DX4 instrument.

5.6 UV-Vis spectroscopy

The absorption spectra were recorded on a UV-Vis spectrophotometer (Thermo Spectronic Helios Beta) in the wavelength range of 400-1000 nm.

5.7 Photoluminescence spectroscopy (PL)

PL spectra were recorded on fluoroSENS–fluorimeter.

5.8 Quantum yields (QY)

QYs were determined by comparison of the integrated fluorescence intensity of nanoparticles dispersion in toluene with that of standard dye solutions (of known QY) with the same optical density at the excitation wavelength.

5.9 References

1. J. R. Kremer, D. N. Mastronarde, J. R. McIntosh, *J. Struct. Biol.* 1996, **116**, 71.

Chapter 6

Conclusion and Future Work

6.1 Conclusion

Current interest in nanoparticles is due to their unique chemical and physical properties which arise at critical dimensions usually best measured in nanometres. Various devices have been fabricated based on nanoparticles, including solar cells, light emitting diodes, sensors, optical detectors, quantum dot lasers and memory units. An ideal, synthetic route should produce a highly crystalline nanoparticle with a narrow size distribution. The thermal decomposition method, hot-injection in particular, has been widely exploited as major route for nanoparticle synthesis with superior control over size and shape of the synthesised nanoparticles. Single source precursors have shown some advantages in nanoparticles synthesis, including overcoming the need to use hazardous compounds such as $CdMe_2$, most of the single source precursors are air and moisture stable, have lower decomposition temperature and help maintaining the stoichiometries of metal and chalcogen.

Synthesis in microfluidic reactors has also been investigated for nanoparticles synthesis due to its potential for superior levels of control. Therefore, single source precursors have been prepared and used for the synthesis of different nanomaterials in the hot-injection method and/or in the microfluidic reactors route.

The second chapter discusses the use of 1,1,5,5-tetra-*iso*-propyl-2-thiobiuret complexes of copper, nickel, iron, zinc, cadmium and indium as single source precursors for the first time for the synthesis of the corresponding metal sulfide nanoparticles by thermolysis in different solvent/capping agent combinations. Copper sulfide (Cu_7S_4) nanoparticles were obtained with different morphologies (spherical, hexagonal disks, and trigonal disks) depending on the reaction conditions. The disk morphology of nanocrystals was confirmed by TEM tilting experiments and electron tomography. Ni_3S_4 and Fe_7S_8 nanoparticles were obtained by the thermolysis of nickel and iron precursors, respectively, in different solvent/capping agent combinations. The morphology of the materials was controlled by changing the injection solvent, capping agent, growth temperature or precursor concentration.

Ni_3S_4 nanoparticles can be obtained in the form of wires, rods, spheres or tetrahedrons. Fe_7S_8 can also be obtained in different morphologies (spheres, rods or plates). The synthesised ZnS and CdS nanoparticles mostly had a cubic crystal structure and a spherical morphology. However, the hexagonal phase could be obtained by controlling the reaction conditions. Ultra-thin (< 1.0 nm) nanorods or nanowires of β-In_2S_3 were synthesized from the thermolysis of the indium precursor in hot oleylamine.

The third chapter described the use of a combination of the 1,1,5,5-tetra-*iso*-propyl-2-thiobiuret complexes for the synthesis of alloy and ternary nanoparticles. Cubic $Zn_xCd_{1-x}S$ nanoparticles were synthesised from the thermolysis of a mixture of the cadmium and zinc precursors in different solvent/capping agent combinations. The lattice spacing of the $Zn_xCd_{1-x}S$ nanoparticles showed a very good agreement with Vegard's law. The optical properties of the $Zn_xCd_{1-x}S$ nanoparticles were highly dependent on the ZnS to CdS precursor ratio and the solvents/capping agents. $CuInS_2$ nanoparticles were synthesized by the thermal decomposition of a 1:1 mixture of copper and indium precursors in different solvent/capping agent combinations. The structure (chalcopyrite or wurtzite) and morphology (spherical, hexagonal, trigonal or conical) of the $CuInS_2$ nanoparticles could be controlled by manipulating the ratios between the solvent and capping agent and or temperature.

The fourth chapter details the synthesis of CdS, CdSe, CdSe/CdS, CdSeS and $Cu_{2-x}S$ nanoparticles in a chip and/or microcapillary reactor. The microcapillary tubes were found to be more efficient than the chip microreactor for the synthesis of monodispersed CdSe nanoparticles; hence, it was used for the synthesis of the rest of the above mentioned nanoparticles. Blue emitting, oleylamine-capped CdSe nanoparticles were synthesised from the single source precursor $[Cd(Se_2P^iPr_2)_2]$, whereas, $[Cd(S_2CNMe^nHex)_2]$ was used as a single source precursor for the synthesis of CdS nanoparticles or CdS shell on top of CdSe nanoparticles. CdSeS alloys were synthesised by mixing the two precursors in oleylamine. Spherical monoclinic Cu_7S_4 nanoparticles, either as a pure phase or with minor impurities of Cu_9S_5, were obtained from a solution of $[Cu(SON(CN^iPr_2)_2)_2]$ in oleylamine.

To summarise, $[M(SON(CN^iPr_2)_2)_n]$ (M = Cu, Ni, Fe, Zn, Cd or In, n = 2,3) have been demonstrated to be good candidates for the synthesis of crystalline, pure

phase and monodispersed metal sulfide, $Zn_xCd_{1-x}S$ and $CuInS_2$ nanoparticles. The thermolysis of the thiobiuret precursors could produce nanoparticles with different morphologies by controlling the reaction conditions (precursor's concentration, growth temperature, reaction time and injection solvent/capping agent combination). Continuous synthesis of CdSe nanoparticles in microcapillary reactors has been shown to be easier than in chip microreactors in terms of the quality of the produced nanoparticles and flexibility of the microreactor. CdS, CdSe, CdSe/CdS, CdSeS and $Cu_{2-x}S$ nanoparticles were successfully synthesised in a microcapillary reactor by the thermolysis of $[Cd(S_2CNMe^nHex)_2]$, $[Cd(Se_2P^iPr_2)_2]$ and $[Cu(SON(CN^iPr_2)_2)_2]$.

6.2 Future Work

In order to further the role of thiobiuret complexes as single source precursors, future work could focus on exploring more of the dithiobiuret complexes. Complexes of other metals such as lead, gallium, silver and tin with thio- and dithiobiuret ligands could be investigated. In addition, quaternary nanoparticles such as $CuIn_{1-x}Ga_xS_2$ and Cu_2ZnSnS_4 nanoparticles may possibly be investigated.

All the above mentioned precursors could be studied in both hot-injection method and microfluidic synthesis. However, the continuous synthesis in microfluidic reactors requires more improvement in terms of the experimental set up in order to provide uniform velocity in the microchannels, prevent the microchannels blockage and permit the use of a wider range of solvents and surfactants.

Appendix

Characterisation of precursors:

[Cu(SON(CN^{i}Pr$_2$)$_2$)$_2$]: Yield 1.0 g (52.08 %), mpt: 169 °C. Elemental analysis: Calc. for $C_{28}H_{56}N_6O_2S_2Cu$: C, 52.8; H, 8.8; N, 13.2; S, 10.0; Cu, 9.9 %. Found: C, 52.5; H, 9.2; N, 12.9; S, 9.9; Cu, 10.3 %.

[Ni(SON(CN^{i}Pr$_2$)$_2$)$_2$]: Yield 0.90 g (46.4 %), mpt : 177 °C. Elemental analysis: Calc. For $C_{28}H_{56}N_6S_2O_2Ni$: C, 53.2; H, 8.8; N, 13.3; S, 10.1; Ni, 9.2 %. Found: C, 53.0; H, 9.1; N, 13.2; S, 10.0; Ni, 9.0 %.

[Fe(SON(CN^{i}Pr$_2$)$_2$)$_3$]: Yield 0.8 g (43 %), mpt: 159 °C. Elemental analysis: Calc. for $C_{42}H_{84}N_9S_3O_3Fe$: C, 55.1; H, 9.1; N, 13.7; S, 10.5; Fe, 6.1 %. Found: C, 54.6; H, 9.2; N, 13.2; S, 9.8; Ni, 6.3 %.

[Zn(SON(CN^{i}Pr$_2$)$_2$)$_2$]: Yield 1.30 g (67 %), mpt : 298 °C. Elemental analysis: Calc. for $C_{28}H_{56}N_6S_2O_2Zn$: C, 52.7; H, 8.7; N, 13.1; S, 10.0; Zn, 10.2 %. Found: C, 53.2; H, 9.0; N, 13.2; S, 9.6; Zn, 10.0 %.

[Cd(SON(CN^{i}Pr$_2$)$_2$)$_2$]: Yield 1.49 g (72 %), mpt : 109 °C. Elemental analysis: Calc. for $C_{28}H_{56}N_6S_2O_2Cd$: C, 49.0; H, 8.1; N, 12.2; S, 9.3; Cd, 16.4 %. Found: C, 48.6; H, 8.2; N, 11.8; S, 9.0; Cd, 15.8 %.

[In(SON(CN^{i}Pr$_2$)$_2$)$_3$]: Yield 1.0 g, (50 %) mpt : 156 °C. Elemental analysis: Calc. for $C_{42}H_{84}N_9S_3O_3In$: C, 51.8; H, 8.6; N, 12.9; S, 9.8; In, 11.8 %. Found: C, 50.9; H, 9.0; N, 12.6; S, 8.8; In, 11.3 %.

[Cd(S$_2$CNMe^{n}Hex)$_2$]: Yield 10.8 g, (74.4 %) mpt : 74 °C. Elemental analysis: Calc. for $C_{16}H_{32}N_2S_4Cd$: C, 39.0; H, 6.5; N, 5.7; S, 26.0; Cd, 22.8%. Found: C, 38.0; H, 6.4; N, 5.5; S, 25.2; Cd, 23.6%.

[Cd(Se$_2$P^{i}Pr$_2$)$_2$]: Yield 2.5 g, (74.5 %) mpt : 200 °C. Elemental analysis: Calc. for $C_{12}H_{28}P_2Se_4Cd$: C, 21.8; H, 4.3; P, 9.4; Cd, 17.0%. Found: C, 22.7; H, 4.3; P, 9.39; Cd, 16.4%.

[(Cd(Se$_2$PPh$_2$)$_2$)$_2$]: Yield 3.4 g, (85.1 %) mpt : 309 °C. Elemental analysis: Calc. for $C_{48}H_{40}P_4Se_8Cd_2$: C, 36.1; H, 2.5; P, 7.8; Cd, 14.1%. Found: C, 36.1; H, 2.5; P, 7.5; Cd, 13.9%.

[Cd($Se_2P^tBu_2$)$_2$]: Yield 3.2 g, (89.1 %) mpt : 247 °C. Elemental analysis: Calc. for $C_{16}H_{36}P_2Se_4Cd$: C, 26.7; H, 5.1; P, 8.6; Cd, 15.6%. Found: C, 26.7; H, 5.1; P, 8.7; Cd, 15.7%.

List of Publications

- **Ahmed Lutfi Abdelhady**, Karthik Ramasamy, Mohammad A. Malik, Paul O'Brien, Sarah Haigh, James Raftery, "New Routes to Copper Sulfide Nanostructures and Thin Films" *J. Mater. Chem.,* 2011, 21, 17888.
- **Ahmed Lutfi Abdelhady**, Mohammad Afzaal, Mohammad A. Malik, Paul O'Brien, "Flow Reactor Synthesis of CdSe, CdS, CdSe/CdS, and CdSeS Nanoparticles from Single Molecular Precursor(s)" *J. Mater. Chem.,* 2011, 21, 18768.
- **Ahmed Lutfi Abdelhady**, Mohammad A. Malik, Paul O'Brien, "Nickel and Iron Sulfide Nanoparticles from Thiobiurets" *J. Phys. Chem. C,* (submitted).
- **Ahmed Lutfi Abdelhady**, Mohammad A. Malik, Paul O'Brien, "Colloidal Synthesis of ZnS, CdS and $Zn_xCd_{1-x}S$ Nanoparticles from Zinc and Cadmium Thiobiuret Complexes" *Chem. Eur. J.,* (submitted).
- **Ahmed Lutfi Abdelhady**, Mohammad A. Malik, Paul O'Brien, "*iso*-Propylthiobiuret-Copper and Indium Complexes as Novel Precursors for Colloidal Synthesis of $CuInS_2$ Nanoparticles" *J. Mater. Chem.*, (submitted).
- Mateusz Banski, Mohammad Afzaal, Artur Podhorodecki, Jan Misiewicz, **Ahmed Lutfi Abdelhady**, Paul O'Brien, "Optical proof of shell formation on $NaYF_4:Eu^{3+}$ nanocrystals" *J. Phys. Chem. C,* (submitted).
- Masood Akhtar, **Ahmed Lutfi Abdelhady,** M. Azad Malik, Paul O'Brien, "Deposition of Iron Sulfide Thin Films by AACVD from Single Source Precursors", *J. Cryst. Growth,* (submitted).

List of Presentations

- CdSe and CdSe/CdS Nanoparticles from Single Molecular Precursors in Microfluidic Reactor. **A. Abdelhady**, Mohammad Afzaal, Mohammad A. Malik and Paul O'Brien, 42^{nd} IUPAC international congress, Glasgow, 2-7, Aug 2009.